Diss. ETH No. 18009

Gas-Phase and Solution-State Chemistry
of Copper(I) Bis-oxazoline Complexes

A dissertation
submitted to the

SWISS FEDERAL INSTITUTE OF TECHNOLOGY
ETH ZÜRICH

for the degree of
Doctor of Sciences
in the subject of
Physical-Organic Chemistry

presented by

Eva Maria Zocher
Dipl.-Chem. Univ., University of Regensburg
born January 3rd, 1980
citizen of Germany

accepted on the recommendation of

Prof. Dr. Peter Chen, examiner
Prof. Dr. Detlef Günther, co-examiner

Zürich, 2008

"Things should be explained as simply as possible,
but no simpler."

Albert Einstein
(1879–1955)

Acknowledgements

I am very grateful to *Prof. Dr. Peter Chen* for supervising my PhD within the multifarious research activities of his working-group. I am not only indebted for the broadening of my chemical scope in this time but also for the freedom I got to pursue own research ideas. Prof. Chen was always a great source of inspiration providing stimulating impulses when needed. In addition I would like to acknowledge the precise correction reading of my dissertation.

I also want to express my gratitude to my co-examiner *Prof. Dr. Detlef Günther* for the great interest in my thesis and the friendly atmosphere during the PhD exam.

A special thanks goes to *Dr. Rolf Dietiker* for the virtuosic technical introduction on our very important measurement instrument TSQ-700. Besides I am indebted to *Heinz Benz* who solved a lot of electronic problems on this machine and even more to *René Dreier* for fabricating a 24-pole for ion thermalization with the required modifications. This project was realized in cooperation with *Dr. Esther Quintanilla* and *Dr. Erik Couzijn*. Especially Erik has to be set apart for his enormous kindness to help me also with the layout settings of my dissertation.

Furthermore, it was a great pleasure to have *Ueli Neuenschwander* and *Raphael Sigrist* as co-workers during their research-internship and I am happy to list Raphael as co-author on one of my publications.

As sort of a regular distraction from our lab work I would like to thank for the funny and "most challenging" table soccer games with *Marc-Etienne Moret*, being frighteningly good in this "sport", as well as with Dr. Luca Castiglioni and Sebastian Torker.

In particular *Dr. Luca Castiglioni* shall be acknowledged for motivating the whole Chen-group to participate in the famous SOLA-relay whereas *Sebastian Torker* guaranteed no interruption in our physical workout by organizing skiing-trips, snow-shoe hikes and mountain climbing events. In this context I am especially indebted to *Michael Gasser* for giving me in Davos some gratis skiing lessons.

Alexey Fedorov I cannot only praise as excellent Salsa-dancing partner but also for the exciting trip he organized for our group to Moscow and St. Petersburg. Our leisure time activities were completed with several friendly invitations of *Dr. Marc*

Bornand to homely video-evenings at his place and some culinary excursions in the Persian cuisine offered by *Dr. Fereshteh Rouholahnejad*. A very entertaining city trip to Amsterdam initiated by *Dr. Chris Slootweg* within the framework of his PhD defense at Vrije Universiteit Amsterdam I would like to mention as well.

In general I can say, I experienced in the Chen-group a very friendly working atmosphere for which I want to thank my colleagues *Jonas Hostettler*, *Dr. Fabio DiLena*, *Dr. Xueyi Chen*, *Dr. Xiangyang Zhang*, *Yu-Ying Lai* and *Déborah Mathis* as well as the more recently arrived group members *Dr. Jann Frey*, *Laurent Batiste* and *Marija Jovic*. I wish especially *Dr. Andreas Bach* a lot of fun and success with supervising the daily-issues of the whole working-group since Prof. Dr. Peter Chen became Vice-President of ETH Zurich.

Special thanks go to our technician *André Müller* for the synthesis of some catalyst precursors, to *Luca Cereghetti* for the computer administration and to our secretaries *Yvonne Ogg*, *Mirella Rutz* and formerly *Annette Ryter* doing silently all the paperwork, which ensured my regular income.

Moreover I am very much obliged to *Dr. Sven Augner* from Bruker Biospin GmbH (Rheinstetten) for the rapid retrieval of a gratis three-month trial version of DNMR, necessary to complete my PhD research.

Finally, I want to thank my parents who continuously supported me over the years and provided me with constructive criticism or encouragement whenever I needed it.

Published Parts of this Thesis

Reviewed Articles

- "Energy-Resolved Collision-Induced Dissociation Cross Sections of 2:1 Bis-oxazoline Copper Complexes. Nonbonded Interactions and Nonlinear Effects"
  Eva Zocher, Rolf Dietiker, and Peter Chen
  Journal of the American Chemical Society **2007**, *129*, 2476–2481

- "Threshold CID Investigation of Isomeric Cu(I) Azabox Complexes"
  Eva Zocher, Raphael Sigrist, and Peter Chen
  Inorganic Chemistry **2007**, *46*, 11366–11370

Conference

- "Mass Spectrometric Measurements of Ligand-Metal Binding Energies for 2:1 Bis-oxazoline Copper Complexes. Nonbonded Interactions and Nonlinear Effects"
  Eva Zocher, Rolf Dietiker, and Peter Chen
  Presented at the *International Conference on Reactive Intermediates and Unusual Molecules (ISRIUM)* Ascona, August 19–24, **2007**

Table of Contents

Abstract

Electrospray tandem mass spectrometry is a very versatile tool for generating and selectively studying reactive intermediates in the gas-phase. Especially when combined with a higher order multipole like the new constructed (RF-)24-pole for thermalization of the reactant ions to a narrow kinetic energy distribution quantitative energy resolved collision induced dissociation (CID) measurements can be performed with high precision.

As chemical target system for this dissertation 2:1 bisoxazoline copper(I) complexes have been chosen. This ligand system appears repeatedly in enantioselective catalysis and opens the possibility to homo- and heterochiral metal ligand combinations being the basic prerequisite for the occurrence of nonlinear effects in asymmetric catalysis.

For the mass spectrometric investigation *pseudo*-enantiomeric chiral ligands are used with different alkyl-labels at the remote site of the ligand backbone. This allows to distinguish via mass difference between the otherwise diastereomeric 2:1 bisoxazoline copper complexes. From the experimental CID threshold curves absolute binding energies of one bidentate ligand to the respective 1:1 copper bisoxazoline fragment can be extracted. Therewith detailed insights in the influence of isopropyl- versus phenyl-substituents as steric groups on the geometrically and electronically different bisoxazoline and aza-bisoxazoline ligands could be gained. Usually the heterochiral complexes were found to be more stable in case of solely repulsive steric interactions, whereas the homochiral analogues can invert the ordering when long-range, nonbonded interactions provide sufficient stabilization.

Interestingly in solution a different situation prevails. π–π Stacking interactions were confirmed to be considerably diminished by competing CH–π interactions between solvent molecules and the aromatic substituents. Additionally, the optimal gas-phase geometry of those complexes is configurationally restricted, which is entropically unfavorable in solution. In contrast congruent solution-state stabilities compared to the respective gas-phase binding energies can only be expected when the structural properties of the noncovalently bound complexes are preserved in both media.

Concerning the originally aimed prediction of nonlinear effects in catalysis the kinetic and thermodynamic complex stabilities were found to differ remarkably. Contrarily to the commonly in the literature accepted 1:1 bisoxazoline copper complex, a 14-electron species, serving as the active catalyst for the catalytic turnover and being presumably generated in the ligand exchange process, this understanding has to be redefined. The results of this dissertation indicate instead a multistep ligand exchange process with initial rupture of only one Cu–N bonding and subsequent association of a second ligand. The 14-electron species is presumably too high in energy and therefore it is neither generated during the metal ligand equilibration of the homo- and heterochiral complexes nor on the way to the carbene formation. Instead associative pathways are preferred in solution.

The discrepancy of the CID-threshold results in comparison the observed nonlinear effects with nonenantiopure bisoxazoline ligands catalyzing asymmetric cyclopropanation reactions clearly demonstrates the failure of the so far accepted but too much simplified mechanistic model. Additionally the measured metal ligand binding energies present very valuable benchmark values, especially when nonbonded interactions like π–π stacking effects play a role. Those noncovalent interactions are evidently poorly described by DFT calculations, which are common practice for such large organometallic complexes, though.

Consequently experimentally determined absolute ligand binding energies provide highly reliable thermodynamic parameters of species presumably acting as reactive intermediates and therewith leading to their definite identification or exclusion. Besides the refinement of the catalytic model for copper bisoxazoline complexes a detailed understanding of specific binding effects like π–π stacking interactions in the gas phase as well as in solution state lead to a significantly improved mechanistic picture.

Zusammenfassung

Elektrospray-Tandem-Massen-Spektrometrie ist eine sehr nützliche Methode um reaktive Zwischenstufen selektiv in der Gasphase zu erzeugen und zu untersuchen. Insbesondere wenn Multipole höherer Ordnung wie der neu konstruierte (RF) 24-Pol zur Thermalisierung der Ionen eingesetzt werden kann eine enge kinetische Energieverteilung der zu studierenden Ionen erreicht werden. Dies ermöglicht eine präzise Bestimmung der Energieabhängigkeit von kollisionsinduzierten Dissoziationen der Ausgangsionen.

Als chemisches System für diese Studien wurden 2:1 Bisoxazolin-Kupfer-Komplexe gewählt. Dieses Ligandensystem hat einen hohen Stellenwert in der enantioselektiven Katalyse und kann homo- und heterochirale Metall-Liganden-kombinationen ausbilden, was eine Grundvoraussetzung für das Auftreten nicht linearer Effekte in der asymmetrischen Katalyse ist.

Um Liganden ungleicher Chiralität massenspektrometrisch unterscheiden zu können, wurden sie an einer möglichst unwesentlichen Stelle am Ligandenrückgrat mit unterschiedlichen Alkylgruppen dekoriert, wodurch die ansonsten diastereomeren homo- und heterochiralen 2:1 Bisoxazolin-Kupfer-Komplexe durch eine leicht veränderte Ionenmasse unterscheidbar werden. Ausgehend von den experimentell bestimmten kollisionsinduzierten Dissoziations-Schwellenmessungen können dann die absoluten Bindungsenergien jeweils eines bidentaten Liganden zu den ent-sprechenden verbleibenden 1:1 Kupfer-Bisoxazolin-Fragmenten bestimmt werden. Dies erlaubt detaillierte Einblicke in die spezifischen Einflüsse von Isopropyl- versus Phenylsubstituenten als sterische Reste an den ausserdem geometrisch und elektronisch differierenden Bisoxazolin- und Azabisoxazolin-Liganden. Im Fall von einzig und allein sterisch repulsiven Wechselwirkungen zwischen den Liganden sind

üblicherweise die heterochiralen Komplexe stabiler als ihre homochiralen Pendante, wohingegen weitreichende, dispersive Wechselwirkungen bei genügend starker Ausprägung diese Einteilung invertieren können.

Interessanterweise herrscht in Lösung eine ganz andere Situation vor. Aromatische Wechselwirkungen werden durch konkurrierende CH–π Interaktionen zwischen den Lösungsmittelmolekülen und den Phenylsubstituenten erwartungs-gemäss merklich vermindert. Folglich ist die optimale Gasphasen-Geometrie jener Komplexe eine von vielen möglichen Konfigurationen in Lösung, die unter Einbeziehung der Lösungsmittelmoleküle nicht einmal notwendigerweise die entropisch günstigste Anordnung darstellt. Übereinstimmende Komplexstabilitäten in Lösung und in Gasphase sind daher nur zu erwarten, wenn die strukturellen Eigenheiten der nicht kovalent gebundenen Komplexe in beiden Medien möglichst identisch wären.

Um auf die ursprünglich angestrebte Vorhersagbarkeit von nicht linearen Effekten in der Katalyse zurückzukommen, muss in diesem Zusammenhang darauf hingewiesen werden, dass sich die kinetischen und die thermodynamischen Komplexstabilitäten drastisch voneinander unterscheiden. Die in der Literatur weit verbreitete Annahme, dass die 1:1 Bisoxazolin-Kupfer-Einheit, ein 14-Elektronen-Komplex, die aktive Katalysatorspezies darstellen würde, die den Katalysezyklus durchläuft und auch während der Ligandenaustauschprozesse am Metall generiert würde, muss grundsätzlich revidiert werden. Die Resultate dieser Dissertation lassen vielmehr auf einen mehrstufigen Ligandenaustauschprozess schliessen, wobei in einem ersten Schritt nur eine Kupfer-Stickstoff-Bindung gebrochen wird, sodass unmittelbar darauf folgend ein weiterer Ligand die freigewordene Koordinations-stelle belegen kann. Die zuvor genannte 14-Elektronenspezies ist höchstwahr-scheinlich energetisch zu hoch angesiedelt, weshalb sie weder während des Ligandenaustauschprozesses zwischen homo- und heterochiralen Komplexen noch als Zwischenstufe bei der Bildung des Carbens eine Rolle spielt. Stattdessen sind in Lösung assoziative Reaktionspfade klar bevorzugt.

Die Diskrepanz zwischen den Dissoziations-Schwellenmessungen und den beobachteten nicht linearen Effekten für nicht enantiomerenreine Bisoxazolin-Kupfer katalysierte Cyclopropanierungen zeigt deutlich, dass das bisherige mechanistische Modell zu stark vereinfacht ist und daher den Katalysezyklus nicht korrekt beschreibt. Zusätzlich stellen die gemessenen Metall-Liganden-Bindungsenergien

natürlich wertvolle Richtwerte dar, die besonders bei auftretenden aromatischen Wechselwirkungen mit den üblichen DFT-Berechnungen, wie sie für grosse organometallische Komplexe üblich sind, nur unzureichend wiedergegeben werden können.

Folglich liefern die gemessenen absoluten Ligandenbindungsenergien sehr verlässliche thermodynamische Erkenntnisse über reaktive Spezies, deren Rolle als tatsächliche Zwischenstufen somit belegt oder begründet verworfen werden kann. Neben der Verfeinerung des katalytischen Modells für Kupfer-Bisoxazolin-Komplexe trugen zudem Informationen über spezielle Bindungseffekte wie aromatische Wechselwirkungen in der Gasphase und in Lösung wesentlich zu einer Verbesserung des mechanistischen Gesamtbildes bei.

Part I

The Role of Bisoxazoline Ligands in

Enantioselective Catalysis

Chapter 1

Development of the Ligand Backbone

1.1 Classification of the most common chiral Nitrogen Donor Ligands

Enantioselective homogeneous catalysis is one of the most efficient ways of introducing asymmetry in organic synthesis. Most prominent examples are the Sharpless oxidation[1] and the enantioselective hydrogenation with chiral rhodium[2] and ruthenium[3] phosphine complexes of Noyori and Knowles, which were awarded 2001 with the Nobel prize.

In the laboratory of Noyori also the first example of an enantioselective cyclopropane formation was found in 1966: under the influence of the chiral salicylaldiminato copper complex **5** (Figure 1.1) achiral olefins and diazo-compounds were converted to optically active cyclopropane derivates.[4] Although the optical yields were low; these results were of crucial importance for the development of enantioselective catalysis as they demonstrated the general principle that a homogeneous metal catalyst can generate enantioselective products upon complexation with a chiral ligand.

5
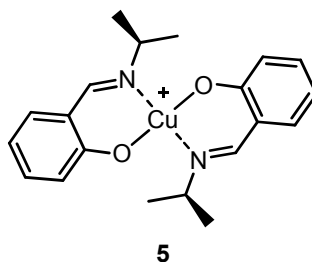
Figure 1.1 Copper(I) catalyst of the first asymmetric cyclopropanation

Subsequently numerous research groups started evaluating various metal-ligand systems to improve the selectivity of this useful C–C bond forming reaction. Bidentate nitrogen donor ligands turned out to be particularly successful for this purpose. For example copper(I) complexes of polypyrazolylborates **6** (Scheme 1.1) were discovered to catalyze cyclopropanation reactions of alkenes with moderate selectivities[5] and to also activate carbene, nitrene and oxo-transfer reactions to form cyclopropenes, aziridines and epoxides.[6]
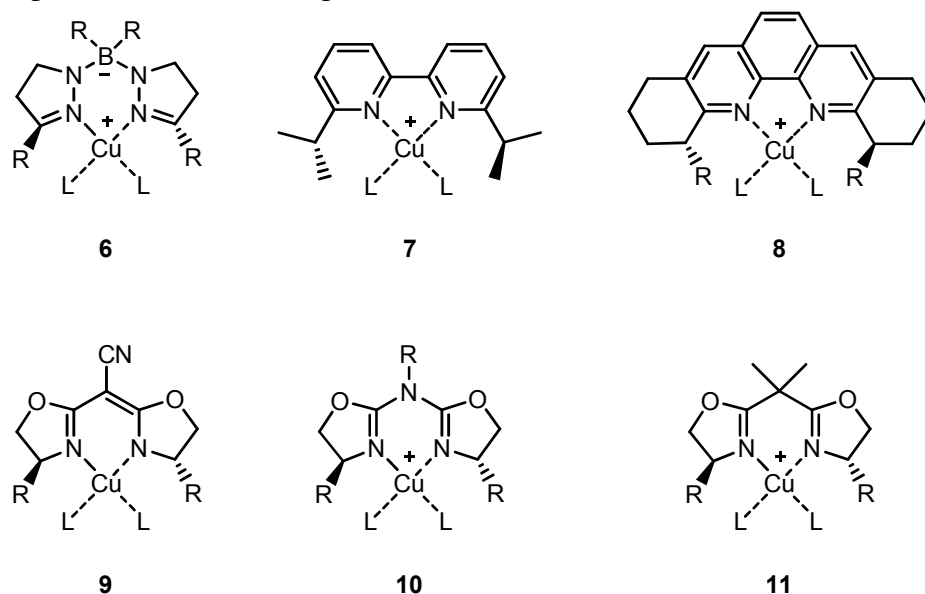
Scheme 1.1 Copper catalysts with bidentate nitrogen donor ligands

Besides the negatively charged borate ligands also the chiral and neutral bipyridines **7**[7] and phenantrolines **8**[8] catalyze in presence of a Cu(I) source cyclopropanations with good selectivities. However, those ligand classes are certainly inferior compared to semicorrin **9,** aza-semicorrin **10** and especially bisoxazoline ligands **11** (displayed as the respective Cu(I) complexes in Scheme 1.1).

Semicorrins and aza-semicorrins were first published by Pfaltz et al. in 1986.[9] They successfully applied semicorrins for cyclopropanation reactions either directly with a copper(I) salt or when starting from Cu(II) by *in situ* reduction due to the diazo-compound or via addition of a reducing agent like phenylhydrazine. Additionally cobalt(II) semicorrin complexes were found to catalyze the reduction of α,β-unsaturated carboxylic esters to the corresponding saturated esters in basically quantitative yield and with high enantiomeric excess.[10]

In contrast, aza-semicorrins or more commonly named aza-bisoxazolines have proven to be particular useful for allylic substitutions[11] and cyclopropanations.[12]

Slightly after the preparation of the semicorrins Evans[13] and Masamune[14] succeeded with the synthesis of bisoxazoline ligands. This was a further evolution of non-symmetric ligand systems containing only one chiral oxazoline ring (ligand **12**, Figure 1.2) like in *e.g.* [Rh(COD)**12**]PF$_6$ complexes which were invented by Brunner et al.[15] end of the 80's for enantioselective hydrosilylations and hydrogenations.

12
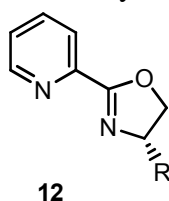
Figure 1.2 A well known mono-oxazoline ligand.[15]

However, the fewer possible reaction channels for C2-symmetric bisoxazoline ligands greatly simplify the prediction of chiral induction and thus favors this ligand class for the rational designing of a specific enantioselective catalyst.

Especially bisoxazoline ligands can be adjusted to their respective catalytic purpose not only by variation of the stereochemical substituents R but also the bridging part between the two oxazoline rings can be chosen rather flexible: a pyridyl-ring offers a third coordination site (ligand **13**, Scheme 1.2) whereas other ligands with zero, one or two carbons are known in the literature. Pybox ligands **13** are useful for asymmetric cyclopropanations,[16] carboxylations,[17] aldol-reactions[18] and allylic oxidations.[19] In contrast ligand **15** is suitable for cyclopropanations,[20] hydrosilylations[21] and allylic substitutions[22] whereas the acetonid-protected "Weinsäure" derivative **14** with its special chiral backbone was found to catalyze cyclopropanations[23] and hydrosilylations[24] successfully.

13   **14**   **15**
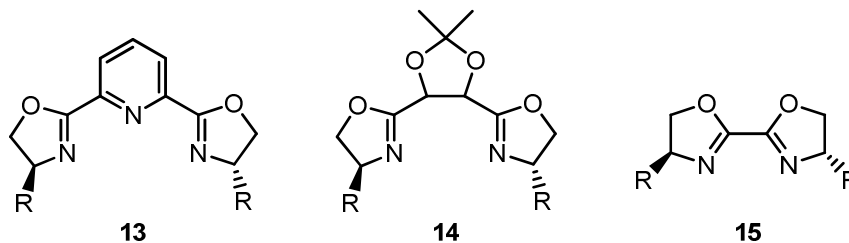
Scheme 1.2 Special bisoxazoline ligands

Bisoxazoline ligands with one bridging carbon (Scheme 1.1, ligand **11**) are by far the most prominent bidentate nitrogen donor ligands, that can form stable complexes

with a large variety of metal ions such as Cu^+, Cu^{2+}, Ag^+, Ni^{2+}, Fe^{3+}, Ru^{2+}, Rh^+, Zn^{2+}, Mg^{2+}, Pd^{2+}, Ir^+ and Li^+.[25] The nitrogen–metal cation–nitrogen bite angle of the bisoxazoline ligands can be ideally adjusted to the size of *e.g.* very small ions like Li^+ by using cycloalkylidenes as spacers whereas metals with larger radii like Ru^{2+} are best complexed by methylene-bridged box ligands.[26] The isopropylidene-connected analogs range between these two extremes.

As divers as the complexed metals is the applicability of these ligands to asymmetric catalytic reactions. In 1991 Evans et al. published the first cyclopropanation of alkenes with copper(I) bisoxazolines[13] and Corey presented an enantioselective diels-alder reaction with an iron(III) bisoxazoline complex.[27] From thereon, bisoxazoline catalyzed aziridinations, aldol reactions, michael-additions, allylic substitutions, hetero-diels-alder-, radical- and ene-reactions, 1,3-dipolar cycloadditions, rearrangements, oxidations, transfer hydrogenations and even an asymmetric version of the CLICK-reaction followed in quick succession.[25,28]

More detailed information about the applicability of oxazolines and semicorrines is collected in review articles of Jørgensen,[25] Pfaltz[10,29] and Reiser.[30]

1.2   Numbering of Compounds

The enantioselective catalyst for the above (Chapter 1.1) listed transformations is conveniently generated in situ from metal salts and free chiral ligand with the disadvantage of not precisely knowing how the active catalyst species looks like.

Certainly the coordinatively saturated 2:1 ligand to copper complexes can be excluded to play this important part; instead they comprise an inactive reservoir from which the much less abundant active species are generated and to which they can return. Crystal structures (as well as DFT geometry optimizations) additionally point out the steric shielding of the metal center in *e.g.* 2:1 pybox[18] or semicorrin[31] copper(II) complexes. Thus, all evidence indicates that the catalytically active metal complexes presumably show a 1:1 stochiometry with one bisoxazoline ligand (if the complex is mononuclear). However, this is solely a plausible assumption with little experimental evidence for or against it.

For many of the under Chapter 1.1 named reactions discrete intermediates and detailed mechanisms are not known; for example the first direct observation of a

copper(I) carbenoid has only recently been accomplished by Straub and Hofmann[32] who designed a highly basic and sterically demanding iminophosphanamide ligand for this purpose.

In contrast for the very common bisoxazoline copper(I) complexes which catalyze cyclopropanations with high enantiomeric excess neither the carbene nor any other intermediate could be studied separately so far.

Consequently ESI-MS Tandem Mass Spectrometry (see Chapter 4 and 6) is applied in this thesis to selectively investigate the 2:1 and 1:1 ligand to copper complexes of the following privileged bisoxazoline (**1**, **2**) and aza-bisoxazoline (**3**, **4**) ligand families (Figure 1.3).

(a) R = H
(b) R = Me
(c) R = Et
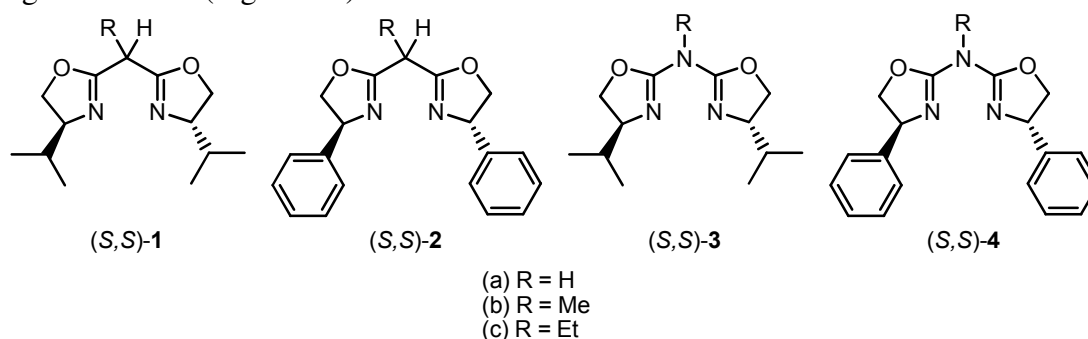
Figure 1.3   Selected bisoxazoline ligands for detailed mechanistic studies

The choice of Cu^+ as central metal opens the possibility to compare the gas-phase results with the solution state reactivity during an aziridination or, even more interestingly, during a cyclopropanation, which can be regarded as "the" classical asymmetric benchmark reaction for bisoxazolines.[25]

The reasoning for this decision is certainly dominated by the importance of enantioselective cyclopropane ring formations in natural product and medical drug development[33] but also corroborated by the difficulty in observing *e.g.* Cu(II) complexes with ESI-MS. Instead repeatedly Cu(I) complexes are obtained, which is attributed to redox reactions occurring during the spray process.[34] Therefore, even with these slight practical limitations which are not disadvantageous, a highly interesting test system, namely copper(I) (aza-)bisoxazoline complexes, could be selected for detailed gas-phase and solution chemical investigations.

1.3   Synthesis

For the selected bisoxazoline and aza-bisoxazoline ligands (see Chapter 1.2) several different and partly very elegant synthetic routes are known in the literature. All these synthetic procedures have one thing in common: the chiral information is implemented via enantiomerically pure β-aminoalcohols which are either gained by reduction of the natural or synthetic α-aminoacids or by asymmetric aminohydroxylation of alkenes.

The synthesis of bisoxazolines can be roughly classified in two categories; either the starting educt contains already the future methylene bridge and reaction with the β-aminoalcohol yields the oxazoline rings in a final cyclisation step or an oxazoline and a dihydrooxazole are separately prepared and coupled in the last reaction step.

For the first possibility several variants exist,[25] starting for example from the dicarboxylic acid chloride **16** which is reacted with two equivalents of the β-aminoalcohol **17** to give the corresponding bis-amide **18** (See Scheme 1.3). This key intermediate is then cyclized to the corresponding bisoxazoline **19** by activation of the hydroxyl groups with mesyl-[35] or tosyl-chloride,[36] chlorination,[37,13] under Mitsunobu conditions[38] or when reacting with the Burgess reagent.[39]
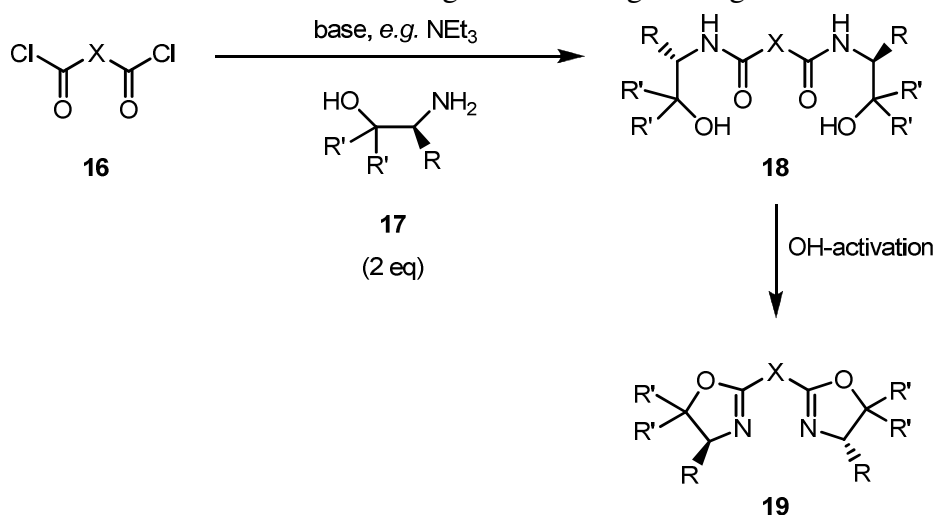
Scheme 1.3 Synthesis of bisoxazolines with bis-amide **18** as intermediate

In comparison a very convenient approach is the one step synthesis[40] starting from the dicarboxylic acid **20** which is *in situ* transformed to the acid chloride or to the *O*-triphenylphosphoniumester. This is immediately trapped by the β-amino-alcohol yielding the amide. Its carbonyl groups are subsequently activated to

O-triphenylphosphoniumamides so that the final cyclisation to bisoxazoline **19** can take place. (See Scheme 1.4). Remarkable is the stereogenic inversion of the carbon formerly bearing the hydroxy-group. Unfortunately this especially elegant method is not applicable to all substrates.
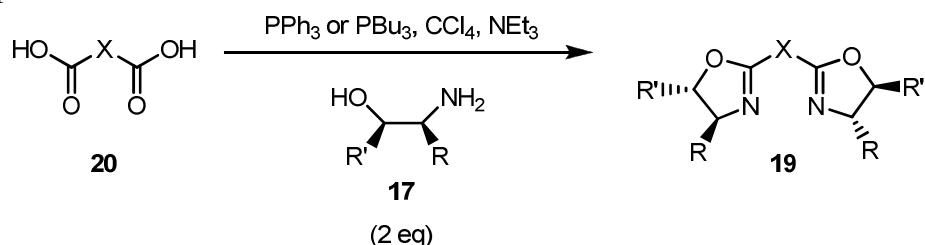
**Scheme 1.4** Bisoxazolines synthesized according to a procedure of Krolikiewicz.[40]

Another very interesting method reacts dinitriles **21** with the respective *β*-aminoalcohols **17** in the presence of catalytic amounts of $ZnCl_2$ or $Cd(OAc)_2*2H_2O$.[41] The configuration of the stereocenters is thereby retained. A second variant being especially suited for acid-labile substances works with catalytic amounts of potassium carbonate.[42] (See Scheme 1.5).
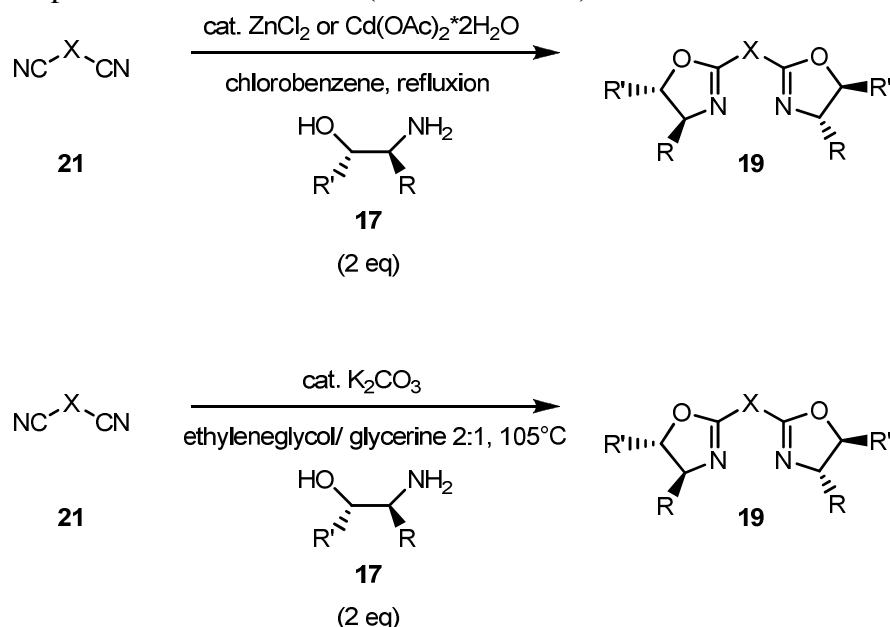
Scheme 1.5 Lewis acid versus potassium carbonate catalyzed synthesis of bis-oxazolines.[41,42]

As final synthetic route for bisoxazoline ligands an additional modification of the above description shall be introduced, which was the personal choice for synthesizing the box ligands **1** and **2**. Therefore commercial bisimidates (gained from reacting dinitriles **21** with gaseous HCl) are simply refluxed in CH_2Cl_2 together with the

chosen β-aminoalcohol **17**.[26,43] This gives after column chromatography the pure desired bisoxazolines **19**. (See Scheme 1.6). This is again a method which does not work with all substrates satisfactorily.
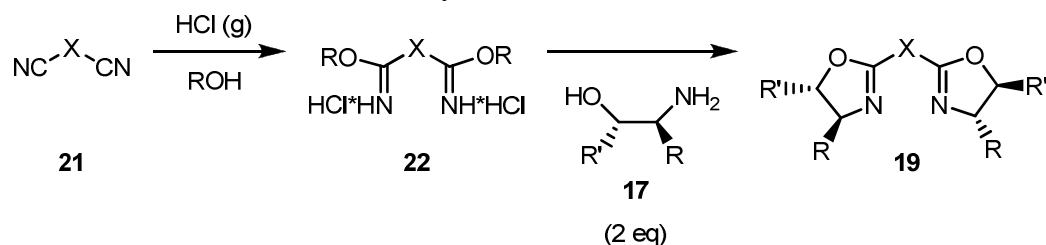
Scheme 1.6 Bisoxazolines synthesized via bisimidate **22**.

In contrast the aza-bisoxazoline ligand families **3** and **4** are synthesized according to the second class of procedures.

The β-aminoalcohol **17** is reacted with in situ produced BrCN to yield the oxazole **23** whereas on a second pathway the oxazolinon **24** is generated from the aminoalcohol and diethylcarbonate. (See Scheme 1.7). The oxazolinone **24** is further transferred to the activated 4,5-dihydrooxazole **25** which is coupled with **23** in the presence of *para*-toluene sulfonic acid to the desired aza-bisoxazoline **10**.[12]
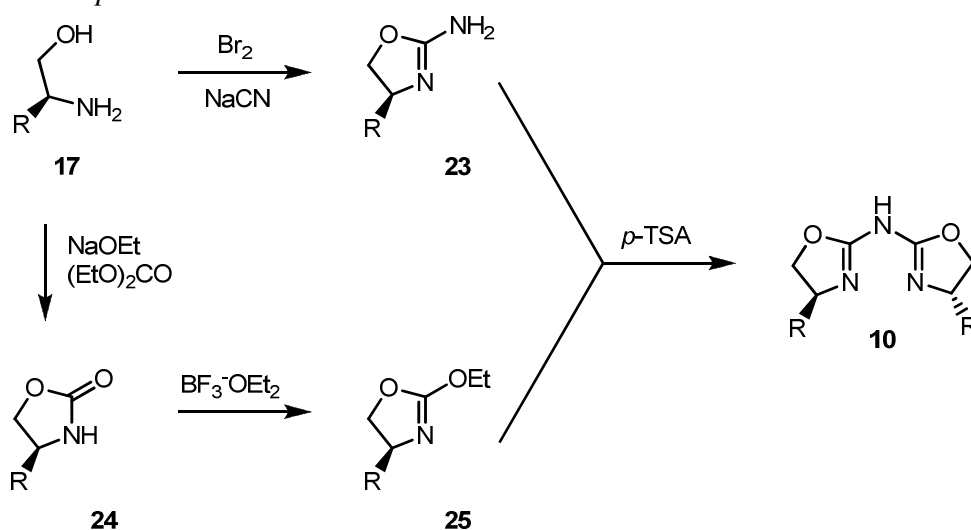
Scheme 1.7 Synthesis of aza-bisoxazolines.

Alternative literature known protocols formally dimerize the oxazole **23** in the presence of benzaldehyde under acid catalysis to yield the bidentate ligand **10** in moderate amounts.[44] However, with this method purification of the aza-bisoxazolines is often problematic why the former method (Scheme 1.7) was favored in this thesis.

The last synthetic step when preparing the ligands **1**–**4** is always the labeling of the CH$_2$ or N–H bridge between the oxazoline rings. For the box ligands **1** and **2** deprotonation with NaH[25] and subsequent reaction with stochiometric amounts of CH$_3$I introduces a single alkyl label whereas for the aza-bisoxazoline ligands deprotonation with butyllithium at −78°C and subsequent addition of alkylhalides was found to give the most clean reaction products.[12]

1.4   References

[1]   Katsuki, T.; Sharpless, K. B.; *J. Am. Chem. Soc.* **1980**, *102*, 5974

[2]   Knowles, W. S.; Sabacky, M. J.; *J. Chem. Soc. Chem. Commun.* **1968**, 1445

[3]   Noyori, R.; Ohta, M.; Hsiao, Y.; Kitamura, M.; Ohta, T.; Takaya, H.; *J. Am. Chem. Soc.* **1986**, *108*, 7117

[4]   Nozaki, H.; Moriuti, S.; Takaya, H.; Noyori, R.; *Tetrahedron Letters* **1966**, *43*, 5239–5244

[5]   Singh, U. P.; Babbar, P.; Hassler, B.; Nishiyama, H.; Brunner, H.; *Journal of Molecular Catalysis A: Chemical* **2002**, *185*, 33–39

[6]   Diaz-Requejo, M. M.; Pérez, P. J.; *Journal of Organometallic Chemistry* **2001**, *617-618*, 110–118

[7]   Ito, K.; Tabuchi, S.; Katsuki, T.; *Synlett* **1992,**575–576

[8]   Chelucci, G.; Gladiali, S.; Sanna, M. G.; Brunner, H.; *Tetrahedron Asymmetry* **2000**, *11*, 3419–3426

[9]   a) Fritschi, H.; Leutenegger, U.; Pfaltz, A.; *Angew. Chem., Int. Ed. Engl.* **1986**, *25*, 1005–1006; b) Fritschi, H.; Leutenegger, U.; Siegmann, K.; Keller, W.; Kratky, Ch.; Pfaltz, A.; *Helv. Chim. Acta* **1998**, *71*, 1541–1552; c) Fritschi, H.; Leutenegger, U.; Pfaltz, A.; *Helv. Chim. Acta* **1988**, *71*, 1553–1565

[10]   Pfaltz, A.; *Acc. Chem. Res.* **1993**, *26*, 339–345

[11]   Leutenegger, U.; Umbricht, G.; Fahrni, C.; von Matt, P.; Pfaltz, A.;
       Tetrahedron **1992**, *48*, 2143–2156

[12]   a) Werner, H.; Vicha, R.; Gissibl, A.; Reiser, O.; *J. Org. Chem.* **2003**, *68*,
       10166–10168; b) Fraile, J. M.; Garcia, J. I.; Herrerias, C. I.; Mayoral, J. A.;
       Reiser, O.; Socuellamos, A.; Werner, H.; *Chem. Eur. J.* **2004**, *10*, 2997–3005

[13]   a) Evans, D. A.; Woerpel, K. A.; Hinman, M. M.; Faul, M. M.; *J. Am. Chem.
       Soc.* **1991**, *113*, 726–728; b) Evans, D. A.; Woerpel, K. A.; Scott, M. J.;
       Angew. Chem., Int. Ed. Engl. **1992**, *31*, 430–432

[14]   a) Masamune, S.; Loewenthal, R. E.; *Tetrahedron Lett.* **1991**, *32*, 7373; b)
       Masamune, S.; Abiko, A.; Loewenthal, R. E.; *Tetrahedron Lett.* **1990**, *31*,
       6005–6008

[15]   Brunner, H.; Obermann, U.; *Chem. Ber.* **1989**, *122*, 499–507

[16]   Park, S.-B.; Sakata, N.; Nishiyama, H.; *Chem. Eur. J.* **1996**, *2*, 303–306

[17]   Komine, N.; Wang, L.-F.; Tomooka, K.; Nakai, T.; *Tetrahedron Lett.* **1999**, *40*,
       6809–6812

[18]   Evans, D. A.; Kozlowski, C.; Murry, J. A.; Burgey, C. S.; Campos, K. R.;
       Connell, B. T.; Staples, R. J.; *J. Am. Chem. Soc.* **1999**, *121,* 669–685

[19]   Gokhale, A. S.; Mindis, A. B. E.; Pfaltz, A.; *Tetrahedron Lett.* **1995**, *36*, 1831–
       1834

[20]   Boulch, R.; Scheurer, A.; Mosset, P.; Saalfrank, R. W.; *Tetrahedron Lett.*
       2000, *41*, 1023–1026

[21]   Lee, S.; Lim, C. W.; Song, C. E.; Kim, I. O.; Jun, C. H.; *Tetrahedron:
       Asymmetry* **1997**, *8*, 2927–2932

[22]   Lee, S.; Lim, C. W.; Song, C. E.; Kim, K. M.; Jun, C. H.; *J. Org. Chem.* **1999**,
       64, 4445–4451

[23] Bedekar, A. V.; Koroleva, E. B.; Andersson, P. G.; *J. Org. Chem.* **1997**, *62*, 2518–2526

[24] Imai, Y.; Zhang, W.; Kida, T.; Nakatsuji, Y.; Ikeda, I.; *Tetrahedron Asymmetry* **1996**, *7*, 2453–2462

[25] Desimoni, G.; Faita, G.; Jørgensen, K. A.; *Chem. Rev.* **2006**, *106*, 3561–3651

[26] Debono, N.; Besson, M.; Pinel, C.; Djakovitch, L.; *Tetrahedron Letters* **2004**, *45*, 2235–2238

[27] Corey, E. J.; Imai, N.; Zhang, H.-Y.; *J. Am. Chem. Soc.* **1991**, *113*, 728–729

[28] Meng, J.-C.; Fokin, V. V.; Finn, M. G.; *Tetrahedron Letters* **2005**, *46*, 4543–4546

[29] a) Pfaltz, A.; *Synlett.* **1999**, 835–842; b) Pfaltz, A.; *Heterocyclic Chem.* **1999**, *36*, 1437–1451

[30] Reiser, O.; *Nachr. Chem. Tech. Lab.* **1996**, *44*, 744–750

[31] Fritschi, H.; *Chirale Kupfer-Semicorrin-Komplexe als enantioselektive Katalysatoren für die Cyclopropanierung von Olefinen,* PhD Thesis, ETH Zürich, **1989**, Diss. No. 8951

[32] Straub, B. F.; Hofmann, P.; *Angew. Chem. Int. Ed.* **2001**, *40*, 1288–1290

[33] Hu, W.; Timmons, D. J.; Doyle, M. P.; *Org. Lett.* **2002**, *4*, 901–904

[34] Teichert, A.; Pfaltz, A.; *Angew. Chem.* **2008**, *120*, 3408–3410

[35] Denmark, S. E.; Stavenger, R. A.; Faucher, A. M.; Edwards, J. P.; *J. Org. Chem.* **1997**, *62*, 3375–3389

[36] a) Evans, D. A.; Peterson, G. S.; Johnson, J. S.; Barnes, D. M.; Campos, K. R.; Woerpel, K. A.; *J. Org. Chem.* **1998**, *63*, 4541–4544; b) Peer, M.; de Jong, J. C.; Kiefer, M.; Langer, T.; Rieck, H.; Schell, H.; Sennhenn, P.; Sprinz, J.; Steinhagen, H.; Wiese, B.; Helmchen, G.; *Tetrahedron* **1996**, *52*, 7547–7583

[37]   a) Nishiyama, H.; Kondo, M.; Nakamura, T.; Itoh, K.; *Organometallics* **1991**, *10*, 500–508; b) Nesper, R.; Pregosin, P. S.; Püntener, K.; Wöhrle, M.; *Helv. Chim. Acta* **1993**, *76*, 2239–2249

[38]   a) Wipf, P.; Miller, C. P.; *Tetrahedron Lett.* **1992**, *33*, 6267–6270; b) Galeotti, N.; Montagne, C.; Poncet, J.; Jouin, P.; *Tetrahedron Lett.* **1992**, *33*, 2807–2810

[39]   a) Rippert, A. J.; *Helv. Chim. Acta* **1998**, *81*, 676–687; b) Wipf, P.; Miller, C. P.; *Tetrahedron Lett.* **1992**, *33*, 907–910

[40]   a) Vorbrüggen, H.; Krolikiewicz, K.; *Tetrahedron* **1993**, *49*, 9353–9372; b) Vorbrüggen, H.; Krolikiewicz, K.; *Tetrahedron Lett.* **1981**, *22*, 4471–4474

[41]   a) Witte, H.; Seeliger, W.; *Liebigs Ann. Chem.* **1974**, 996–1009; b) Bolm, C.; Weickhardt, K.; Zehnder, M.; Ranff, T.; *Chem. Ber.* **1991**, *124*, 1173–1180

[42]   Schumacher, D. P.; Clark, J. E.; Murphy, B. L.; Fischer, P. A.; *J. Org. Chem.* **1990**, *55*, 5291–5294

[43]   a) Hall, J.; Lehn, J. M.; DeCian, A.; Fischer, J.; *Helv. Chim. Acta* **1991**, *74*, 1–6; b) Gosh, A. K.; Mathivanan, P.; Cappiello, J.; *Tetrahedron Lett.* **1996**, *37*, 3815–3818

[44]   a) Wittekind, R. R.; Rosenau, J. D.; Poos, G. I.; *J. Org. Chem.* **1961**, *26*, 444–446; b) Poos, G.; Carson, J.; Rosenau, J.; Roszkowski, A.; Kelley, N.; McGowin, J.; *J. Med. Chem.* **1963**, *6*, 266–272

Chapter 2

Enantioselective Control of Metal catalyzed Reactions

2.1　Mechanistic Background for Enantioselectivity

So far semicorrine and (aza-)bisoxazoline ligands have been presented as particularly effective ligands for the stereocontrol of metal-catalyzed reactions, but the rational, mechanistic explanation for the excellent enantioselective induction with such ligands was not yet given.

The first formulation of such a reaction model which allows to predict the major enantiomers in copper bisoxazoline catalyzed cyclopropanation reactions originates from Pfaltz.[1,2] Although his model was at that time not based on any direct experimental or theoretical evidence, but only on the assumption of a direct carbene insertion (instead of a two-step mechanism over a cyclobutadiene like structure) Pfaltz's explanation rationalizes the origin of enantioselectivities extremely well.

Namely the big advantage of these C2-symmetric bidentate nitrogen donor ligands like bisoxazolines is their strong copper complexing ability in combination with their conformationally rather rigid and distinct framework upon metal ion coordination. This restricts according to Pfaltz the number of possible catalyst-substrate arrangements as well as the number of competing diastereomeric transition states.[3]

Thus, the three dimensional structure of the copper bisoxazoline fragment can be seen as a plane defined by the metal cation and the two oxazoline rings, whereas the

stereogenic centers shield the central metal from two opposite directions. The high face discriminating ability of these substituents located in so close proximity to the coordination site is then attributed to the steric repulsion with the alkoxycarbonyl-group in the transition state.[3]

This original interpretation of Pfaltz was recently refined by Fraile et al.,[4] who realized that the reactant like nature of the transition state cannot totally account for the high enantioselectivities usually found for cyclopropanations. They pointed out an additional noticeable interaction between the chelate substituent and the alkoxycarbonyl-group in the ground state catalyst carbene complex. Thus, the copper carbenoid carbon bond deviates in reality relative to the C2-symmetry axis of the naked catalyst, which is neglected in Pfaltz's simplified model.

Both aspects complement each other and explain the high predominance of olefin molecules to approach from the *Si*-face of the plane defined by the Cu=C–C arrangement.[4] (See Scheme 2.1).
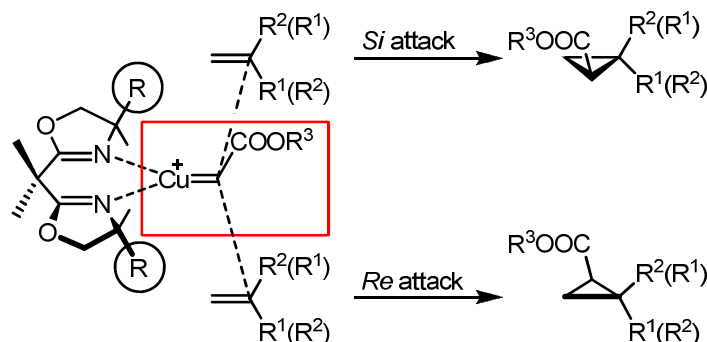
Scheme 2.1 Asymmetric induction model for enantioselective copper complex catalysts.[4]

Due to steric interactions with the chiral ligand it is reasonable to suppose that the monosubstituted alkene will always be oriented with the substituent far away from the ligand backbone. This reduces the originally eight possible transition state structures to four, namely *Re*-cis, *Si*-cis, *Re*-trans and *Si*-trans. The strongly favored alkene attack to the *Si* instead of the *Re*-face of the chiral catalyst carbene complex causes the high enantiomeric excess of the formed cyclopropanes.[5,6]

However the cis versus trans stereochemistry is determined by the steric repulsion between the alkoxycarbonyl-group and the substituent bonded to the prochiral carbon of the olefin.[4] Consequently larger alkene substituents cause more trans-selectivity, whereas for small steric residues the cis and trans product ratios

assimilate. Thus high diastereoselectivity towards the cis-isomer cannot be obtained with bisoxazoline or semicorrine ligands. Instead it requires specific tris(pyrazolyl) borate Cu^{+}[7] or Co(II)salen complexes[8] to induce high cis-selectivity which shall not be discussed in this section focusing on the explanation for enantioselectivity.

2.2 Nonlinear Effects in Catalysis

As already mentioned asymmetric synthesis is necessarily performed with the help of a chiral auxiliary which is either used in stochiometric or catalytic amounts depending on the reaction type. With the intention of maximizing the enantiomeric yield of the reaction product, enantiomerically pure chiral auxiliaries are usually preferred – if possible. The observed enantioselectivity of the product, EE_{prod}, is normally supposed to follow the simple relationship of equation (2.1), where EE_0 stands for the enantiomeric excess of the product when using an enantiopure chiral auxiliary.

$$EE_{prod} = EE_0\, ee_{aux} \qquad\qquad (2.1)$$

However, Kagan[9] was the first to question the hypothesis of a generally linear correlation between the enantiomeric excess of the product and the enantiomeric purity of the chiral auxiliary, ee_{aux}. Instead he could identify and explain the first examples in asymmetric synthesis which deviate from the classical linear correlation and thus display a nonlinear effect (abbreviated NLE). In case the observed product enantioselectivity is better than the linear relationship the NLE is termed "positive" and for the opposite case it is called a "negative" NLE.[10]

According to Kagan the prerequisite for the occurrence of a nonlinear effect is that one or more species in the system have to contain more than one unit of the chiral ligand, opening up the possibility of homochiral and heterochiral complexes.[9] Further, he could also derive a quantitative description for the sign and magnitude of the observed nonlinear effects.

This so called ML_n model[9] where M represents the central metal-cation being complexed by n chiral ligands L is based on several assumptions.[11,12] For example a fast initial metal-ligand equilibration is required to obtain one constant value for the equilibrium constant K serving as a fit parameter. If this point is not fulfilled K would vary together with ee_{aux}. The next important criterion is that the reaction rate has to

be zero order in substrate for all catalytic species participating in the reaction. As last point in this row also any changes to the catalyst species occurring during the catalytic reaction have to be excluded. In case one of these points is not met Kagan's model is not suited to describe these reactions correctly.

Especially the last aspect concerning the formation of new metal-ligand species through binding of the reaction product sets Kagan's NLEs apart from a second class of reactions with nonlinear behavior, namely catalysis with either product inhibition or autocatalysis. A highly cited example therefore is Soai's autocatalytic formation of a chiral pyrimidyl alcohol in a reaction starting with almost racemic alcohol but displaying increasing enantioselectivity as conversion proceeds.[13]

For the third source of nonlinear effects in catalysis, namely the ones caused by physical phase behavior[14] Kagan suggested an additional attempt apart from the ML_n model. Thus, for the case of only partially resolved chiral ligands in a catalytic system he proposed the so called "Reservoir Effect"[15] to illuminate such complicated systems. Further, this model particularly implies reactions where aggregation takes place before or in parallel with the catalytic cycle reaching its steady state. Thus nonlinear effects originating from both, equilibrium and kinetic behavior, are subsumed in this general attempt and therefore only a very generalized mathematical expression can be derived.

Starting from a molar amount of ligand with a defined ee_{aux} that forms different metal ligand species, then a part of this (α) will be unproductive in catalysis and can be diverted towards a reservoir described by ee_{res}. These reservoir species are often higher oligomeric structures whereas complexes with low aggregation numbers probably behave as the catalyst or the catalyst precursor. This active $(1-\alpha)$ portion of complexes has then a different enantiomeric excess (ee_{eff}), which can be calculated from equation (2.2).[15]

$$ee_{eff} = \frac{ee_{aux} - \alpha\, ee_{res}}{1 - \alpha} \qquad (2.2)$$

Of course this gives only a mechanistic explanation of nonlinear effects observed in mixed phase systems but does not allow to model the final product enantioselectivities.

An especially interesting example for nonlinear effects originating from (equilibrium) physical phase behavior is the proline catalyzed aldol reaction of

acetone and 2-chlorbenzaldehyde.[16,17] As soon as the concentration of proline exceeds the maximum solubility of the aminoacid a strongly pronounced nonlinearity is observed and can be qualitatively explained with the ternary phase diagram of D-proline, L-proline and DMSO.

In contrast to these nonlinear effects caused either by autocatalysis/product-inhibition or physical phase behavior the ones of a true chemical origin such as described by Kagan's ML_n model[9,10] are certainly the most common ones in homogeneous catalysis.

In the most simple case of a ML_2 or $(ML)_2$ system a steady state for the complexes ML_RL_R, ML_SL_S and ML_RL_S with the respective amounts x, y and z is assumed. k_{RR}, k_{SS} and k_{RS} are the apparent rate constants for the irreversible product forming step. Racemic product is generated by the meso catalyst while enantiomeric products are obtained from the two homochiral complexes. The resulting enantiomeric excess of the product is then described by equation (2.3)[10]

$$EE_{prod} = EE_0 \, ee_{aux} \, \frac{1+\beta}{1+g\beta} \tag{2.3}$$

β expresses the relative amounts of the meso- and homochiral complexes ($\beta = z/x+y$) while g defines the relative reactivities of the hetero- and homochiral catalysts ($g = k_{RS}/k_{RR}$). In case of either no meso catalyst ($\beta = 0$) or identical reactivities of meso and homochiral catalyst ($g = 1$) equation (2.3) simplifies into equation (2.1) and displays again the linear correlation. In contrast a "positive NLE" is achieved with $g < 1$ and thus with a less reactive meso complex than the homochiral analogues. A "negative NLE" occurs for $g > 1$.

If the distribution of the metal ligand complexes is, as initially assumed, close to the thermodynamic equilibrium with $K = z^2/xy$, the equilibrium constant, then the ratio β can be expressed as follows (equation 2.4).[9]

$$\beta = \frac{-K \, ee_{aux}^2 + \sqrt{-4K \, ee_{aux}^2 + K(4 + K \, ee_{aux}^2)}}{4 + K \, ee_{aux}^2} \tag{2.4}$$

When fitting experimental catalysis data to Kagan's ML_2 model, both K and g are fitting parameters. An extremely strong "positive NLE" can be modeled with large values for K and small numbers for β.

The respective ML_3 and ML_4 models with four and five different metal ligand species allow to explain multi-shaped NLE-curves. The analogue expressions for the observed product enantioselectivites are given in reference.[9]

In general NLEs have a very profound importance since the biomolecular homochirality might be linked to these effects,[16] but also their practical importance for enantioselective catalysis is very valuable. Clever application of these results allows to obtain high product enantioselectivities with nonenantiopure chiral auxiliaries.[18] Considering that the effort and price for racemic chiral ligands is certainly lowered compared to enantiopure amounts explains the interest in determining the nonlinear effects for various catalysts and reactions.

Some literature known examples are given in Figure 2.1,[19] Figure 2.2,[20] Figure 2.3.[15]
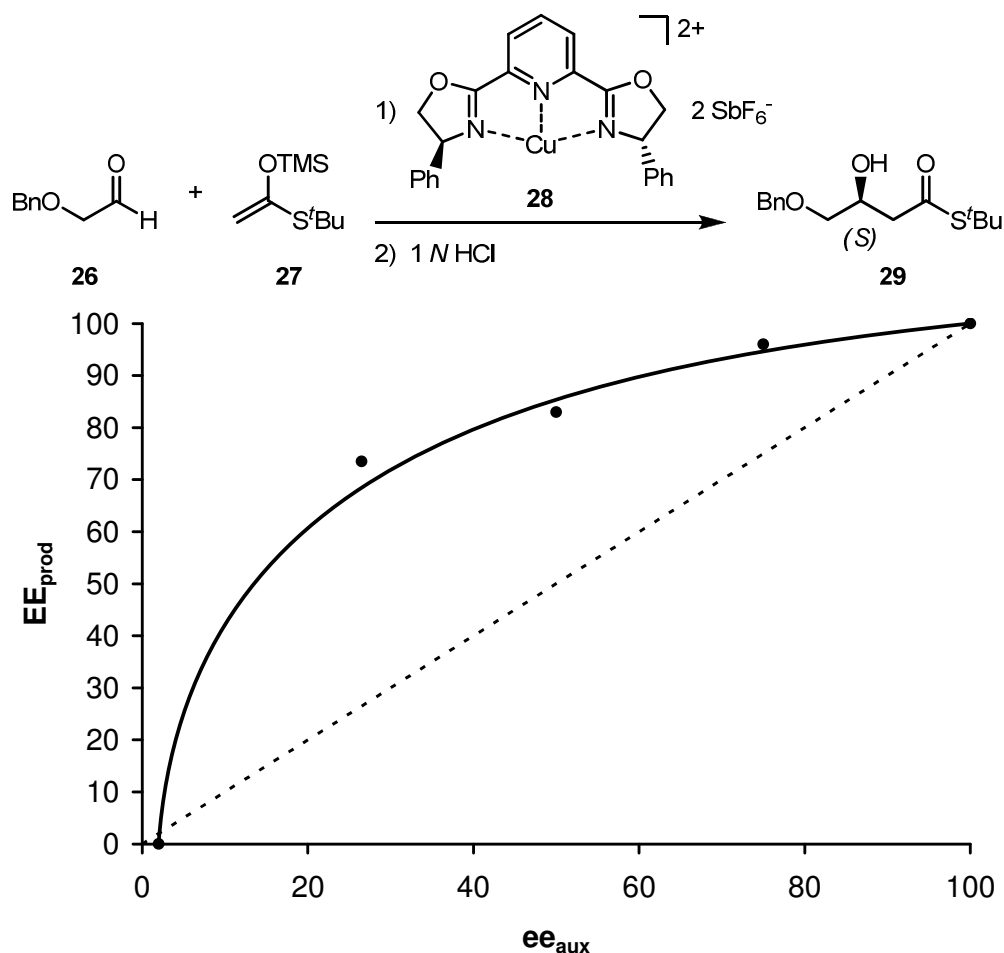
Figure 2.1 Positive nonlinear effect in the benzyl-oxyacetaldehyde aldol reaction with the [Cu(Ph-pybox)](SbF$_6$)$_2$ catalyst.[19]
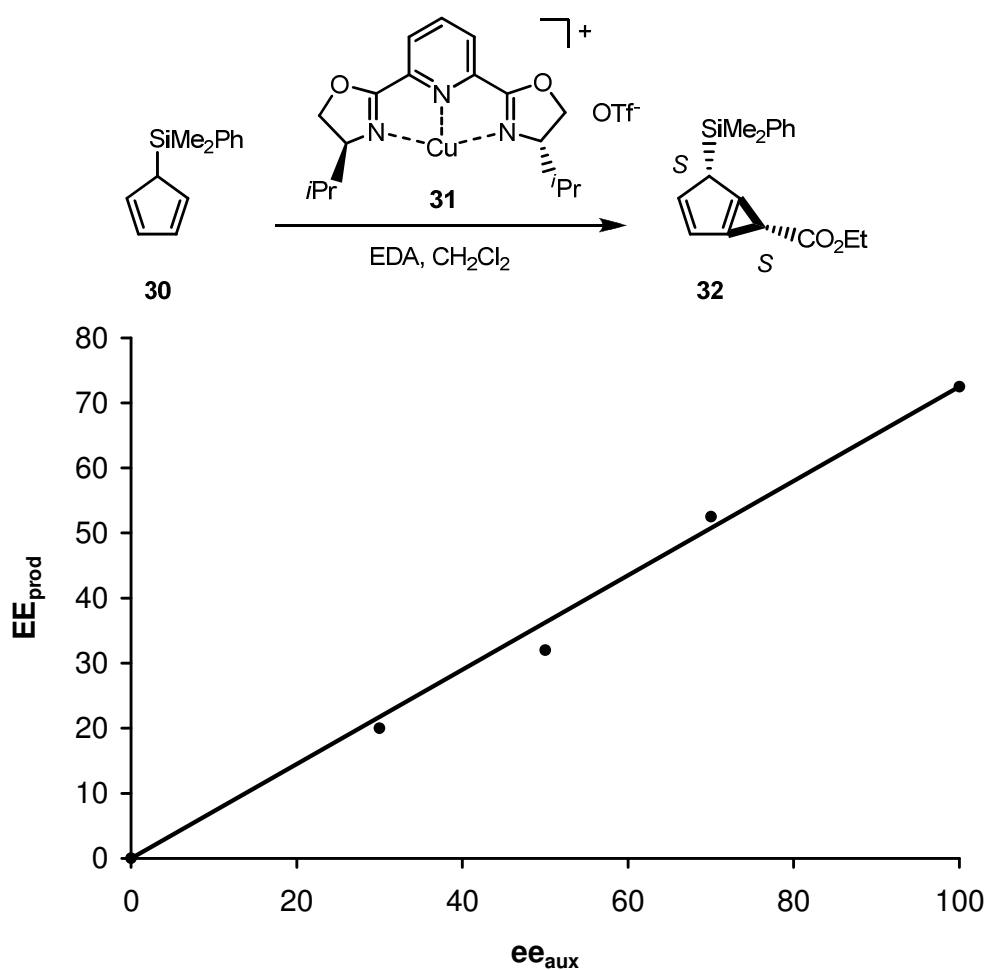
Figure 2.2 Linear dependence for the cyclopropanation of silylcyclopenta-2,4-diene
with the [Cu(Iso-pybox)]OTf catalyst.[20]

The first case (Figure 2.1), the aldol reaction between benzyloxyacetaldehyde **26**
and the depicted silylketenacetal **27** displays a very strong positive NLE when
catalyzed with the [Cu(Ph-pybox)](SbF_6)$_2$ catalyst **28**.[19] In contrast the Cu(I)
catalyzed cyclopropanation of silylcyclopenta-2,4-diene **30** with isopropyl substituted
pybox ligands **31** is simply linear (see Figure 2.2).[20] Both reactions can most likely
be described with Kagan's ML_2 model. They only differ in the relative reactivity and
the relative abundance of the respective homo- versus heterochiral catalyst species.
Thus, the oxidation state of the metal and the choice of the substituents have an
obvious influence on the NLEs for catalysis reactions applying pybox ligands.
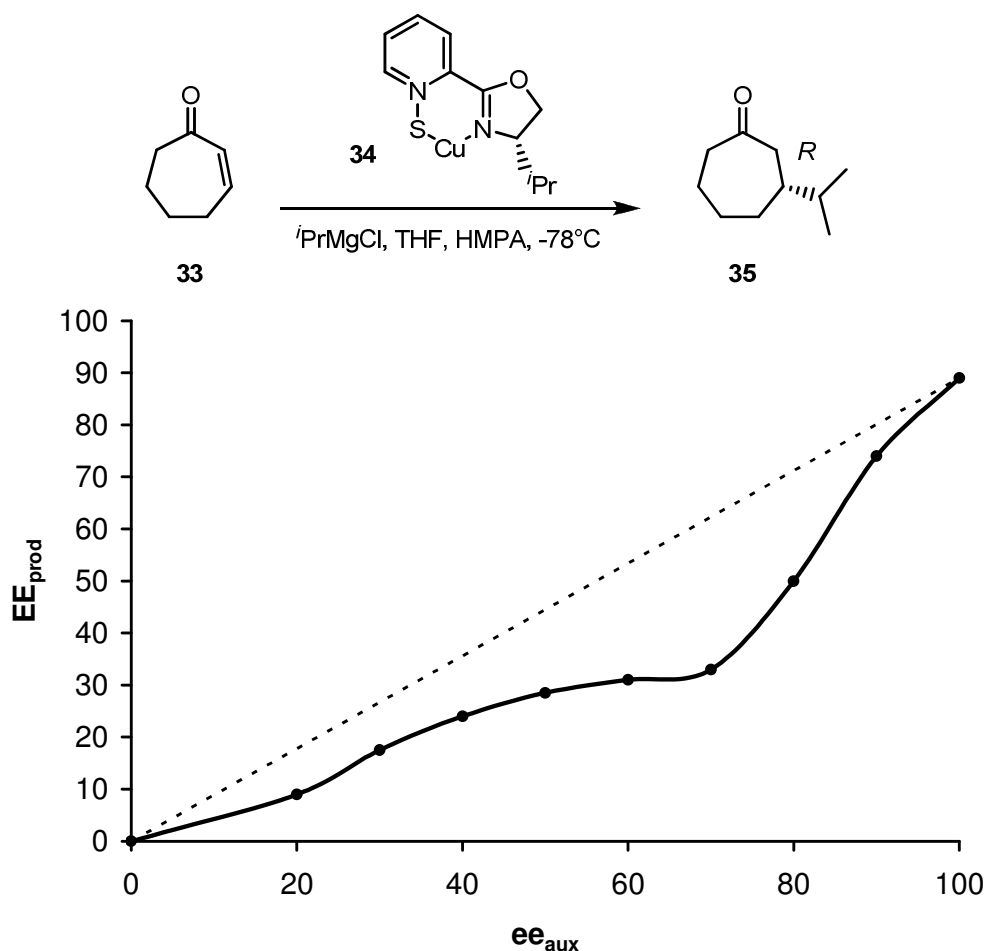
Figure 2.3 Negative NLE for the 1,4-addition of ^{i}PrMgCl to cycloheptenone
catalyzed by chiral copper oxazolinethiolate.[15]

For comparison a negative NLE is presented in Figure 2.3. There the 1,4-addition
of isopropylcuprate to cycloheptenone **33** is studied which yields compound **35**.[15]
The use of a chiral copper oxazolinethiolate **34** generates the displayed multi-shaped
curve which is possible to model with a ML_4 model, but additional information on
the structure of the catalytic species like NMR-data is necessary to fully assign the
catalysis results to one of Kagan's ML_n models.

2.3   Open Questions

Since nonlinear effects are quite common for diastereomeric metal ligand complexes
in enantioselective catalysis the interest prevails to fully understand and derive them.
Further, the phenomenon has been postulated as an explanation for the predominance
of only one enantiomer of aminoacids and sugars in the natural world.[16] Also the

practical importance of these effects, namely opening the possibility to obtain high product enantioselectivities with nonenantiopure chiral auxiliaries is a very fascinating aspect.[18]

Quantitative descriptions of the sign and magnitude of the NLEs are solely possible with Kagan's ML_n model[9,15] given its underlying assumptions are fulfilled.[11,12] However this model is in principle only a hypothesis fitting to the current status of knowledge.

Up to now thermodynamic ligand binding energy measurements[21] were never performed to corroborate the condition of differently stable homo- and heterochiral metal-ligand complexes.[15] Thus tandem mass spectrometric collision induced dissociation experiments yielding absolute thermochemical information should allow to complement the picture and to validate Kagan's model. The impact of kinetic influences for the ligand exchange on the metal center could additionally be concluded from the solution state reactivity.[22]

As the chemical system copper(I) is chosen as the central metal together with the (aza-)bisoxazoline ligands **1**–**4**, which are very popular in enantioselective catalysis. This allows to test the predictions from the gas phase measurements with the typical asymmetric benchmark reaction in condensed phase, namely the enantioselective cyclopropanation. The choice of (aza-)bisoxazoline copper complexes is additionally driven by the limited number of atoms the initially solely existing data processing program for CID threshold curves can handle.[23] Consequently pybox ligands were not implemented in the studies of this dissertation, although some published NLEs with these ligands exist.[19,20]

Apart from examining whether thermodynamic ligand metal binding energies can predict nonlinear effects in catalysis also the commonly in the literature accepted assumption of the 1:1 bisoxazoline copper complex acting as the active catalyst species[3,24] which undergoes the catalytic cycle can be probed. The CID measurements free exactly this 14-electron complex when cleaving one of the two bidentate ligands from the homo- and heterochiral 2:1 complexes.

2.4   References

[1]   Pfaltz, A.; *Cyclopropanation and C–H Insertion with Cu. In Comprehensive Asymmetric Catalysis*; Jacobson, E. N.; Pfaltz, A.; Yamamoto, H., Eds.; Springer-Verlag: Berlin, **1999**; Vol. 2, 513–538

[2]   Fritschi, H.; Leutenegger, U.; Pfaltz, A.; *Helv. Chim. Acta* **1988**, *71*, 1553–1565

[3]   Pfaltz, A.; *Chimia* **1990**, *44*, 202–213

[4]   Fraile, J. M.; Garcia, J. I.; Martinez-Merino, V.; Mayoral, J. A.; Salvatella, L.; *J. Am. Chem. Soc.* **2001**, *123*, 7616–7625

[5]   Gupta, A. D.; Bhuniya, D.; Singh, V. K.; *Tetrahedron* **1994**, *50*, 13725–13730

[6]   Lötscher, D.; Rupprecht, S.; H, Stoeckli-Evans, H.; von Zelewsky, A.; *Tetrahedron Asymmetry* **2000**, *11*, 4341–4357

[7]   a) Diaz-Requejo, M. M.; Belderrain, T. R.; Trofimenko, S.; Pérez, P. J.; *J. Am. Chem. Soc.* **2001**, *123*, 3167–3168; b) Diaz-Requejo, M. M.; Caballero, A.; Nicasio, M. C.; Belderrain, T. R.; Trofimenko, S.; Pérez, P. J.; *J. Am. Chem. Soc.* **2002**, *124*, 978–983

[8]   a) Niimi, T.; Uchida, T.; Irie, R.; Katsuki, T.; *Tetrahedron Lett.* **2000**, *41*, 3647–3651; b) Niimi, T.; Uchida, T.; Irie, R.; Katsuki, T.; *Adv. Synth. Catal.* **2001**, *343*, 79–88

[9]   Guillaneux, D.; Zhao, S.-H.; Samuel, O.; Rainford, D.; Kagan, H. B.; *J. Am. Chem. Soc.* **1994**, *116*, 9430–9439

[10] Kagan, H. B.; *Synlett* **2001**, No. SI, 888–899

[11] Blackmond, D. G.; *J. Am. Chem. Soc.* **1997**, *119*, 12934–12939

[12] Blackmond, D. G.; *J. Am. Chem. Soc.* **1998**, *120*, 13349–13353

[13]   Soai, K.; Shibata, T.; Sato, I.; *Acc. Chem. Res.* **2000**, *33*, 382–390

[14]   Klussmann, M.; Mathew, S. P.; Iwamura, H.; Wells Jr., D. H.; Armstrong, A.;
       Blackmond, D. G.; *Angew. Chem.* **2006**, *118*, 8157–8160

[15]   Girard, C.; Kagan, H. B.; *Angew. Chem. Int. Ed* **1998**, *37*, 2922–2959

[16]   Klussmann, M.; Iwamura, H.; Mathew, S. P.; Wells Jr., D. H.; Pandya, U.;
       Armstrong, A.; Blackmond, D. G.; *Nature 04780* **2006**, *441*, 621–623

[17]   Kellogg, R. M.; *Angew. Chem.* **2007**, *119*, 498–502

[18]   Kagan, H. B.; *Adv. Synth. Catal.* **2001**, *343*, 227–233

[19]   Evans, D. A.; Kozlowski, M. C.; Murry, J. A.; Burgey, C. S.; Campos, K. R.;
       Connell, B. T.; Staples, R. J.; *J. Am. Chem. Soc.* **1999**, *121*, 669–685

[20]   Allais, F.; Angelaud, R.; Camuzat-Dedenis, B.; Julienne, K.; Landais, Y.; *Eur.
       J. Org. Chem.* **2003**, 1069–1073

[21]   Rodgers, M. T.; Ervin, K. M.; Armentrout, P. B.; *J. Chem. Phys.* **1997**, *106*,
       4499

[22]   Kalsani, V.; Schmittel, M.; *Inorganic Chemistry* **2006**, *45*, 2061–2067

[23]   CRUNCH, version D1, was kindly provided as an executable by Prof. P.
       Armentrout

[24]   Diaz-Requejo, M. M.; Belderrain, T. R.; Nicasio, M. C.; Prieto, F.; Pérez, P. J.;
       Organometallics **1999**, *18*, 2601–2609

Part II

Gas-Phase Studies to determine

Thermochemistry

Chapter 3

Unimolecular Dissociation of Gaseous Ions

3.1 The Collision induced Dissociation Measurement

The collision induced dissociation process (CID) for structural elucidation of an ionic complex was found almost immediately when electrospray mass spectrometry was developed as a new analytical method.[1,2] However, the ability to determine also accurate thermodynamic information is more recent, dating back to the early 1980s with Armentrout's pioneering work[3] and has been refined extensively over the past decade.

The underlying concept is simple: the dissociation of the parent complex $(AB)^+$ is studied as a function of the kinetic energy available to the reactants.

$$AB^+ + Rg \longrightarrow A^+ + B + Rg$$
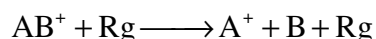
Rg is in the most simple case a rare gas atom, *e.g.* Xenon, since it can contribute only kinetic energy and no internal energy to the collision event. The parent complex can be cationic or anionic.

The method has so far been applied with great success to determine absolute ligand binding energies for a variety of different small systems: Metal-ligand complexes with atomic metal cations throughout the periodic table and ligands such as H_2, N_2, CO_2, H_2O, NH_3, CH_4, alkenes, alkynes, alcohols, amines, amino acids or crown ethers.[4] Also metal clusters of 3d, 4d and 5d transition metals like V_n^+ (n=2–20), Nb_n^+ (n = 2–11) and Ta_n^+ (n=2–4) are present in the literature.[5] In organic chemistry the heat of formation of several radical structures like biradicals of benzene derivatives[6] or carbenes *e.g.* the vinyl-carbene have been studied.[7]

Therefore, it is remarkable that for "real life catalysts" with many more than only a few atoms the CID threshold measurement technique has almost not yet been applied.[8]

This lack of information gave rise to the present doctoral-thesis: Exploring the absolute thermodynamic stabilities of homo- versus heterochiral 2:1 bis-oxazoline copper complexes by cleaving one of the bidentate nitrogen donor ligands to generate the 1:1 bis-oxazoline copper complex (see Scheme 3.1). This 14 electron species is commonly expected to react with the substrates to undergo the catalytic cycle, whereas the 2:1 complexes act as resting states. Depending on their relative stabilities a positive or negative nonlinear effect is supposed to occur in asymmetric catalysis (as outlined in chapter 2.2).

X = CH, N   A = H, CH$_3$
R = (CH$_3$)$_2$CH, Ph   B = CH$_3$, CH$_2$CH$_3$
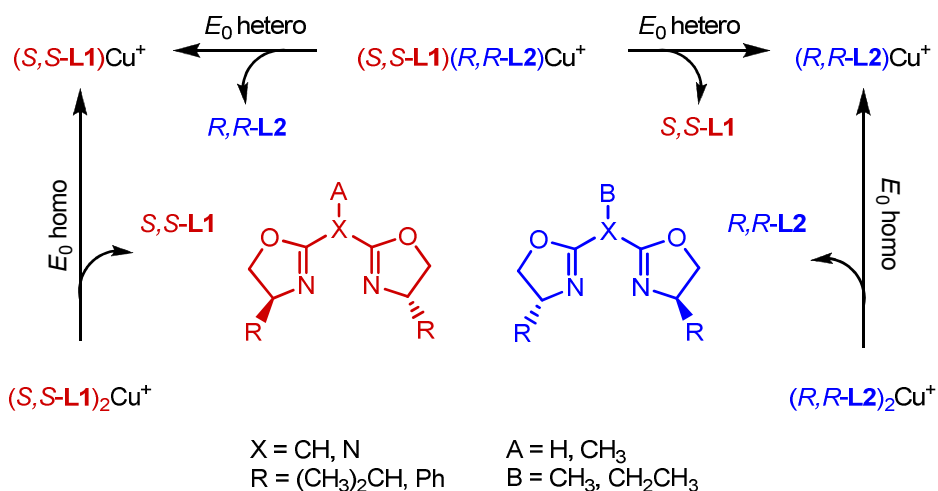
Scheme 3.1 Overview over the studied CID-reactions.[9,10] *Pseudo*-enantiomeric ligands with *e.g.* H versus CH$_3$-labeling are used to differentiate between homo- and heterochiral 2:1 bis-oxazoline complexes by mass difference.

A typical CID-threshold curve of one of the studied systems, the $(S,S\text{-}\mathbf{L1})_2\text{Cu}^+$ parent ion, is shown in Figure 3.1. It is obvious, that the CID reaction is exclusively endothermic, since the rupture of two Cu–N bonds for cleaving one of the two bisoxazoline-ligands requires extra energy. Formation of the fragments augments progressively as the kinetic energy of the reactant ion increases and thus collisions with the stationary Xenon gas as collision partner deposit sufficient energy for the reactant ion to decompose.
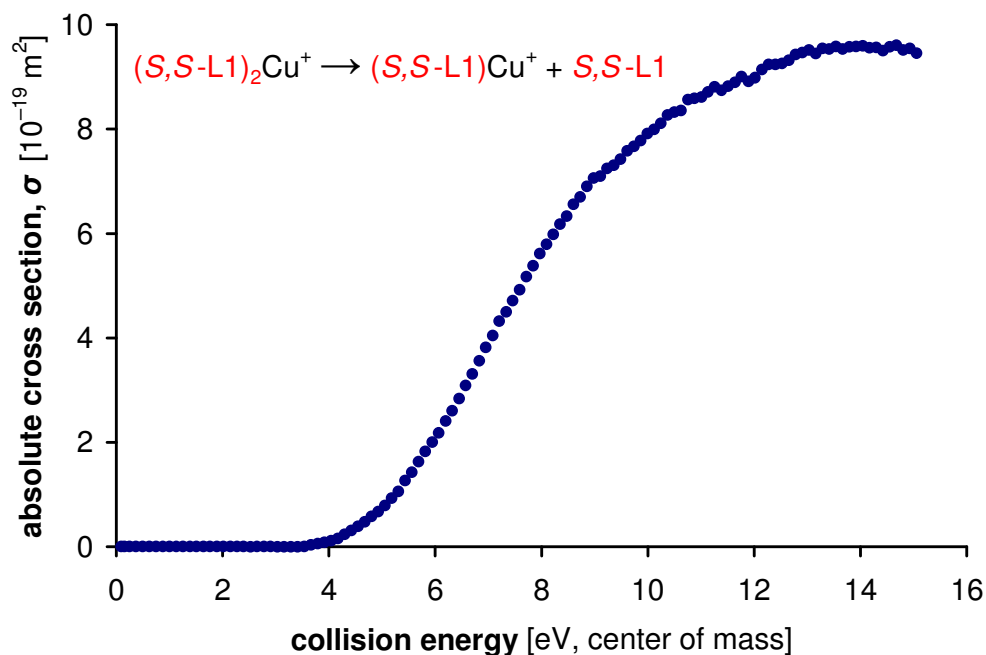
Figure 3.1 Absolute cross section for the CID of $(S,S\text{-}\textbf{L1})_2Cu^+$ with Xenon at extrapolated zero pressure, as a function of the collision energy in center of mass frame.

3.2 Theories of Unimolecular Reaction

Rearrangements, isomerizations and collision induced dissociations belong altogether to the class of unimolecular reactions with the latter ones being subject of the present work.

As proposed by Lindemann,[11] the theory of thermal unimolecular reactions is based on the collisional energy transfer between reagent molecule $(AB)^+$ and any other gas-phase species, *i.e.* another reagent molecule or a rare gas atom Rg.

The mechanism for the collisional energy transfer under single collision conditions is essentially a two step process, consisting of activation and subsequent dissociation of the activated complex $(AB^+)^*$.

$$(AB^+) + Rg \rightleftharpoons (AB^+)^* + Rg \quad \text{(I)}$$

$$(AB^+)^* \longrightarrow A^+ + B \quad \text{(II)}$$
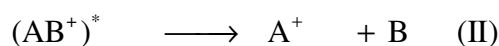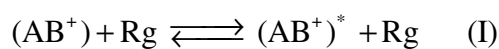
This understanding accounts for the peculiar transition from a second to a first order reaction as the gas pressure of Rg is increased. It also explains, why the time scale of activation in comparison is much shorter than the time scale for the reaction step towards the products.

Theoretically unimolecular dissociation reactions can be described statistically using the Rice-Ramsperger-Kassel-Markus (RRKM) theory.[12]

Alternative attempts like classical trajectory calculations would be too elaborate for this purpose. Also microscopic models, which take into account the individual interaction potential of the reaction partners, would be too complex to solve. Therefore, RRKM theory is the most appropriate level of theory in order to describe unimolecular reactions[13] with sufficient accordance to experiment.

The microcanonical RRKM rate constant can be expressed by the fairly simple ratio of the sum of states of the transition state $W^{\ddagger}(E - E_0)$ with an energy less or equal to $E - E_0$ over the total density of states of the reactant ion $\rho(E)$.

$$k(E) = \frac{W^{\ddagger}(E - E_0)}{h\rho(E)} \tag{3.1}$$

In order to calculate a microcanonical RRKM rate constant it is therefore necessary to determine the vibronic density and the sum of states, both to be computed from the vibrational frequencies.

However, there is explicitly to point out that RRKM theory is valid only with some simplifying assumptions which have to be fulfilled in the underlying experiment.[14]

One of the most important points in this row is the description of the transition state as a configuration of "no return". This implies that phase points once they have crossed the critical surface in phase space dividing reactant and product region, will never cross back from the product side. This a priori exclusion of a recrossing is indeed a reasonable assumption if the barrier for crossing the transition state is high compared to the available energy of the reactants, or particularly, because gas-phase dissociation processes are irreversible. Otherwise, the rate constant $k(E)$ can provide at best an upper limit to the actual rate constant.

Relying on this background, equation (3.1) can be rewritten in the following descriptive form:

$$k(E) = \frac{1}{\rho(E)\delta E} \times W^{\ddagger}(E - E_0) \times \frac{\delta E}{h} \qquad (3.2)$$

This gives in the first term the number of initial states in the interval $E, E + \delta E$ in comparison to the second part of equation (3.2) representing the total number of states of the transition state in the range $E - E_0$, and finally both parts linked with the elementary flux $\delta E/h$ of phase points through the critical surface. (A point in the phase space represents the instantaneous state of a system. The dynamic evolution of the system is consequently described by the trajectory of a phase point.)

The second important assumption in the RRKM theory to merit attention is the ergodicity assumption. It states that the coupling between the various vibrational degrees of freedom in the activated complex is sufficiently strong to randomize the initial excitation energy rapidly among all the active degrees of freedom of the activated complex. Thus, every state corresponding to energy E is represented with equal probability within a microcanonical distribution. This rapid intramolecular vibrational redistribution (*IVR*) is supposed to happen on a very short time scale compared to the relative lifetime of the decomposing molecule $(AB^+)^*$.

Further it is assumed that the reaction coordinate which could be just a bond stretch for a simple bond fission or the torsional angle in *e.g. cis-trans* isomerization is a separable degree of freedom evolving directly into the relative translation of the products. This vibration is missing in the sum of states of the transition state and is treated classically whereas all the other degrees of freedom of the transition state are treated quantum mechanically.

The last hypothesis in this series is the criterion of having the reaction taking place on an adiabatic potential energy surface which constraints the internal energy of the reagent molecule to be stored exclusively in vibrational and rotational degrees of freedom.

In order to relate the microcanonical rate constant $k(E)$ at a specific energy E with the observable rate constant k_{eff} in a typical experiment, it is necessary to assess the mean value over all $k(E)$ with the energy distribution $P(E)$, so that

$$k_{eff} = \frac{\int_0^\infty P(E)\rho(E)k(E)\ dE}{\int_0^\infty P(E)\rho(E)\ d(E)} \tag{3.3}$$

and $\rho(E)$ being the density of states of the reactant at total energy E.

This expression (3.3) simplifies at high pressures, because the total energy of the educt molecules can be described by a Boltzmann distribution $P(E) = e^{-E/kT}$ due to frequent collisions within the reagent molecules at temperature T (equation 3.4) which is synonym for equilibrium conditions.

$$k_{eff}^\infty(T) = \frac{kT}{h} \cdot \frac{Q^\ddagger}{Q} \cdot \exp\left(-\frac{E^\ddagger}{RT}\right) \tag{3.4}$$

$Q^\ddagger$ and Q are hereby assigned to the partition function of the transition state and the partition function of the reagent molecule.

Equation (3.4) is more commonly known as the transition state equation of Eyring for the reaction rate, expressed in the pseudo-thermodynamic form with

$$\begin{aligned} k_{eff}^\infty(T) &= \frac{kT}{h}\exp\left(-\frac{\Delta G^\ddagger}{RT}\right) \\ &= \frac{kT}{h}\exp\left(-\frac{\Delta H^\ddagger}{RT}\right)\exp\left(-\frac{\Delta S^\ddagger}{R}\right) \end{aligned} \tag{3.5}$$

which connects the enthalpy $\Delta H^\ddagger$ and the entropy $\Delta S^\ddagger$ of activation with the high pressure rate constant.

Isolated ion dissociations thus are theoretically very closely related to thermal molecular dissociations as they occur in high pressure gas-phase studies as well as in solution state reactions, where the Eyring equation is commonly known from. This demonstrates the neat applicability of gas-phase results to illuminate the thermodynamic and kinetic behavior of a system also in the condensed phase (at least under some premises; see Chapter 7 and 8).

3.3 Thermodynamic versus Kinetic Control of Ion Dissociations

Collision induced ion dissociation reactions as they are theoretically described with equations (3.1) and (3.4) (see Chapter 3.2) can be further classified depending on the sign and the magnitude of the activation entropy $\Delta S^{\ddagger}$ of the activated complex $(AB^{+})^{*}$.[15]

A fairly positive $\Delta S^{\ddagger}$ indicates a so called loose transition state, most common for the majority of gas phase dissociation reactions.

This is due to the long rang attractive potential between ion and charge induced dipole of the neutral fragment helping to overcome small activation barriers.

Therefore, simple bond cleavages have a monotonically rising energy profile as the reaction coordinate proceeds towards the products (see Scheme 3.2).
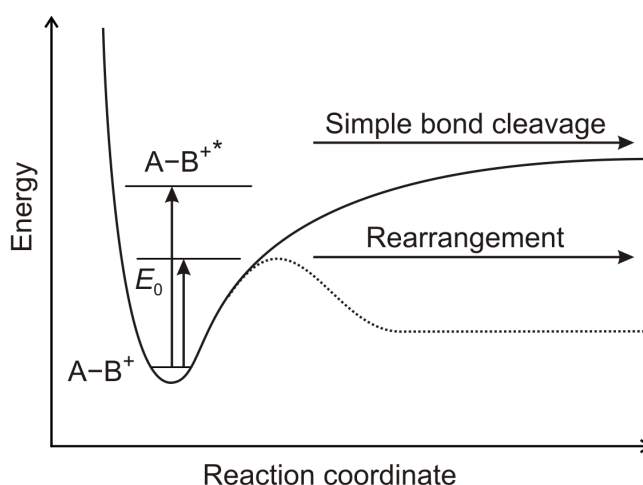
Scheme 3.2 Schematic potential energy profile for reaction over a loose or a tight transition state.[16]

The situation changes in case of rearrangement reactions with cyclic transition state structures. The additional bond making in the transition state leads to a significant reverse activation energy barrier which stabilizes the product side (see Scheme 3.2). The experimentally accessible threshold energy, always the highest energy along the reaction coordinate for dissociation, describes for a tight transition state consequently the actual barrier height. This threshold energy is not equivalent to a simple bond dissociation energy as it is for a loose transition state.

In general, simple bond cleavages tend to have higher activation energy thresholds than rearrangements, where the bond formation in the transition state decreases the energetic cost of a simultaneous bond rupture.

This thermodynamic picture with the potential energy profiles for loose versus tight transition states[17] still has to be refined by the kinetic aspects. In this context it is important to restart the argumentation again with the RRKM expression for the microcanonical rate constant (equation 3.1). It implies that dissociation of the reactant ion can occur only, if the reactant internal energy E exceeds the energy needed to cross over the potential energy barrier E_{TS}, (which is a real barrier for tight transition states and only a minor additional barrier due to centrifugal effects on the otherwise monotonically rising potential energy for a loose transition state (see Chapter 5.2) towards the products.

The kinetic aspect comes into play, because tight transition states have a lower density of rovibronical states available for the transition state, since some bending and twisting modes are embedded in a cyclic transition state geometry.

As a consequence thereof, also the entropy of activation $\Delta S^{\ddagger}$ has a much lower value for tight than for loose transition states, whereas for the latter ones all existing rotational and vibrational modes are accessible in the transition state geometry.

Comparing a competitive reaction that can either react via a tight TS2 or alternatively over a second channel via a loose TS1, than it is clear that at lower internal energies only the lower activation barrier of the tight transition state will be surmounted which denotes that the rate constant $k_2(E)$ plotted versus the internal energy of the activated complex also starts rising at a lower value of the internal energy E (see Figure 3.2).
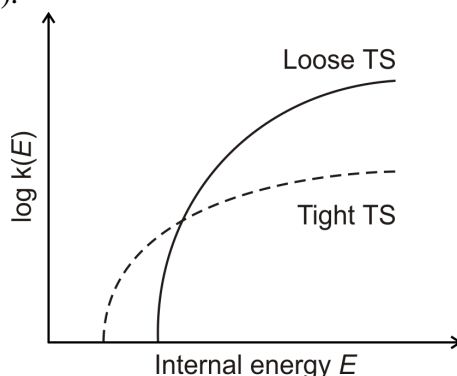
Figure 3.2 Comparison of the evolution of the rate constant $k(E)$ with increasing internal energy for loose and tight transition state reactions.[17]

However at higher internal energy the situation inverts and the rate constant for a reaction over a loose transition state $k_1(E)$ exceeds the rate constant for the tight transition state reaction $k_2(E)$ because a larger number of quantum states are available and can be populated, which leads to a larger enumerator in the RRKM expression for the unimolecular rate constant $k(E)$ (see equation 3.1).
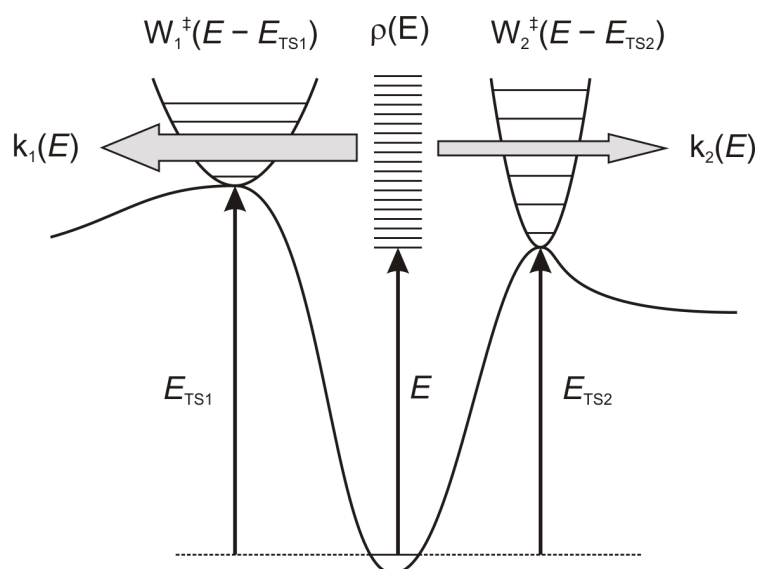
Scheme 3.3 Competitive dissociation over a tight versus a loose transition state.[17]

Thus, at high internal energies the reaction over a loose transition state proceeds faster, although the threshold energy E_{TS1} for the loose TS1 is larger than the threshold energy E_{TS2} for the tight TS2. (See Scheme 3.3).

3.4   References

[1]   Cooks, R. G., Ed.; *Collision Spectroscopy*, Plenum: New York, **1978**

[2]   Yamashita, M.; Fenn, J. B.; *J. Phys. Chem.* **1984**, *88*, 4451–4459

[3]   a) Armentrout, P. B.; *Acc. Chem. Res.* **1995**, *28*, 430–436; b) Rodgers, M. T.; Ervin, K. M.; Armentrout, P. B.; *J. Chem. Phys.* **1997**, *106*, 4499–4508

[4]   Rodgers, M. T.; Armentrout, P. B.; *Mass Spectrom. Rev.* **2000**, *19*, 215–247

[5]   a) Armentrout, P. B.; Hales, D. A.; Lian, L.; *Advances in Metal and Semi-conductor Clusters*, *Vol 2*; Duncan, M. A., Ed.; JAI: Greenwich **1994**, 1–39; b) Armentrout, P. B.; *Ann. Rev. Phys. Chem.* **2001**, *52*, 423–461

[6]   Wenthold, P. G.; Hu, J.; Squires, R. R.; *J. Am. Chem. Soc.* **1996**, *118*, 11865–11871

[7]   Poutsma, J. C.; Nash, J. J.; Paulino, J. A.; Squires, R. R.; *J. Am. Chem. Soc.* **1997**, *119*, 4686–4697

[8]   Hammad, L. A.; Gerdes, G.; Chen, P.; *Organometallics* **2005**, *24*, 1907–1913

[9]   Zocher, E.; Dietiker, R.; Chen, P.; *J. Am. Chem. Soc.* **2007**, *129*, 2476–2481;

[10] Zocher, E.; Sigrist, R.; Chen, P.; *Inorganic Chemistry* **2007**, *46*, 11366–11370

[11] Lindemann, F. A.; *Trans. Faraday. Soc.* **1922**, *17*, 598–606

[12] Baer, T.; Mayer, P. M.; *J. Am. Soc. Mass. Spectrom.* **1997**, *8*, 103–115

[13] Holbrook, K. A.; Pilling, M. J.; Robertson, S. H.; *Unimolecular Reactions*, Wiley, **1996**

[14] Forst, W.; *Unimolecular Reactions; A Concise Introduction*, Cambridge University Press, **2003**, Chapter3

[15] Futrell, J. H.; *Gaseous Ion Chemistry and Mass Spectrometry*, John Wiley & Sons, New York, **1986**, Chapter 1

[16] Armentrout, P. B.; *Top. Curr. Chem.* **2003**, *225*, 233–262

[17] Gross, M. L.; Caprioli, R.; *The Encyclopedia of Mass Spectrometry, Fundamentals of and Applications to Organic (and Organometallic) Compounds*, Vol 4; Nibbbering, N. M. M., Ed.; Elsevier, Oxford **2005**, Chapter 1

Chapter 4

Instrumentation

4.1 Operation Principle of the Triple-Quadrupole Tandem Mass Spectrometer

Ideally suited for qualitative and quantitative studies of gas-phase reactions are triple quadrupole tandem mass spectrometers, of which our working group possesses two Finnigan type TSQ-700 instruments, with one of the two being especially configured to collision induced dissociation measurements. (See Chapter 3.1.1)

4.1.1 Structure of a TSQ-700

A schematic overview over the latter modified TSQ 700 instrument is given in Scheme 4.1[1]
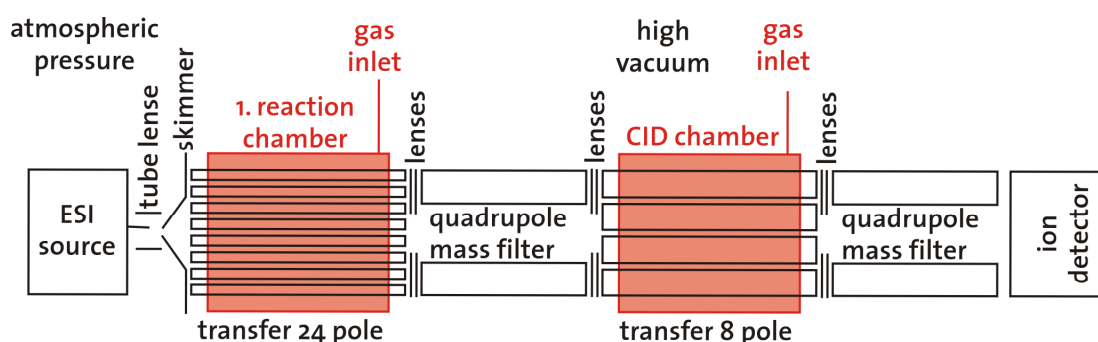
Scheme 4.1 The TSQ-700

The ESI spray source first of all transfers the intact molecular ions from a dilute solution (~ 10^{-5} M) directly to the gas-phase via a complicated process[2] involving charged droplet formation, desolvation and fission[3,4] to generate "nanodroplets" that

finally release gas phase ions either according to the "single ion in droplet" theory[5] or by evaporation of single ions including their solvation shell with subsequent desolvation to the naked gas-phase ion.[6,7]

In the TSQ-700 the electrospray process is supported by a coaxial nitrogen stream and by the preheating of the gas stream taking place in the heater capillary (100–200 $^\circ$C), which both facilitates the desolvation of the ions.

The gas stream is then expanded in a prechamber, which gets pumped down to 1 Torr, and meets the skimmer, where final desolvation or fragmentation occurs depending on the potential of the tube lens. Low potentials (20–50 V) mean very mild conditions, high potentials (100–150 V) equal rather harsh conditions enabling deliberate fragmentation processes. Also, the DC potential of the subsequent ion guide together with the temperature of the heater capillary allow precise tuning of the desolvation conditions.

After the skimmer the ions are transferred in the first reaction chamber, containing instead of the original octapole a self constructed (RF-)24-Pole.[8] Therein pre-coordinations with a reactant gas or ion thermalization with a buffer gas and residual solvent molecules of pressures up to 10^{-2} Torr are performed which equals thermal conditions of typically 70 $^\circ$C, with up to 10^5 collisions per reactant molecule. The advantages of higher order multipoles for producing narrow Gaussian shape kinetic energy distributions of the reactant ions is outlined in Chapter 4.2. The quite high operation gas pressure in the 24-pole region has caused another modification of the commercial TSQ-700 instrument, that is the installation of a second turbo pump at the end of this ion transfer region to reduce the gas load in the subsequent analyzer region.

In the first quadrupole the reactant ions are mass selected and then injected in the RF octapole collision cell where they can undergo reactions, *e.g.* CID with a neutral target gas of well defined pressure while the octapole rod offset can be scanned in order to vary the kinetic energy of the reactant ion (see subsection 4.1.3). The "effective path length" of 23 ± 5 cm was measured for a representative ion passing the octapole.[9]

The reaction fragmentation products are finally mass analyzed in the second quadrupole.

4.1.2   Operation Modes of a TSQ-700

A TSQ-700 instrument can be run in three different scan modes: the parent-mode, the neutral loss scan and the daughter mode,[10] whereas the latter one is especially important for CID measurements.

The different operation modes take further advantage of the two possibilities how to use the quadrupoles; either for sharp mass selection or in "RF-only" mode as high pass mass filters and thus ion guides for a large number of ions with different *m/z* values.

Daughter mode

Consequently, for daughter mode there are two variants: Either Q1, the first quadrupole, is adjusted to selective transmission of only one mass, or it is run as high pass mass filter, whereas Q2, the second quadrupole, works in normal mass scan mode to time select the different masses of the reaction products. "RF-only" mode is known to show more narrow kinetic energy distributions of the reactant ions being an advantageous issue for CID-measurements, but suffering from reduced practicability in case there are higher masses than the ion of interest. Such a situation would require setting the high pass limit just above and just below the target mass. Consequently an additional measurement curve still under constant pressure settings of the octapole and stable spraying conditions would be needed.

This fact leads to the decision in the current PhD-thesis to exclusively use the daughter mode with sharp mass selection in Q1, because the problem arising from non-comparable rfd-spectra for "cuts" before and after the ion of interest could hardly be compensated with the slightly better kinetic energy distribution (1.7 versus 2.0 eV energy in laboratory frame).

Parent mode

The next possible mode to operate a TSQ-700 is the parent mode, where Q1 is used in normal mass scan mode, so that ions with different masses cross the collision cell time separated with the possibility to react or fragment in transit. Q2 either selectively transmits one specific *m/z* value or it is run in "RF-only" mode as a high pass mass filter.

Neutral loss scan

For neutral loss scan, both, Q1 and Q2, are operated in the mass scan mode with always a fixed mass difference between the scanned masses in Q1 and Q2. Consequently, this setting allows to investigate which ions out of a whole population undergo a certain mass-change.

4.1.3   The DAC Scan Method

For CID threshold measurements, the invention of the so called "DAC scan method" is a significant practical improvement.

Originally it was standard fashion to acquire a single CID-spectrum with parent and daughter peaks for every manually set collision offset of the octapole, to sample in small steps the whole range of E_{lab} energies for which the meaningful parts of the threshold curve, like onset and rising part up to the plateau, are achieved.

It is self-evident that this method is enormously hampered by its time consuming manner, not even with respect to the overall effort but more concerning the difficulties to maintain stable spraying conditions and stable pressures of the target gas inside the octapole for the extended measurement times.

The obvious solution to that problem was the development of an automation for sweeping through the required range of E_{lab} energies and acquiring therefore the product and the parent-ion-intensities separately.

Sole condition for defining such a "DAC scan method" are some instrument dependent parameters,[11] like the machine decay half life of 300 ms and the time an ion needs to pass the octapole. The latter variable could be assigned via two different experimental routes to a range of 30–60 μs, with increasing tendency for larger ions.

It is either possible to calculate the residence time of the gaseous ion when relating the entry velocity (experimentally determined with retardation measurements; see Chapter 5.3.1) and the exit velocity (delimited with ion mobility) of the ions passing the octapole, or, alternatively the same information can be gained from (too) fast neutral loss scans of only few mass units difference, so that an additional artificial mass shift of the parent ion can be related to its residence time in the octapole.

As a consequence scan times per point on the threshold curve of 1–3 s have proven to be reliable and don't show any change of the detected ion intensities compared to even longer scan times.

However, there has to be caution in applying the "DAC method", because it requires manual adjustment of the octapole-collision-offset to the lowest offset, that is present in a chosen scan range.

This important instruction was discovered in the current phd-thesis in cooperation with Rolf Dietiker,[11] because the large DAC scan ranges from −110 V → +10 V, required for CID threshold measurements of 2:1 bisoxazoline copper complexes, differ significantly from the preloaded standard setting of the TSQ-700 at −28.5 V. Such a value would be only suitable for rather weakly bound molecules, that reach already the plateau of the threshold curve at these low accelerations.

Further, it is obvious that executing a DAC command on the collision offset does not automatically alter all the voltages after this region to keep constant conditions at the exit of the octapole.

This is only automatically adjusted by the original control software of the TSQ-700 for manual changes of the collision offset, but there is no linkage for an appropriate change of the collision offset simultaneously when applying the DAC command. The result of neglecting a proper choice of the collision offset is presented in Figure 4.1.

If the manually set collision offset differs more than 10–20 V from the minimal DAC scanned voltage of −50V (which equals the maximal applied collision energy) severe changes in the rising part of the threshold curve are observed, caused by the various distinct cutoff ramps for a part of the ions.

Especially with the manual offset at 10 V, only ions with the highest kinetic energy (often the anyways as good as possible minimized, non-statistical behaving high energy tail) out of the total distribution curve can still reach the detector, which obviously leads to very wrong threshold energies.
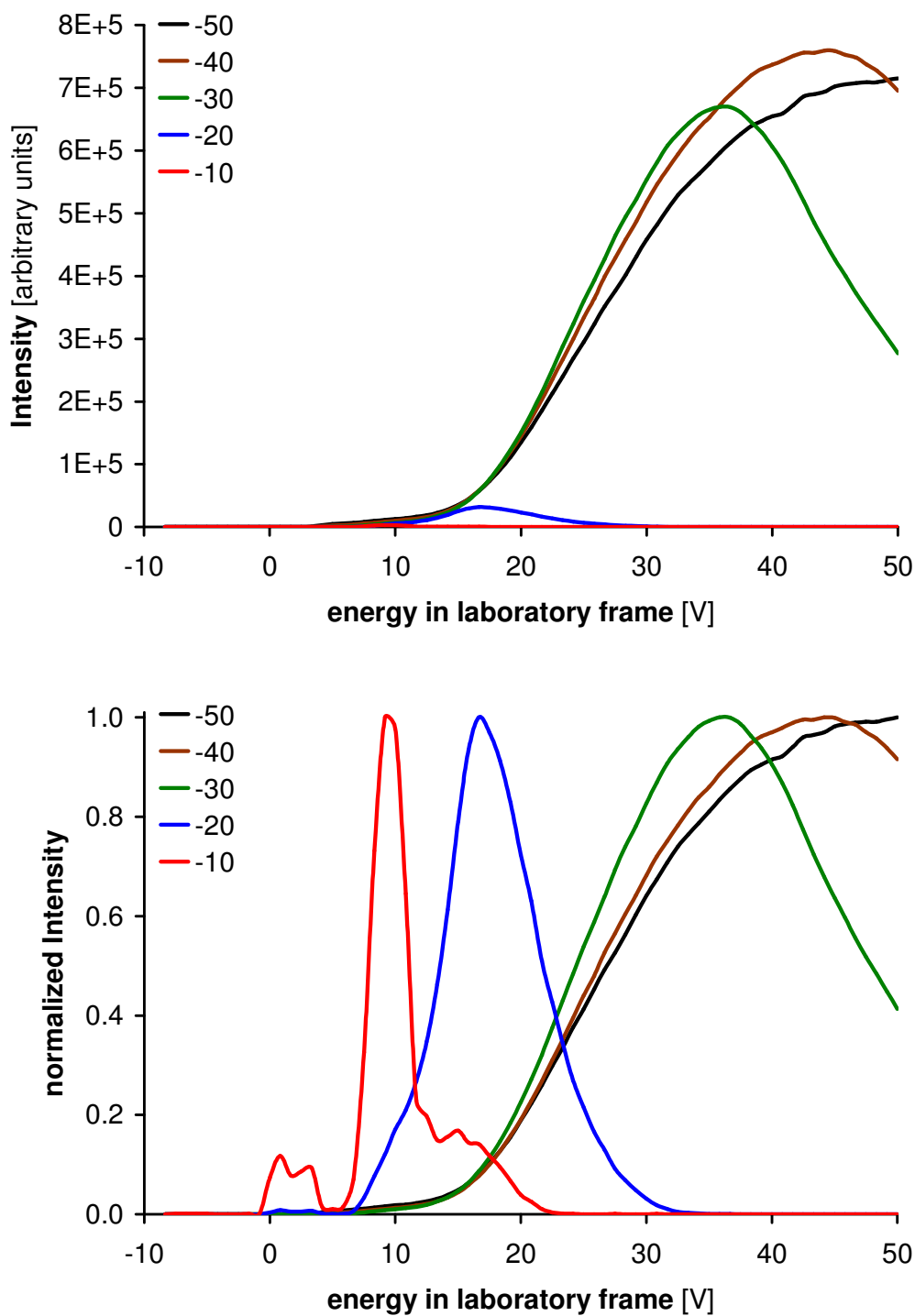
Figure 4.1 CID threshold measurements at different collision offsets using the new "DAC scan method" for a 2:1 bisoxazoline copper(I) complex. Top: absolute intensities of the daughter peak. Bottom: normalized intensities of the daughter fragment.

Considering the above outlined manual settings of the collision offset opens with the the "DAC scan method" a tremendous practical improvement, that is perfectly suited to replace the old "integration method" without any loss of reliability. (See Figure 4.2).
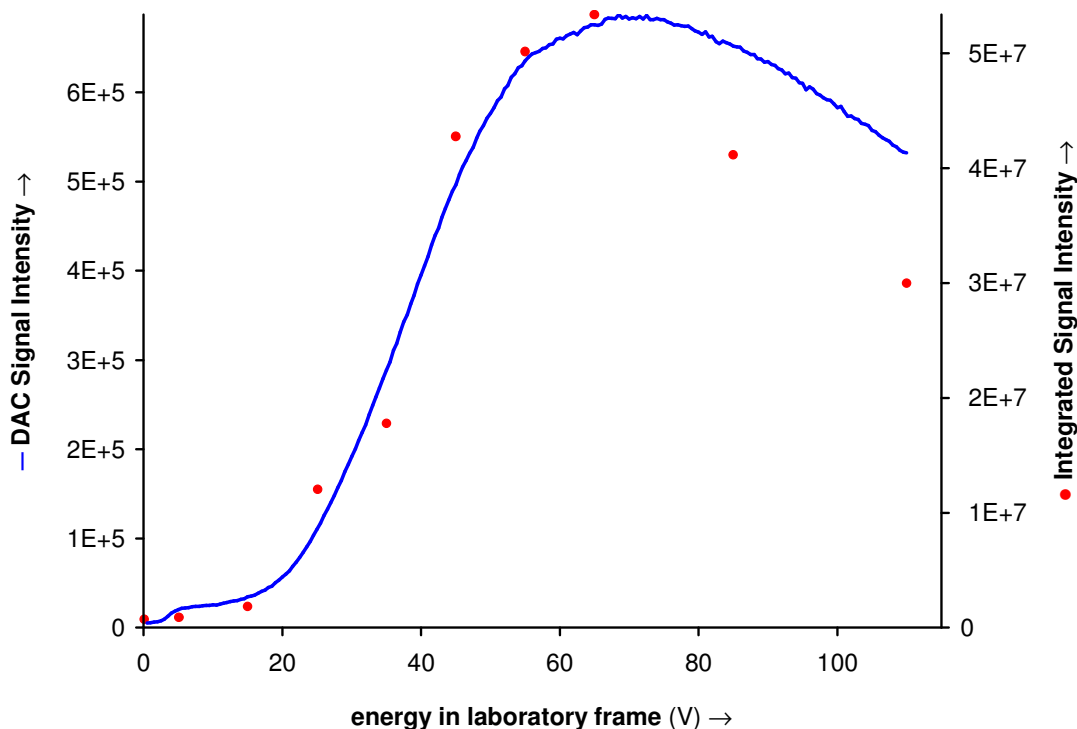
Figure 4.2 Comparison of the old (●, integrals) and the new (——, dac) method for the daughter fragments of a 2:1 bisoxazoline copper(I) complex when measuring a CID-threshold.

4.2   Multipoles as Ion Guides and Mass-Filters

In ESI-tandem mass spectrometry there are two different ways to apply multipoles: either for sharp mass selection, conveniently performed with quadrupoles, or confinement and guidance of ions within a steep potential well under the inclusion of collisions with a buffer gas to gain a preferably narrow Gaussian distribution of ion kinetic energies.

In the following section the operation principle of multipoles as ion guides will be outlined,[12] leading to an improved design of the previously implemented prototype 24-pole in the TSQ-700.

4.2.1   Adiabatic Ion Transmission in Inhomogeneous RF-Fields

Exposing an ion of mass m and charge q to a quasi-stationary electric field composed of a static part $\mathbf{E}_s(\mathbf{r})$ and a time dependent component $\mathbf{E}_0(\mathbf{r}) \cos{(\Omega t + \delta)}$, then the equation of motion equals

$$m\ddot{\mathbf{r}} = q\mathbf{E}_0(\mathbf{r})\cos{(\Omega t + \delta)} + q\mathbf{E}_s(\mathbf{r}) \qquad (4.1)$$

$\mathbf{E}_0(\mathbf{r})$ is the field amplitude, Ω is the radiofrequency and δ is the phase.

The differential equation (4.1) is easily solved for the simple case of a parallel plate capacitor characterized by a homogeneous electrical field, that is per definition independent of the spatial vector $\mathbf{r}$.

A charged particle oscillates herein as a function of time with constant amplitude $\mathbf{a} = q\mathbf{E}_0 / m\Omega^2$ and without changing its mean position $\mathbf{r}(0)$, so that its motion is described as

$$\mathbf{r}(t) = \mathbf{r}(0) - \mathbf{a}\cos{(\Omega t)} \qquad (4.2)$$

However, the situation changes drastically if the electrical field becomes inhomogeneous, *e.g.* in the textbook example of a cylindrical capacitor. The charge experiences now a varying field strength during its oscillatory motion, causing a force that pushes the charged particle into regions of weaker fields. Since equation (4.1) can no longer be derived analytically for such a case, only numerical integration or approximate analytical attempts are possible.

The effective Potential in Inhomogeneous RF-Fields

As a consequence, in order to determine some general properties of the motion of a charged particle in an inhomogeneous RF-field,[12] some premises have to be taken.

It is assumed that the electrical field varies smoothly as a function of the coordinate $\mathbf{r}$ and that the radio-frequency is high enough to keep the amplitude $\mathbf{a}$ small. This allows to express a solution for equation (4.1) by superimposing a smooth drift term $\mathbf{R}_0(t)$ and a rapidly oscillating motion $\mathbf{R}_1(t)$:

$$\mathbf{r}(t) = \mathbf{R}_0(t) + \mathbf{R}_1(t) \qquad (4.3)$$

with $\mathbf{R}_1(t) = -\mathbf{a}(t) \cos{(\Omega t)}$.

From the smooth motion $\mathbf{R}_0(t)$ (also called guiding center or secular motion) the differential equation for the time-averaged effect of the oscillatory field can be derived under the given assumptions. This so called field gradient force, caused by the inhomogeneity of the field, equals

$$m\ddot{\mathbf{R}}_0 = -\frac{q^2}{4m\Omega^2}\nabla E_0^2 \qquad (4.4)$$

and gives rise, when also considering the electrostatic potential Φ_s, to the "effective potential" as the total, time independent mechanical potential V^*

$$V^*(\mathbf{R}_0) = q^2 E_0^2 / 4m\Omega^2 + q\Phi_s \qquad (4.5)$$

The equation of motion describing the smooth trajectory becomes then simply

$$m\ddot{\mathbf{R}}_0 = -\nabla V^*(\mathbf{R}_0) \qquad (4.6)$$

which is again a differential equation, but much easier to solve than the original one (4.1), since it does not contain time explicitly.

The superimposed sinusoidal oscillation with its amplitude depending on the RF-field is given straightforward

$$\mathbf{R}_1(t) = -q\mathbf{E}_0(\mathbf{R}_0) / m\Omega^2 \cos(\Omega t) \qquad (4.7)$$

Adiabaticity and safe Ion Transmission

An important variable to explain the principle of ion transmission in an inhomogeneous RF-field is the total energy E_m of an ion being under adiabatic conditions a constant of the motion.[12]

$$\tfrac{1}{2}m\dot{\mathbf{R}}_0^2 + q^2 E_0^2 / 4m\Omega^2 + q\Phi_s = E_m \qquad (4.8)$$

Therefore, for an ion moving in such an inhomogeneous field, permanent exchange between the three different forms of energy, namely the kinetic energies $\tfrac{1}{2}m\dot{\mathbf{R}}_0^2$ and $\tfrac{1}{2}m\dot{\mathbf{R}}_1^2$ and the electrostatic potential energy $q\Phi_s$ takes place, since the second term of equation (4.8) is proven to equal the kinetic energy of the fast oscillatory motion.

As an empirical criterion for safe confinement of ions within an inhomogeneous RF-field it can be postulated, that the effective potential V^* at the closest allowed

approach of the ion to the electrode surface, $\mathbf{r}_m$, must be larger than E_m. If not, the ion will be lost by collision with the electrode.

$$V^*(\mathbf{r}_m) > E_m \qquad\qquad (4.9)$$

Note that $\mathbf{r}_m$, the maximum turning radius, is smaller than the radius of the aligned electrodes, to provide sufficient space for the small oscillatory motions $\mathbf{R}_1(t)$ at the radial turning-points of the ion. (See equation 4.7)

Since the derivation of the total ion energy E_m is solely valid for adiabatic conditions, the criteria implied therewith shall be introduced more detailed in the following paragraph.

In general, adiabaticity is synonymous for constant total ion energies E_m without resonant energy build up from the RF-field.

This is based on the assumptions of applying a rather high radio frequency, whereas all the other changes in time like the amplitude $\mathbf{a}(t)$ and the phase of the oscillatory motion are supposed to be slow. Also the variation of the electric field is postulated to be a very smooth function of the coordinate $\mathbf{r}$.

Consequently the adiabatic approximation demands over the full distance of the oscillation, that is over $2\mathbf{a}$, the change of the electromagnetic field to be much smaller than the field itself.

$$\left|2(\mathbf{a}\nabla)\mathbf{E}_0\right| < \left|\mathbf{E}_0\right| \qquad\qquad (4.10)$$

This basic requirement for safe confinement of charged particles in effective potential wells leads to the definition of the adiabaticity parameter

$$\eta = \left|2(\mathbf{a}\nabla)\mathbf{E}_0\right| / \left|\mathbf{E}_0\right|. \qquad\qquad (4.11)$$

Since there is no general mathematical solution to characterize rigorously stable and unstable ion trajectories within an inhomogeneous RF-field (equation 4.1), the adiabaticity parameter is used to differentiate in this connection. The empirical limit $\eta_m = 0.3$ guarantees adiabaticity for most practical applications. (See Figure 4.3 and Figure 4.4 in comparison.)
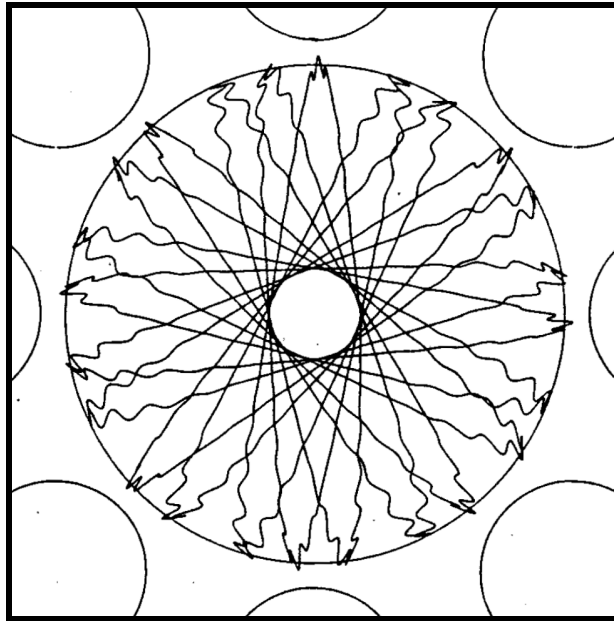
Figure 4.3 Typical trajectory of an ion in an octapole under adiabatic conditions.
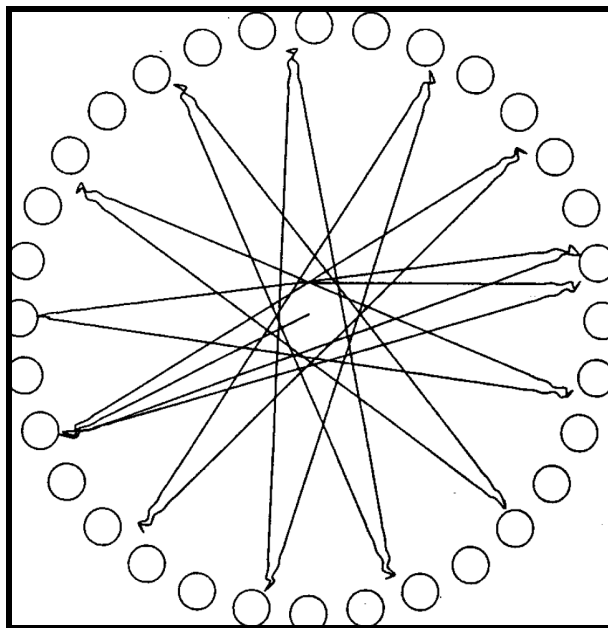
Figure 4.4 Trajectory in a 32-pole with the adiabatic approximation being not fulfilled. The angular momentum is no longer conserved because the closest approach of the trajectory to the center changes.

Two Dimensional Multipoles

Among the most important electrode systems to confine ions within inhomogeneous RF-fields, the two dimensional multipoles have to be named. The maybe most prominent device, the quadrupole for sharp mass selection, will be subject of Chapter 4.2.3, whereas in the following part the role of multipoles for ion guidance[12] will be outlined.

Multipoles consist in general of circular aligned electrodes with alternating polarity for each two adjacent electrodes of

$$+\Phi_0 = U_0 - V_0 \cos(\Omega t) \text{ and}$$
$$-\Phi_0 = -U_0 + V_0 \cos(\Omega t)$$

(4.12)

The applied potential $\Phi_0 = U_0 - V_0 \cos(\Omega t)$ consists of a static voltage U_0, the so called "DC"-part and a sinusoidal time dependent voltage with amplitude V_0, named "AC-signal".

The electrostatic potential of a multipole with $2n$ electrodes is given in equation (4.13)

$$\Phi(r, \varphi) = \Phi_0 \hat{r}^n \cos(n\varphi)$$

(4.13)

with the reduced variable $\hat{r} = r / r_0$, where r_0 is the inner radius of the multipole and φ is the azimuthal angle.

Deriving the electrostatic field as the negative gradient of the electrostatic multipole potential and inserting the thus obtained amplitude of the oscillatory field together with the expression for the static multipole potential in equation (4.5) leads to the general expression for the effective potential of a charged species within a 2n-pole (equation 4.14).

$$V^* = \frac{n^2}{4} \frac{q^2}{m\Omega^2} \frac{V_0^2}{r_0^2} \hat{r}^{2n-2} + qU_0\hat{r}^n \cos(n\varphi)$$

(4.14)

The effective multipole potential consists only of the radial symmetric first term in equation (4.14) in case of a solely applied AC-signal (Figure 4.5), but looses the radial symmetry as soon as the static voltage U_0 is superimposed (Figure 4.6).
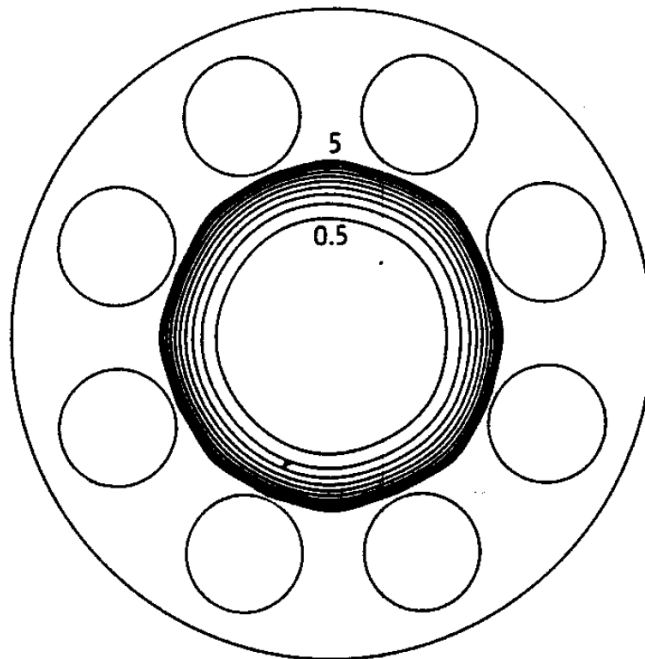
Figure 4.5 Effective potential of an octapole with circular rods and solely applied
AC-Signal. [12]
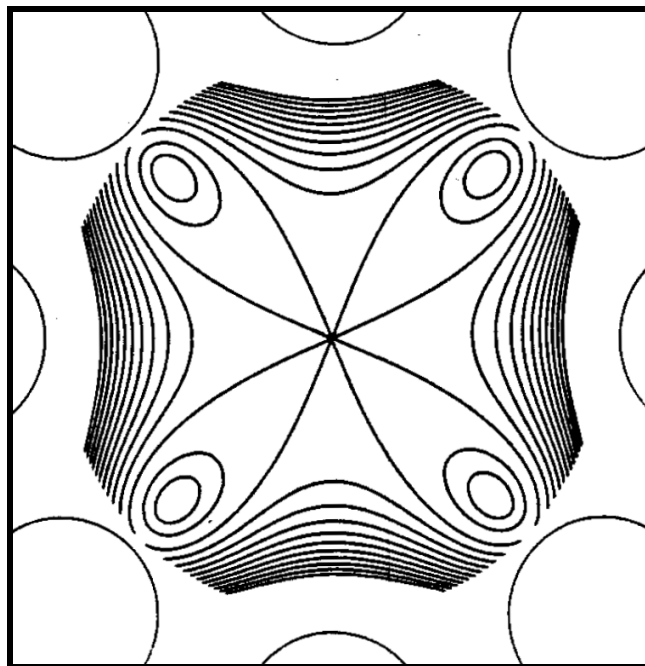
Figure 4.6 Effective potential in an octapole with superimposed static field. The ion
spends most of the time in the four potential minima located in the
vicinity of the negatively biased rods.[12]

For multipoles used as ion guides the DC-potential is usually set to zero and the ions are gently driven through by the longitudinal field from the space-charge effect,[13] or alternatively, the same DC-offset value U_0 is applied to all the rods, which accelerates the ion towards the multipole and maintains the radial symmetry of the effective multipole potential.

The most important characteristic of higher order multipoles is, however, the increasing steepness of the potential walls including an also larger field-free region in the radial direction. According to equation (4.13) quadrupoles have a $\hat{r}^2$ dependence, whereas an octapole possesses already a $\hat{r}^6$ dependence for the effective potential. Steeper potential walls have the advantage of a decreased reflection time of the ion on the wall and thus an also decreased probability for the ion to gain energy from the RF-field.[12] This reduces the undesirable high energy tail in the ion kinetic energy distribution, which cannot be described statistically with a Gaussian-distribution. Of course the accuracy of any subsequent data processing in *e.g.* CID threshold experiments is seriously hampered by such a high energy tail.

The whole problematic is solved when using higher order multipoles, such as for example a 24-pole,[8] which suppresses the negative effect of heating up a severe part of the ions.

A self-built prototype of a 24-pole has so far been applied with great success for ion thermalization and/or pre-coordination reactions in the TSQ-700. Only one restriction turned out to be very unpleasant for some chemical systems of interest. This first model of a 24-pole was obviously blocking ions with masses lower than $m/z = 150$ and thus preventing any gas phase experiments with such ions.

4.2.2   Construction of a new 24-Pole

In order to correct the low-mass-cut-off caused by the prototype 24-pole, two different attempts were tried simultaneously to overcome this handicap.

Possible Attempts

First of all, there was the suggestion that the PEEK-tube sitting directly on the PEEK-carriers, which hold the electrodes of the multipole in line, should be moved along the 24-pole to be located further away from the analyzer region of the TSQ-700. This PEEK tube covering 40% of the total length of the 24-pole allows to

introduce locally concentrated the reaction gas for ion-thermalization or pre-coordination. As a consequence, moving this tube with its two open ends more in the direction of the skimmer, should allow more effective pumping of the introduced gas-pressure, so that certainly less thermalization gas can leak into the first quadrupole. It is straightforward to assume that this effect should be more problematic for a sharp mass selection of ions with small masses, since they are more easily deflected.

Consequently, the design of the new 24-pole should allow a flexible adjustable location of the gas-inlet chamber in order to study the pressure dependence of the small ion transmission.

The second attempt to handle the low-mass-cut-off of the original 24-pole is based on the theory of inhomogeneous RF-fields.[12]

In this content it is necessary to introduce an additional parameter, the characteristic energy ε

$$\varepsilon = \frac{1}{2n^2} m\Omega^2 r_0^2 \ , \tag{4.15}$$

which combines the important parameters mass, frequency and inner radius of the multipole.

The adiabaticity parameter from equation (4.11) can be refined with the expression for the electrostatic field of the multipole and the definition of the characteristic energy to

$$\eta = \frac{n-1}{n} \ \frac{qV_0}{\varepsilon} \hat{r}^{n-2} \tag{4.16}$$

With equation (4.15) also the effective potential V^* of a 2n-pole can be rewritten to

$$V^* = \frac{1}{8} \frac{(qV_0)^2}{\varepsilon} \hat{r}^{2n-2} + qU_0 \hat{r}^n \cos(n\varphi) \tag{4.17}$$

The maximum energy E_m, (equation 4.8), defined as the sum of the effective potential and the kinetic energy of the smooth drift term can be expressed for the static voltage $U_0 = 0$ and the ion temporarily located at a turning point with $r = \hat{r}_m$ (=>½$m\dot{\mathbf{R}}_0^2 = 0$) as follows

$$E_m = \frac{1}{8} \frac{(qV_0)^2}{\varepsilon} \hat{r}_m^{2n-2} \tag{4.18}$$

Combination of (4.18) and (4.16) finally leads to the two important equations (4.19) and (4.20)

$$qV_0 = 8 \frac{n-1}{n} \frac{E_m}{\eta_m \hat{r}_m^n} \tag{4.19}$$

and

$$\varepsilon = 8 \frac{(n-1)^2}{(n\eta_m \hat{r}_m)^2} E_m. \tag{4.20}$$

with $\hat{r}_m = 0.8$ the empirical maximum turning radius of the ion as a reduced parameter and $\eta_m = 0.3$ the empirical maximum value for the adiabaticity variable.

The practical importance of this derivation is obvious, since equations (4.19) and (4.20) allow to calculate a value for the characteristic energy ε from all known parameters in order to relate this value to a specific radio-frequency for a certain ion mass in equation (4.15).

Even simultaneous confinement of two masses $m_1 < m_2$ with a common maximum transverse energy E_m can be derived by replacing η_m in equations (4.19) and (4.20) with

$$\eta_m' = (m_1 / m_2)^{n/(2n-2)} \eta_m \tag{4.21}$$

The mass range for which safe ion transmission through a multipole occurs, obviously depends directly on the applied radio frequency. Thus, a higher frequency should lead to stable trajectories for lower mass species.

The only problem arising thereby is caused by the very high capacitance of the prototype 24-pole with annular aligned plates representing the electrodes. In order to avoid changes on the RF-generator due to the increased load with such higher frequencies, the only alternative was to reconsider the design of the 24-pole.

This could be done all in once with the construction of an easily movable PEEK-tube for a flexible adjustable gas-inlet in the 24-pole region.

Design of the new 24-Pole

The requirement to reduce the capacitance for a new constructed 24-pole can only be fulfilled with rods instead of plates serving as electrodes.

According to the expositions of D. Gerlich, there exists an ideal combination for the inner radius r_0 of the multipole and the diameter d of the rods[12]

$$r_0 = (n-1)d / 2 \qquad (4.22)$$

Besides this empirical relationship for an "ideal multipole" it is also known from experience, that an increasingly large inner diameter of the multipole would require very high peak operating voltages of the AC-signal. Therefore the design of a higher order multipole like a 24-pole is required to handle rods with a rather small diameter.

Table 4.1   Dimensions in mm of the different multipoles
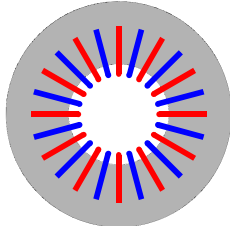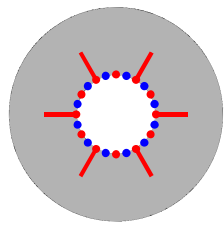
	Old multipole with plates	New multipole with rods	Ideal theoretical multipole with rods
d (plate/rod thickness)	0.450	0.700	0.545
x (distance between rods)	0.337	0.175	0.309
r_0 (inner radius of multipole)	3.000	3.000	3.000

Table 4.1 gives an overview over the geometrical details of the new constructed multipole with stainless steel rods in comparison to the old model with annular mounted stainless steel plates and an ideal theoretical multipole with rods according to the descriptions of Gerlich. For all three types the inner radius of the multipole is kept at 3.000 mm. However, it is remarkable, that for the newly designed multipole the diameter of the rods is the largest one in this row with 0.7 mm and the distance in between is approximately only half as big as for the old 24-pole or the theoretical model 24-pole. Fortunately, no problems with corona-discharge effects emerged for

the new 24-pole kept under standard operation conditions of 1 mTorr inside the TSQ-700.

Even smaller diameters for the rods would have been practically impossible, because all the rods have to be mounted radially exclusively along their outside surface. The inner half of the rods pointing towards the axis of the multipole have to be completely free for the ion beam not to come in contact with insulating layers. Otherwise charge build up effects would drastically perturb the electrical field and thus the operation of the multipole. This requirement was very trivial to fulfil for the multipole with rounded plates presenting a circular cross-section locally but then possessing a longer "width" for mounting the plate in the PEEK support and installing the electrical connections.[9]

In comparison, for the new multipole with these thin rods quite some fine mechanics were necessary: The rods are clicked in specifically milled PEEK surroundings of the carrier discs, so that only the outer half of the rods is covered with insulator. Two of the altogether 5 carrier discs, spread over the whole length of the 24-pole, bear electrical contacts in order to apply the positive and negative potential to each 12 of the 24 poles in an alternating manner.

The PEEK carriers for making the electrical contacts are screwed into two stainless-steel round plates in front and on the back side of the PEEK support. The whole unit possesses one electrical pin to feed in the electrical potential, which is distributed onto the rods via six bronze contacts from each of the two stainless steel plates. The bronze contacts are not welded, but touch the specific rod they have to support only due to mechanical tension. (See Figure 4.7).

This design offers maximum variability, because all the PEEK-supports (also the ones with the electrical contacts) holding the electrodes of the multipole in line can be slided independently. This allows to position the gas inlet chamber completely flexible, since for a stable alignment it simply needs to sit on two of the easily movable PEEK carriers. (See Figure 4.8).
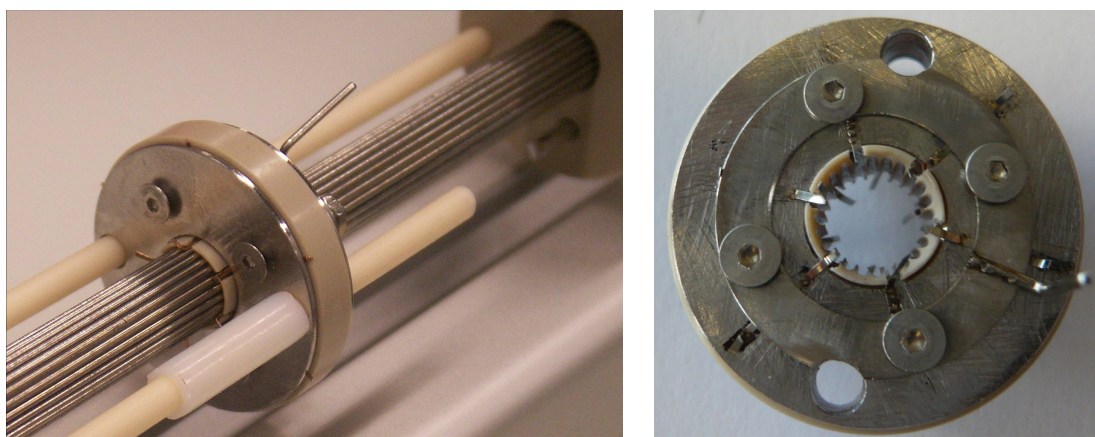
Figure 4.7 Details of the new 24-pole: PEEK carrier with electrical contacts (left) and electrical connections out of bronze (right).
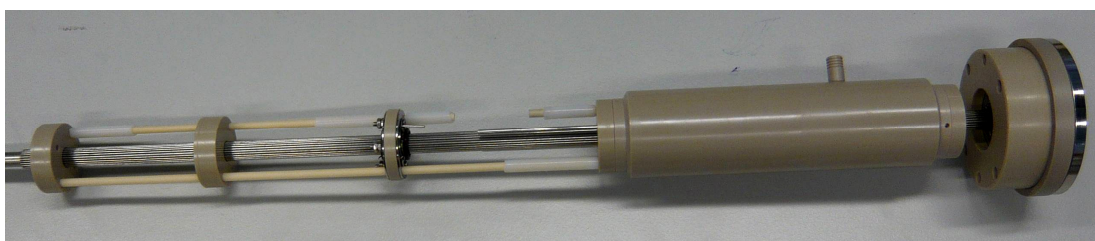
Figure 4.8 The complete new 24-pole with the gas inlet chamber located directly after the skimmer.

Characteristics of the new Multipole

In the following subsection the most important characteristics of the new designed 24-pole shall be subsumed.

As already mentioned, the use of rods instead of plates reduces the capacitance of the multipole. Thus, higher frequencies can be applied without increasing the load on the RF-generator tremendously.

The second task was the construction of a flexible movable gas inlet chamber for thermalization or pre-coordination. The chamber is at the moment positioned directly after the skimmer. Typical pressures herein are $7.3*10^{-3}$ Torr without and $1.1*10^{-2}$ Torr with Argon as collision gas.

The effect of moving the gas inlet chamber flexibly over the whole length of the multipole can now be investigated. A position directly after the skimmer leads to very high background pressures due to the not yet removed solvent molecules in this

region, whereas locating it at the end of the 24-pole might cause some leaking of thermalization gas in the analyzer region of the TSQ-700.

Further, the ion kinetic energy distributions for the new multipole were found to be ~2 eV in laboratory frame without thermalization gas and ~3 eV with Argon thermalization.

The broader kinetic energy distribution for Argon can most probably be explained with the assumption, that pure solvent molecules and pure Argon might thermalize to different average energies. Consequently, a combined thermalization of the reactant ions by both of them could account for the broader kinetic energy distribution. It is straightforward to conclude that with the reaction chamber all in front, sufficient thermalization occurs already with the solvent molecules from the spraying process.

The next characteristic of the new 24-pole concerns the average kinetic energies of the reactant ions. Those values tend to be higher than with the old multipole, by slightly over 1 eV.

Possible explanations for this observation are, *e.g.* that the old multipole contained more geometrical defects causing loss of the high energy ions. Also, the ions and solvent molecules have now a longer contact time, because both are sprayed into the thermalization chamber directly after the skimmer. The solvent molecules, which were heated in the spray capillary, can thus transfer more vibrational energy. Even the radio-frequency of the multipole influences the average kinetic energy of the ions, since it determines the maximum kinetic energy for which a particle still follows a stable trajectory. However, between 2.54 MHz for the old and 2.70 MHz for the new multipole is only a minor difference.

Anyways, when processing CID-data the energies will always be corrected for the average kinetic energy of the ions, being the absolute zero of the energy scale.

Finally, as the most important advantage of the new multipole, the successful transmission of low mass ions, *e.g.* with $m/z = 126$, can be presented.
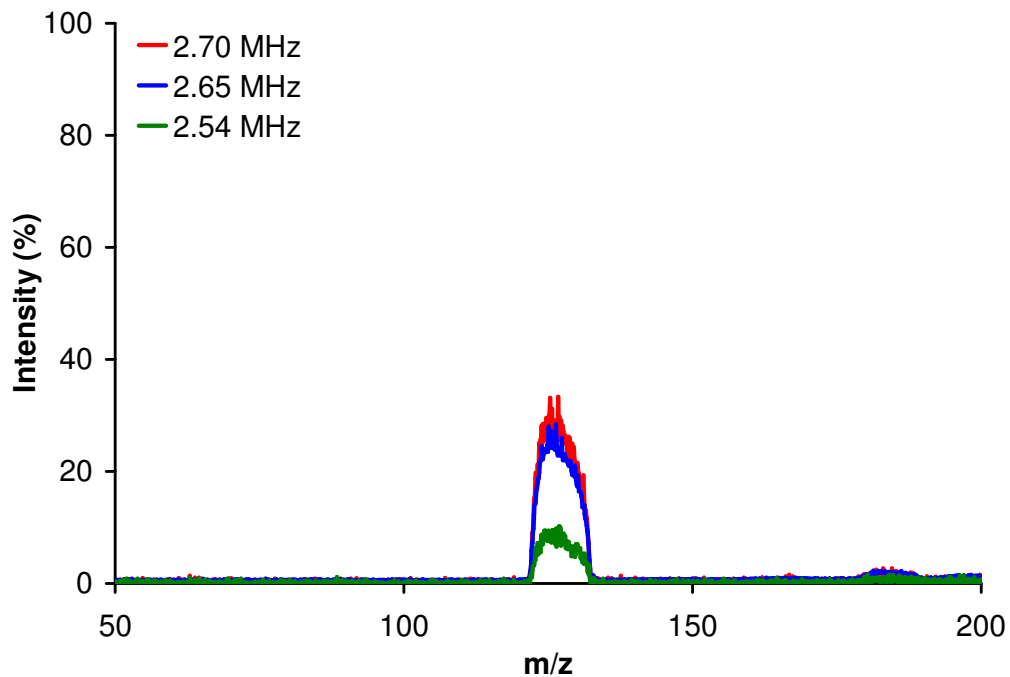
Figure 4.9 For an AC amplitude of 120 V and a DC-offset of −2.00 V on both channels a multiple increase of the ion signal can be detected when adjusting the radiofrequency to 2.70 MHz for the current setup.

The only slight disadvantage of the new 24-pole compared to the old model is its lower electrical and mechanical rigidity due to the fact that thin rods instead of plates were mounted together. Therefore, maintenance works require a more sensitive handling of the new model.

However, since ion guidance rather than sharp mass selection is intended with this 24-pole, slight irreversible deformations of the multipole geometry are uncritical. (See Figure 4.10). The only effect is that ions with the highest transverse energies will be lost. Solely drastic changes of the electric field like floating rods or misaligned electrical connections have to be excluded.
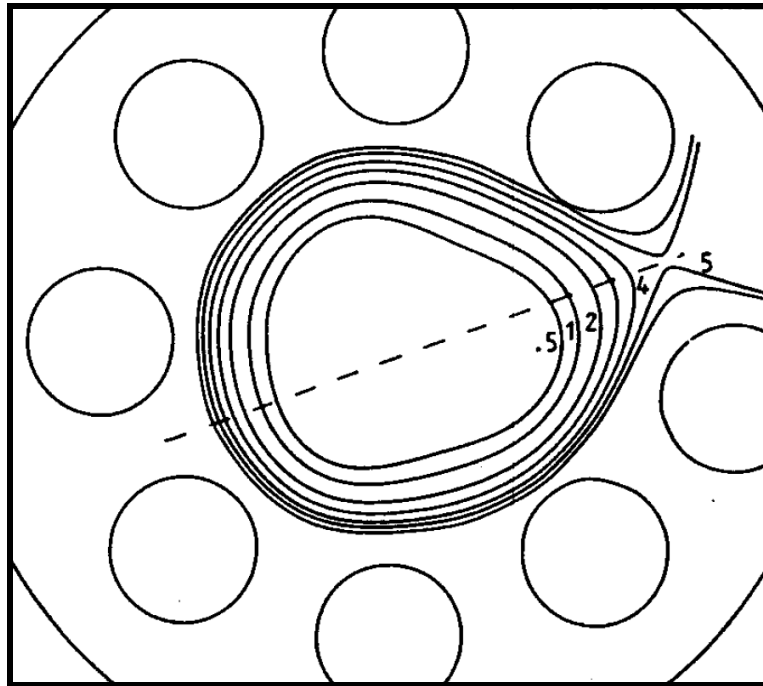
Figure 4.10 The effective potential of a mechanically distorted but still working octapole with $U_0 = 0$.[12]

4.2.3 Operation Concept of a Quadrupole Mass Filter

The most prominent and also theoretically best understood example of a multipole is the quadrupole mass filter.[12] It is always run with a static voltage U_0 in addition to the sinusoidal time dependent AC-signal with amplitude V_0. In contrast to the settings of the 24-pole as ion guide, the DC-offset of the quadrupole mass filter has an alternating polarity on each two adjacent electrodes. (For comparison see Chapter 4.2.1)

Remarkable for a quadrupole mass filter is, that the differential equations for the motion of an ion in such an electric field can be practically split up for the x and y-coordinate separately.[14]

$$\frac{d^2x}{dt^2} + \frac{\Omega^2}{4} \cdot \left[a_2 + 2 \cdot q_2 \cdot \cos(\Omega t) \right] \cdot x = 0 \qquad (4.23)$$

$$\frac{d^2y}{dt^2} + \frac{\Omega^2}{4} \cdot \left[a_2 + 2 \cdot q_2 \cdot \cos(\Omega t) \right] \cdot y = 0 \qquad (4.24)$$

This is only possible for the simple case of a quadrupole, but not for any other higher order multipoles, where the differential equations are nonlinear and coupled. Consequently, as already outlined in Chapter 4.2.1, there is no mathematical criterion to rigorously characterize stable and unstable solutions from equation (4.1), describing the motion of an ion in any other higher order multipole field than a quadrupole. Instead the criterion for stability, that is adiabatic conservation of energy and stable confinement in a geometrical region can solely be generalized by the empirical stability condition of having an adiabaticity parameter $\eta \leq 0.3$. Therewith most practical applications assuming the validity of the adiabatic approximation can be described sufficiently.

In the case of a quadrupole the specific differential equations (4.23) and (4.24) can still be solved directly. The solutions derived by Mathieu are classified as being either bounded or unbounded.[15] Physically a bounded solution corresponds to a stable trajectory, where the x and y coordinates of the particle remain finite. In contrast, an unbounded solution refers to the case where the radial displacement of the particle increases without bound such that it will collide with the electrodes.

The entirety of the Mathieu solutions can be clearly illustrated with the famous a_2q_2-stability diagram (see Figure 4.11), where the triangularly shaped border lines enclose the range of (a_2, q_2) parameters for stable ion trajectories.
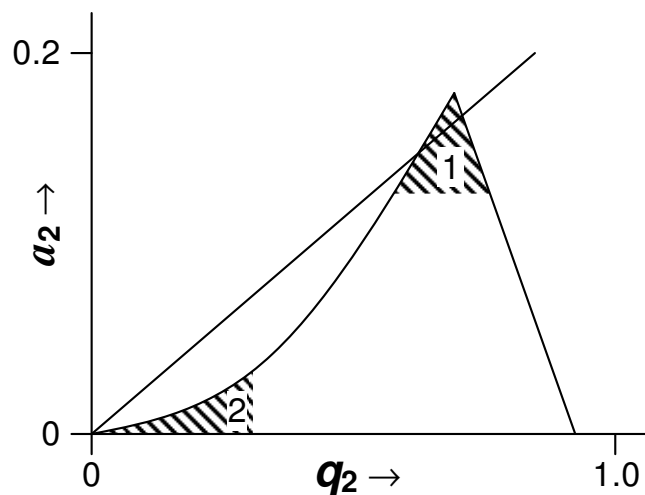
Figure 4.11 The a_2q_2-stability diagram of a quadrupole.

Therefore, the dimensionless parameters a_2 and q_2 have to be introduced

$$a_2 = \frac{4 \cdot q \cdot U_0}{\Omega^2 \cdot r_0^2 \cdot m} \qquad q_2 = \frac{2 \cdot q \cdot V_0}{\Omega^2 \cdot r_0^2 \cdot m} \qquad (4.25)$$

with U_0 representing the static DC-voltage and V_0 being the amplitude of the time dependent AC-signal.[14]

In practice, quadrupoles are usually operated such that a_2 and q_2 are always related by a simple ratio. Therefore U_0 / V_0 is kept constant and only the magnitudes of U_0 and V_0 are increased simultaneously.

This is equivalent to restricting the operation of the mass filter to a set of points lying on a straight line with zero intercept. The slope of this so called mass-scan line is adjusted via the U_0 / V_0 ratio in such a way that only a small portion of the mass-scan line crosses the tip of the stability diagram. Physically this setting is used to create a narrow bandpass mass filter.

Increasing U_0 and V_0 in a fixed ratio results in a successive transmission of all scanned masses. Thus the quadrupole is transparent for only a small mass range at a time and the mass scan window is continuously swept over the whole mass-scan range.

This operation as a sharp mass filter (region 1 in Figure 4.11) does of course not meet the adiabatic approximation (Chapter 4.2.1), which is only valid in region 2 of the a_2, q_2 stability diagram.

Besides its purpose as mass filter a quadrupole can also be run in RF-only mode as ion guide. In the stability diagram this case is represented for $a_2 = 0$. (Region 2 in Figure 4.11)

Now a rather large portion of the mass scan line falls within the stability region of the a_2, q_2 diagram. As a consequence a large number of ions with different m/z values has now stable trajectories and the quadrupole works as high pass mass filter.

4.3   References

[1]   Adlhardt, C.; *Intrinsic Reactivity of Ruthenium Carbenes: A Combined Gas Phase and Computational Study,* PhD Thesis, ETH Zurich, **2003**, Diss. ETH No. 15073

[2]   Rayleigh, L.; *Philos. Mag.* **1882**, *14*, 184

[3]   Hagers, D. B.; Dovici, N. J.; Klassen, J.; Kebarle, P.; *Anal. Chem.* **1994**, *66*, 3944

[4]   Gometz, A.; Tang, K.; *Phys. Fluids* **1994**, *6*, 404

[5]   Schmelzeisen-Redeker, G.; Buttering, L.; Röllgen, F. W.; *Int. J. Mass. Spectrom. Ion Proc.,* **1989**, *90*, 139

[6]   Iribarne, J. V.; Thomson, B. A.; *J. Chem. Phys.* **1976**, *64*, 2287

[7]   Thomson, B. A.; Iribarne, J. V.; *J. Chem. Phys.* **1979**, *71*, 4451

[8]   Hinderling, C. R.; *Elektrospray-Tandem- Massenspektrometrie als vielseitiges Werkzeug zum mechanistischen Studium von organometallischen Reaktionen,* PhD Thesis, ETH Zurich, **1999**, Diss. ETH Nr. 13158

[9]   Hammad, L. A.; Gerdes, G.; Chen, P.; *Organometallics* **2005**, *24*, 1907–1913

[10]   Plattner, D.A.; *Internat. Journal of Mass Spectrometry* **2001**, *207*, 125–144

[11]   Dietiker, R.; *Steps towards Structural Information in ESI-MS Gas Phase Investigations,* PhD Thesis, ETH Zurich **2006**, Diss. ETH Nr. 16455

[12]   Gerlich, D.; *Inhomogeneous RF Fields: A versatile Tool for the Study of Processes with slow Ions;* Ng, C.-Y.; Baer, M., Ed.; John Wiley & Sons, **1992**

[13]   Chen, P.; *Angew. Chem. Int. Ed.* **2003**, *42*, 2832–2847

[14]   Miller, P. E.; Denton, M. B.; *Journal of Chemical Education* **1986**, *63*, 617–
       622

[15]   Mc Lachlan, D. W.; *Theory and Applications of Mathieu Functions;*
       Clarendon: Oxford **1947**

Chapter 5

Statistical Modeling of CID-Thresholds

5.1   Simplified Collision Theory of hard-spheres

In order to connect collision theory and kinetic gas-phase theory it is appropriate to turn, first of all, to the simple model of hard sphere collisions.[1]

The effective potential does not give rise to an attractive force to pull the collision partners together, why it is only due to the conservation of energy that the particles collide when moving on a head-on path.

Thus, the effective potential is zero, if the particles don't contact and infinity as soon as they touch,

$$U(r) = \begin{cases} 0 & r > r_A + r_B \\ \infty & r \leq r_A + r_B \end{cases} \tag{5.1}$$

with, r_A, r_B being the radii of the collision partners.

The collision cross section σ (see Scheme 5.1) can be described depending solely on the geometric parameters r_A and r_B, so that $\sigma = \pi \cdot (r_A + r_B)^2$.
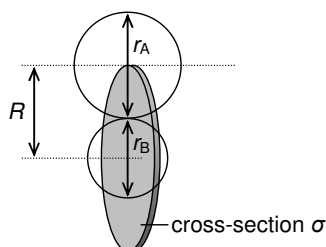
Scheme 5.1 The cross-section of two hard sphere molecules A and B can be seen as area around target molecule B, which has to be hit by molecule A.

For determining the number of collisions between A and B molecules per units of time and volume, Z_{AB}, the collision frequency can be expressed as[2]

$$Z_{AB} = \sigma \cdot \langle v \rangle \cdot N_A{}^2 \cdot [A]\,[B] \qquad\qquad (5.2)$$

with

$$\langle v \rangle = \int_0^\infty v\,f(v)\,dv = \sqrt{\frac{8kT}{\pi\mu}} \qquad\qquad (5.3)$$

as the average Boltzmann velocity, N_A the Avogadro constant and [A] and [B] the concentrations of molecules A and B, respectively.

For expressing the reaction rate of this bimolecular reaction (A + B → P and P = Product or activated complex) (see Chapter 3.2) the change of the molar concentration of A can be linked with the collision frequency, when scaled with the probability f for the collision to be energetic enough to cause formation of the product (equation 5.4).

$$\frac{d[A]}{dt} = -\frac{Z_{AB} \cdot f}{N_A} \qquad\qquad (5.4)$$

f equals equation (5.5) for an underlying Boltzmann-Distribution of particle energies.

$$f = \int_{E_A}^\infty f(E)\,dE = \frac{1}{kT}\int_{E_A}^\infty e^{-E/kt}\,dE = e^{-E_A/kT} \qquad\qquad (5.5)$$

Combination of equation (5.2) – (5.5) leads to

$$\frac{d[A]}{dt} = -\sigma\left(\frac{8kT}{\pi\mu}\right)^{1/2} N_A \cdot e^{-E_A/RT}[A]\,[B] \qquad\qquad (5.6)$$

with an Arrhenius-type rate constant for reactive events k_2

$$k_2 = \sigma\langle v \rangle N_A \cdot e^{-E_A/RT} \qquad\qquad (5.7)$$

since the overall reaction rate of bimolecular reactions is well known as $v = k_2[A]\,[B]$.

Further, it can be pointed out, that the rate constant for reactive events, k_2, differs from the rate constant for any collisions taking place, either reactive or elastic, by the

factor $(N_A \cdot e^{-E_A/RT})$, which allows to simply describe the rate constant for any appearing collision by

$$k = \sigma \langle v \rangle \qquad (5.8)$$

In either case the collision cross section is always constant and independent of the kinetic energy of the colliding particles, because in this model the conservation of angular momentum is neglected. This is a valuable approximation for collisions that happen solely with small impact parameters, being true for hard sphere collisions, but turns out to be quite poor for real ion-molecule reactions that can have much larger impact collisions due to attractive ion-induced dipole interactions (see further below).

5.2   The Langevin Cross Section

As already pointed out, the hard sphere potential is quite far away from truth for real ion molecule collisions and has to be redefined for a realistic description of collision trajectories and capture collisions caused by the attractive forces between ions and neutral molecules.[3, 4]

An ion of charge Q induces in a molecule of polarizability α and at distance r the dipole μ_i

$$\mu_i = \frac{\alpha Q}{(4\pi\varepsilon_0)r^2} \qquad (5.9)$$

where ε_0 is the permittivity of the vacuum.

The force between ion and molecule is then the product of the induced dipole and the derivative of the field:[5]

$$F = \mu_i \cdot \frac{d}{dr}\left(\frac{Q}{(4\pi\varepsilon_0)r^2}\right) = \frac{-2\alpha Q^2}{(4\pi\varepsilon_0)^2 r^5} \qquad (5.10)$$

The potential being zero at infinite separation is given by

$$V(r) = -\int_\infty^r F \cdot r\, dr = \frac{-\alpha Q^2}{2r^4(4\pi\varepsilon_0)^2} \qquad (5.11)$$

and describes the attractive interaction between ion and molecule with an r^{-4} dependence of their separating distance.

The next effect that has to be considered in contrast to the simplified hard sphere collisions is the fact that two particles, approaching each other not perfectly in line of their mass centers, automatically generate an angular momentum $L = \mu \cdot \vec{r} \times \vec{v}_{center}$ with μ the reduced mass, $\vec{r}$ the vector of their intermolecular distance and $\vec{v}_{center}$, the part of the relative collision velocity of the two particles, named $\vec{v}_{coll}$, that is perpendicular to the intermolecular distance $\vec{r}$ (Scheme 5.2). [6]
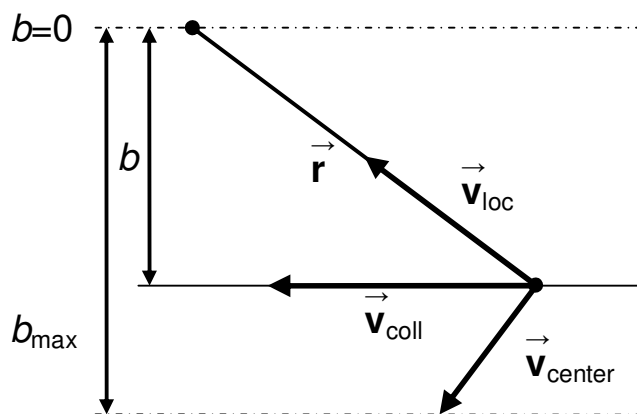
Scheme 5.2 Two dimensional approach of two colliding particles.

The part of the collision velocity $\vec{v}_{coll}$ being parallel to $\vec{r}$ is termed velocity in line of the mass-centers $\vec{v}_{loc}$ and the component of the $\vec{r}$ vector perpendicular to the relative velocity of the molecules, $\vec{v}_{coll}$, is the so called impact parameter b, defined prior to collision, when the two collision partners are still further away.

From physical understanding it is obvious that, the larger the impact parameter is for two approaching molecules, the more the centrifugal repulsion $L^2/2\mu r^2$ increases up to that point with $b > b_{max}$ from whereon the collision energy of the two molecules, $E_{coll} = \frac{1}{2}\mu v_{coll}^2$, and the ion-induced dipole attraction cannot surmount the centrifugal barrier any longer, so that the two molecules pass each other without colliding (Scheme 5.3).
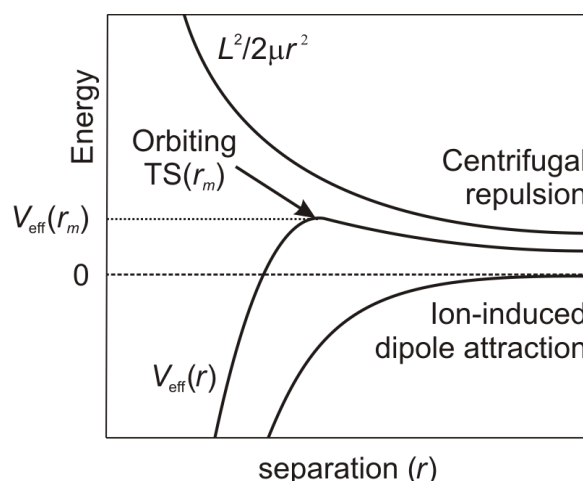
Scheme 5.3 The potential energy surface for an ion molecule collision, when exploring the potential energy surface from the right side with an initially large separation of the collision partners.

The picture is also valid vice versa: The dissociation of an activated ionic complex $(A–B^+)^*$ in a neutral and an ionic fragment over a loose orbiting transition state (see Chapter 3.3) located at the centrifugal barrier, can also be illustrated when going from negligible to increasing spacious separation of the two fragments.

The origin of the centrifugal barrier can be pointed up by the r^{-4} dependence of the attractive ion dipole potential and the r^{-2} dependence of the centrifugal repulsion which gives, when superimposed, the centrifugal barrier at the intermolecular distance $r = r_m$ (equation 5.12).[7]

$$V_{eff}(r_m) = \frac{-\alpha Q^2}{2(4\pi\varepsilon_0)^2 r_m^4} + \frac{L^2}{2\mu r_m^2} = \text{max}. \qquad (5.12)$$

For a collision between ionic reactant and neutral reaction partner Rg to happen, the centrifugal barrier has to be overcome which is only possible up to some maximal impact parameter $b_{max.}$

The latter is easily derived for the effective potential maximizing and the centrifugal repulsion being expressed with some geometric advisement as fraction of the collision energy E_{coll} (equation 5.13 and 5.14).

$$E_{coll} = \frac{-\alpha Q^2}{2(4\pi\varepsilon_0)^2 r_m^4} + E_{coll} \cdot \frac{b_{max}^2}{r_m^2} = max. \tag{5.13}$$

$$\left. \frac{\partial V_{eff}(r)}{\partial r} \right|_{r=r_m} = 0$$

$$\Rightarrow b_{max} = \left(\frac{2\alpha Q^2}{(4\pi\varepsilon_0)^2 \cdot E_{coll}} \right)^{1/4} \tag{5.14}$$

Comparing the expression for the centrifugal term in equation (5.12) and equation (5.13) allows to denote b_{max} in dependence of the maximum angular momentum L_{max} [5]

$$b_{max} = L_{max} (2\mu E_{coll})^{-1/2} \tag{5.15}$$

This relationship accomplished by Langevin, is applied in his theory to define the collision cross section σ_L for ion-molecule reactions to

$$\sigma_L = \pi \cdot b_{max}^2 = \frac{2\pi Q}{(4\pi\varepsilon_0) v_{coll}} \left(\frac{\alpha}{\mu} \right)^{1/2} \tag{5.16}$$

It can be noted that the Langevin cross section increases with decreasing v_{coll} and that it comprises the hard sphere approximation for b_{max} set to the sum of the radii of the colliding molecules.

The Langevin rate constant for an underlying Maxwell-Boltzmann distribution of collision energies is consequently derived as

$$k_L = \int_0^\infty v \, \sigma_L \, f(v) \, dv = \frac{2\pi Q}{(4\pi\varepsilon_0) v} \left(\frac{\alpha}{\mu} \right)^{1/2} \tag{5.17}$$

so that large cross section collisions at low velocity react slower because the particles move slower, whereas small cross-section collisions at high velocity react faster. The consequence is that the rate constant does not depend on the average velocity of the collision partners, in contrast to the clear dependence of the Langevin-cross section from the collision energy.

5.3   Conversion of raw data with CRUNCH

The subsequent paragraph will demonstrate how collision cross sections can be derived in a typical CID-threshold measurement (see Chapter 3.1) from the directly accessible experimental parameters.

Further data extraction with the CRUNCH-Program including its empirical approach to model experimental cross sections will be detailed subsequently

5.3.1   General Attempts

In a conventional CID-threshold experiment the intensities of the reactant ion (= parent) and the intensities of the produced fragments (= daughters) are recorded against a continuous sweep through the range of ion kinetic energies from the onset of the threshold curve, where first dissociation takes place until complete saturation at the plateau, when basically every reactant ion undergoes dissociation. (See Chapter 3.1).

The variation of the average kinetic energy of the reactant ion is achieved by a time dependent alternation of the parent acceleration with the "DAC scan method" as outlined in Chapter 4.1.3

To measure the thermodynamic quantities it is crucial to know the exact kinetic energy distribution of the parent molecules at a given energy prior to collision as well as the absolute zero of the energy scale for reaction.[8]

Both is achieved by performing retardation measurements, where the reactant ion intensity is recorded as a function of the *dc*-bias potential applied to the entire octapole as this is swept through the zero of energy. The ion beam energy distribution is then obtained by taking the derivative of this retarding energy analysis curve and fitting it to a Gaussian curve. The apparent full width at half-maximum (FWHM$_{exp}$) equals the kinetic energy distribution of the reactant ions, being typically in the range of 1.7–1.9 eV for the bisoxazoline copper complexes studied in this thesis.[9,10] (See Figure 5.1).
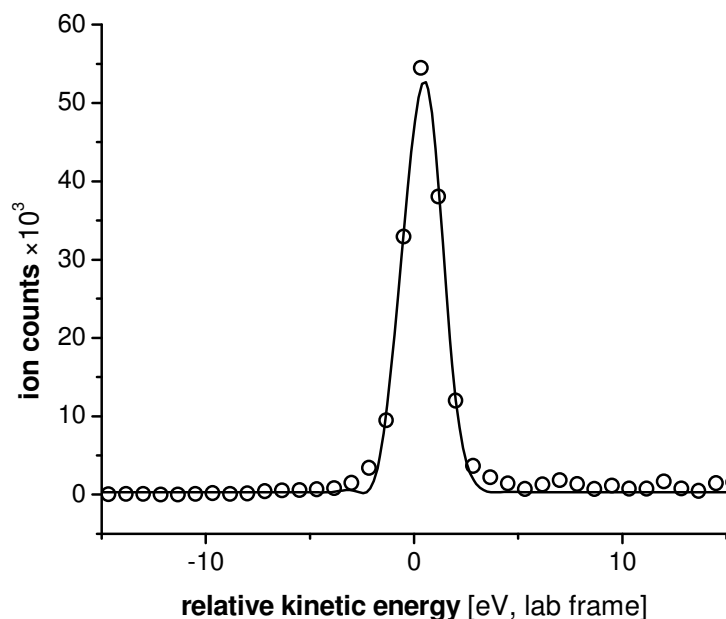
Figure 5.1 Kinetic energy distribution in the laboratory frame of the electrosprayed L_2Cu^+ ions after thermalization in the (RF-)24-pole ion guide. (See Chapter 4).

The maximum of the Gaussian-fit determines the absolute zero of energy. Both parameters have to be determined for each CID-threshold measurement again in order to correct the data for otherwise unpredictable interferences from non-ideal field effects, space charge effects, contact potentials or surface charging.

The next point in the data-work-up process is concerned with the fact that not all the translational energy of the two colliding particles, E_{lab}, is also available for reaction.[11]

The relative translational motion of the two reactants and the motion of the entire collision system through the laboratory have to be differed, with only the first one, the energy in center of mass frame (E_{CM}) being available for chemical change during the reaction.

Under the assumption of stationary target molecules, E_{CM} can be calculated as a fraction of E_{lab}, in which M represents the mass of the parent ion and m the mass of the target molecule.

$$E_{CM} = E_{lab} \cdot \frac{m}{(m+M)} \qquad (5.18)$$

The reaction cross section σ, as the probability that two particles collide and proceed to products, is readily obtained[11] from the reactant and product ion intensities over a relationship analogue to the Lambert-Beer Law,

$$I = I_0 \exp(-\rho \sigma l) \qquad (5.19)$$

where I is the reactant ion intensity after passing through the collision cell, I_0 is the reactant ion intensity before entering the collision cell, l is the effective path length of the collision cell (accounting for the distribution in pressures across the length of the collision cell) and ρ is the density of the neutral reactant, which equals $P/k_B T$ with P and T the pressure and temperature of the target gas.

If no ions are lost during the collision and detection, then $I_0 - I = \Sigma I_p$, is the sum of intensities of all product ions. In the thin target limit, which can be applied due to the small values of ρ in a CID threshold experiment, the exponential term in equation (5.19) reduces to $(1 - \rho \sigma l)$, which allows to rewrite the sum of products as $\Sigma I_p = I_0 \rho \sigma l$, so that the total reaction cross section equals[11]

$$\sigma = \Sigma I_p / (I_0 \rho l) \qquad (5.20)$$

and the reaction cross section for individual product ions is given by

$$\sigma_p = \sigma (I_p / \Sigma I_p) \qquad (5.21)$$

Cross section curves have to be acquired for several low pressures of the target gas, e.g. 30, 50, 70, 90 and 110 µtorr and extrapolated to zero pressure to yield rigorously single collision conditions. (See Figure 5.2 and Figure 5.3).

Otherwise the finally achieved threshold energy would be too low, since multiple collisions can deposit more energy than a single collision at the same laboratory ion energy.
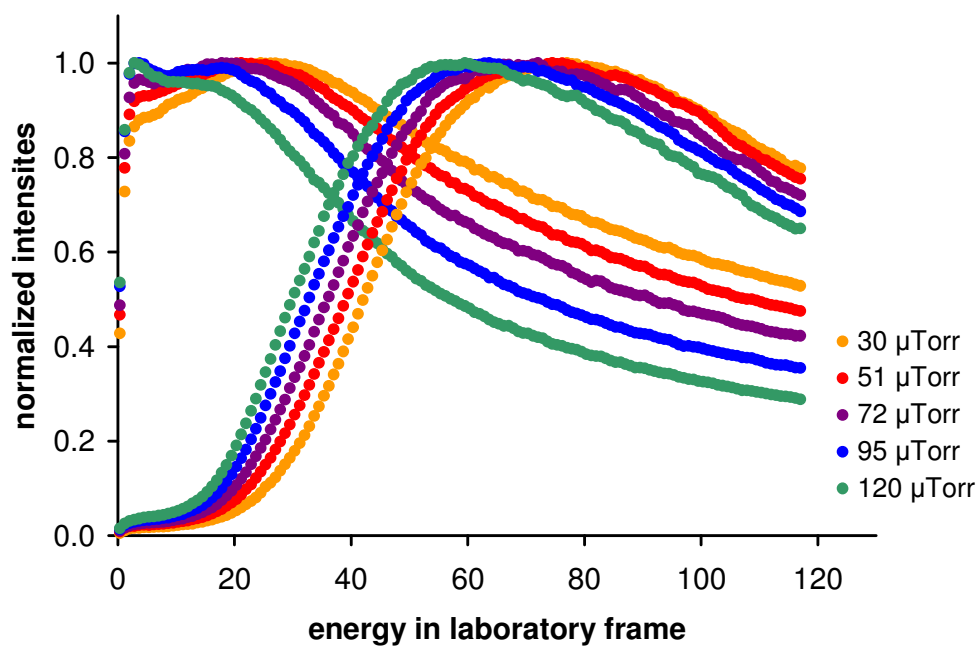
Figure 5.2 Pressure dependence of the parent (declining) and daughter (augmenting) intensities at scanned energies in the laboratory frame.
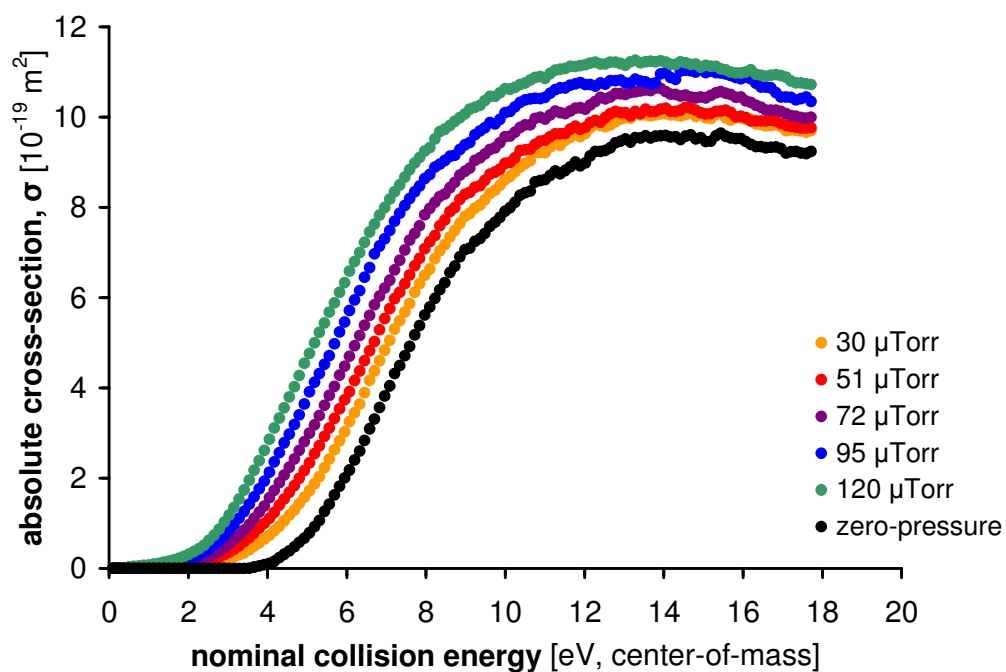
Figure 5.3 Extrapolation to zero pressure of the product cross sections at different Xenon pressures

5.3.2   The empirical Cross Section Formula

The basic CRUNCH equation

The experimental cross section curve (after extrapolation to zero pressure, see Chapter 5.3.1) is fitted in Armentrout's CRUNCH program, version D1[12] to the following empirical expression[13]

$$\sigma(E_{coll}) = \sigma_0 \sum_i g_i (E_{coll} + E_i - E_0)^n / E^m \tag{5.22}$$

where E_0 is the reaction threshold at 0 K, σ_0 is an energy independent scaling factor and E_{coll} is the collision energy in center of mass frame. E_{coll} consists of the experimentally determined kinetic energy distribution in center of mass frame inherent in the incident ion beam convoluted with the distribution in center of mass energy inherent in the thermal motion of the target gas (*e.g.* Xenon), which causes the so called Doppler broadening of the initial parent ion distribution.

The summation in equation (5.22) is over i rovibrational states (all accessible degrees of freedom of the energized molecule) with energies E_i and populations g_i; the latter being assumed to follow a Maxwell-Boltzmann distribution at the temperature of the experiment. Thus E_i describes all sources of reactant internal energy which are under adiabatic conditions solely vibrational and rotational contributions. Adiabaticity also assigns the variable m to one.

The exponent n in equation (5.22) would equal unity in the limit of hard sphere collisions (see Chapter 5.1) but serves as additional fitting parameter to correct empirically for the otherwise neglected conservation of angular momentum. This has a large impact on the shape of the empirical threshold function which rises with the hard sphere approximation much too steeply to model real ion molecule collision cross sections. In other words, CRUNCH is originally based on a line-of-centers collision model, whose cross section function has to be adjusted with the n-parameter to produce a sigmoidal function with variable steepness in order to account also for the frequent collisions with larger impact parameters b in the range $(r_A + r_B) \leq b \leq b_{max}$. (See Chapter 5.2).

The kinetic shift

Another feature that has to be incorporated especially for large reactant ions with a significant number of degrees of freedom, is the so called "kinetic shift" treatment.

A first attempt in this direction to describe an experimental threshold function was achieved by Cotter,[14] using a parameterized exponential expression $\sigma(E) = Q_0 \{1 - \exp[-A(E - E_0)]\}$ with Q_0, A and E_0 (threshold energy) as fitting parameters. A statistical explanation was provided by Rosenstock,[15] who claimed that after collisional activation the reactant ion will not dissociate within the time of one vibration, but rapidly and statistically redistributes its energy among all degrees of freedom. Unimolecular dissociation will only take place with sufficient vibrational energy concentrated in the suitable mode representing the reaction coordinate.

From thereon, it was then self-evident for Chupka[16] to realize that only for small molecules dissociation is sufficiently rapid so that the initial association/collision complex (AB^+-Rg) between reactant ion and target gas Rg is never observed and CID of $(AB^+)^*$ occurs faster than the flight time of the ions in the collision cell, once the internal energy of the activated complex exceeds the bond energy.

However, as the molecules get larger and have an increased number of degrees of freedom in the complex where energy can be stored without leading to reaction, the lifetime of the complexes increases and may exceed the experimental time scale. Solely increasing the energy in such long-lived complexes enhances the dissociation rate and leads to an observable product formation at kinetic energies shifted to higher values than for similar strongly bound but smaller metal-ligand complexes.

Consequently, accurate thermochemical data can only be obtained when the kinetics of the dissociation get included.

This is realized in CRUNCH by incorporating an integration over an unimolecular dissociation probability in form of an exponential decaying function

$$\sigma(E_{\text{coll}}) = \frac{n\sigma_0}{E_{\text{coll}}} \sum_i g_i \int_0^{E_{\text{coll}} + E_i - E_0} [1 - e^{-k(E_{\text{coll}} + E_i - \Delta E)\cdot\tau}] (\Delta E)^{n-1} d(\Delta E) \qquad (5.23)$$

τ is hereby the average experimental time available for dissociation (the ion time-of-flight through the collision cell to the quadrupole mass analyzer which is for the present TSQ-700 approximately 60 μs); $k(E_{\text{coll}} + E_i - \Delta E)$ is the unimolecular dissociation rate constant calculated using statistical RRKM theory (see Chapter 3.2)

and ΔE represents the energy that remains in translation after collision, thus the kinetic energy of the leaving target molecule.

For small ions with dissociation rates faster than the time of flight of the ions the primary equation (5.22) is recovered.

However, it has to be pointed out explicitly that the accuracy of the calculated kinetic shift highly depends on the experimental validity of all the assumptions performed within the microcanonical transition state theory. (Chapter 3.2)

Competitive reaction channels

In general, multiple channel reactions are characterized by having the same energized molecule that can decompose over different pathways and therefore, form different products. It is quite common that the various reaction channels influence or even suppress each other, which requires simultaneous analysis of such cross sections.

An example for two competing channels is depicted in Figure 5.4 for the dissociation of the collisionally excited $(H_2O)Li^+(CH_3OH)$.[17,18]
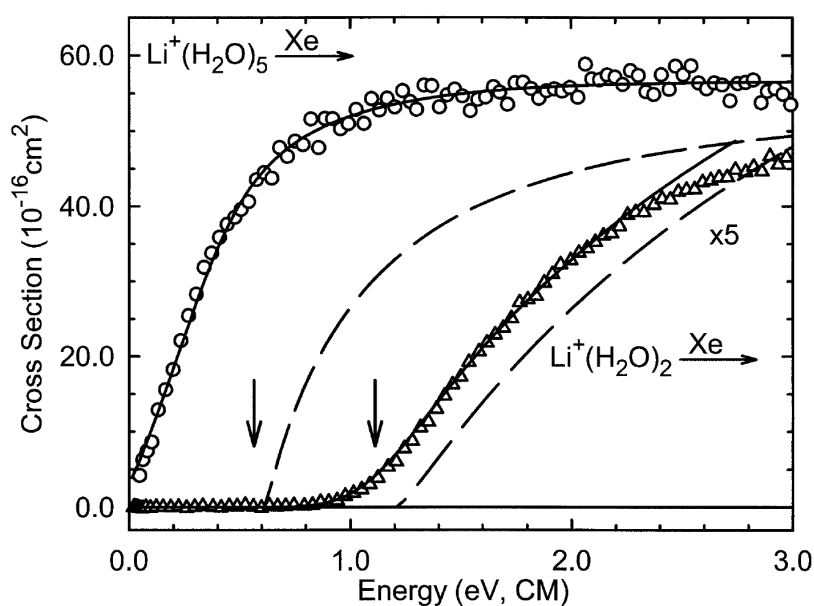
Figure 5.4 Experimental cross sections for the collision-induced dissociation of $(H_2O)Li^+(CH_3 OH) + Xe$

The lower energy channel, $Li^+(CH_3OH) + H_2O$, has statistically a much higher number of states available than the higher energy channel with Methanol dissociating.

Therefore, the second channel rises way more slowly from its threshold, but simultaneously causes the first product channel to level out. At even higher collision energies, the statistical difference in the two channels diminishes and the maximum cross sections approach each other.

To quantify the effect that such competition can have on the threshold determinations of statistically behaved processes, the CRUNCH equation (5.23) was extended with the ratio of the dissociation rates k_j/k_{tot}. (See equation 5.24). This branching ratio describes the coupling between the product channels j with $k_{tot} = \Sigma k_j$, the sum of all single rate constants based on RRKM theory.[17,18]

$$\sigma_j(E_{coll}) = \frac{n\sigma_{0,j}}{E_{coll}} \sum_i g_i \int_0^{E_{coll}+E_i-E_0} \frac{k_j(E^*)}{k_{tot}(E^*)} [1-e^{-k_{tot}(E^*)\cdot\tau}] (\Delta E)^{n-1} d(\Delta E) \qquad (5.24)$$

$\sigma_{0,j}$ are separate scaling factors, but are ideally the same for each product channel and $E^* = E_{coll} + E_i - \Delta E$.

5.4 Improved Fitting of reactive Cross-Sections with L-CID

An operationally much simpler method than Armentrout's CRUNCH program for the extraction of thermochemical data from collision-induced dissociation cross sections, is the so called L-CID program[19] developed in our own working-group.

One of its three advantages is a physical correct treatment of the electrostatic potential for the approach of ion and collision partner with a proper treatment of the centrifugal barrier due to conservation of the angular momentum. (See Chapter 5.2 and 5.3.2).

The effect is especially severe for collisions with high impact parameters, b, because an increasing fraction of the collision energy E_{coll} is needed to surmount the

centrifugal barrier and can not be transferred to internal energy of the association/collision complex (AB$^+$–Rg).

This energy partitioning is completely neglected in CRUNCH. As a consequence, CRUNCH is (incontrast to L-CID) able to model only the onset of the threshold curve (Figure 5.5 in comparison to Figure 5.6), where the angular momentum $L = \mu \cdot \vec{r} \times \vec{v}_{center}$ is still small due to the overall small collision energy.
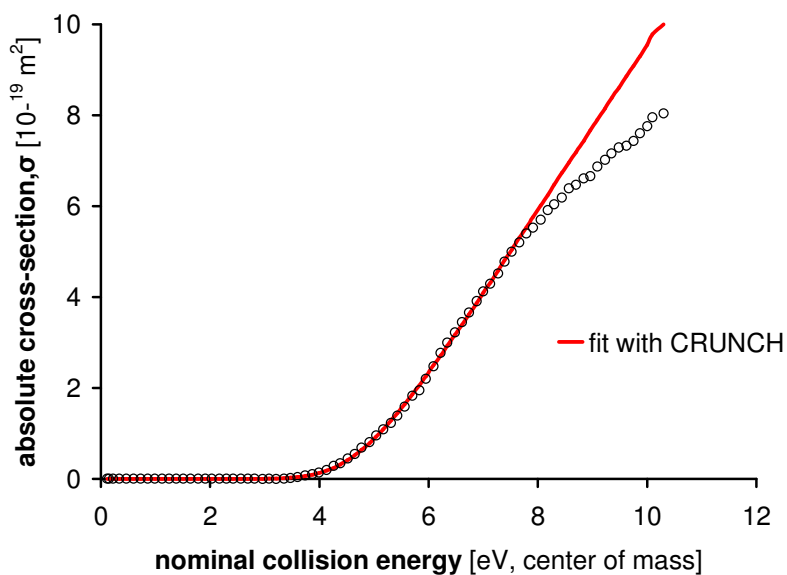
Figure 5.5   Reactive cross section fitted with CRUNCH-D1.[10]
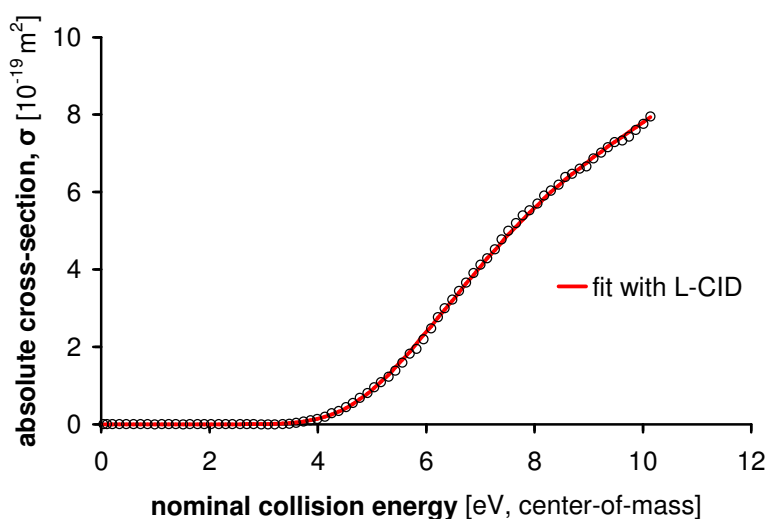
Figure 5.6   Fit of a CID-threshold with L-CID over the entire energy range.[10]

Ignoring the centrifugal repulsion $L^2/2\mu r^2$ is ergo an acceptable simplification at lower threshold energies but not any longer justifiable in the high energy region of the cross-section curvature.

Moreover, the remaining part of E_{coll}, that solely leads to collisional activation of (AB^+), is the energy in line of the mass centers of the two approaching particles:

$$E_{loc} = E_{coll}\left(1 - \frac{b^2}{b_{max}^2}\right) \tag{5.25}$$

b_{max} is derived in Chapter 5.2 as maximal impact parameter (with inverse proportionality on the collision energy) for which collision occurs, so that $0 < b \leq b_{max}$. The probability for each collision of an ensemble of ions, all having the same E_{coll} and therefore, the same b_{max} is given by the function.[4]

$$P_{coll}(b) = \frac{b}{b_{max}} \tag{5.26}$$

Equation (5.26) implies that the larger the relative translational energy of the ions, the less probable is a collision that can surmount the centrifugal barrier, which explains once more the "fall-off" region in the high energy part of the experimental cross-section curve (Figure 5.3).

Besides the proper description of the energy transfer in an inelastic ion molecule reaction, also the cross-section function of L-CID is based on the Langevin theory. (See Chapter 5.2).

A collision with an impact parameter in the range $b + db$ has to cross the target through a ring of radius b and width db, such that the collision cross section equals the area of the ring $d\sigma_{coll} = \int 2\pi b\, db$, whereas for all possible values of b the total collision cross section

$$\sigma_{coll} = \int 2\pi b\, db \tag{5.27}$$

is obtained. (See Scheme 5.4).
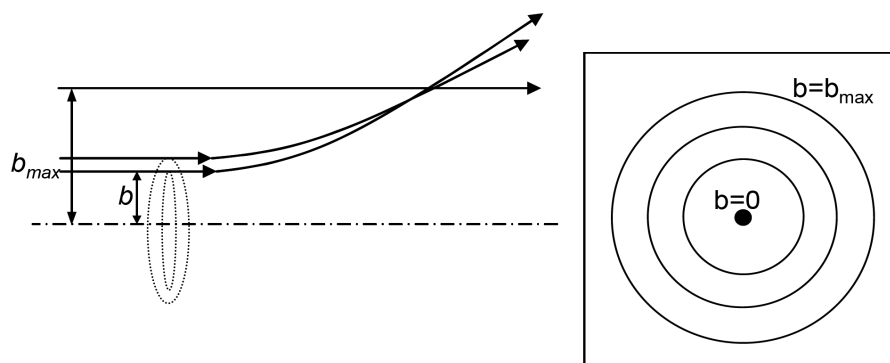
Scheme 5.4 Two dimensional view of the cross section. The probability for a collision with the impact parameter b increases with augmenting b, so that for a given initial translational energy the most probable collision has an impact parameter of of b_{max}.[4]

Since an ensemble of ions with a finite number of particles is characterized with this physical model, the integral has to be replaced by a sum. Considering further, that the collision cross-section does not only measure the geometrical aspect of the "effective size" of the molecules, but rather their propensity to react at a given collision energy, the reaction probability $P_{coll}(b)$ has to be included.

$$\sigma_{coll} = \sum_{b=0}^{b=b_{max}} \pi b^2 P_{coll}(b) \tag{5.28}$$

Analogues incorporation of the "kinetic shift" treatment, a branching ratio for multiple channel reactions and an additional scaling factor for each channel, as already known from the expanded CRUNCH equation (5.24), leads to the absolute reaction cross section of L-CID in it's final form (equation 5.29).

$$\sigma_{abs,j} = \sigma_{0,j}^{exp} \sum_{b=0}^{b=b_{max}} \pi b^2 P_{coll}(b) \frac{k_j(E^*)}{k_{tot}(E^*)} [1 - e^{-k_{tot}(E^*-E_0)\cdot\tau}] \tag{5.29}$$

$\sigma_{0,j}$ represent the magnitude of the absolute cross-section of each channel in order to correct the original two-dimensional collision-picture (Scheme 5.4) for the molecular three-dimensionality. Thus $\sigma_{0,j}$ are not arbitrary as in the case of the anyways empirical cross-section function of CRUNCH.

Further, the total unimolecular rate constant, defined by RRKM theory, is given by the sum of the rate constants for individual channels j

$$k_{\text{tot}}(E^*) = \sum_j k_j(E^*) \tag{5.30}$$

and E^*, the total energy available for dissociation, equals $E^* = E_{\text{loc}} + E_i - \Delta E$ with ΔE being the factor of energy going into the relative translation of the rare gas atom and the energized ion. τ symbolizes the experimental time window for the dissociation to take place and E_i represents the internal energy of the reactant ion.

It has to be noted that equation (5.29) involves too many variables in order to be derived analytically, why the total cross section has to be calculated numerically by applying the Monte Carlo Simulation (see further below).

The second advantage of L-CID compared to CRUNCH relates to the treatment of the density of states function $\rho(E)$. The density of states appear multiple times in the deconvolution process, starting already with the computation of the internal energy distribution of the incident ion

$$P(E_i) = \frac{\rho(E_i)}{Q(T)} \ \exp\left(\frac{-E_i}{RT}\right) \tag{5.31}$$

with E_i being the vibrational energy, T the temperature of thermalization in the 24-pole region and $Q(T)$ the partition function at the given temperature.

Also , the estimation of the kinetic shift requires knowledge of the density of states of the energized molecule, as well as the sum of states at the transition state $W^{\ddagger}(E^*-E_0)$ with an energy less or equal to (E^*-E_0), in order to assign the microcanonical RRKM rate for reaction. [20] (See equation 3.1).

Finally, the correct collisional energy transfer with the partitioning between internal energy of the ion and relative translation of the ion and the departing collision partner energy in the inelastic collision (KERD)[21] has to be listed in the row of components all depending on the density of states $\rho(E)$.

CRUNCH uses the Beyer-Swinehart direct state count[22] or the Whitten-Rabinovitch approximation for $\rho(E)$, [20] both well established, but with the disadvantage that explicit frequencies for the ion and the transition state are required.

Those electronic structure calculations, usually performed on DFT level, happen to be a quite non-trivial undertaking when applied to coordinatively unsaturated, often open shell complexes, which are commonly encountered as reactive intermediates in homogeneous catalysis.

However, it can be assumed that, when the molecule is large enough, sufficient averaging occurs, so that the precise correlation of one frequency to one particular mode does not affect the overall result for the density of states.[20] Much more important is the number of degrees of freedom, as well as some minimized structure based input like the number of rotors in the molecule. The density of states $\rho(E)$ can then be derived from a single effective frequency, υ, serving as one out of three fitting parameters in L-CID.

Given, that the canonical transition state theory which is embedded in the RRKM assumptions, is fundamentally a two parameter model with $\Delta H^{\ddagger}$ and $\Delta S^{\ddagger}$ and given, that the RRKM rate constant $k(E)$ depends on the density and sum of states, it is a justifiable prediction that the microcanonical RRKM rate, as an energy dependent rate, should rely on two parameters:[23] the already outlined single effective frequency, related to the activation entropy and the threshold energy E_0, related to the enthalpy of activation.[19]

Yet a third variable, α, is needed in L-CID in order to describe the "looseness" or "tightness" of the transition state.[19]

In comparison, in CRUNCH the density of states of loose, orbiting transition states located at the centrifugal barrier, is calculated with the vibrational modes of the products. The transitional modes of the loose TS are assigned as rotors with rotational constants equivalent to those of the products.

For tight transition states either the frequencies of an *ab initio* optimized transition state geometry are used or, otherwise, the frequencies from the parent molecule are taken and the mode that resembles most the reaction coordinate is removed.

In L-CID the transition state treatment is more simple: in either case of a loose or a tight TS the same effective frequency υ is used under the assumption that most of the frequencies in a large enough molecular species would not change much, going from the starting ion to the transition state.

This is completely true in case of a tight TS because the density-of-states function for the energized molecule and that for the transition state are almost identical.

Only for a loose TS the five transition modes increase the density of states significantly and have to be treated separately. This is realized by introducing the additional structure related parameter α which is for tight transition states in the range of 0 to 500cm^{-1} and for loose transition states it is between 5000 and 6500cm^{-1}.

The only restriction in terms of the great operationally simplification of L-CID is the fact that the nature of the TS can not be extracted from the experimental cross section curve, but needs to be chosen upon auxiliary informations *i.e.* quantum chemical calculations or structural and reactivity considerations from other sources.

The third and last area in which L-CID and CRUNCH differ, is the fitting procedure:[19] Because the variables v and E_0 influence multiple steps of the L-CID routine consecutively, the fitting must be done to self-consistency. The conventional Marquardt-Levenburg non-linear least-squares routine of CRUNCH with partial derivatives of the error function with respect to the fitting parameters would not fulfill this task.

Therefore, L-CID uses the Monte Carlo method with 50.000 ions in the simulation to create an ensemble of simulated collision events in order to reproduce the experimental cross section curve for each of the nominal collision energies.

The genetic algorithm[24] optimizes then the two parameters v and E_0 by a biologically inspired, diversity based process, so that the two parameters have their own distributions from which statistically valid uncertainty bounds can be derived. In contrast to that, fitting with CRUNCH implies a subjective choice of the best fit.

(For a description of the uncertainties of the CID-threshold method and data processing in either CRUNCH or L-CID see the Experimental Section).

In general, both L-CID and CRUNCH open the possibility to examine the kinetic energy dependence of ion molecule reactions and give rise to thermodynamic data like bond energies and enthalpies of formation. They differ however, significantly in the amount of molecular parameters that are needed as auxiliary input to get an

unambiguous E_0. The minimized structural input for L-CID is therefore, a highly appreciable improvement in terms of operational practicability.

5.5   References

[1]   Futrell, J. H.; *Gaseous Ion Chemistry and Mass Spectrometry;* John Wiley & Sons, New York, **1986**, Chapter 2.4

[2]   Atkins, P.W.; *Physikalische Chemie,* Wiley-VCH Verlagsgesellschaft mbH, Weinheim, **1996**, Chapter 27

[3]   Gross, M. L.; Caprioli, R.; *The Encyclopedia of Mass Spectrometry, Theory and Ion Chemistry*, Vol. 1; Armentrout, P.B., Ed.; Elsevier, Oxford, **2003**, Chapter 1

[4]   Gioumousis, G.; Stevenson, D. P.; *J. Chem. Phys.* **1957**, 29, 294 - 299

[5]   Langevin, P.; *Ann. Chim. Phys. Ser. 8* **1905**, *5*, 245–288

[6]   Narancic, S.; *Mechanistic Studies of Organometallic Complexes*, PhD Thesis, ETH Zürich, **2007**, Diss. No. 17337

[7]   Futrell, J. H.; *Gaseous Ion Chemistry and Mass Spectrometry;* John Wiley & Sons, New York, **1986**, Chapter 3.2

[8]   Armentrout, P. B.; *J. Am. Soc. Mass Spectrom* **2002**, *13*, 419–434

[9]   Zocher, E.; Dietiker, R.; *J. Am. Chem. Soc.* **2007**, 129, 2476–81

[10]   Zocher, E.; Sigrist, R.; *Inorganic Chemistry* **2007**, *46*, 11366–11370

[11]   Ervin, K. M.; Armentrout, P. B.; *J. Chem. Phys.* **1985**, *83* (1), 166–189

[12]   CRUNCH, version D1, was kindly provided as an executable by Prof. P.B. Armentrout

[13] Rodgers, M. T.; Ervin, K. M.; Armentrout, P.B.; *J. Chem. Phys.* **1997**, *106*, 4499–4508

[14] Cotter, R. J.; Rozett, R. W.; Koski, W. S.; *J. Chem. Phys.* **1972**, *57*, 4100

[15] Rosenstock, H.M.; Wallenstein, M. B.; Wahrhaftig, A. L.; Eyring, H; *Proc. Nat. Acad. Sci. USA* **1952**, *38*, 667

[16] Chupka, W.A.; *J. Chem. Phys.* **1959**, *30*, 191

[17] Rodgers, M. T.; Armentrout, P. B.; *J. Chem. Phys.* **1998**, *109*, 1787–1800

[18] Mc Cleverty, J. A.; Meyer, T. J.; *Comprehensive Coordination Chemistry II, From Biology to Nanotechnology,* Elsevier Pergamon, Oxford, **2004**, Chapter 2.12

[19] Narancic, S.; Bach; A.; Chen, P.; *J. Phys. Chem. A* **2007**, *111*, 7006–7013

[20] Holbrook, K. A.; Pilling, M. J.; Robertson, S. H.; *Unimolecular Reactions, 2ⁿᵈ Ed.,* Wiley, New York, **1996**

[21] Lorquet, J. C. ; *Int. J. Mass. Spec.* **2000**, *201*, 59

[22] Beyer, T.; Swinehart, D. F; *Communications of the ACM* **1973**, *16*, 379

[23] Le Page, V.; Snow, T.P.; Bierbaum, V. M ; *Astrophys. J.* **2001**, *132*, 233

[24] Goldberg, D. E.; *Genetic Algorithms in Search, Optimization and Machine Learning*, Addison-Wesley: Reading, MA, **1989**; pp 77, 106 - 122

Chapter 6

Experimental and Computational Results

6.1   Design of the Project

Stereoselectivity in asymmetric catalysis and in particular Kagan's nonlinear effects[1] are attributed to small differences in stability of the participating diastereomeric metal-ligand complexes.

Surprisingly few absolute ligand binding energies are reported in the literature compared with the fact that most mechanistic models in enantioselective catalysis are based thereon. For example, nonlinear effects have been shown for a wide range of catalytic reactions including the Sharpless epoxidation[2] and diethyl zinc additions[3] or, when combined with autocatalysis, for Soai's spontaneous enantioselective automultiplication of chiral molecules.[4] (For further details on nonlinear effects see Chapter 2.2 and 7.1).

As derived by Kagan, a nonlinear effect arises when one or more species in the system contain more than one unit of the chiral ligand, opening up the possibility of homochiral and heterochiral complexes. Depending on the system there are several other conditions for a positive nonlinear effect, but one common feature is that the heterochiral complex must be more stable than its homochiral analogue. In favorable instances NMR spectroscopy experiments allow to directly observe the equilibrium between homochiral and heterochiral complexes and to establish a $\Delta\Delta G$, but such favorable conditions are not always available and the measurement gives only relative, as opposed to absolute thermochemical information. More usually, the relative stability of the diastereomeric complexes is inferred from molecular modeling, or simply guessed post facto. Given the multiple subtle factors that can

move $\Delta\Delta G$ by a few kcal/mol for or against the heterochiral complex, a priori predictions cannot be made with any claim of reliability.

In principle there is an impressive amount of catalytic systems, for which no discrete intermediates and detailed mechanisms are known.

So the experimental design required two choices: firstly the choice of the chemical system and secondly the choice of the experimental technique.

In this study, bisoxazoline ligands, a group of "privileged structures" popularized by Evans,[5] are selected. Those ligands are synthetically readily available[5,6] and appear repeatedly in asymmetric catalysis (see Chapter 1.1). The economic copper has been chosen as central metal whose catalytic chemistry spans a broad range of reactions in which the catalyst is usually generated *in situ* from metal salts and free ligands.

In solution bisoxazoline ligands form with an added copper source like CuOTf or $Cu(CH_3CN)_4PF_6$ predominantly the 2:1 ligand copper complex.[7] This species comprises an inactive reservoir from which the much less abundant active species is generated and to which it can return. Although there is little experimental evidence, copper bisoxazoline complexes with 1:1 stochiometry[8] are presumed to be the catalytically active species (if the complex is mononuclear) since they are coordinatively non-saturated.

In the event that the bis-oxazoline ligand is enantimerically impure, and if the heterochiral 2:1 complex were to be more stable than the homochiral one, then this mechanistic picture would validate the occurrence of a positive nonlinear effect.

The perfectly suited technique for the determination of absolute ligand binding energies to a metal ion are energy resolved collision induced dissociation cross-section measurements.[9]

This gas-phase and mass spectrometric technique has so far been applied by Armentrout and others[10] to small-to-medium-sized ions. However, the underlying theory (Chapter 3.2) does not imply any restrictions for the actual size of the reactant ions and thus it is only a question of addressing interesting, real-life catalytic problems with it.

6.2   CRUNCH Binding Energies for 2:1 Bisoxazoline Copper Complexes

The particular box and aza-box ligands presented in this study,[7] with isopropyl or phenyl substituents are the most commonly used ligands in their family (Figure 6.1).

(S,S)-**1**   (S,S)-**2**   (S,S)-**3**   (S,S)-**4**

(a) R = H
(b) R = Me
(c) R = Et
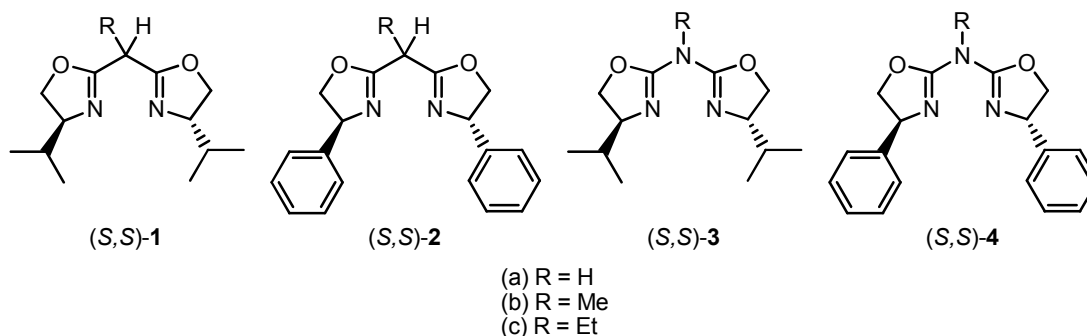
Figure 6.1   Selected (aza-)bisoxazoline ligands for detailed gas-phase measurements

Isopropyl and phenyl substituents show similar steric, but different electronic properties, which permits an interesting separation of these effects in the experiment.

Because mass spectrometry distinguishes ions according to the *m/z* ratio, *pseudo*-enantiomers of **1– 4** were employed for this study.

The technique of substituting a remote site with a distinguishing label on two otherwise enantiomeric structures has been extensively used in pharmacological/metabolic studies[11] and has been more recently resurrected by Reetz[12] and by Pfaltz[13] for the investigation of enantioselectivity in asymmetric catalysis using mass spectrometry. Of course, the assumption, that the kinetic and thermodynamic behavior of the *pseudo*-enantiomers were comparable to that of a pair of true enantiomers, has to be confirmed by experiment.

The CID threshold measurements in this thesis directly address the relative stability of the hetero- versus homochiral complexes because the loss of one ligand from either 2:1 bisoxazoline copper complex can produce the same 1:1 complex (or its enantiomer; see Scheme 6.1).
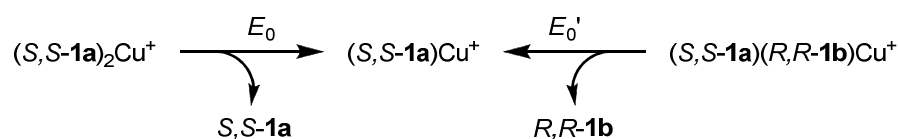
Scheme 6.1 CID   threshold   measurements   with   homo-   and   heterochiral   2:1 bisoxazoline copper(I) complexes.

Accordingly the difference between the dissociation threshold energies for the hetero- and homochiral complexes should exactly give the difference in stability which is named as one of the criteria for the occurrence of a nonlinear effect in catalysis.

Practically, the *in situ* generated copper ligand complexes were sprayed from dry CH_2Cl_2 having a final concentration of 13 μM per ligand. (A detailed description for the preparation of the ligand and copper stock solutions, the mixing and dilution procedure is given in the experimental section.)

The electrospray mass spectrum[7] clearly shows peaks corresponding to the 2:1 ligand-copper species, as well as 1:1 complexes and free ligand (visible as the protonated species). Given the absence of other ligands in the observed 1:1 complexes, they are probably daughter ions formed from the 2:1 complexes during the spray or desolvation process.
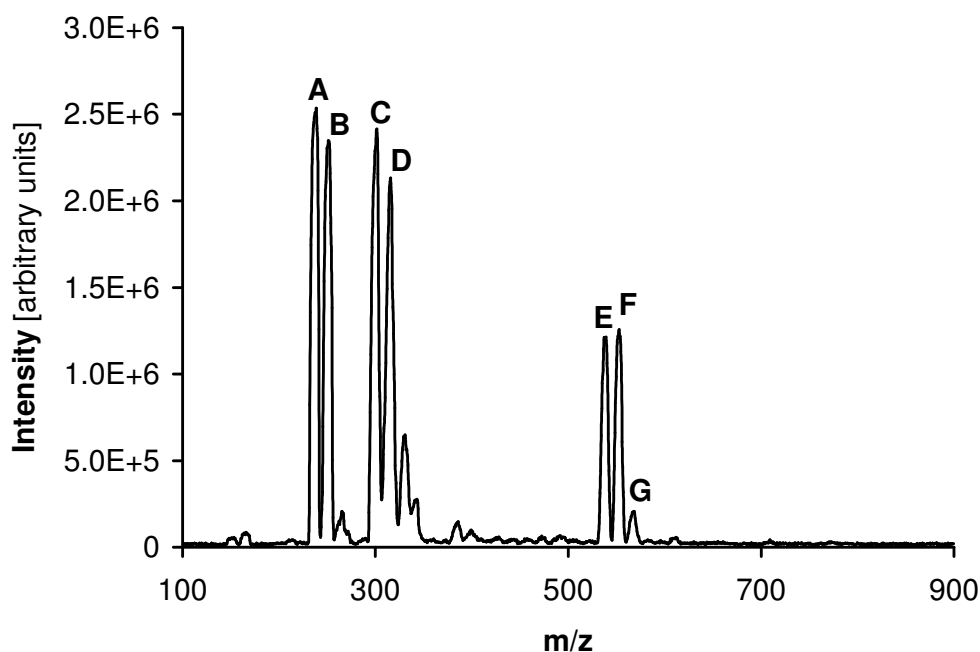
Figure 6.2 ESI-MS of the solution prepared from $Cu(CH_3CN)_4PF_6$, *S,S*-**1a** and *R,R*-**1b**. The $(S,S$-**1a**$)_2Cu^+$ homochiral complex (m/z = 539, **E**), the $(S,S$-**1a**$)(R,R$-**1b**$)Cu^+$ heterochiral complex (m/z = 553, **F**) and the $(R,R$-**1b**$)_2Cu^+$ homochiral complex (m/z = 567, **G**) as well as the corresponding 1:1 complexes (m/z = 301, **C** and m/z = 315, **D**) and the free ligands (m/z = 238, **A** and m/z = 252, **B**) appear in this mass spectrum. The $^{63}Cu/^{65}Cu$ splitting is not resolved.

For example, the solution of the heterochiral complex (*S*,*S*-**1a**)(*R*,*R*-**1b**)Cu⁺ shows, apart from the expected 2:1 heterochiral complex, also the corresponding homochiral complexes, (*S*,*S*-**1a**)$_2$Cu⁺ and (*R*,*R*-**1b**)$_2$Cu⁺ with the relative peak intensities depending on the concentrations and relative stabilities of the various species in the particular example. (See Figure 6.2).

The homochiral complexes, *e.g.* (*S*,*S*-**1a**)$_2$Cu⁺ and (*R*,*R*-**1b**)$_2$Cu⁺ again, could also be generated independently, which was done in the cases where the equilibrium heavily favored the heterochiral complexes in solution.

Collision induced dissociation (CID) of a mass-selected 2:1 complex proceeds with loss of one of the two bisoxazoline ligands, as can be seen in the representative spectrum shown in Figure 6.3. The reaction is ideal for modeling the energy-resolved CID cross section since no other fragmentation products are observed.

Importantly, complexes, such as (*S*,*S*-**1a**)(*R*,*R*-**1b**)Cu⁺, which can lose either a labeled or unlabeled ligand, show both channels with nearly identical product intensity, indicating that the labeling itself has no large effect on the ligand binding energy in the best cases.
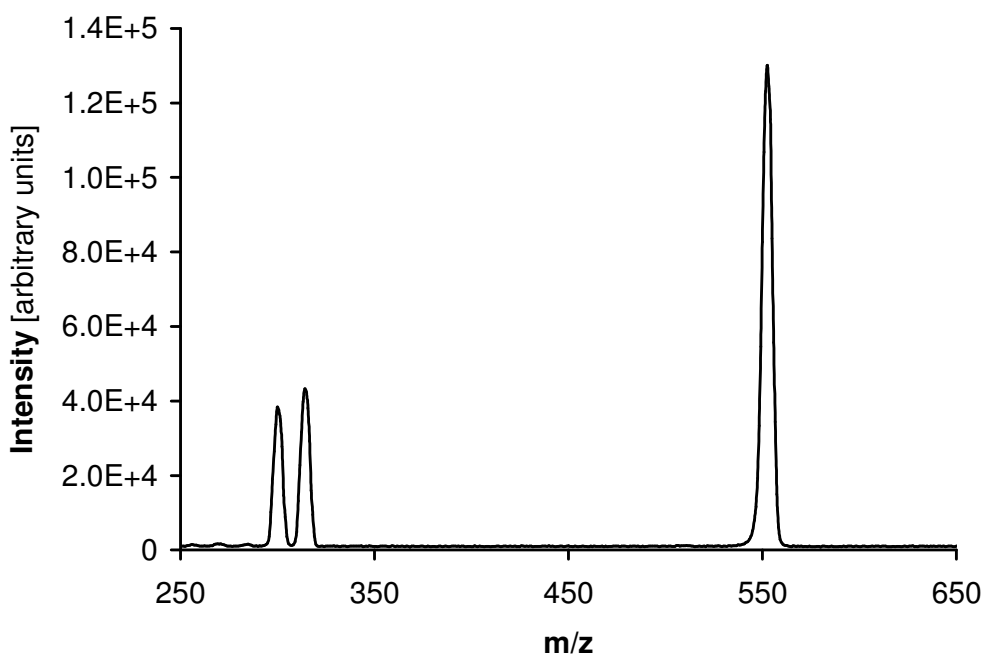
Figure 6.3 CID measurement of the (*S*,*S*-**1a**)(*R*,*R*-**1b**)Cu⁺ heterochiral complex after mass selection of the parent, showing loss of either *S*,*S*-**1a** or *R*,*R*-**1b** (553 → 315 and 553 → 301).

Retarding potential measurements for the reactant ions confirm that the modified TSQ-700 (see Chapter 4) displays a close-to-Gaussian distribution of ion kinetic energies with a full width at half-maximum (fwhm) of 1.9–2.4 eV in the laboratory frame. The ion kinetic energy distribution showed no perceptible high-energy tail that would be otherwise present when the ion guide is of too low an order.

The CID cross sections as a function of energy were measured for three to five different pressures of the xenon collision gas (between 30 and 110 µTorr) and extrapolated to zero pressure. Absolute cross sections, σ_p, were calculated[14] as described in Chapter 5.3.1 using a measured effective path length of 23 ± 5 cm. The uncertainty in the absolute cross section is estimated to be ±50%.

Extraction of thermochemical information from the datasets in this subsection was performed with the CRUNCH-D1 program,[15] which fits the dissociation cross section σ to the empirical formula, presented already in more detail in Chapter 5.3.2.

$$\sigma(E_{\text{coll}}) = \frac{n\,\sigma_0}{E_{\text{coll}}} \sum_i g_i \int_0^{E_{\text{coll}}+E_i-E_0} [1 - e^{-k(E_{\text{coll}}+E_i-\Delta E)\cdot\tau}]\,(\Delta E)^{n-1}\,d(\Delta E) \qquad (6.1)$$

E_{coll} is hereby the collision energy in center-of-mass frame, E_0 is the reaction threshold energy at 0 K, σ_0 is a scaling factor and n is an adjustable parameter. E_i are the energies of the rovibrational states with the populations g_i. The latter are assumed to follow a Maxwell-Boltzmann distribution at the temperature of the experiment. The parameter k is the RRKM dissociation rate for the ion with residence time τ in the collision cell. The parameters σ_0, n and E_0 are then optimized with a nonlinear least-squares analysis to give the best fit to the data.

The above presented cross section formula embedded in CRUNCH requires the explicit frequencies for the complexes and transition states as input parameters. They are used to compute the RRKM rate k as well as the density-of-states of the incident ion by applying the Beyer-Swinehart direct state count within the harmonic oszillator approximation. Thus quantum chemical calculations using Gaussian 03[16] had to be performed. The structures for the 2:1 complexes as well as the dissociation products were optimized with density functional theory (DFT) at the B3LYP/LANL2DZ level. The optimized structures were checked with frequency calculations to verify that they were in fact minima. The computed energies for the ligands and complexes in the experiment are listed in Table 6.1. Representative views of a pair of homo- versus heterochiral 2:1 complexes are shown in Figure 6.4.

Table 6.1 B3LYP/LANL2DZ Energies at DFT-Optimized Geometries for the Ions and Ligands

Calculated substance	CID-measured substance	Absolute energies (hartree)
$(R,R$-**1a**$)_2$Cu$^+$	$(S,S$-**1a**$)_2$Cu$^+$	−1732.953641
$(R,R$-**1a**$)(S,S$-**1b**$)$Cu$^+$	$(S,S$-**1a**$)(R,R$-**1b**$)$Cu$^+$	−1772.267293
$(R,R$-**1b**$)_2$Cu$^+$	$(R,R$-**1b**$)_2$Cu$^+$	−1811.564599
$(R,R$-**1b**$)$Cu$^+$	$(R,R$-**1b**$)$Cu$^+$	−1003.762153
$(R,R$-**1a**$)$Cu$^+$	$(S,S$-**1a**$)$Cu$^+$	−964.453522
S,S-**1b**	R,R-**1b**	−807.746190
S,S-**1a**	S,S-**1a**	−768.439351
$(R,R$-**2a**$)_2$Cu$^+$	$(R,R$-**2a**$)_2$Cu$^+$	−2185.327646
$(R,R$-**2a**$)(S,S$-**2b**$)$Cu$^+$	$(R,R$-**2a**$)(S,S$-**2b**$)$Cu$^+$	−2224.644683
$(R,R$-**2b**$)$Cu$^+$	$(S,S$-**2b**$)$Cu$^+$	−1229.943122
$(R,R$-**2a**$)$Cu$^+$	$(R,R$-**2a**$)$Cu$^+$	−1190.634321
S,S-**2b**	S,S-**2b**	−1033.925763
S,S-**2a**	R,R-**2a**	−994.618742
$(R,R$-**3b**$)_2$Cu$^+$	$(S,S$-**3b**$)_2$Cu$^+$	−1843.640926
$(S,S$-**3b**$)(R,R$-**3c**$)$Cu$^+$	$(S,S$-**3b**$)(R,R$-**3c**$)$Cu$^+$	−1882.959327
$(R,R$-**3c**$)$Cu$^+$	$(R,R$-**3c**$)$Cu$^+$	−1059.110978
$(R,R$-**3b**$)$Cu$^+$	$(S,S$-**3b**$)$Cu$^+$	−1019.799587
S,S-**3c**	R,R-**3c**	−863.085130
S,S-**3b**	S,S-**3b**	−823.775157
$(R,R$-**4a**$)_2$Cu$^+$	$(R,R$-**4a**$)_2$Cu$^+$	−2217.421835
$(R,R$-**4a**$)(S,S$-**4b**$)$Cu$^+$	$(R,R$-**4a**$)(S,S$-**4b**$)$Cu$^+$	−2256.727747
$(R,R$-**4b**$)_2$Cu$^+$	$(S,S$-**4b**$)_2$Cu$^+$	−2296.015923
$(R,R$-**4a**$)(R,R$-**4b**$)$Cu$^+$	$(S,S$-**4a**$)(S,S$-**4b**$)$Cu$^+$	−2256.718888
$(R,R$-**4b**$)$Cu$^+$	$(S,S$-**4b**$)$Cu$^+$	−1245.979895
$(R,R$-**4a**$)$Cu$^+$	$(R,R$-**4a**$)$Cu$^+$, $(S,S$-**4a**$)$Cu$^+$	−1206.681830
S,S-**4b**	S,S-**4b**	−1049.955004
S,S-**4a**	S,S-**4a**, R,R-**4a**	−1010.658793

$(R,R\text{-}\mathbf{1a})(S,S\text{-}\mathbf{1b})\text{Cu}^+$ $(R,R\text{-}\mathbf{1a})_2\text{Cu}^+$

$(R,R\text{-}\mathbf{2a})(S,S\text{-}\mathbf{2b})\text{Cu}^+$ $(R,R\text{-}\mathbf{2a})_2\text{Cu}^+$
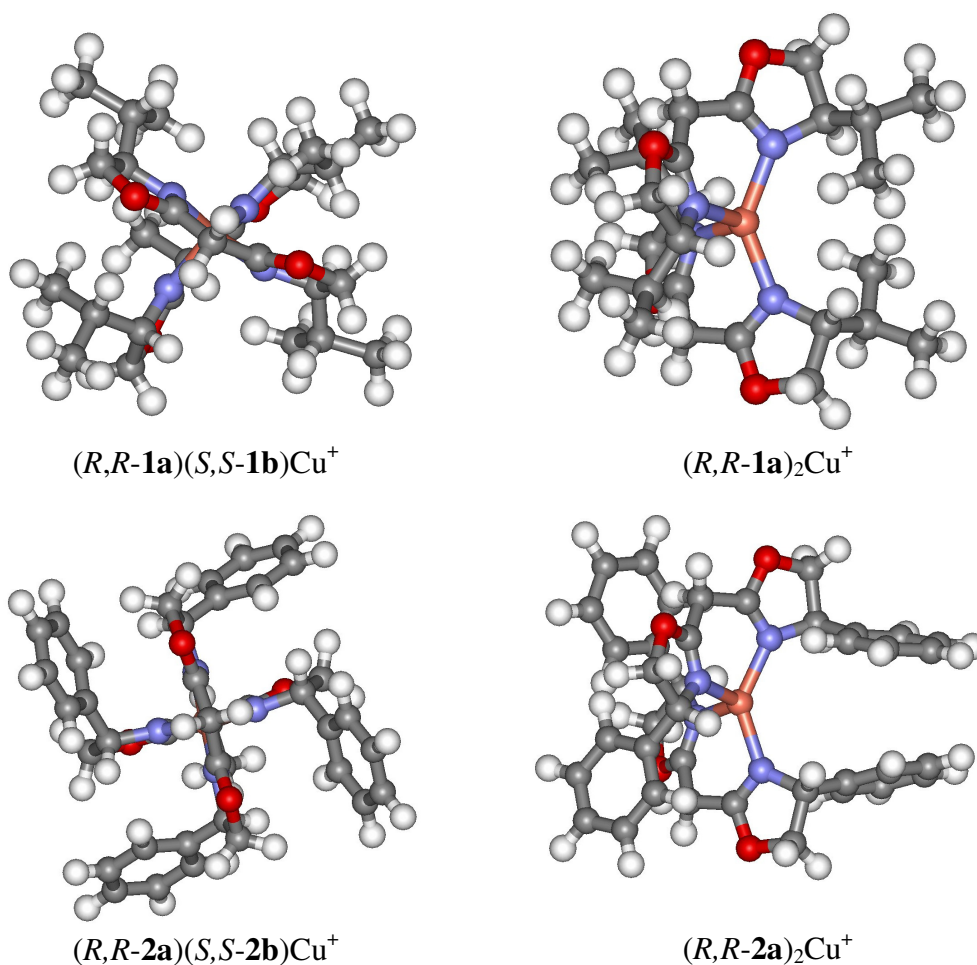
Figure 6.4 B3LYP/LANL2DZ-optimized geometries for $(R,R\text{-}\mathbf{1a})(S,S\text{-}\mathbf{1b})\text{Cu}^+$, $(R,R\text{-}\mathbf{1a})_2\text{Cu}^+$, $(R,R\text{-}\mathbf{2a})(S,S\text{-}\mathbf{2b})\text{Cu}^+$ and $(R,R\text{-}\mathbf{2a})_2\text{Cu}^+$.

For all the CID thresholds a loose orbiting transition state was assumed using the phase space model,[17] since cleaving off one bisoxazoline ligand from the 2:1 complex requires simple bond ruptures of two Cu–N bondings. There is no indication for a tight, cyclic transition state geometry. (See Chapter 3.3).

The two channel treatment of CRUNCH with an additional scaling factor was used for collision induced dissociations which produce different sets of products by way of two reaction pathways.[18] This treatment is for example always necessary for the CID of the heterochiral complexes. Since for single channel fits an excellent agreement between fit and experimental data is achieved more easily, the experimental energy-resolved dissociation cross sections of the two channel reactions were also fit individually as single channels. This is not formally correct from the physical point of view, but a glance at Table 6.2 shows that the differences are not

Table 6.2 Thermochemical Data from the Energy-Resolved Collision-Induced Dissociation Measurements and Comparison to DFT Predictions[a]

complex[b]	ligand cleaved	single channel fit			two-channel fit			DFT calc	entry
		E_0 (eV)	$\Delta S^{\ddagger}$ (eu)	ΔH (kcal/mol)	E_0 (eV)	$\Delta S^{\ddagger}$ (eu)	ΔH (kcal/mol)	ΔH (kcal/mol)	
$(S,S\text{-}\mathbf{1a})_2$Cu⁺	$S,S\text{-}\mathbf{1a}$	1.93	30	44.3				38.1	1
$(S,S\text{-}\mathbf{1a})(R,R\text{-}\mathbf{1b})$Cu⁺	$R,R\text{-}\mathbf{1b}$	2.05	26	47.2	2.05	26	47.2	42.2	2
$(S,S\text{-}\mathbf{1a})(R,R\text{-}\mathbf{1b})$Cu⁺	$S,S\text{-}\mathbf{1a}$	1.95	27	45.0	1.98	27	45.7	41.3	3
$(R,R\text{-}\mathbf{1b})_2$Cu⁺	$R,R\text{-}\mathbf{1b}$	1.84	24	41.9				35.3	4
$(R,R\text{-}\mathbf{2a})_2$Cu⁺	$R,R\text{-}\mathbf{2a}$	2.21	33	50.7				46.8	5
$(R,R\text{-}\mathbf{2a})(S,S\text{-}\mathbf{2b})$Cu⁺	$S,S\text{-}\mathbf{2b}$	1.96	28	44.6	1.98	29	45.2	53.1	6
$(R,R\text{-}\mathbf{2a})(S,S\text{-}\mathbf{2b})$Cu⁺	$R,R\text{-}\mathbf{2a}$	1.97	27	44.9	2.01	27	45.9	52.0	7
$(S,S\text{-}\mathbf{3b})_2$Cu⁺	$S,S\text{-}\mathbf{3b}$	2.06	25	47.0				41.5	8
$(S,S\text{-}\mathbf{3b})(R,R\text{-}\mathbf{3c})$Cu⁺	$R,R\text{-}\mathbf{3c}$	2.33	26	53.4	2.37	26	54.2	45.9	9
$(S,S\text{-}\mathbf{3b})(R,R\text{-}\mathbf{3c})$Cu⁺	$S,S\text{-}\mathbf{3b}$	2.27	25	52.0	2.31	25	52.8	46.8	10
$(R,R\text{-}\mathbf{4a})_2$Cu⁺	$R,R\text{-}\mathbf{4a}$	2.28	31	52.0				51.0	11
$(R,R\text{-}\mathbf{4a})(S,S\text{-}\mathbf{4b})$Cu⁺	$S,S\text{-}\mathbf{4b}$	2.28	24	51.9	2.43	24	55.4	57.0	12
$(R,R\text{-}\mathbf{4a})(S,S\text{-}\mathbf{4b})$Cu⁺	$R,R\text{-}\mathbf{4a}$	2.17	28	49.6	2.24	28	51.0	55.9	13
$(S,S\text{-}\mathbf{4b})_2$Cu⁺	$S,S\text{-}\mathbf{4b}$	2.07	31	47.3				50.8	14
$(S,S\text{-}\mathbf{4a})(S,S\text{-}\mathbf{4b})$Cu⁺	$S,S\text{-}\mathbf{4b}$	2.48	22	56.7	2.66	22	60.6	51.5	15
$(S,S\text{-}\mathbf{4a})(S,S\text{-}\mathbf{4b})$Cu⁺	$S,S\text{-}\mathbf{4a}$	2.19	27	50.0	2.23	27	50.8	50.3	16

[a] The absolute uncertainties in E_0, ΔH, and $\Delta S^{\ddagger}$ are ±0.09 eV, ±2 kcal/mol, and ±0.03 eu, respectively. [b] Labeling: **a** = H, **b** = Me, **c** = Et.

large in a quantitative sense, and moreover, all qualitative trends remain unchanged. Presumably, the similar entropies of activations for the two channels make the energy dependences of the respective cross sections similar.

Nevertheless, the quoted binding energies are given for the two-channel fits and the values from the respective single channel treatments were used as initial guess in this more complicated fitting procedure.

The ligand binding energies extracted from the experimental threshold curves are listed in Table 6.2, for which a representative data set, with the CRUNCH-fit, is shown in Figure 6.5.
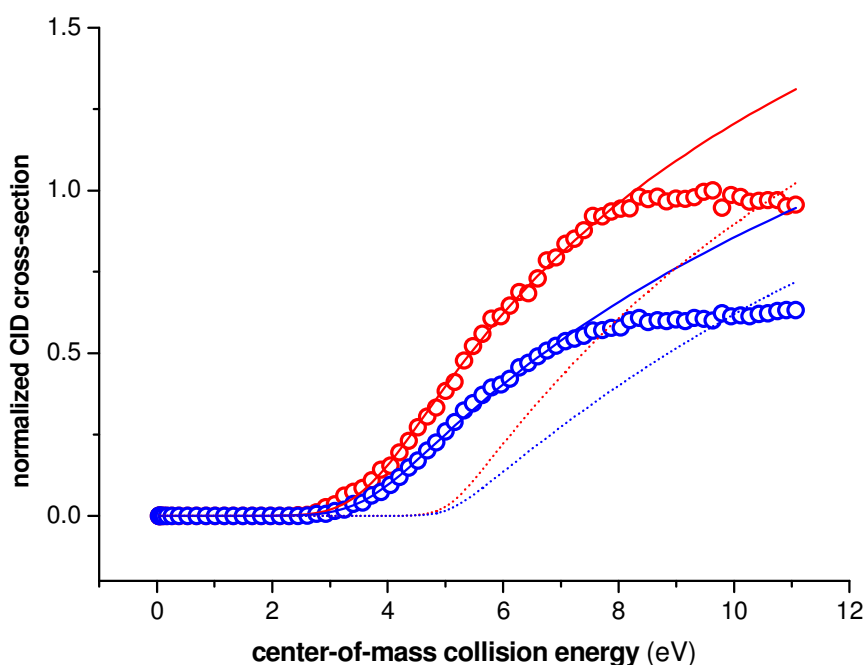
Figure 6.5 Two-channel fit for the collision-induced dissociation of (*S*,*S*-**1a**)-(*R*,*R*-**1b**)Cu$^+$. The red data points and the heavy red fitted curve belong to the (*R*,*R*-**1b**)Cu$^+$ fragment, whereas the blue ensemble belongs to the (*S*,*S*-**1a**)Cu$^+$ fragment. The dotted lines show the unconvoluted thresholds.

Although the data quality is excellent, the assumptions built into the CRUNCH process introduce a certain range to the absolute ligand binding energies, E_0, typically cited to be 0.1 eV or, equivalently about ±2 kcal/mol. Control measurements and data analysis under various assumptions were performed to establish the uncertainty

bounds. Also the effect of replacing low frequency torsions with adiabatic rotors was examined and showed no significant effect on the derived E_0.

As detailed in the experimental section, we find a global uncertainty of 0.08–0.09 eV, consistent with the usual bounds expressed in the literature. The structural similarity of all the compounds, however, should lead to cancelation of systematic errors, giving a much better relative accuracy. From the reproducibility of the curves and fittings, we estimate that the relative ligand binding energies, ΔE_0, to be better than ±1 kcal/mol. A necessary control for the cases of *pseudo*-racemates are the comparisons of the extracted thresholds for loss of differently labeled ligands which are noted in Table 6.2.[7]

Results for the 2:1 complexes with ligands **1** are given in entries 1– 4 of Table 6.2. Comparing the loss of one ligand from each of the two homochiral complexes, (*S,S*-**1a**)$_2$Cu$^+$ and (*R,R*-**1b**)$_2$Cu$^+$, one finds similar thresholds, 44.3 and 41.9 kcal/mol, respectively. The heterochiral mixed complex, (*S,S*-**1a**)(*R,R*-**1b**)Cu$^+$ loses either *S,S*-**1a** or *R,R*-**1b** upon CID with thresholds of 47.2 or 45.7 kcal/mol, respectively (Scheme 6.1). One sees first for the homochiral and then for the heterochiral complexes, that the label, R = H or CH$_3$, introduces only a small perturbation on the complexes. Secondly, the binding energy for the ligand to the heterochiral complex is significantly higher than the corresponding binding energy in the homochiral complexes. If one takes arithmetic means of the binding energies for the homo- versus heterochiral complexes, one finds that the heterochiral complex is more stable than the homochiral complex by 3.4 kcal/mol.

For the azabox ligands with isopropyl substituents, **3**, the results for the dissociation of the 2:1 complexes are listed in entries 8–10 in Table 6.2. One would expect that the label of methyl versus ethyl for the azabox ligands would introduce a perturbation to the *pseudo*-enantiomers smaller than that in the hydrogen versus methyl pairs. In practice, both sets of labels produce acceptable control values, *e.g.* the heterochiral complex, (*S,S*-**3b**)(*R,R*-**3c**)Cu$^+$, shows for loss of either *S,S*-**3b** or *R,R*-**3c** closely similar thresholds of 52.8 and 54.2 kcal/mol. The single measured homochiral complex, (*S,S*-**3b**)$_2$Cu$^+$, shows for loss of *S,S*-**3b** a much lower threshold of 47.0 kcal/mol. Again taking the mean for the heterochiral complex, the results indicate that the heterochiral complex is 6.5 kcal/mol more stable than the homochiral analog.

Turning to the ligands **2**, in which the oxazoline rings bear phenyl rather than isopropyl substituents, the situation changes, as seen in entries 5–7 in Table 6.2. The heterochiral complex, $(R,R$-**2a**$)(S,S$-**2b**$)Cu^+$, loses R,R-**2a** or S,S-**2b** with thresholds of 45.9 and 45.2 kcal/mol, respectively, even for the case of labels R = H versus CH_3. This indicates that the different labels in the *pseudo*-enantiomeric ligands really are innocuous for this complex. The homochiral complex, $(R,R$-**2a**$)_2Cu^+$, gives a much higher threshold of 50.7 kcal/mol. Taking the mean for the two thresholds from the heterochiral complex, the results indicate a reversal of stability, relative to the isopropyl-substituted cases, with the homochiral complex being more stable than its heterochiral relative by 5.1 kcal/mol when the oxazoline moiety carries a phenyl substituent.

The last combination of ligand backbone and oxazoline substituent, listed in entries 11–16 in Table 6.2, is the azabox ligand with phenyl substituents, **4**, which proved to be problematic. If the R = H or CH_3 labels were to behave innocuously, then both the two homochiral combinations, $(R,R$-**4a**$)_2Cu^+$ and $(S,S$-**4b**$)_2Cu^+$, and the two channels for the heterochiral combination, $(R,R$-**4a**$)(S,S$-**4b**$)Cu^+$, would not show large deviations. However, $(R,R$-**4a**$)_2Cu^+$ shows a significantly higher threshold of 52.0 kcal/mol than does $(S,S$-**4b**$)_2Cu^+$, with 47.3 kcal/mol. Similarly unsatisfactory are the thresholds for loss of R,R-**4a** versus S,S-**4b** from $(R,R$-**4a**$)(S,S$-**4b**$)Cu^+$, which, at 51.0 and 55.4 kcal/mol, are simply too far apart. Lastly, as a control experiment, a *pseudo*-homochiral complex, $(S,S$-**4a**$)(S,S$-**4b**$)Cu^+$, dissociates by losing either S,S-**4a** or S,S-**4b**, two channels which should have the same, or very similar thresholds. Experimentally, we find 50.8 and 60.6 kcal/mol, which means that the labels distinguishing *pseudo*-enantiomers exercise a strong influence on the stability of this 2:1 complex. In this case, the data cannot be used to judge the relative stability of homochiral versus heterochiral complexes. A pair of labels, such as R = C_2H_5 versus n-C_3H_7, would be expected to behave better, but these labels make the complex too large to be handled by CRUNCH, since CRUNCH has an arbitrary dimension limit of 87 atoms.

6.3 Investigation of Cu(I) Phenyl-Azabox Complexes with L-CID

As described in the previous section, the CID threshold results for the phenyl-azabox ligands with methyl- versus proton labeling were uninformative. It is not possible to assign therefrom, whether the homo- or heterochiral 2:1 complex is more stable.[7] This thermodynamic classification is supposed to give an indication about the sense and magnitude of a Kagan-type nonlinear effect for a 1:1 catalyst system in which the 2:1 complex serves as a reversibly formed reservoir species.[1] However, the internal consistency checks could not validate the experimental approach for the *pseudo*-enantiomeric ligands of ligand class **4** in contrast to all the other ligand families **1– 3**.[7] For this problematic case first of all the heterochiral complex $(R,R\text{-}\mathbf{4a})$-$(S,S\text{-}\mathbf{4b})\text{Cu}^+$ does not show the different ligand losses with identical or at least rather similar binding energies. Furthermore, the ligand binding energies for the two analogous homochiral complexes do absolutely not agree with each other.

The failure of the control experiments for $(\mathbf{4})_2\text{Cu}^+$ can be attributed to structural (and presumably energetic as well) distortions brought in by the substituents that were introduced to distinguish between *pseudo*-enantiomers, that is, the labels are not innocuous. When comparing the DFT-optimized structures of the two homochiral complexes $(R,R\text{-}\mathbf{4a})_2\text{Cu}^+$ and $(S,S\text{-}\mathbf{4b})_2\text{Cu}^+$ a significant geometrical difference can be observed.

$(S,S\text{-}\mathbf{4a})_2\text{Cu}^+$ $(S,S\text{-}\mathbf{4b})_2\text{Cu}^+$

∡ 125.362°   ∡ 121.852°
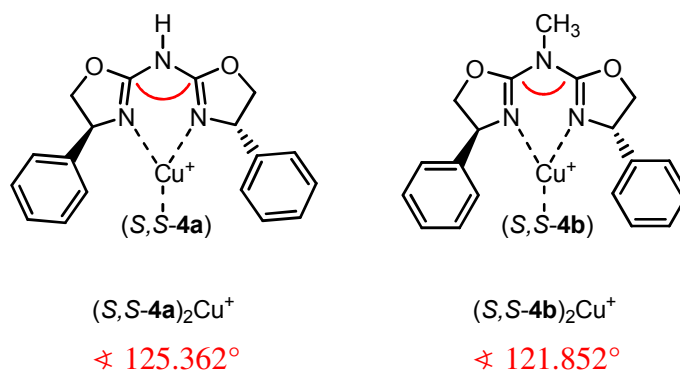
Figure 6.6 The substituent dependent bridging angle for the homochiral complexes $(\mathbf{4})_2\text{Cu}^+$.

Whereas for the unlabeled homochiral complex an angle of the bridging nitrogen between the two oxazoline units of 125.362° is present, the same angle for the methyl-labeled homochiral complex is squeezed down to 121.852° (Figure 6.6). Thus

the unfavorable steric interactions of the methyl-label with the two oxazoline rings are balanced by a decrease of the C–NCH$_3$–C angle.

In contrast this effect is only very minor for the box ligands with one methyl-label on the bridging carbon (approximately one degree difference), since the connecting C–CH$_3$ bond does not lie in the plane of the oxazoline rings as it is the case with the N–CH$_3$ unit.

The influence of the label for the free phenyl-azabox ligands *R,R*-**4a** and *S,S*-**4b** with 127.096 versus 119.758° and the concerning 1:1 complexes with 128.018 versus 124.424° is consistently strong.[7]

It has to be stressed, that the hydrogen versus CH$_3$, rather than the better CH$_3$ versus C$_2$H$_5$, labels for that system were chosen, because the current CRUNCH program cannot analyze data for ions with more than 87 atoms. This placed complexes with **4c** out of reach. A smaller model-ligand certainly could have been used, but only at the cost of applicability of the results to real catalytic systems. Since ligand class **4** is one of the privileged structures which appears repeatedly in catalysis,[19] there was decided not to abandon it.
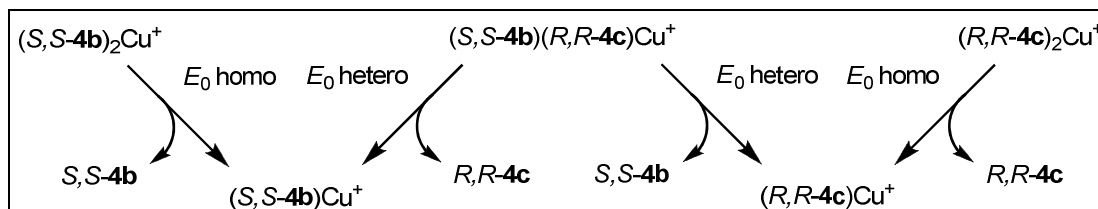
Scheme 6.2 CID threshold measurements with methyl- versus ethyl-labeled phenyl-azabox ligands

The only solution to this problem was to study methyl- versus ethyl-labeled phenyl-azabox copper complexes (Scheme 6.2) with an improved method for deconvoluting energy-resolved CID cross sections.

This program, L-CID,[20,21] developed in our group, has apart from the relaxed constraints on size the practical advantage, that no quantum chemical frequency calculations are required.

The single effective frequency approach of L-CID for the treatment of the density of states function ρ(E) eliminates the need to enter explicitly enter all the

rovibrational modes for the starting ion and the transition state without loss of accuracy relative to direct state counts. (See Chapter 5.4). Therewith a considerable practical improvement is achieved, when considering the difficulties in calculating reliable structures for the unsaturated, often open shell intermediates of interest. Also the structural diversity of the usually multiple, energetically similar isomers for both, the starting complex and the CID products, can be elegantly subsumed in the minimal structural input necessary for L-CID. Thus, no arbitrary decision on a specific isomeric structure has to be made for deconvoluting CID threshold curves with L-CID.

Solely the experimental data acquisition for computing the CID cross sections from the respective daughter and parent ion intensities as well as the determination of the absolute zero of the measurement and the ion kinetic energy distribution is just the same as for a data processing with CRUNCH.

In Figure 6.7 the threshold CID curves for the heterochiral 2:1 complex $(S,S$-$\mathbf{4b})(R,R$-$\mathbf{4c})$Cu$^+$ are depicted together with the respective L-CID-fits.
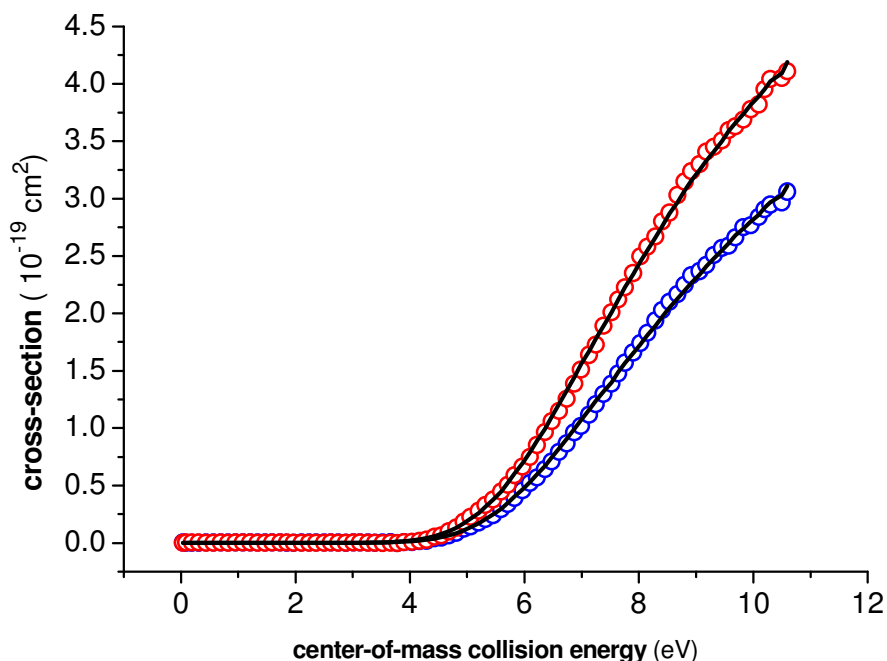
Figure 6.7 Threshold CID curves for the dissociation of $(S,S$-$\mathbf{4b})(R,R$-$\mathbf{4c})$Cu$^+$, $m/z = 719$, to $(S,S$-$\mathbf{4b})$Cu$^+$, $m/z = 384$ (blue), and $(R,R$-$\mathbf{4c})$Cu$^+$, $m/z = 398$ (red). L-CID fits are shown using the two (competing) channel model with loose transition states.

Therefore, a two-channel fit was performed whereas the comparable curves for $(S,S\text{-}\mathbf{4b})_2Cu^+$ and $(R,R\text{-}\mathbf{4c})_2Cu^+$ were fit as single channel dissociations. For all systems a loose orbiting transition state is assumed.[17]

It is important to notice that the heterochiral 2:1 complex $(S,S\text{-}\mathbf{4b})(R,R\text{-}\mathbf{4c})Cu^+$ can lose either of the ligands with the same $E_{0,\,hetero}$ in the limit that the remote label is indeed innocuous. Nevertheless, the two threshold CID curves in Figure 6.7 are not co-incident.[22] While L-CID does not constrain E_0 for the two channels to be identical, or even similar, a two-channel fit uses a common effective frequency. This means that the difference between the two competing transition states is manifested by slightly different α parameters, which correspond physically to transition states of slightly different looseness.[20]

Further, L-CID is evidently able to model the entire region of the threshold curve from the onset of the dissociation up to and including the energy at which the cross-section plateaus. In CRUNCH, one typically scales the parameter σ_0 to produce a satisfactory fit only for the region around the onset of the CID threshold. At higher energies the CRUNCH-fit can deviate markedly from the experimental curve, which means that CRUNCH can use less data points to extract the same thermochemical information as L-CID. The reason for this is the more realistic treatment of the electrostatic potential[20] and thus a non empirical threshold function in L-CID. (For more details see Chapter 5.)

The binding energies achieved from L-CID fits for the ethyl- versus methyl labeled ligands $(\mathbf{4})_2Cu^+$ are finally summarized in Table 6.3.[22]

Table 6.3   Ligand binding energies extracted from threshold CID curves by L-CID.

Complex	Cleaved ligand	E_0 (loose TS) (eV)	E_0 (tight TS) (eV)
$(R,R\text{-}\mathbf{4c})_2Cu^+$	$R,R\text{-}\mathbf{4c}$	2.00 ± 0.04	1.40
$(S,S\text{-}\mathbf{4b})(R,R\text{-}\mathbf{4c})Cu^+$	$R,R\text{-}\mathbf{4c}$	2.15 ± 0.03	1.53
$(S,S\text{-}\mathbf{4b})(R,R\text{-}\mathbf{4c})Cu^+$	$S,S\text{-}\mathbf{4b}$	2.12 ± 0.05	1.48
$(S,S\text{-}\mathbf{4b})_2Cu^+$	$S,S\text{-}\mathbf{4b}$	2.00 ± 0.05	1.40

It can be seen from the two homochiral complexes and from the two channels of the heterochiral complex that the present labeling is indeed innocent. For the homo-

and heterochiral diastereomers the clear stability ordering $E_{0, \text{hetero}} > E_{0, \text{homo}}$ is found. The uncertainties listed in Table 6.3 are computed from multiple applications of the genetic algorithm for each of the three repeated measurements. The convergence criterion is hereby set to the statistical indistinguishability of the fits for the respective data set.

This is possible since L-CID uses instead of the usual Marquardt Levenburg least squares routine a Monte Carlo Simulation and a genetic algorithm, which produce statistically relevant error bounds on the derived fit parameters.

(A complete evaluation of all the various sources of uncertainties influencing CRUNCH and L-CID results is given in the experimental section.)

Table 6.3 also lists the extracted binding energies for the hypothetical case of a tight transition state. Those E_0 values have the same relative ordering but are simply displaced by about 0.6 eV relative to those for the loose transition state.

As a final remark it has to be warned to compare the absolute values extracted with L-CID directly to those extracted with CRUNCH in case the expected differences in the binding energies should be about 0.1 eV or smaller. A discrepancy in this range was found for the absolute threshold energies gained from data work-up with L-CID versus CRUNCH for the $(S,S\text{-}\mathbf{4b})_2\text{Cu}^+$ complex. Consequently, it is best to compare always the binding energies derived from the same program.

6.4   Interpretation of the Threshold Results

Whereas the two previous sections 6.2 and 6.3 are focused on the experimental data achievement and the subsequent deconvolution with either CRUNCH or L-CID to extract ligand binding energies for the 2:1 bisoxazoline copper complexes, the interpretation of these results was kept for the following part.

Thus the threshold results listed in Table 6.2 and Table 6.3 can now be discussed in a complete composition. They are compared to the respective B3LYP/LANL2DZ energies of the ions and ligands which were treated with CRUNCH (Table 6.1).

Within the experimental threshold values several trends are evident.[7,22]

For the isopropyl-substituted ligands, **1** and **3**, the heterochiral 2:1 complex is more stable, with the difference, ΔE_0, between the (average) ligand binding energies of the hetero- versus homochiral complexes, increasing from 3.4 kcal/mol in the box ligands **1** to 6.5 kcal/mol in the azabox ligands **3**. The experimentally observed higher stability of the hetero- versus homochiral complex is readily explained on the basis of steric interactions if one looks at the computed geometry of the complexes in Figure 6.4. The homochiral complexes $(S,S\text{-}\mathbf{1a})_2Cu^+$ and $(S,S\text{-}\mathbf{3b})_2Cu^+$, are destabilized relative to the diastereomeric, heterochiral complexes, $(S,S\text{-}\mathbf{1a})$-$(R,R\text{-}\mathbf{1b})Cu^+$ and $(S,S\text{-}\mathbf{3b})(R,R\text{-}\mathbf{3c})Cu^+$, by unfavorable steric interactions of the isopropyl groups on the two ligands. Interestingly, the stability order is reversed for the bisoxazoline complex with phenyl-substituted ligands, $(R,R\text{-}\mathbf{2a})_2Cu^+$ versus $(R,R\text{-}\mathbf{2a})(S,S\text{-}\mathbf{2b})Cu^+$, with the homochiral complex being in this case more stable.

As can be seen in Figure 6.4 and Figure 6.8, the homochiral 2:1 complex puts the phenyl groups in close proximity with each pair being oriented approximately parallel displaced, from which a stabilizing non-bonded interaction, *e.g.* dispersion, or more specifically, π–π stacking, could come into play.[7]
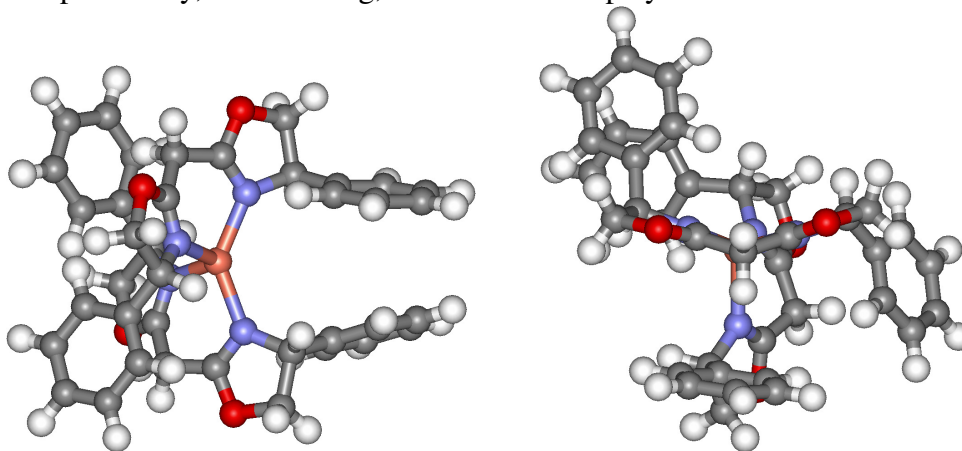
Figure 6.8 B3LYP/LANL2DZ-optimized geometry for $(R,R\text{-}\mathbf{2a})_2Cu^+$ in two different views.

In the computed geometry the distance between one hydrogen of the one phenyl-group to the center of the other phenyl-group is 3.436 and 3.922 Å respectively. For the phenyl-CH distance to the plane of the second phenyl substituent 3.491 Å and 4.198 Å are found whereas for the phenyl center–center distance 4.559 Å can be measured.

Figure 6.8 gives also a second view of $(R,R\text{-}\mathbf{2a})_2Cu^+$ from which still another type of a non-covalent interaction can be identified. The hydrogens of the bridging

carbon, which are rather acidic due to the proximity of the oxazoline rings, point directly to one phenyl ring of the second ligand. This interaction exists twice for the 2:1 complex with a hydrogen to ring center distance of 2.652 Å and 2.628 Å or the concerning distances of the hydrogen to the phenyl planes of 2.645 Å and 2.622 Å.

Those H– to ring center distances are very close to the 2.5 Å for a T-shaped benzene dimmer[23] or the literature known CH–π interaction in a benzene-ethylene complex with exactly 2.6 Å separation.[24] The benzene-ammonia and benzene-water complexes show similar H–π distances of 2.6 and 2.4 Å, respectively.[25]

Also the center–center distance for the parallel displaced phenyl rings meets exactly the published range of 4.0–4.5 Å for an ideally pronounced π–π stacking between parallel displaced phenyl groups.[26,27]

Interestingly, the DFT calculations summarized in Table 6.1 predict the heterochiral complex to be more stable than the homochiral for both, the isopropyl and phenyl substituents. The computational level, DFT/LANL2DZ, is not particularly high, but it is representative of the current level one commonly finds for medium-to-large organometallic compounds in the literature. Whereas many studies have reported that DFT calculations reproduce geometries of organometallic complexes acceptably, the energies can be quite wrong.[28] In the present case, the DFT calculations underestimate the ligand binding energies by up to 10 kcal/mol, but more importantly, they reverse the stability order for 2:1 complexes with phenyl-substituted ligands. Most likely, this discrepancy can be attributed to the known difficulty in DFT descriptions of long-range, non-bonded interactions.

In a comparison of various DFT methods to CCSD(T) calculations for benzene dimers in various configurations, parallel face-to-face, T-shaped, and parallel displaced, the DFT methods, without corrections, missed attractive non-bonded minima identified by CCSD(T) calculations.[26] The latter found interaction energies for typical slipped-parallel benzene dimers of −2.07 to −2.63 kcal/mol for the above named center–center distances of 4.5 to 4.0 Å with the aug-cc-pVQZ* basis set.[26] Uncorrected DFT calculations found purely repulsive potentials with absolute errors of ~5 kcal/mol at CCSD(T)-detected energy minima.

The already mentioned CCSD(T) interaction energy in a benzene-ethylene complex with aug(d,p)-6-311G** as basis set is published to be −1.63 kcal/mol.[24]

Attractive CH–π interactions are known to augment with increasing acidity of the respective hydrogen.

All this makes it plausible that, even the relative stability, homo- versus heterochiral, predicted by B3LYP/LANL2DZ could indeed be wrong for ligand class **2** by more than 5 kcal/mol, which is consistent with the experimental gas-phase results.[7]

The last ligand family which is still missing in this discussion are the phenyl substituted azabox ligands, **4**. Superficially, one would expect the same $E_{0, \text{hetero}} < E_{0, \text{homo}}$ ordering as for the phenyl-box complexes $(\mathbf{2})_2 Cu^+$, which, however, is not borne out by the experiment.

Comparing the B3LYP/LANL2DZ computed structures for $(R,R\text{-}\mathbf{2a})_2 Cu^+$ (Figure 6.8, 2nd view) and $(R,R\text{-}\mathbf{4a})_2 Cu^+$ (Figure 6.9) shows that the box ligand is less nearly planar than the comparably substituted azabox ligand.[7]
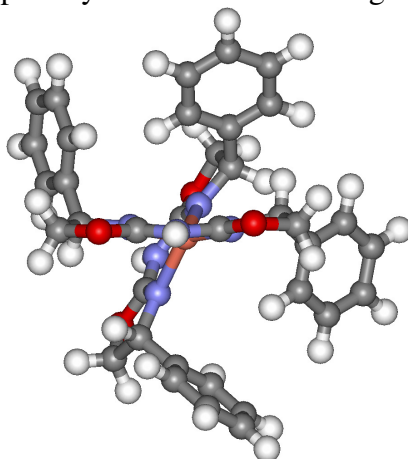
Figure 6.9 B3LYP/LANL2DZ-optimized geometry of $(R,R\text{-}\mathbf{4a})_2 Cu^+$

Probably, this slightly different backbone of the azabox ligands leads to a geometry less favorable for a π–π stacking interaction of sufficient magnitude to reverse the steric preference.

Further, the original methyl- versus proton labeling for the phenyl-substituted azabox ligands was found to perturb this system too much.

A methyl group with its electron donating role increases presumably the electrostatic metal-ligand interaction (and enhances eventually the electron donor character of the oxazoline nitrogens) but implies also a higher sterical demand. The

latter seems to be more crucial for homo- than for heterochiral complexes, where the electrostatic effect dominates the threshold results.

The same proton versus methyl labeling, however, causes for the box ligands **1** and **2** only a very small effect and all the internal consistency checks were passed successfully.[7]

Thus, the steric impact of an alkyl-label can be assumed to be more severe for the rather planar azabox ligands. Additionally, the stronger electron donating ability of the bridging nitrogen is supposed to cause a higher electronic coupling within the ligand. This could transmit the electronic effect of the alkyl-label to the oxazoline nitrogens in a larger extent than it can be expected for the box ligands **1** and **2**. As a consequence thereof, the electrostatic metal ligand binding energies might increase more for azabox than for box ligands upon alkyl-labeling.

The more comparable methyl- versus ethyl labeling was initially only possible for the isopropyl-azabox ligands, **3**, whereas the same attempt for ligand class **4** was prevented by the dimension limit of CRUNCH.

Applying the new deconvolution method L-CID to this specific ligand system showed a clear stability preference of the heterochiral complex, $(S,S\text{-}\mathbf{4b})(R,R\text{-}\mathbf{4c})Cu^+$, over the respective homochiral complexes $(S,S\text{-}\mathbf{4b})_2Cu^+$ and $(R,R\text{-}\mathbf{4c})_2Cu^+$.[22] This can be attributed solely to steric reasons.

Considering those results, it is clear that if a non-linear effect is based on the thermodynamic stabilities of homo- versus heterochiral metal ligand complexes, then the isopropyl substituted ligands **1** and **3** and the alkyl-labeled phenyl-azabox ligands **4** should display a positive non-linear effect, but the phenyl substituted box ligands **2** should not.

6.5   Conclusion

Quantitative energy resolved collision induced dissociation measurements are a successful technique for providing absolute thermochemical information. In this thesis the ligand binding to bis-oxazoline complexes of Cu(I) is extensively studied. Those complexes appear repeatedly in catalysis and can show non-linear effects, which should depend in the simplest kind on the thermodynamic stability of the homo- versus heterochiral 2:1 complexes. It can be seen from the experimental

results, that the heterochiral complexes are usually more stable in case of solely repulsive steric interactions between the substituents. However, the stability order can invert when long-range non-bonded interactions stabilize the homochiral complex sufficiently. Theoretical predictions by DFT calculations fail in such cases. Also argumentations based on structural analogy are difficult, since the studied complexes are influenced by a sum of multiple finely balanced interactions. Thus, solely the direct experimental measurement of the specific binding energies allows a reliable characterization for validating mechanistic models like the one of Kagan to explain non-linear effects in asymmetric catalysis.

6.6   References

[1]   Kagan, H. B.; *Adv. Synth. Cat.* **2001**, *343*, 227

[2]   Puchot, C.; Samuel, O.; Dunach, E.; Zhao, S.; Agami, C.; Kagan, H. B.; *J. Am. Chem. Soc.* **1986**, *108*, 2253

[3]   Kitamura, M.; Okada, S.; Suga, S.; Noyori, R.; *J. Am. Chem. Soc.* **1989**, *111*, 4028

[4]   Soai, K.; Shibata, T.; Sato, I.; *Acc. Chem. Res.* **2000**, *33*, 382

[5]   Evans, D. A.; Woerpel, K. A.; Hinmann, M. M.; Faul, M. M.; *J. Am. Chem. Soc.* **1991**, *113*, 726

[6]   a) Debono, N.; Besson, M.; Pinel, C.; Djakovitch, L.; *Tet. Lett.* **2004**, *45*, 2235; b) Werner, H.; Vicha, R.; Gissibl, A.; Reiser, O.; *J. Org. Chem.* **2003**, *68*, 10166; c) Fraile, J. M.; Garcia, J. I.; Herrerias, C. I.; Mayoral, J. A.; Reiser, O.; Socuellamos, A.; Werner, H.; *Chem. Eur. J.* **2004**, *10*, 2997

[7]   Zocher, E.; Dietiker, R.; Chen, P.; *J. Am. Chem. Soc.* **2007**, *129*, 2476–2481

[8]   Johnson, J. S.; Evans, D. A.; *Acc. Chem. Res.* **2000**, *33*, 325

[9]   Ervin, K. M.; *Chem. Rev.* **2001**, *101*, 391

[10]   a) Armentrout, P. B.; *Thermochemical Measurements by Guided Ion Beam Mass Spectrometry*, Greenwich, CT, **1992**, Vol 1; b) Dalleska, N. F.; Honma, K.; Armentrout, P. B.; *J. Am. Chem. Soc.* **1993**, *115*, 12125; c) Khan, F. A.; Clemmer, D. E.; Schultz, R. H.; Armentrout, P. B.; *J. Phys. Chem.* **1993**, *97*, 7978; d) Poutsma, J. C.; Paulino, J. A.; Squires, R. R.; *J. Phys. Chem. A* **1997**, *101*, 5336; e) Rodgers, M. T.; Armentrout, P. B.; *J. Phys. Chem. A* **1997**, *101*, 1238; f) Hammad, L. A.; Wenthold, P. G.; *J. Am. Chem. Soc.* **2000**, *122*, 11203; g) Hammad, L. A.; Wenthold, P. G.; *J. Am. Chem. Soc.* **2001**, *123*, 12311

[11]   a) Jacques, J.; Collet, A.; Wilen, S. H. ; *Enantiomers, Racemates, and Resolutions*, Krieger Publishing Co., Malabar FL, **1994**; b) Lettre, H.; Barnbeck, H.; Staunau, H.; *Chem Ber.* **1936**, *69b*, 1594

[12]   Reetz, M. T.; Becker, M. H.; Klein, H.-W.; Stöckigt, D.; *Angew. Chem. Int. Ed. Engl.* **1999**, *38*, 1758

[13]   Markert, C.; Pfaltz, A.; A*ngew. Chem. Int. Ed. Engl.* **2004**, *43*, 2498

[14]   a) Ervin, K M.; Armentrout, P. B.; *J. Chem. Phys.* **1985**, *83*, 166; b) Schultz, R. H.; Crellin, K. C.; Armentrout, P. B.; *J. Am. Chem. Soc.* **1991**, *113*, 8590; c) Dalleska, N. F.; Honma, K.; Sunderlin, L. S.; Armentrout, P. B.; *J. Am. Chem. Soc.* **1994**, *116*, 3519

[15]   CRUNCH, version D1, was kindly provided as an executable by Prof. P. B. Armentrout

[16]   Gaussian 03, Revision C.02, Frisch, et al.; Gaussian, Inc., Wallingford CT, **2004**

[17]   Rodgers, M. T.; Ervin, K. M.; Armentrout, P. B.; *J. Chem. Phys.* **1997**, *106*, 4499

[18]   a) Rodgers, M. T.; Armentrout, P.B.; *J. Chem. Phys.* **1998**, *109*, 1787; b) Amicangelo, J. C.; Armentrout, P. B.; *Int. J. Mass Spec.* **2001**, *212*, 301; c) Amicangelo, J. C.; Armentrout, P. B.; *J. Phys. Chem. A* **2004**, *108*, 10698

[19] Fraile, J. M.; Garcia, J. I.; Herrerias, C. I.; Mayoral, J. A.; Reiser, O.; Socuellamos, A.; Werner, H.; *Chem. Eur. J.* **2004**, *10*, 2997–3005

[20] Narancic, S.; Bach, A.; Chen, P.; *J. Phys. Chem. A* **2007**, *111*, 7006–7013

[21] Narancic, S.; *Mechanistic Studies of Organometallic Complexes*, PhD Thesis, ETH Zurich, **2007**, Diss. ETH No. 17337

[22] Zocher, E.; Sigrist, R.; Chen, P.; *Inorganic Chemistry* **2007**, *46*, 11366–11370

[23] Kollmann, P. A.; *J. Am. Chem. Soc.* **1996**, *118*, 11217

[24] Tsuzuki, S.; Honda, K.; Uchimaru, T.; Mikami, M.; Tanabe, K.; *J. Am. Chem. Soc.* **2002**, *124*, 104–112

[25] Tsuzuki, S.; Honda, K.; Uchimaru, T.; Mikami, M.; Tanabe, K.; *J. Am. Chem. Soc.* **2000**, *122*, 11450–11458

[26] Sato, T.; Tsuneda, T.; Hirao, K.; *The Journal of Chemical Physics* **2005**, *123*, 104307

[27] Jorgensen, W. L.; Severance, D. L.; *J. Am. Chem. Soc.* **1990**, *112*, 4768–4774

[28] Bühl, M.; Kabrede, H.; *J. Chem. Theory Comput.* **2006**, *2*, 1282

Part III

Reaction of Copper(I) Bisoxazoline

Complexes in Solution

Chapter 7

Ligand Exchange Dynamics

7.1 Preequilibrium in a Catalytic Cyclopropanation Reaction

After determining absolute ligand binding energies of 2:1 bis-oxazoline copper(I) complexes with gas-phase collision induced dissociation (CID) measurements, these thermodynamic results shall be probed upon their ability to explain the occurrence of non-linear effects in homogenious catalysis. As classical catalytic test reaction the asymmetric cyclopropanation of styrene and ethyldiazoacetate (EDA) has been chosen.(See Figure 7.1).[1]
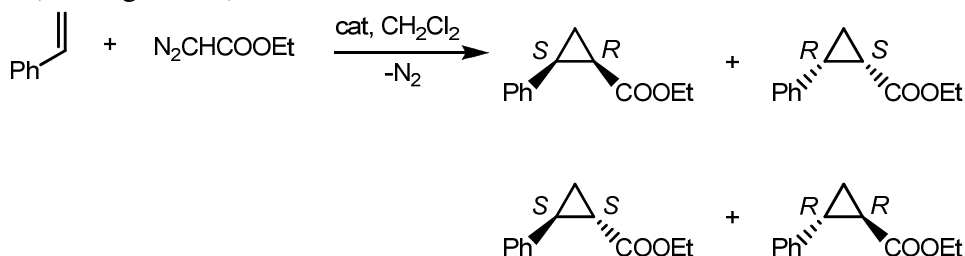
Figure 7.1 Cyclopropanation of EDA and Styrene

It is known from calculations that this catalytic transformation is characterized by a large negative Gibbs free energy for the overall course of the reaction,[2] which is consistent with its irreversibility.

As rate limiting step the formation of the copper carbene intermediate was identified from competition experiments with various alkenes,[3,4] whereas the step controlling the stereochemistry (Chapter 2.1) takes place at lower activation energies.

Interestingly, kinetic studies have shown, that excess of olefin or copper coordinating ligands slow down the rate of the cyclopropanation. This result is

attributed to the existence of a preequilibrium involving the formation of catalyst olefin complexes or coordinatively saturated 2:1 complexes of the bidentate ligands with copper(I).

Diaz-Requejo et al.[4] have used for their kinetic studies dihydridobis-(1-pyrazolyl)borate (= Bp) as negatively charged catalyst precursor for the olefin cyclopropanation reaction including the proposition of the electronically and coordinatively unsaturated 14-electron fragment BpCu, a neutral species, as the real catalyst in those transformations (Scheme 7.1).
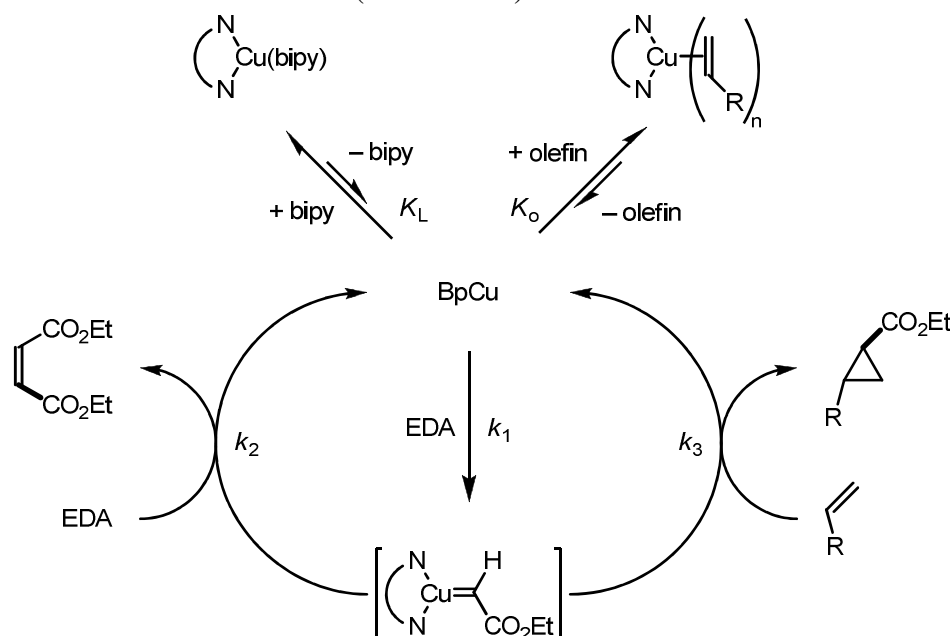
Scheme 7.1 Overview over the proposed preequilibrium and the catalytic cycle for a cyclopropanation reaction of EDA and styrene catalyzed by the complex BpCu.[4]

As additional nitrogen donor ligands the neutral 2,2'-bipyridines (= bipy) are chosen and their participation in the preequilibrium can be studied conveniently since they trap the [BpCu] species as expected but cannot complicate the equilibrium mixture. Thus, the presence of a (bipy)Cu$^+$ species can be excluded due to the large difference in the copper binding ability of the negatively charged Bp ligand compared to the neutral bis-pyridines.

The proposed mechanistic pathways depicted in Scheme 7.1 can be split up in three parts, which can be validated in separate kinetic experiments:[4]

(i) the decomposition of EDA to solely the side-products fumarate and maleate in the absence of styrene and with perfect 1:1 stochiometry of Bp and Cu(I)

(ii) the same reaction design as under the previous point but with an excess of copper coordinating bipy ligands.

(iii) the reaction with styrene and EDA to form the cyclopropane and the side-products without excess of copper coordinating ligands.

In all cases a steady-state approximation for the copper-carbene species is assumed and the rate constant for EDA consumption, k_{obsd}, is determined experimentally via periodic GC measurements of the EDA concentration during the course of the specific test reaction.

For the first reaction design (i) the simple first order relationship of the overall rate constant

$$k_{obsd} = 2k_1[Cu]_{tot} \tag{7.1}$$

is found to reproduce the experimental data perfectly. k_1 is the rate constant for the carbene formation whereas $[Cu]_{tot}$ represents the summed concentrations of all copper containing species present in the test reactions (i), namely the postulated 14-electron species and the carbene.

If n equivalents of free bipy ligand referred to the total concentration of copper(I) are added to the reaction mixture (case (ii)), the observed rate constant (equation 7.2) confirms the assumption of a preequilibrium between BpCu, free bipy and BpCu(bipy) with the corresponding equilibrium constant K_L.

$$\frac{1}{k_{obsd}} = \frac{1}{2k_1[Cu]_{tot}} + \frac{n}{2k_1K_L} \tag{7.2}$$

Evidently the presence of the additional nitrogen-donor ligands diminishes the amount of catalytic active species, which is reflected by the decrease of the reaction rate, k_{obsd}, with augmenting concentrations of bipy ligands.

For the EDA decomposition in the presence of olefin (reactions (iii)) and the limiting case of a large olefin excess a rather simplified expression for the approximate overall rate constant, k_{app}, can be derived for the assumed mechanism (equation 7.3).

$$\frac{1}{k_{\mathrm{app}}} = \frac{1}{k_1[\mathrm{Cu}]_{\mathrm{tot}}} + \frac{K_{\mathrm{o}}}{k_1[\mathrm{Cu}]_{\mathrm{tot}}}[\mathrm{olefin}] \qquad\qquad (7.3)$$

Herein, K_{o} represents the equilibrium constant for the olefin complexation of BpCu and $[\mathrm{Cu}]_{\mathrm{tot}}$ is again the total concentration of all copper-containing species or simply the total concentration of Cu(I), since no dinuclear copper complexes are assumed to be relevant for the mechanistic picture.

Clearly the rate of the cyclopropanation, k_{app}, decreases with higher olefin concentrations, since the presumed active species, BpCu, is trapped more likely via coordination of olefin molecules to the active site of the catalyst.

Also the second limiting case with EDA excess for the test reactions (iii) gave a perfect agreement between experiment and the kinetic rate (equation 7.4) based on the proposed mechanism:

$$\ln[\mathrm{olefin}] = \ln[\mathrm{olefin}]_{\mathrm{in}} - \frac{k_1 k_3[\mathrm{Cu}]_{\mathrm{tot}}}{k_2} \cdot t \qquad\qquad (7.4)$$

$[\mathrm{olefin}]_{\mathrm{in}}$ is the initial concentration of olefin and the ratio k_2/k_3 displays the kinetics of the EDA dimerization compared to the cyclopropanation. This value is found to be larger than one which is consistent with the need for excess olefin and the use of EDA slow addition techniques to improve the yields in cyclopropanation reactions.

However, the experimentally observed inhibition of the catalytic cycle in terms of low overall reaction rates can clearly be attributed to the presence of large concentrations of olefin, which diminish the amount of the catalytic active species. The same effect is observed, when an excess of nitrogen donor ligands is present. Considering for example crystallographically characterized [Cu$^{\mathrm{I}}$(bipy)(π–CH$_2$=CHC$_6$H$_5$)][PF$_6$] complexes,[5] then the ability of Cu(I) complexes to coordinate styrene is of striking evidence and substantiates the proposition of the 14-electron fragment BpCu as the real catalyst, whereas the BpCu-styrene and the 2:1 bidentate ligand to copper complexes are supposed to serve as resting states.[4]

Thus the experimental test reactions (i) – (iii) which have selectively illuminated specific parts of the proposed mechanism of a cyclopropanation reaction give in their entirety a convincing indication, that the previously outlined mechanism

(Scheme 7.1) resembles the true catalytic process at least in a so far consistent manner.

Similar kinetic experiments with neutral bipy or bisoxazoline ligands have shown a similar retardation of the kinetic rate in the presence of either excess of olefin or copper coordinating ligands.[4] Also monodentate ligands like I, THF or CH_3CN have the same influence and participate in the preequilibrium (see Scheme 7.2).
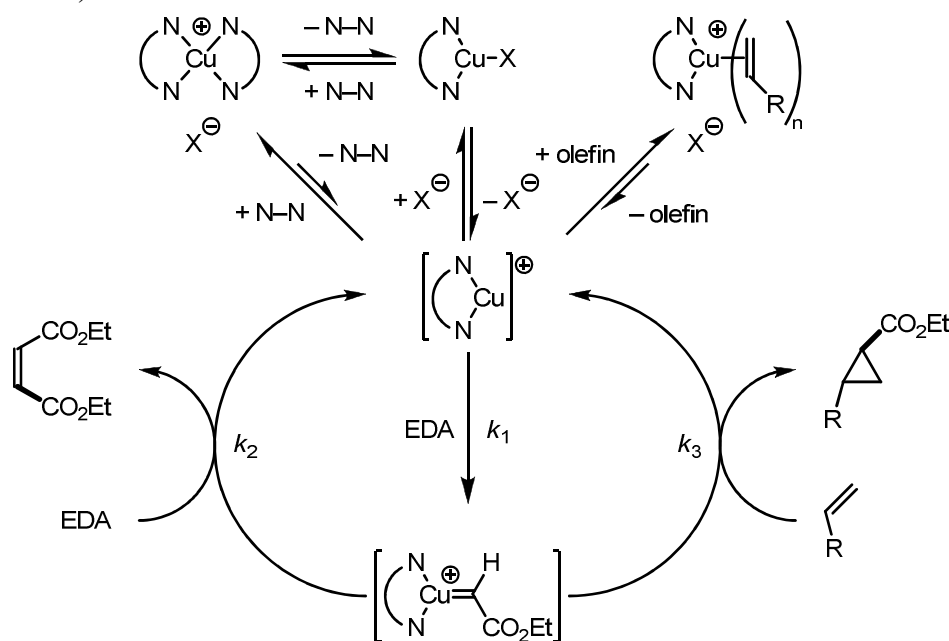
Scheme 7.2 The proposed catalytic cycle of a cyclopropanation with copper(I) and neutral bisoxazoline ligands. Additional monodentate ligands X^- and styrene compete with free bisoxazoline ligands to coordinate on the 1:1 bisoxazoline copper complex.[4]

The only difference between negatively charged and neutral bidentate nitrogen donor ligands is, that of the latter ones, more than one equivalent is needed to complex all the CuOTf in the reaction mixture. (Free Cu^+ would of course lower the enantioselectivity in asymmetric, catalytic reactions.)

These kinetic results with the implied assumption of a 14-electron species acting as the active catalyst for the catalytic turnover[4] are of course the linking key to the energy resolved collision induced dissociation experiments presented in Chapter 6.[6,7] Cleaving one of the two bidentate chiral ligands from the 2:1 bisoxazoline copper(I) complexes produces exactly those above named electronically and coordinatively unsaturated species. The differences in the absolute ligand binding

energies should thus reflect the relative ease of the homo- versus heterochiral 2:1 complexes to release the highly reactive 1:1 fragment, which determines the stereochemistry of the products[2] (see Chapter 2.2).

Consequently, it is the next logical step to probe the gas-phase ligand binding energies[6,7] as well as the mechanistic model[4] (Scheme 7.2) with asymmetric cyclopropanation reactions catalyzed by *e.g.* nonenantiopure Isobox (**1a**) and Phenylbox (**2a**) ligands with CuOTf. The experiences gained from the above described kinetic studies lead to an especially designed reaction set-up for these particular cyclopropanations of EDA and styrene: Since the aim is to monitor the thermodynamic stability differences of the homo- and heterochiral 2:1 bisoxazoline copper complexes, the reaction conditions should not impede their formation. Thus, any other competing copper coordinating substances should be avoided, why CuOTf instead of $Cu(CH_3CN)_4PF_6$ was chosen as copper source. All reagents as well as the solvent CH_2Cl_2 need to be dried before use and the catalysis has to be performed under argon atmosphere. Referring to EDA only 1.2 equivalents of styrene are used to reduce the olefin concentration as much as possible, while accepting that the latter value is not any longer approximately constant during the catalytic reaction. In order to diminish the kinetically favored formation of fumarate and maleate EDA is added very slowly with a syring pump over 8 hours.

As last choice, in the practical realization solely pure enantiomeric ligand pairs without the obligatory labeling of the gas-phase studies were taken for the catalysis experiments. Different reaction rate laws for the otherwise *pseudo*-enantiomeric copper ligand species might unnecessarily complicate the interpretation of the observed nonlinear effect, since methyl-labeling generates a new stereocenter on the bisoxazoline ligands **1** and **2**.

For each catalysis 2 mol% CuOTf and 6 mol% of the nonenantiopure ligands **1a** or **2a** are used. It should be noted, that an exact dosing of Cu(I) and the respective ligand mix is extremely important. The enantiomeric excess of the product cyclopropanes (EE_{prod}) from EDA and styrene are determined after column chromatography by chiral GC-MS (see experimental part).

The cyclopropanation results for the *in situ* generated catalyst from the ligands *R,R*-**1a**, *S, S*-**1a** and CuOTf are depicted in Figure 7.2. The analogue outcome for *R,R*-**2a** and *S,S*-**2a** in varied ratios as chiral auxiliary for the copper catalyzed cyclopropanation are shown in Figure 7.3.
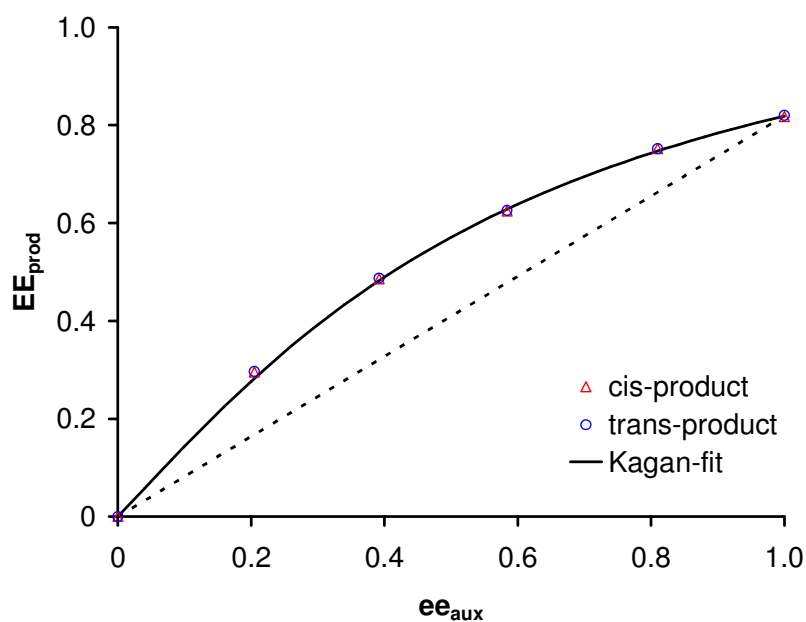
Figure 7.2 Asymmetric cyclopropanation of styrene with EDA for a varying enantiopurity of Isobox ligands **1a** with CuOTf (triangles and circles). The solid line is the Kagan-fit of an ML_2 model[8] to the experimental data points.

Figure 7.3 Nonenatiopure ligands **2a** serve as chiral auxiliary for the copper catalyzed cyclopropanation of styrene and EDA. The data points are fit according to Kagans ML_2 model[8] (solid line).

Interestingly, for both ligands **1a** and **2a** a better EE_{prod} was found than described in the literature (Table **7.1**).

Table 7.1 Enantiomeric excess for the asymmetric copper catalyzed cyclopropanation of styrene with EDA according to a modified procedure (second and third columns) and compared with literature values (columns 4 and 5).

	cis	trans	cis_{Lit}	$trans_{Lit}$
1a	81	82	64^a	48^a
2a	78	77	58^b	49^b

[a] See Reference 1. [b] See Reference 9.

This is due to two reasons: a real chemical difference and a surprisingly common imprecision not yet pointed out in the data integration of the GC-MS peaks for the cis and trans enantiomers. In the case of a simple ML_2 model according to Kagan,[8] there should be no difference in the EE_{prod} of the cis and the trans substituted cyclopropane. The discrepancy, anyhow observed, for those literature values can be assigned to an artefact when comparing our own GC-MS spectra. With the best optimized method (see experimental part) it was possible to separate the cis enantiomers perfectly, but the trans enantiomers could not be base line separated. The effect is more severe if the first of the two "trans"-peaks corresponding to the (1*R*,2*R*)-enantiomer is large, because its overlap adds considerably to peak of the (1*S*,2*S*)-cyclopropane with the larger retention time. A simple integration until the minimum between the two peaks can give rather wrong EE_{prod}-values, since the enantiomeric excess is defined as the normalized difference in the amount of the two enantiomers. However, with the proper choice of (*R*,*R*)-bisoxazoline as chiral auxiliary, the (1*S*,2*S*)-cyclopropane can be favored over its enantiomer; thus, this inexact GC-MS integration was probably ignored for a long time, although it causes the artificial difference in the EE_{prod} values of the cis and trans diastereomers.

In this thesis the problem was overcome by measuring for the cis cyclopropanes the precise peak heights and areas whereas for the trans-products only the experiment peak heights were noted. The peak areas for the trans cyclopropanes were then calculated with the scaling factors derived from the cis-products. This method assumes similar peak shapes for all the cyclopropanes, which is in very good agreement with the obtained GC-MS spectra.

The second reason for the improved ee-values for the cyclopropanation of EDA and styrene with the enantiopure **1a** and **2a** ligands addresses now both, the cis and trans diastereomers simultaneously, because it can be attributed to the modified cyclopropanation procedure.

In contrast to the literature known variants[1] only one fifth of the usual amount of olefin but an almost 1.5 times larger chiral ligand to copper ratio is used in the present study. This recipe should effectively decrease the amount of copper species that are not bound to a chiral ligand but maybe only surrounded by styrene ligands, since their catalytic activity leads of course to an overall lower asymmetric induction.

Apart from this positive side-effect of improving the EE_{prod} of the particular cyclopropanation, the fact of having twice a positive NLE is surprising. The ligand binding studies from Chapter 6[6] would have suggested a positive NLE for ligands **1a** but a negative one or, at least, no non-linear effect for the ligands **2a**. However, the experiment shows a very clear and simple outcome of twice a positive NLE, that can be perfectly fitted according to Kagan's ML_2 model (see Chapter 2.3).

For the isobox ligands **1a** (Figure 7.2) the equilibrium constant K of the hetero- over the homochiral complex stabilities is approximately 29 and therewith clearly larger than four which would otherwise indicate a statistical distribution of homo- versus heterochiral complexes in the equilibrium mixture. The parameter $g \approx 0.4$ being smaller than one shows the reduced reactivity of the meso-complex compared to the homochiral ones.

The positive NLE is even more pronounced for the phenyl-box ligands **2a** with the equilibrium constant $K = 2500$ and $g = 0.14$ for the displayed Kagan-fit of Figure 7.3.

The only conclusion to be drawn from these surprising results is that the mechanism of the catalytic reaction has to deviate remarkably from the one commonly accepted in the literature and presented in the beginning of this chapter (Scheme 7.1 and Scheme 7.2).

7.2   The Multistep Ligand Exchange Process

According to Kagan's theory[8] the occurrence of a NLE should originate in the pre-equilibrium between the differently ligated metal complexes, whereas some of these species should contain more than one chiral ligand. Thus, the equilibrium constant K and the ability of all the various metal ligand complexes to release the (or maybe more than one) catalytic active species is supposed to explain the peculiar NLE's in asymmetric catalysis.

In case the real catalyst undergoing the catalytic cycle of *e.g.* a cyclopropanation reaction would indeed be a coordinatively unsaturated 1:1 bisoxazoline copper complex,[4] then the different ligand binding energies for the homo- versus heterochiral 2:1 bis-oxazoline copper complexes[6,7] should ideally explain the manner of an occurring NLE. However, for the phenyl-box ligands **2a** the predictions derived from the thermodynamic gas-phase ligand binding measurements failed completely.

So various possible explanations for this unexpected behaviour had to be evaluated.

As a first potential problem a maybe too slow approach of the equilibrium was considered. It is a known observation that the isomerization at the copper center can be slowed down by introducing bulky substituents in positions adjacent to the nitrogen atoms of *e.g.* phenantroline ligands.[10] This steric inhibition can prevent the geometric reorganization needed for a ligand exchange on the metal center.

However, the phenyl- and isopropyl-substituents of the particular bisoxazoline ligands in this study are rather small compared to the *tert*-butyl-4-methoxyphenyl-groups of the kinetically locked phenantroline ligands.[10]

Further, mixing of homochiral $(R,R\text{-}\mathbf{2a})_2Cu^+$ and $(S,S\text{-}\mathbf{2a})_2Cu^+$ showed a very rapid formation of $(R,R\text{-}\mathbf{2a})(S,S\text{-}\mathbf{2a})Cu^+$ detected by NMR or analogous with *pseudo*-enantiomeric ligands $R,R\text{-}\mathbf{1a}$ and $S,S\text{-}\mathbf{1b}$ the presence of the respective heterochiral complex could be monitored after very short mixing times via MS.

As a last check also catalytic amounts of CH_3CN were added to the metal ligand mixture, since the copper coordinating ability of CH_3CN might facilitate an eventually inhibited ligand exchange, but no change of the equilibrium for the heterochiral copper ligand mixtures could be observed.

Even the temperature dependent ligand exchange dynamics for homochiral $(S,S$-**2c**$)_2$Cu$^+$ and free S,S-**2c** are not visibly influenced by catalytic amounts of CH$_3$CN according to VT-NMR experiments. In contrast to this large quantities of CH$_3$CN, *e.g.* when it is used as solvent, "break" the 2:1 ligand copper complexes in favor of [(bisoxazoline)Cu$^+$(CH$_3$CN)$_2$] combinations.

All this leads to the conclusion, that for the studied bisoxazoline copper complexes equilibrium conditions are reached.

Consequently, the deviations between the gas-phase ligand binding energies[6,7] and the solution chemistry results have to be caused by a somehow different ligand exchange process than the so far assumed simple dissociation of one of the two bidentate ligands to generate the active species.[4]

As a next step VT-NMR studies were performed to get more insight in the actual ligand exchange process in solution. The activation parameters were fully characterized for the isoenergetic ligand exchange of $(S,S$-**2c**$)_2$Cu$^+$ with free S,S-**2c**, since the six protons of the two methyl groups on the bridging carbon display an intense and highly temperature dependent signal. (Figure 7.4)
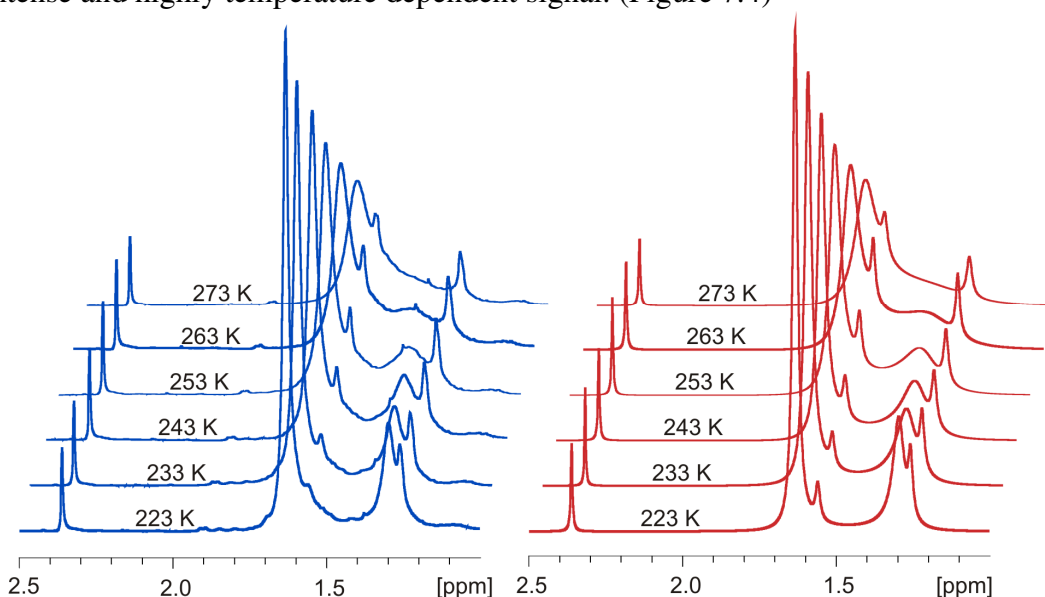
Figure 7.4 Temperature dependent spectra of $(S,S$-**2c**$)_2$Cu$^+$ exchanging with free S,S-**2c**. Blue: experiment; red: fitted spectra with DNMR.[11] At 223 K the complex appears at 1.3 ppm. The resonances at 1.55 and 1.24 ppm correspond to water and probably to an alken as impurities, but do not broaden and therewith, do not interfere in the exchange process. The signal at 2.36 ppm corresponds to toluene from CuOTf.

Evidently at 223 K the signal of free ligand (1.62 ppm) and the homochiral 2:1 complex (1.3 ppm) are fully separated and the interligand exchange is frozen out.

At 273 K though, only one broad signal for both species is observed, indicating a faster exchange with higher temperature.

Line shape analysis of these spectra with the commercial DNMR-software from BRUKER[11] gave the exchange rates k(T) for each temperature. The toluene signal, used as reference, as well as the impurities at 1.55 ppm (water) and 1.24 ppm (alkene) were treated as single spin systems.

Via the Eyring equation (Chapter 3.2) the Gibbs free energies of activation, $\Delta G^{\ddagger}$, can be readily computed from the exchange rates. When plotting $\Delta G^{\ddagger}$ against the temperatures of the NMR measurements, then the enthalpy of activation $\Delta H^{\ddagger}$ for the ligand exchange equals the intercept of the straight line whereas the slope gives the entropy of activation $\Delta S^{\ddagger}$. (Figure 7.5)
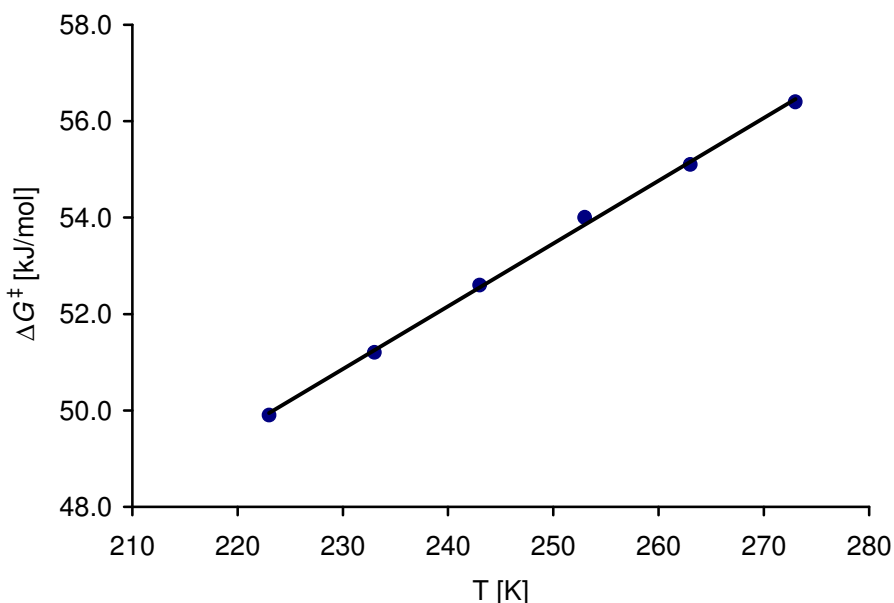
Figure 7.5 The activation parameter $\Delta G^{\ddagger}$ obtained from VT-NMR line shape analysis for (S,S-**2c**)$_2$Cu$^+$ and free S,S-**2c**.

In the present experiment is $\Delta H^{\ddagger} = 20.7$ kJ/mol and $\Delta S^{\ddagger} = -131$ J/mol·K. The inaccuracy of the line shape analysis is certainly more pronounced for the $\Delta H^{\ddagger}$ value since a slight change in the slope can cause a considerable change for the intercept. The current $\Delta H^{\ddagger}$ value might thus be wrong by a factor of two approximately.

Even though these activation parameters contain a certain error, the entropy of activation is definitely very negative for the rate limiting step in the studied ligand

exchange process. This is a very clear indication for an associative mechanism,[12] because the incoming ligand leads to more disorder in the transition state.

Also the fact, that the ligand exchange is faster the more excess ligand is added supports an associative mechanism. Some additional indication about the nature of the rate limiting step can be concluded from the solvent dependence of the ligand exchange rate. In the less polar chloroform higher exchange rates are observed for the specific $(S,S\text{-}2c)_2Cu^+$ solution than in CH_2Cl_2, indicating a less polar activated complex at the rate limiting TS according to the "like-dissolves-like rule".[13]

However, so far the question of an S_N2 type or rather solvent assisted S_N1 exchange mechanism cannot yet be answered. It is only clear that there must be a somehow associative rate limiting step.

In case of a classical S_N2 type ligand exchange the metal should act as electrophile and the incoming ligand as nucleophile. Thus, low lying metal LUMO orbitals should favor the nucleophilic attack.[14,15] (See Scheme 7.3).
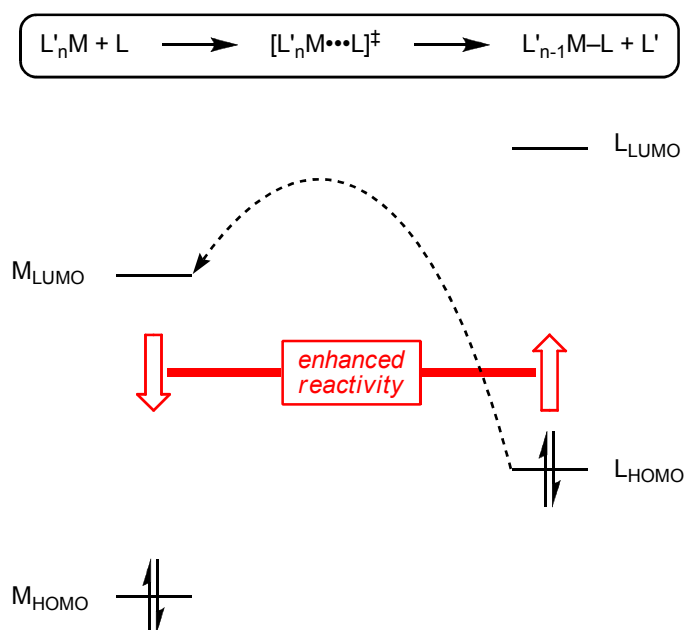
Scheme 7.3 Simplified molecular-orbital analysis of an associative ligand substitution reaction at a transition-metal center. The primary orbital overlap occurs between a ligand-based HOMO and a metal based LUMO, and improved overlap will lead to higher reaction rates.[14]

To probe this, UV-Vis Spectra of the homo- and heterochiral $(2a)_2Cu^+$ and $(2c)_2Cu^+$ complexes were taken, but the observed MLCT bands do not explain why the homochiral 2:1 complexes of the ligands **2a** and **2c** should be more easily attacked than the in solution heavily favored heterochiral ones. (The MLCT bands are just congruent for $(S,S$-**2a**$)_2Cu^+$ and $(S,S$-**2a**$)(R,R$-**2a**$)Cu^+$ whereas $(S,S$-**2c**$)$-$(R,R$-**2c**$)Cu^+$ possesses even a lower lying band than its homochiral analogue. This is even contradictory to the expected behavior in case the MLCT transitions of the 2:1 complexes were important for the ligand exchange process.)

Also, an inverse electron demand ligand substitution as published for Pd^0-olefin complexes[14] is for the bisoxazoline copper complexes rather unrealistic, since it requires sufficiently low lying ligand LUMO orbitals, which should interact with the metal HOMO orbital. However, bisoxazoline ligands are certainly better nitrogen donors than electrophiles and enantiomeric ligands show anyways no difference in their $\pi^*(C=N)$ orbital. So this substitution mechanism can also be ruled out.

Considering additionally the steric shielding of the copper center in both, the homo- and heterochiral 2:1 complexes, then a S_N2 mechanism for the ligand exchange can be excluded. (See therefore the Gaussian optimized 2:1 complex geometries in Chapter 6.2[6]).

Knowing from VT-NMR, that the rate limiting step in the bisoxazoline ligand exchange process has to be associative but, as outlined above, cannot be a S_N2 type substitution then the only remaining possibility is a S_N1 mechanism.

The first step herein has to be the dissociation of one of the copper nitrogen bonds to produce a three coordinate copper species that can react further in an associative step with a free ligand.

This initial dissociation is for the studied 2:1 complexes a very realistic assumption, especially when unfavorable steric interactions of the substituents lead to a ground state destabilization[16] and therewith to a lengthening of some Cu–N bonds. Additionally the σ-donating ability[16] of the bisoxazoline nitrogens should lead to a sufficient accumulation of electron density even on the three coordinate copper atom. Consequently this low valent species should be energetically "reachable". The characteristically smaller π-acceptor ability of the $\pi^*(C=N)$ orbital in bisoxazoline ligands compared to *e.g.* the expanded $\pi\pi^*$-orbitals of phenantrolines **36** supports the

idea of having enough electron-density at a three coordinate copper species even more.

Phenantrolines **36** have, apart from their different electronical behavior, also a second important distinction to bisoxazoline ligands **38**: the rigid phenantroline backbone fixes the two nitrogen donor atoms relative to each other, whereas bisoxazoline **38** or bispyridine ligands **37** can rotate around the bridging C–C bonds. (See Figure 7.6). Their donating nitrogens are only forced in a vicinal position upon metal coordination.
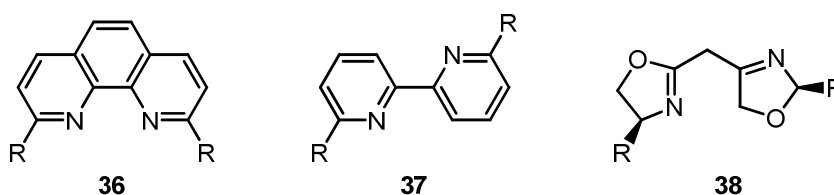
Figure 7.6 Free phenantroline **36**, 2,2'-bispyridine **37** and bisoxazoline ligands **38**.

As a consequence thereof phenantroline ligands **36** react with Al(dmso)$_6$ in a concerted manner according to stopped-flow Fourier-transform ^{1}H-NMR measurements, whereas bispyridine ligands **37** clearly show a two step process with two different rate constants.[17] In polar solvents usually the initial metal-ligand bond formation is more slow than the chelate ring closure.[18]

The existence of singly bound bidentate ligands in reactive intermediates is further secured by the observation that acid accelerates the hydrolysis of [Fe(bipy)$_3$]$^{2+}$ **39**.[19] This effect can be simply explained on the basis of small amounts of metal-ligand complexes **40**, which have only one ligand linked to a donor atom whereas the other one is free and can be protonated to yield structure **41**. Therewith the back-coordination of this ligand side to the metal center is hampered and a ligand exchange gets more likely. (Scheme 7.4)
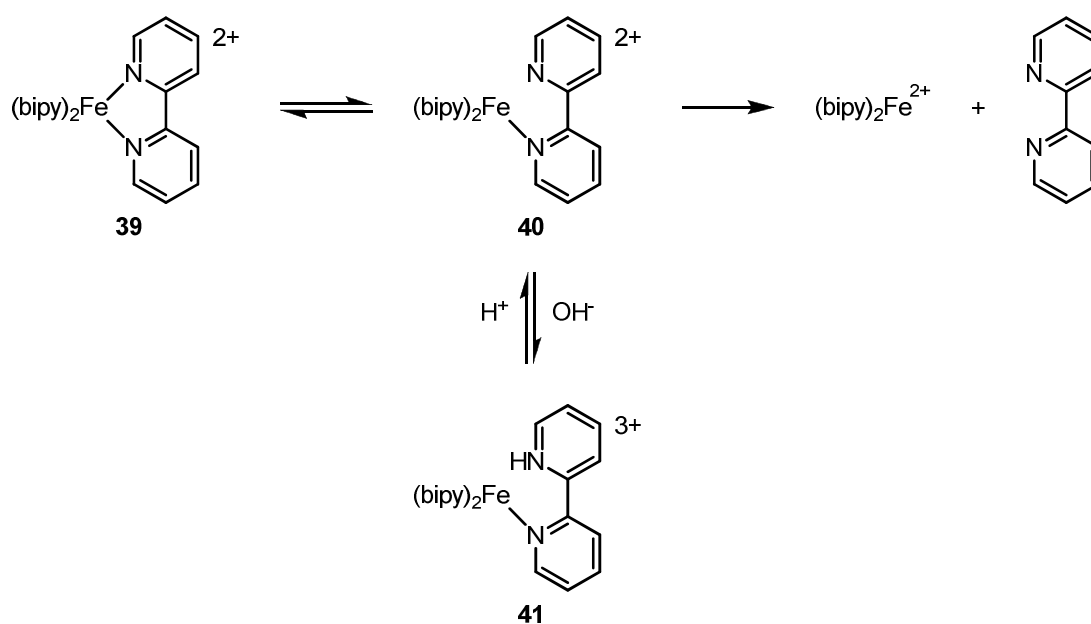
Scheme 7.4 The acid supported ligand exchange of [Fe(bipy)₃]²⁺.

Apart from the proven existence of low coordinate copper species also some statements about their stability can be made: from CID threshold measurements of *e.g.* $[Cu(pyridine)_4]^+$ [20] it is known that successive cleavage of each of the monodentate pyridine ligands takes place with augmenting threshold energies (0.69, 0.85, 2.45 and 2.72 eV). It is clear that the four coordinate copper complex is most stable and dissociation of already the first Cu–N bond is endothermic.

Probably this picture holds also for the behavior of 2:1 bisoxazoline copper complexes in solution. It is very likely, that the enthalpy for the resolvation of the Cu^+ is less negative than the enthalpy for the endothermic bond rupture is positive. Further there should not be a striking enthalpy-entropy cancellation for the dissociation of one Cu–N bond in a 2:1 bisoxazoline copper complex because the entropy gain therefrom is presumably much smaller than for the analogue dissociation of a monodentate ligand which can leave the environment of the respective metal ligand complex. Consequently it is questionable whether the first Cu–N bond dissociation for monodentate ligands is really endothermic in solution. However for bidentate ligands this should clearly be the case.

Those theoretical considerations agree nicely with NMR experiments of the studied bisoxazoline copper complexes. At $-80\,^{\circ}C$ rather sharp and symmetrical signals are observed clearly indicating the presence of the most stable 2:1 complexes

with all four nitrogens coordinated to copper. The three coordinate "opened" copper complexes must be higher in energy but can still act as reactive intermediates in the ligand exchange process, whereas the 1:1 bisoxazoline copper complexes are clearly out of reach. Instead the reaction proceeds over the associative step, which was identified by VT-NMR measurements as rate limiting. (Scheme 7.5)
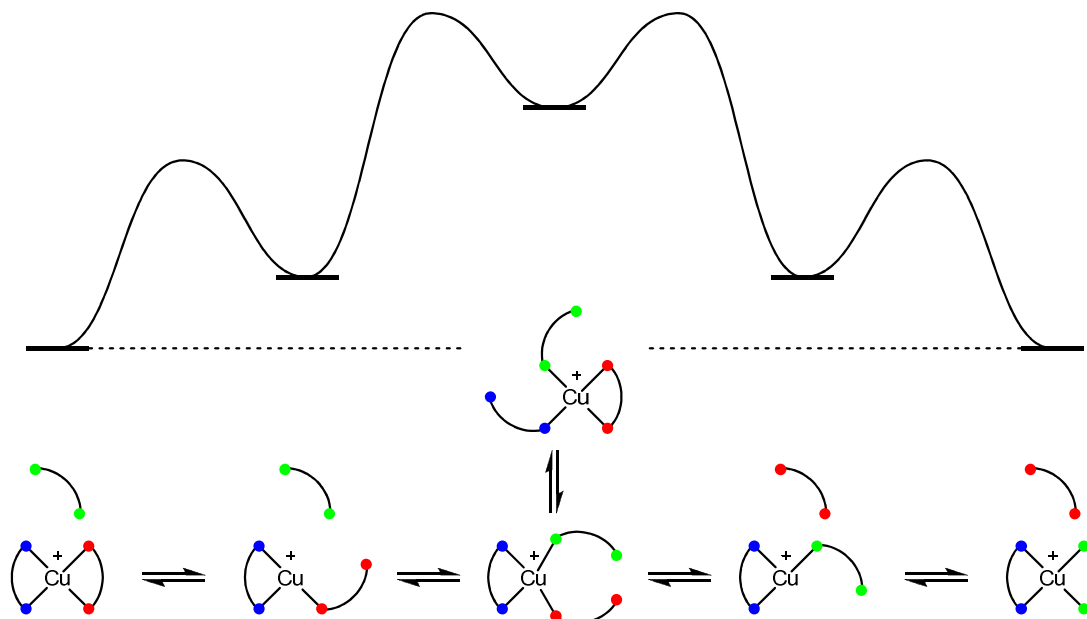
Scheme 7.5 Potential energy surface for the bidentate ligand exchange process of homochiral 2:1 bisoxazoline copper complexes.

Calculations on B3LYP/6-31G(d) level follow these trends and suggest further, that there might even be scrambling between mono- and bidentate ligands in the 3:1 ligand copper complex.[21]

It is needless to stress that a heterochiral ligand copper mixture has even more possible exchange pathways. The equilibrium of such a multi-component and also multistage exchange reaction depends on all the individual rate constants for each particular step.[22]

Therewith, the CID threshold results for cleaving one of the two bidentate ligands from the 2:1 bisoxazoline copper complexes[6,7] cannot predict the solution state reactivity. Also the initial dissociative step in the ligand exchange process which means breaking one Cu–N bond cannot be explained upon those gas-phase results because every further Cu–N bond rupture requires more energy[20] and the measurements presented in Chapter 6 display always the sum of two Cu–N binding energies when cleaving one bidentate bisoxazoline ligand.[6,7]

Another logical consequence from the discrepancy between gas-phase and solution chemistry is the fact, that the literature known mechanisms for a catalytic cycle with copper bisoxazoline complexes are wrong or at least imprecise: The postulation of a 14-electron species as "the active catalyst" simplifies the didactic model and allows to explain certain observations like smaller overall rate constants in the presence of either excess chiral ligand or excess styrene, but does not resemble the true mechanistic behavior.

7.3   References

[1]   Evans, D. A.; Woerpel, K. A.; Hinman, M. M.; Faul, M. M.; *J. Am. Chem. Soc.* **1991**, *113*, 726–728

[2]   Fraile, J. M.; Garcia, J. I.; Martinez-Merino, V.; Mayoral, J. A.; Salvatella, L.; *J. Am. Chem. Soc.* **2001**, *123*, 7616–7625

[3]   Salomon, G. R.; Kochi, J. K.; *J. Am. Chem. Soc.* **1973**, *95*, 3300–3310

[4]   Diaz-Requejo, M. M.; Belderrain, T. R.; Nicasio, M. C.; Prieto, F.; Perez, P. J.; *Organometallics* **1999**, *18*, 2601–2609

[5]   Ricardo, C.; Pintauer, T.; *Journal of Organometallic Chemistry* **2007**, *692*, 5165–5172

[6]   Zocher, E.; Dietiker, R.; Chen, P.; *J. Am. Chem. Soc.* **2007**, *129*, 2476–2481

[7]   Zocher, E.; Sigrist, R.; Chen, P.; *Inorganic Chemistry* **2007**, *46*, 11366–11370

[8]   Guillaneux, D.; Zhao, S.-H.; Samuel, O.; Rainford, D.; Kagan, H. B.; *J. Am. Chem. Soc.* **1994**, *116*, 9430–9439

[9]   Clarke, R. J.; Shannon, I. J.; *Chem. Commun.* **2001**, 1936–1937

[10]   Kalsani, V; Schmittel, M; Listorti, A.; Accorsi, G.; Armaroli, N.; *Inorganic Chemistry* **2006**, *45*, 2061–2067

[11]   DNMR Lineshape Analysis, Version 1.1 Revision 071103, BRUKER

[12]   Pianet, I.; Vincent, J.-M.; *Inorganic Chemistry* **2004**, *43*, 2947–2953

[13]   Schmid, R.; *Monatshefte für Chemie* **2001**, *132*, 1295–1326

[14]   Popp, B. V.; Thorman, J. L.; Morales, C. M.; Landis, C. R.; Stahl, S. S.; *J. Am. Chem. Soc.* **2004**, *126*, 14832–14842

[15]   Chen, L. X.; Shaw, G. B.; Novozhilova, I.; Liu, T.; Jennings, G.; Attenkofer, K.; Meyer, G. J.; Coppens, P.; *J. Am. Chem. Soc.* **2003**, *125*, 7022–7034

[16]   Plutino, M. R.; Scolaro, L. M.; Romero, R.; Grassi, A.; *Inorganic Chemistry* **2000**, *39*, 2712–2720

[17]   Brown, A. J.; Howarth, O. W.; Moore, P.; Parr, W. J. E.; *J.C.S. Dalton* **1978**, 1776–1781

[18]   a) Sutin, N.; *Annu. Rev. Phys. Chem.* **1966**, *17*, 119–172; b) Holyer, R. H.; Hubbard, C. D.; Kettle, S. F. A.; Wilkins, R. G.; *Inorganic Chemistry* **1965**, *4*, 929

[19]   Wilkins, R. G.; *Kinetics and Mechanism of Replacement Reactions of Coordination Compounds*, *Quarterly Reviews*, 316 – 342

[20]   Rannulu, N. S.; Rodgers, M. T.; *J. Phys. Chem. A* **2007**, *111*, 3465–3479

[21]   unpublished results in cooperation with Dr. E. P. A. Couzijn

[22]   Tekkaya, A.; Özkar, S.; *Journal of Organometallic Chemistry* **1999**, *590*, 208–216

Chapter 8

Differences in Gas Phase versus Solution State Stabilities

As already mentioned in the previous Chapter 7.2, there are several important differences for the dissociation of noncovalently bound complexes in the gas phase compared to the equivalent reaction in solution.

In solution the enthalpy of the reaction can be divided between an endothermic dissociation process and an exothermic resolvation of the surfaces which were involved in the formation of the complex.

Entropically, the increase in the translational degrees of freedom favors the dissociation, but on the other hand, the disappearance of the vibrational degrees of freedom associated with the intermolecular bonds in the complex is entropically unfavorable.[1]

The exact extent of enthalpic and entropic contributions to the Gibbs free energy for dissociation in solution is of course completely dependent on the studied acceptor ligand system.

In the gas phase a very different situation prevails. Any dissociation without charge separation is endothermic and the electrostatic interactions between acceptor and ligand are far more pronounced.[2] Considering for example the attractive potential between a charged (= metal) and a fixed dipolar (= ligand) species then the inverse dependence on the scaled dielectric constant $\varepsilon\varepsilon_0$ is conspicuous. (Equation 8.1: Q = charge, μ = dipole, r = distance, θ = angle between dipole and vector connecting the interacting particles).

$$V_e(r) = -\frac{Q\mu\cos\theta}{4\pi\varepsilon\varepsilon_0 r^2} \tag{8.1}$$

With $\varepsilon_0 = 1$ being the dielectric constant of vacuum and $\varepsilon(CH_2Cl_2) = 9.08$ the respective scaling factor of dichloromethane the decrease of electrostatic attraction in condensed media can be demonstrated impressively on a representative example. All the other various interaction energies based on charges, dipoles and polarizability diminish in a similar way when going from gas phase to solution state.[2]

Nevertheless electrostatic and hydrogen bonding interactions are at least structural properties of noncovalent complexes that exist in both media, only with somewhat different magnitudes.[3]

A notable exception are hydrophobic interactions, though, which arise commonly between two hydrophobic binding partners in water. Conversely in the absence of such polar solvents *e.g.* in vacuum these attractions are not preserved.[4]

As a consequence thereof it is a very interesting question how nonbonded interactions like π–π stacking effects might be influenced by the respective media.

(So far a π–π stacking interaction was detected for the $(S,S\text{-}\mathbf{2a})_2Cu^+$ homochiral complex in gas phase.)

For the extensively studied benzene dimer as the smallest representative model system it is known that the binding is primarily due to London dispersion forces, which arise from favorable instantaneous multipole / induced multipole charge fluctuations.[5]

The original London equation which is based on quantum mechanics and second order perturbation theory for describing the Coulomb interaction between the electrons and the nuclei of the two nonpolar molecules is given in equation 8.2.[2,6]

$$V_{London}(r) = -\frac{3}{2}\frac{\alpha_1\alpha_2}{(4\pi\varepsilon\varepsilon_0)^2 r^6}\frac{I_1 I_2}{I_1 + I_2} \tag{8.2}$$

α_1 and α_2 are the polarizabilities of the two molecules, I is their first ionization potential and r is the intermolecular distance. Although this equation does not formally display the more modern explanation for the benzene attraction due to instantaneous dipole fluctuations it has a descriptive quality. Besides the $1/(\varepsilon\varepsilon_0)^2$ term, causing a decreased dispersion energy in the presence of any medium,

remarkable is also the r^{-6} proportion which all van der Waals energies have in common.

However according to recent literature[7] about the benzene dimer it is common practice to calculate the electron correlation interaction energy E_{corr}, whose major part is dispersion energy, via a different protocol than manually applying equation 8.2. The accepted method is to equal E_{corr} with the difference between the exact non-relativistic energy of the studied system E_{exact} and the Hartree-Fock energy at the complete basis set limit, E_{HF}. (See equation 8.3)

$$E_{corr} = E_{exact} - E_{HF} \qquad (8.3)$$

To assign E_{exact} most accurately CCSD(T) interaction energies at the basis set limit are the most precise option. These energies are usually approximated from "less expensive" MP2 calculations with a large basis set near saturation and a correction term ΔCCSD(T) (see equation 8.4) so that

$$E_{exact} \approx E_{CCSD(T)(limit)} = E_{MP2} + \Delta CCSD(T) . \qquad (8.4)$$

The fortuous weak basis set dependence of ΔCCSD(T) allows to calculate this correction term from coupled cluster and MP2 calculations at rather small basis sets.

The total binding energy for *e.g.* a benzene dimer is then defined as the sum of the electron correlation energy E_{corr}, the electrostatic (E_{es}) and the repulsive ($E_{rep} = E_{HF} - E_{es}$) energy contributions.

A glance at Table 8.1[7] shows indeed, that the thus obtained dispersion interaction is the major source of attraction in the benzene dimer. The sign and magnitude of the electrostatic energy E_{es} can be explained when considering the benzene molecule as sort of an electronic quadrupole with the p-π electron clouds on top and below and the electropositive hydrogens in the middle. The electronic benzene–benzene interaction is thus repulsive when the two quadrupoles have a linear orientation (stacked dimer) while it is attractive when they are perpendicular aligned to each other (T-shaped benzene dimer).

Since both long range interactions, the electronic and also the dispersion part, are highly orientation dependent, they cause the directionality of the benzene dimer interaction. (See Table 8.1).

Table 8.1   Electrostatic and Dispersion Energies of the Benzene Dimers in Gas-
Phase

Energy	Parallel	T-shaped	Parallel displaced
E_{total}	−1.48	−2.46	−2.48
E_{es}	1.24	−0.55	0.90
E_{rep}	3.02	1.57	2.76
E_{corr}	−5.74	−3.48	−6.14

Energies in kcal/mol are taken from Reference 7. The center – center distance for the parallel stacked benzene dimer is 3.8 Å, for the T-shaped analogue it is 5 Å and the parallel displaced version studied here has a vertical distance of 3.5 Å and a horizontal displacement of 1.8 Å.

It has to be stated, that all the cited CCSD(T) and MP2 calculations are only feasable for such a small system like the benzene dimer, whereas the bisoxazoline copper complexes[8,9] presented in this thesis are clearly too big since MP2 scales roughly with N^5 and coupled cluster calculations even with N^7.

As a consequence thereof the benzene dimer shall be used to explain some general trends in gas phase and in solution which presumably affect the phenyl-substituted bisoxazoline copper complexes in a similar way.

Whereas the previous subsection is focusing on the interaction energy of a benzene dimer in gas phase the influence of solvent will be discussed below.

A first pioneering work addressing this topic is reported by Jørgensen and Severance,[10] who investigated an orientationally averaged benzene homodimer in water. From their Monte Carlo (MC) potential mean force (PMF) simulation these authors discovered two distinct potential energy minima with a depth of 4–5 kJ at 5.4 and 7.8 Å separated by a barrier of 2 kJ/mol.

However at separations near 4 Å where only face to face stacking is possible the net interaction in solution was found to be repulsive by ca. 1 kcal/mol. In contrast the gas-phase interaction energies indicate an attraction of approximately 2 kcal/mol for a stacked or parallel displaced benzene dimer with center–center distances of 3.8 and 4.5 Å respectively.[10]

This initial study was subsequently corroborated by classical molecular dynamics (MD) PMF simulations of Linse,[11] who showed for the same system but with a more sophisticated potential energy function, that in solution the T-shaped dimer is thermodynamically preferred over the stacked analogue.

The reason for this are both, favourable benzene–benzene and benzene–water interactions, since the T-shaped motive exposes a remarkably larger area towards the solvent than the stacked dimer.

In contrast, the sandwich structure suffers not only due to the repulsive electrostatic energy but also due to reduced exothermic interactions between the π-electrons of the benzene rings and the water molecules.

Those disadvantages can even not be compensated by the hydrophobic effect, which is more dominant for the parallel benzene dimer.

Further, for both forms, the T-shaped and the stacked version Linse[11] determined the relative interaction energies for each possibility, a close contact and a solvent separated geometry (Figure 8.1).
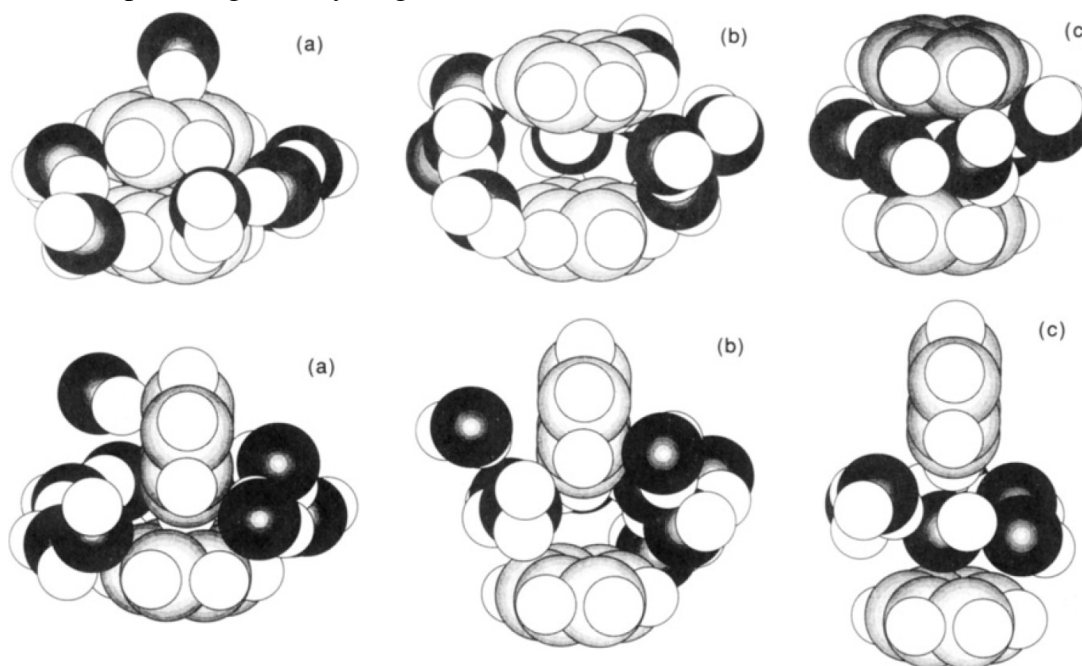
Figure 8.1 Top row: the solvated stacked benzene dimer at intermolecular separations of 3.5, 5.3 and 7.1 Å. Bottom row: the analogue outcome for the T-shaped benzene dimer at center–center distances of 4.7, 6.5 and 8.3 Å. For each case only the 6–10 closest water molecules are displayed.[11]

The T-shaped dimer was found to be most stable at a center – center distance of 4.7 Å whereas the solvent separated equivalent at 8.3 Å is disfavored. Contrarily for the stacked dimer the solvent separated minimum at 7.1 Å is more advantageous than the close contact version at 3.5 Å.

This agrees well with Jørgenson's double minimum for the rotationally averaged benzene dimer:[10] The first minimum is likely to be dominated by the close contact T-shaped dimers, whereas the latter one could be constituted of solvent separated stacked dimers.

Considering again, that the attractive interaction for a benzene dimer mainly originates from dispersion interactions which scale reciprocal with $(\varepsilon\varepsilon_0)^2$ and possess a r^{-6} dependence,[2,6] explains why the free energy for a solvent separated stacked benzene dimer is solely −0.43 kcal/mol whereas for the solvated close contact T-shaped analogue at least −1.94 kcal/mol are reported.[12]

Thus, the respective gas-phase interaction energies of −1.48 and −2.46 kcal/mol are remarkably diminished in water or other solvents with large dielectric constants.[7]

Interestingly no stable parallel displaced structure is reported for a solvated benzene dimer.[11,12] The corresponding intersolute separation is at close contact even slightly smaller than for true sandwich motives, which have already been named to be unfavourable, especially when not solvent separated. On the other hand hydrophobic effects favour the parallel over the parallel displaced dimer structure, which is probably too disadvantageous to be observed in solution[12] although a large attractive gas-phase binding energy of −2.48 kcal/mol (see Table 8.1) has been determined for it.[7]

Consequently solvent competition and entropic effects associated with thermal configurational averaging considerably damp out the optimal gas-phase interaction energies.[10] This can even lead to the practical abandonment of some geometries in solution which are very favourable in gas phase, though.[12]

These examinations of the π–π stacking within a simple benzene dimer already shed light on some peculiar literature known observations, which can certainly be enriched with the specifity of stacking interactions in solution. As an example therefore the interesting solid state and solution chemical behaviour of 2,9-diphenyl-

1,10-phenantroline (= dpp) ligands complexed by copper(I) shall be introduced here.[13]

Crystal structures of the literature known 2:1 homochiral complex display a stacked interaction at a vertical separation of 3.4 Å between always one phenyl-group of one ligand and the other phenantroline-backbone. However, in solution a ^{1}H-NMR spectrum at room temperature shows four equivalent phenyl-substituents. This result indicates that the molecule is fluxional in solution. According to the solid state structure the molecular motion is assigned to a rocking between two enantiomeric C_2-symmetric structures via an intermediate of C_s symmetry (when neglecting the phenyl-substituents). Thus in solution this molecule is assumed to oscillate between the two structures where at best either the first two or the other two phenyl-groups are involved in a π–π stacking interaction.[13]

A very similar behaviour is examined for the homochiral $(S,S$-$\mathbf{2a})_2Cu^+$ complex, which has shown a higher threshold energy than its heterochiral analogue[8] (Chapter 6). This was attributed to stabilizing nonbonded interactions in the gas phase, namely one parallel displaced π–π stacking and two CH–π interactions between the hydrogens of the bridging carbon and always one phenyl-group of each ligand.

However, already when calculating the low level B3LYP/LANL2DZ geometry for $(S,S$-$\mathbf{2a})_2Cu^+$ with the PCM model of Gaussian03 for CH_2Cl_2 the minimum energy structure displays no more stacking interactions. The formerly parallel displaced phenyl-groups are more separated, so that the hydrogens of one phenyl-ring do not any longer point towards the electron cloud of the other one. Additionally, the shielding of always one bridge proton by a phenyl-group of the other ligand is also absent (Figure 8.2).
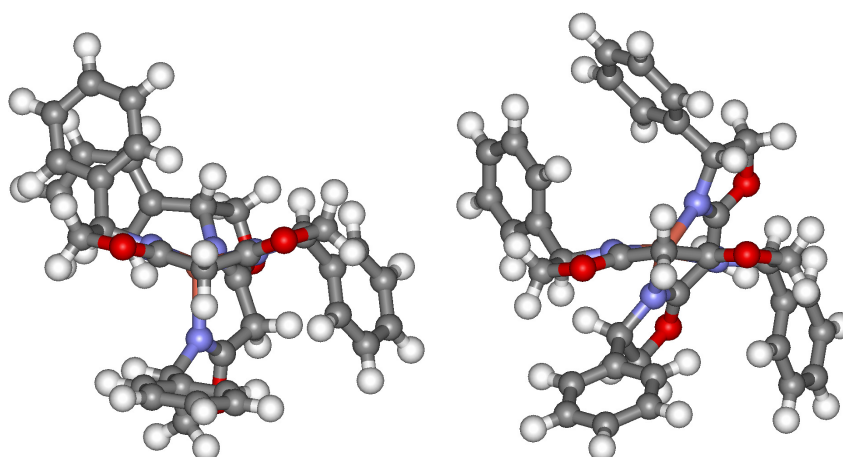
Figure 8.2 B3LYP/LANL2DZ optimized geometries for $(S,S\text{-}\mathbf{2a})_2Cu^+$. Left side: gas phase; right side: optimization with the PCM model for CH_2Cl_2

Of course the energies of these low level calculations which are nevertheless the standard fashion for computing large organometallic complexes are known to be quite wrong, but the geometries are assumed to be reasonable.[14]

Thus these structures allow an interesting conclusion concerning the expected NMR-shifts of a $(S,S\text{-}\mathbf{2a})_2Cu^+$ complex. If nonbonded interactions like in the left-hand structure (Figure 8.2) also dominate the geometry in solution, then two separate signals for the bridging CH_2-group should be observable. Especially the bridge-proton directly pointing to a phenyl-group should be shielded considerably and appear at lower ppm-values. A similar behaviour is found for $(S,S\text{-}\mathbf{2a})(R,R\text{-}\mathbf{2a})Cu^+$ or respective heterochiral Zn^{2+} complexes,[15] where the proton vicinal to a phenyl-substituent is shielded by a phenyl-group of the other ligand.

However, when comparing the NMR spectra of $(S,S\text{-}\mathbf{2a})_2Cu^+$ in CD_2Cl_2 at $-89°C$ only one CH_2-bridge-signal for the 2:1 complex at 2.4 ppm and one signal at 3.5 ppm for the free ligand is observed (Figure 8.3). All the higher resonances belong to the oxazoline unit and are not resolved for the copper bound and the free ligand.
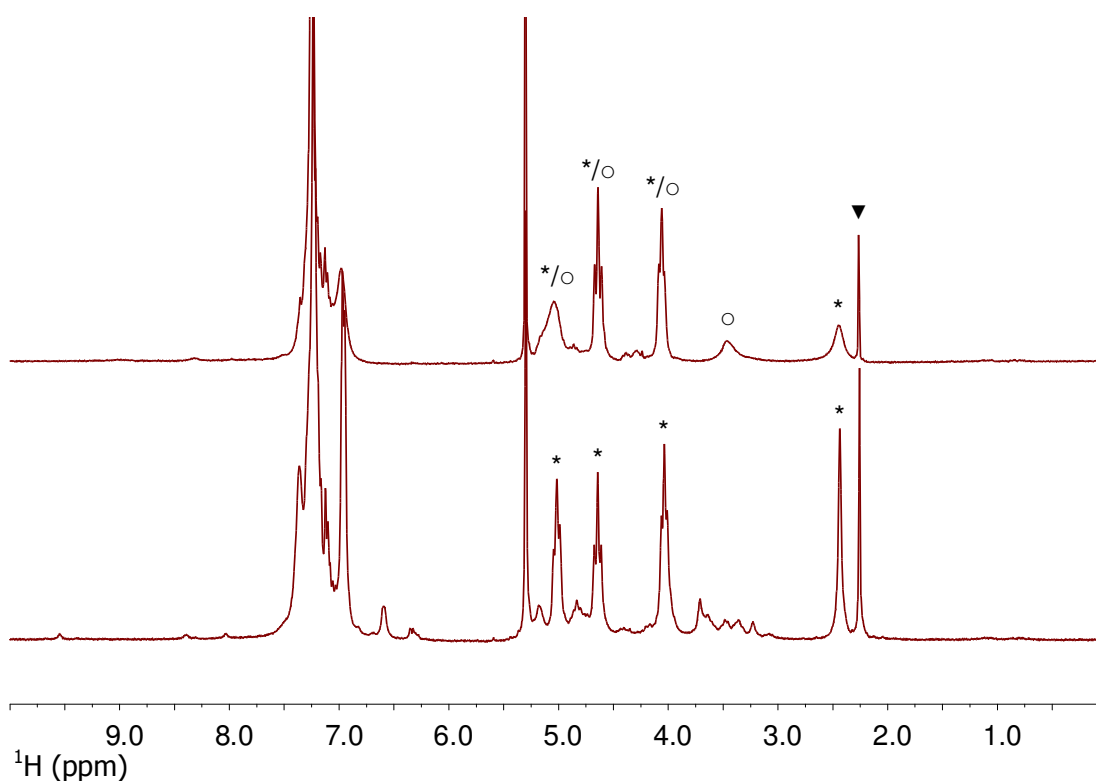
Figure 8.3 ^{1}H-NMR spectra of (*S,S*-**2a**)$_2$Cu$^+$ (∗) and variable amounts of free ligand (○) at −89°C in CD$_2$Cl$_2$. Top: excess of *S,S*-**2a**; bottom: exact 2:1 stochiometry of *S,S*-**2a** and CuOTf. The singlet at 2.36 ppm belongs to toluene (▼). For an assignment of the other resonances see the text.

The condition of having an exact 2:1 ligand to copper stochiometry is supposed to retard the ligand exchange process between the 2:1 complex and free ligand as much as possible (see Chapter 7). Only with these high copper amounts also various low valent copper species appear as small signals in the base line.

Anyways, both spectra display only one singulet for the bridging CH$_2$-group.

The only conclusion to be drawn from this observation is either that the (*S,S*-**2a**)$_2$Cu$^+$ complex is very fluxional in solution and even at −89°C the rocking between the two enantiomeric π–π stacking structures is still very fast, or that such a parallel displaced aromatic interaction at a calculated center–center distance of 4.5 Å (3.34 Å vertical and 3.00 Å horizontal displacement) is unfavourable in solution.[12] A rearrangement of the parallel displaced phenyl-groups prevents automatically the CH–π interaction between the bridge-protons and the other two phenyl-substituents. Calculations including solvation support the second hypothesis.

Consequently these experimental data indicate strongly, that the geometry of the $(S,S\text{-}\mathbf{2a})_2Cu^+$ complex deviates (at least time averaged) seriously from the optimal gas-phase geometry. Ideally pronounced non-bonded interactions are therefore only possible in the gas-phase, whereas in solution the $(S,S\text{-}\mathbf{2a})_2Cu^+$ complex experiences certainly less stabilization.

Thus another reason for the discrepancy between the thermodynamic ligand binding energies from the gas-phase CID-measurements and the true solution state reactivity of 2:1 bisoxazoline copper complexes could be identified.

8.1   References

[1]   Jørgensen, T. J. D.; Delforge, D.; Remacle, J.; Bojesen, G.; Roepstorff, P.; *International Journal of Mass Spectrometry* **1999**, *188*, 63–85

[2]   Daniel, J. M.; Friess, S. D.; Rajagopalan, S.; Wendt, S.; Zenobi, R.; *International Journal of Mass Spectrometry* **2002**, *216*, 1–27

[3]   Catalina, M. I.; de Mol, N. J.; Fischer, M. J. E.; Heck, A. J. R.; *Phys. Chem. Chem. Phys.* **2004**, *6*, 2572–2579

[4]   Nesatyy, V. J.; *International Journal of Mass Spectrometry* **2002**, *221*, 147–161

[5]   Sinnokrot, M. O.; Valeev, E. F.; Sherrill, C. D.; *J. Am. Chem. Soc.* **2002**, *124*, 10887–10893

[6]   Israelachvili, J. N.; *Intermolecular and Surface Forces*, Academic Press, London **1991**

[7]   Tsuzuki, S.; Honda, K.; Uchimaru, T.; Mikami, M.; Tanabe, K.; *J. Am. Chem. Soc.* **2002**, *124*, 104–112

[8]   Zocher, E.; Dietiker, R.; Chen, P.; *J. Am. Chem. Soc.* **2007**, *129*, 2476–2481

[9]   Zocher, E.; Sigrist, R.; Chen, P.; *Inorganic Chemistry* **2007**, *46*, 11366–11370

[10]   Jørgensen, W. L.; Severance, D. L.; *J. Am. Chem. Soc.* **1990**, *112*, 4768–4774

[11]   Linse, P.; *J. Am. Chem. Soc.* **1992**, *114*, 4366–4373

[12]   Chipot, C.; Jaffe, R.; Maigret, B.; Pearlman, D. A.; Kollman, P. A.; *J. Am. Chem. Soc.* **1996**, *118*, 11217–11224

[13]   Miller, M. T.; Gantzel, P. K.; Karpishin, T. B; *Inorganic Chemistry* **1998**, *37*, 2285–2290

[14]   Bühl, M.; Kabrede, H.; *J. Chem. Theory Comput.* **2006**, *2*, 1282

[15]   Takacs, J. M.; Hrvatin, P. M.; Atkins, J. M.; Reddy, D. S.; Clark, J. L.; *New J. Chem.* **2005**, *29*, 263–265

Chapter 9

Conclusion

In this thesis the absolute binding energies of various (aza-)bisoxazoline ligands to their respective 1:1 copper ligand fragments have been determined. Therefrom detailed insights in the sterical and electronical properties of phenyl- versus isopropyl substituents at the rather different ligand backbones of bisoxazoline (**1**, **2**) and aza-bisoxazoline ligands (**3**, **4**) could be gained.

However, when comparing these threshold energies with the solution state behaviour of the respective homo- and heterochiral 2:1 complexes a nonexpected equilibrium formation as well as catalytic reactivity was found. Obviously the kinetic lability of the 2:1 ligand copper complexes differs remarkably from their thermodynamic stability. Thus, it does not matter how exothermic the formation of the 2:1 reservoir species from the 1:1 complex and free ligand is, since the ligand exchange mechanism does not proceed via this high energetic 14-electron species.

Instead a multistep ligand exchange mechanism could be identified, which requires an initial Cu–N bond rupture with subsequent association of a free ligand to the three coordinate copper species in the rate limiting step. Considering that at this point even scrambling between mono- and bidentate ligands is possible, explains why for heterochiral ligand copper mixtures several parallel exchange pathways are possible.

These determine in their entity the equilibrium concentrations of the different species. Further, it has to be stated that the initial step in this ligand exchange mechanism, the single Cu–N bond rupture, cannot be compared with the CID-threshold results for cleaving one bidentate ligand and therewith two Cu–N bonds at

a time. Consequently the gas-phase results have no predictive ability for the solution state reactivity of the diastereomeric 2:1 ligand copper complexes.

This clearly proves the in the literature commonly accepted mechanism[1] to be wrong: A 14-electron species neither serves as intermediate for the ligand exchange process nor as "the active catalyst" during *e.g.* a cyclopropanation reaction. Further from computational studies there is evidence that also the formation of the carbene proceeds over a styrene bound 1:1 complex which coordinates EDA and then expels the olefin to form the carbene via final nitrogen extrusion.[2] Of course the stepwise ligand exchange can presumably also be enriched with such additional pathways when adding styrene to the preequilibrium mixture.

However, the energetic preference of three- over two coordinate copper precursors for the subsequent associative step is not the only difference between the gas-phase and solution chemistry properties of copper bisoxazoline complexes. The nonbonded interactions stabilizing the homochiral $(S,S$-$\mathbf{2a})_2$Cu$^+$ complex are only pronounced in gas phase, whereas in solution the complex is presumably very fluxional and oscillates between a variety of different geometries.

As an additional point also the possibility for an enthalpy/entropy compensation in condensed phase shall be named, whereas in gas phase every bond dissociation is endothermic.[3] The latter aspect always favours bidentate over monodentate ligation in solution even if the respective metal-ligand bonds possess very similar gas phase binding energies.[4]

Otherwise monodentate ligand complexes have certainly a higher chance to give concurring gas-phase and solution chemistry results since only simple dissociative or S_N2 type reactions are conceivable. The latter possibility which would again abolish the desired mechanistic agreement can certainly be suppressed with the choice of bulky substituents. Consequently a proper choice of the system to study has to consider all these criteria.

Although in this thesis the kinetic lability and the thermodynamic stability of the examined systems is not comparable and thus also nonlinear effects in catalytic reactions cannot be predicted, the underlying mechanistic model could be refined.

Additionally, the experimental absolute ligand copper binding energies are, especially when nonbonded interactions like π–π stacking effects come into play,

very interesting benchmark values for probing different computational levels and new promising functionals.[5,6]

Apart from the convenience to compare the calculated and measured gas phase binding energies directly, the unique possibility is given to examine the binding mechanism without disturbing solvation effects. Thus, the various superimposed influences can even be distinguished and addressed separately, which certainly leads to a deeper mechanistic understanding of the catalytic process in condensed phase.

9.1   References

[1]   Diaz-Requejo, M. M.; Belderrain, T. R.; Nicasio, M. C.; Prieto, F.; Pérez, P. J.; *Organometallics* **1999**, *18*, 2601–2609

[2]   Fraile, J. M.; Garcia, J. I.; Martinez-Merino, V.; Mayoral, J. A.; Salvatella, L.; *J. Am. Chem. Soc.* **2001**, *123*, 7616–7625

[3]   Jørgensen, T. J. D.; Delforge, D.; Remacle, J.; Bojesen, G.; Roepstorff, P.; *International Journal of Mass Spectrometry* **1999**, *188*, 63–85

[4]   Rannulu, N. S.; Rodgers, M. T.; *J. Phys. Chem. A* **2007**, *111*, 3465–3479

[5]   Zhao, Y.; Truhlar, D. G.; *Organic Letters* **2007**, *9*, 1967–1970

[6]   Rokob, T. A.; Hamza, A.; Pápai, I.; *Organic Letters* **2007**, *9*, 4279–4282

Part IV

Appendix

Chapter 10

Experimental Section

10.1 Synthesis

10.1.1 Preparation of Ligand 3c

Bis[4,5-dihydro-(4R)-(1-methylethyl)-1,3-oxazol-2-yl]-ethylamine (*R,R*-**3c**):

Bis[4,5-dihydro-(4R)-(1-methylethyl)-1,3-oxazol-2-yl]-amine, *R,R*-**3a**, (239 mg, 1.00 mmol) was dissolved in absolute tetrahydrofurane (10 ml) and then treated with *n*-butyllithium (1.10 mmol, 690 µL of a 1.6 N solution in hexane) at –78 °C. After 20 minutes ethyl iodide (780 mg, 5 mmol, 405 µL) was added. The reaction mixture was allowed to warm up to room temperature and stirred for 24 h before the solvent was removed. The resulting residue was dissolved in CH_2Cl_2 and washed with sat. Na_2CO_3 (10 ml). The aqueous phase was further extracted with CH_2Cl_2 (3 x 10 mL), the combined organic phases then dried with $MgSO_4$ and the solvent evaporated under reduced pressure to yield *R,R*-**3c** as a pale yellow oil. Yield: 256 mmol (96%).

^{1}H-NMR (CDCl$_3$, 300 MHz): δ 4.31 (t, *J* = 9 Hz, 2H, (C*H$_2$*-CH)), 4.07 (t, *J* = 7.4 Hz, 2H, (C*H$_2$*-CH)), 3.78 – 3.88 (m, 2H, (CH$_2$-C*H*)), 3.78 – 3.88 (m, 2H, (C*H$_2$*-CH$_3$)), 1.63 – 1.79 (m, 2H, (C*H*(CH$_3$)$_2$)), 1.20 (t, *J* = 7.2 Hz, 3H, (CH$_2$-C*H$_3$*)), 0.89 (d, *J* = 6.9 Hz , 6H, (CH(C*H$_3$*)$_2$)), 0.81 (d, *J* = 6.9 Hz, 6H, (CH(C*H$_3$*)$_2$))

^{13}C-NMR: δ 156.8 (C$_{quart}$-O), 71.0 (*C*H$_2$-CH), 69.7 (*C*H$_2$-CH), 45.3 (*C*H$_2$N), 32.9 (*C*H(CH$_3$)$_2$), 18.8 (CH(*C*H$_3$)$_2$), 17.7 (CH(*C*H$_3$)$_2$), 13.3 (CH$_2$-*C*H$_3$)

10.1.2 Synthesis of Ligand 4c

(4*R*)-Bis[4,5-dihydro-(4-phenyl)-1,3-oxazol-2-yl]-ethylamine (*R,R*-**4c**):

(4*R*)-Bis[4,5-dihydro-(4-phenyl)-1,3-oxazol-2-yl]-amine, *R,R*-**4a**, (307 mg, being equivalent to 1.00 mmol) was dissolved in absolute tetrahydrofurane (10 ml) and then treated with *n*-butyllithium (1.10 mmol, 690 μL of a 1.6 N solution in hexane) at –78 °C. After 20 minutes ethyl iodide (780 mg, 5 mmol, 405 μL) was added. The reaction mixture was allowed to warm up to room temperature and stirred for 24 h before the solvent was removed. The resulting residue was dissolved in CH_2Cl_2 and washed with sat. NaCl solution (10 ml). The aqueous phase was further extracted with CH_2Cl_2 (3 x 10 mL), the combined organic phases then dried with $MgSO_4$ and the solvent evaporated under reduced pressure to yield *R,R*-**4c** as a pale yellow oil. Yield: 325 mg (97%).

^{1}H-NMR (CDCl$_3$, 300 MHz): δ 7.36-7.26 (m, 10H, Aryl-*H*), 5.28 (dd, *J* = 9.6, 7.8 Hz, 2H, (C*H*$_2$-CH)), 4.80 (dd, *J* = 9.6, 8.1 Hz, 2H, (C*H*$_2$-CH)), 4.25 (dd, *J* = 8.1, 7.8 Hz, 2H, (CH$_2$-C*H*)), 4.06 (q, *J* = 7.2 Hz, 2H, (NC*H*$_2$-CH$_3$)), 1.37 (t, *J* = 7.2 Hz, 3H, (NCH$_2$-C*H*$_3$)).

^{13}C-NMR: δ 158.2, 142.6, 128.6, 127.5, 126.5, 76.1, 67.6, 45.7, 13.6.

10.2 General Aspects concerning the Mass Spectrometric Analysis

10.2.1 Preparation of the Spraying Solutions

Typical procedure:

The solutions are prepared in a glove-box in the following manner:

25 μmol of the enantiopure chiral ligands **Xa** and **Xb** each are dissolved in 2.5 mL of dry CH_2Cl_2. A third stock solution is prepared by dilution of 2 mg (5.4 μmol) of tetrakis(acetonitrile)copper(I)hexafluorophosphate as a copper(I) source in 2.5 mL of dry CH_2Cl_2.

Formation of a heterochiral 2:1 ligand copper complex:

50 μL of the **Xa**-, 50 μL of the **Xb** ligand solution (0.5 μmol each) and 50 μL of the Cu(I) stock solution (0.12 μmol) were combined and stirred for approximately 15 minutes at room temperature.

Formation of a homochiral 2:1 ligand copper complex:

100 μL (1 μmol) of one of the enantiomeric pure stock solutions (**Xa** or **Xb**) was mixed with 50 μL of the copper(I) stock solution (0.12 μmol) and stirred for 15 minutes at room temperature.

For ESI-MS detection of these copper ligand solutions 10 μL of the copper ligand stock solution was diluted in 2.5 mL dry CH_2Cl_2 which gives a final concentration of $2 \cdot 10^{-9}$ mol/L per ligand-species in case of the heterochiral stock solution. The mass spectrum clearly shows signals that correspond to the 2:1 ligand copper complex, the 1:1 complex as well as to free protonated ligand.

The heterochiral solution contains apart from the expected heterochiral complex (**Xa**)(**Xb**)Cu$^+$ also the homochiral analogues according to their formation and stability in solution.

To obtain homo- and heterochiral complexes in the same solution the homochiral complex can still be formed when adding *e.g.* three times the amount of ligand **Xa** compared to ligand **Xb** and twice the amount of copper in case of an otherwise favored formation of the heterochiral complex. In this manner both complexes can undergo mass spectrometric measurements under the exact same circumstances.

Preparation of the *Pseudo*-Homochiral CuPhAzaBox Spraying Solution

7 mg (18.78 μmol) of the copper(I) salt were diluted in 2.5 ml of dry CH_2Cl_2. When mixing 40 μL of this stock solution (0.34 μmol) with 60 μL of the above described ligand stock solution *S,S*-**4a** (0.14 μmol) and 30 μL of ligand stock solution *S,S*-**4b** (0.07 μmol), formation of the *pseudo*-homochiral complex (*S,S*-**4a**)(*S,S*-**4b**)Cu$^+$ as well as the homochiral complex (*S,S*-**4b**)$_2$ was observed by mass spectrometry.

10.2.2 Representative ESI-MS Fragmentation Products
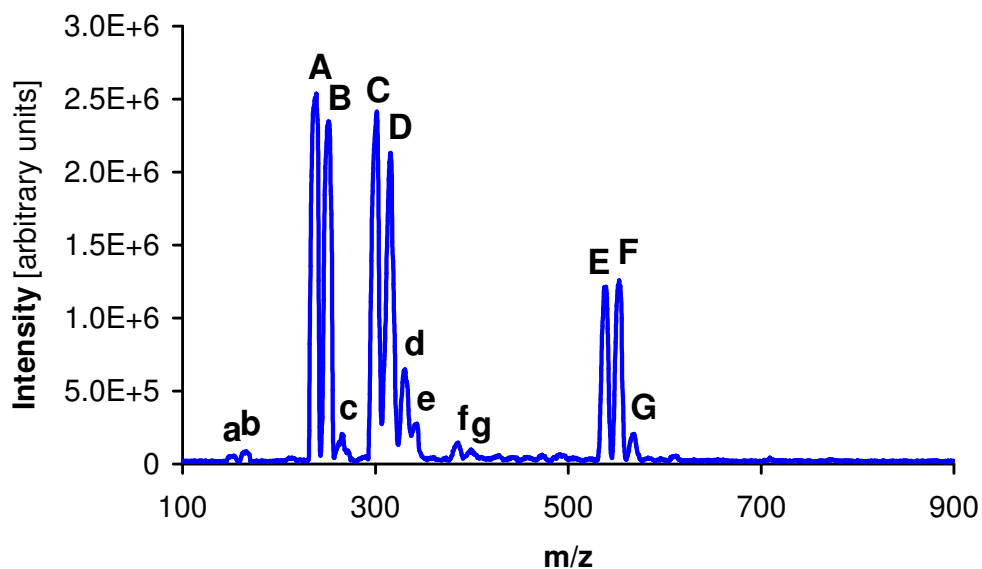
The major peaks of the spectrum are assigned to:

(S,S-**1a**)$_2$Cu$^+$ homochiral complex (**E** m/z = 539), (S,S-**1a**)(R,R-**1b**)Cu$^+$ heterochiral complex (**F**, m/z = 553), (R,R-**1b**)$_2$Cu$^+$ homochiral complex (**G**, m/z = 567), the corresponding 1:1 complexes (**C**, **D**, m/z = 301, 315) and the free ligands (**A**, **B**, m/z = 238, 252). The ^{63}Cu/^{65}Cu splitting is not resolved in the spectrum.

The minor peaks of the spectrum are assigned to:

Structure **a** (m/z = 153), **b** (m/z = 165), **c** (m/z = 266), **d** (**C** + N$_2$, m/z = 329), **e** (**D** + N$_2$, m/z = 343), **f** (**C** + 2 CH$_3$CN, m/z = 383), **g** (**D** + 2 CH$_3$CN, m/z = 397)

Structures **a** and **b** are generated from the concerning free ligand by cleaving off fragment **d** and reduction of the methyl-label. Free ligand has been discovered to be in general more labile than the copper bound species *e.g.* ligand **B** can also be oxidized during the spray process to structure **c**.
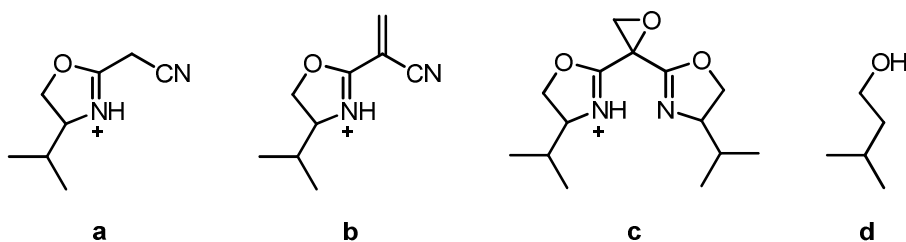
10.2.3 Multiple Channel Treatments

For the CRUNCH data workup an additional scaling factor was allowed for all the two-channel treatments.[1] As initial guess in the fitting procedure the relation of the integrated daughter peaks was used at collision offsets where the respective threshold curves are rising almost linearly. For the data processing with L-CID such an arbitrary scaling is not necessary. (See Chapter 5.4 for the theoretical background).

10.2.4 Uncertainties

Uncertainty Range of the CRUNCH Ligand Binding Energies

From replicate measurements, a statistically-based standard deviation of 0.05 eV (E_{cm}) for the E_0 value was determined. However, we observed that the standard deviation for measurements within a given day is substantially smaller with an observed upper bound of 0.026 eV (E_{cm}). Since one complete ligand set was always treated on one measurement-day, the higher accuracy is expected for the relative binding energies within one ligand class. The only exception was the (*S,S*-**4a**)(*S,S*-**4b**)Cu$^+$ system, which was studied on a different day than the rest of ligand class **4**.

Typically the standard deviation for the *n*-parameter of the CRUNCH threshold function was 0.04 for replicate measurements of the same species on different measurement days. It was always extracted using the same fitting-range per single species.

The uncertainty of the transition state model gives a contribution of 0.06–0.07 eV (E_{cm}), as is approximated according to the expression ($R \cdot \Delta E_0$)/ $\Delta \Delta S^{\ddagger}$. R is the ideal gas constant and ΔE_0 and $\Delta \Delta S^{\ddagger}$ represent the differences in the threshold energies and the entropies of activation for a loose compared to a tight transition state fitting with CRUNCH. To obtain the molecular frequencies for the tight transition state the frequency that resembles most the reaction coordinate is removed from the frequencies of the parent molecule. Within this uncertainty of the transition state is also the choice of this particular normal mode which should have the largest component of Cu–N stretching. For the studied complexes it is typically a frequency just below 200 cm^{-1},which, however, contains also minor contributions from other motions in the complex.

Furthermore, the treatment of torsions as hindered rotors in the fitting procedure made no significant difference in the extracted thermochemical results. Taking, for instance, the limit of a free adiabatic rotor for the methyl substituent in the two-channel fit for $(S,S$-$\mathbf{1a})(R,R$-$\mathbf{1b})$Cu$^+$ produces $e.g.$ for cleavage of ligand R,R-$\mathbf{1b}$ the following values: $E_0 = 2.05$ eV, $\Delta H = 46.8$ kcal/mol, and $\Delta S^{\ddagger} = 26$ eu. As may be seen when comparing with Table 6.2, Chapter 6 only an insignificant change occurs.

The uncertainty of the energy-scale is 0.15 eV (lab frame) which gives for the studied complexes 0.02–0.03 eV in center of mass scale.

Combining the uncertainties produces an estimate of the global/absolute uncertainty of 0.08–0.09 eV (E_{cm}) for the E_0 values in this study.

Uncertainties of L-CID Ligand Binding Energies

The standard deviations for the loose transition state model (Table 6.3, Chapter 6) contain the reproducibility of the data sets (usually for three different measurements) together with the uncertainty of the L-CID fitting with the genetic algorithm for each data set. Therefore the slightly different energy-values of approximately 10 fits that reproduce the experimental data acceptably well are considered. In summary, a maximum uncertainty for the measured systems of 0.05 eV (E_{cm}) was found for the two above named aspects. (In contrast, the standard deviation for the threshold energies fitted with CRUNCH-D1 solely describes the reproducibility of the measurements implying a subjective choice of the best fit.)

Despite this, for every data set the error of the energy-scale contributes 0.15 eV (laboratory frame), which gives for the studied complexes 0.02 eV in center of mass scale being identical for both data processing programs.

The next point to be considered is the uncertainty of the transition state. This value cannot be approximated similarly to the CRUNCH results, since L-CID in its current version does not compute an entropy of activation. Concerning the absolute threshold energies for a tight transition state these values are found to be systematically 0.62 eV lower in energy than the comparable ones for a loose, orbiting transition state. However, the simple bond ruptures of bisoxazoline copper complexes are presumably best described by the loose transition state model.

In summary, both, L-CID and CRUNCH threshold energies can be characterized having an overall uncertainty of approximately 0.1 eV in center of mass frame.

10.3 Gas-Phase Results processed with CRUNCH

10.3.1 CID Threshold Results for the Phenyl-Box-Ligands

Mass scan of the $(R,R\text{-}\mathbf{2a})_2Cu^+$ solution: the homochiral complex (675) as well as the 1:1 complex (369) and free ligand (306) are visible.
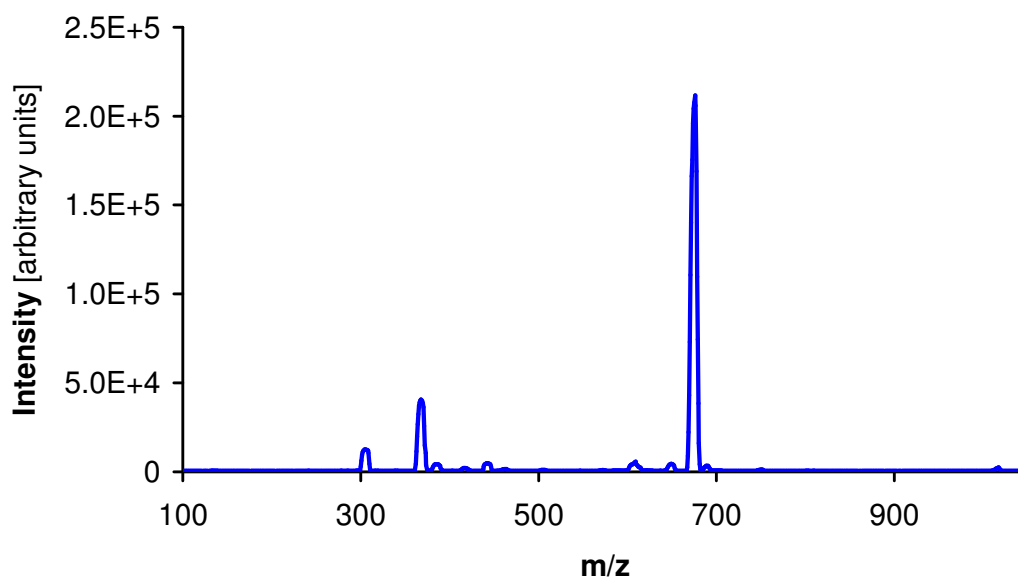
CID measurement of the homochiral complex $(R,R\text{-}\mathbf{2a})_2Cu^+$ (675 → 369) at 107 µtorr. The half-width of the kinetic energy distribution without collision gas is 2.1385 eV, the variation is 0.90856.
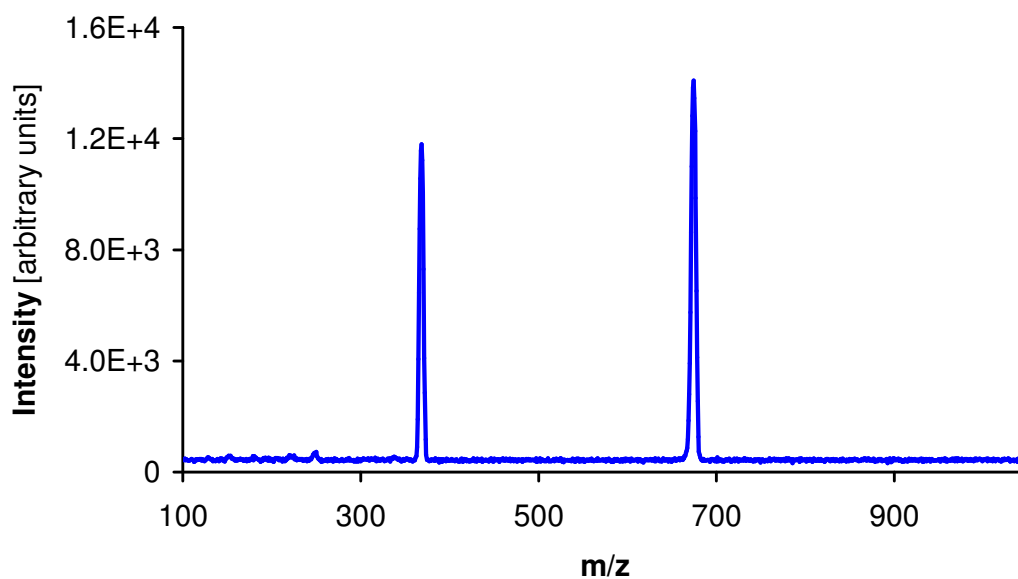
Extrapolation to zero pressure (green line) for the homochiral complex $(R,R\text{-}\textbf{2a})_2Cu^+$ with loss of $R,R\text{-}\textbf{2a}$ (675 → 369): black squares: 50.85 μtorr, blue squares: 71.40 μtorr, red squares: 91.23 μtorr. Scan range of the instrument offset was from −100 to 10 V.
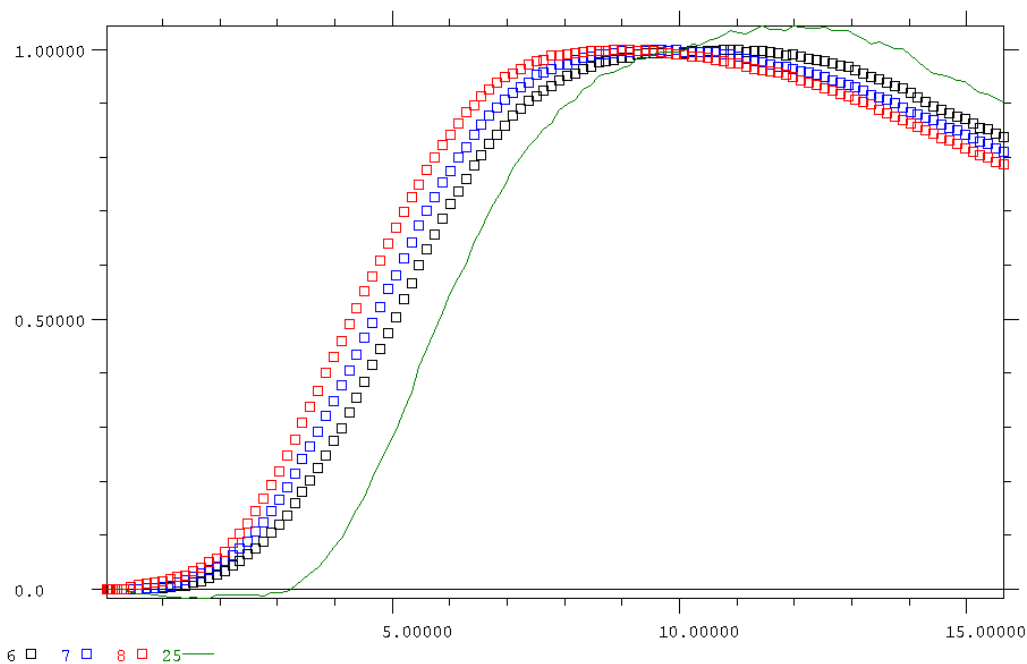
Fitted zero-pressure-extrapolation curve of the homochiral complex $(R,R\text{-}\textbf{2a})_2Cu^+$ with loss of $R,R\text{-}\textbf{2a}$:
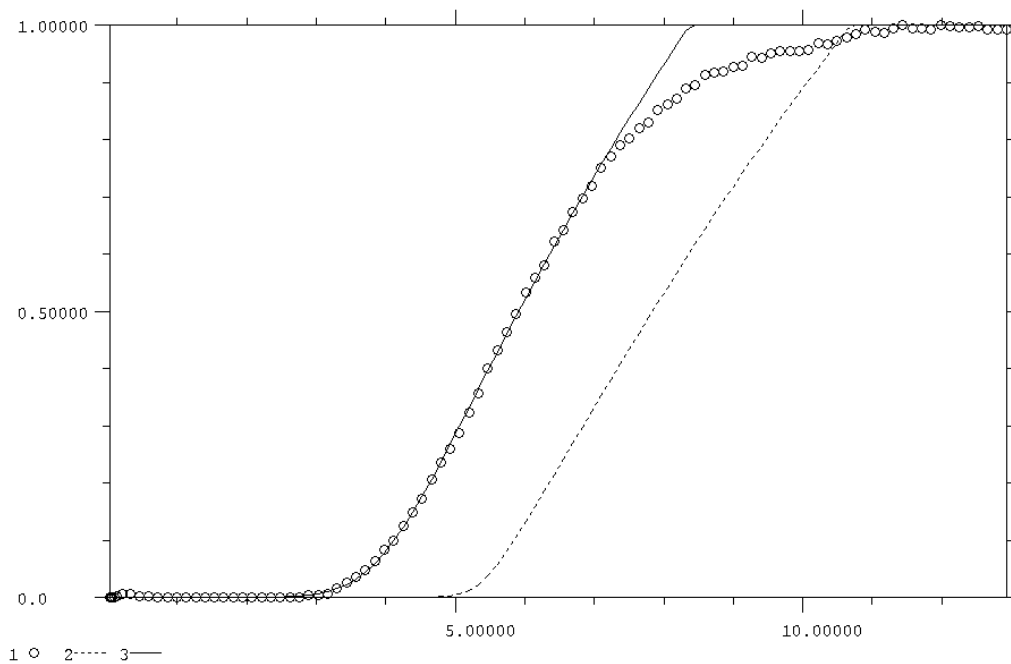
Mass scan of the (*R,R*-**2a**)(*S,S*-**2b**)Cu$^+$ solution: the heterochiral complex (689), the homochiral complexes (675, 703), the 1:1 complexes (369, 383) and the free ligands (306, 320) are visible.
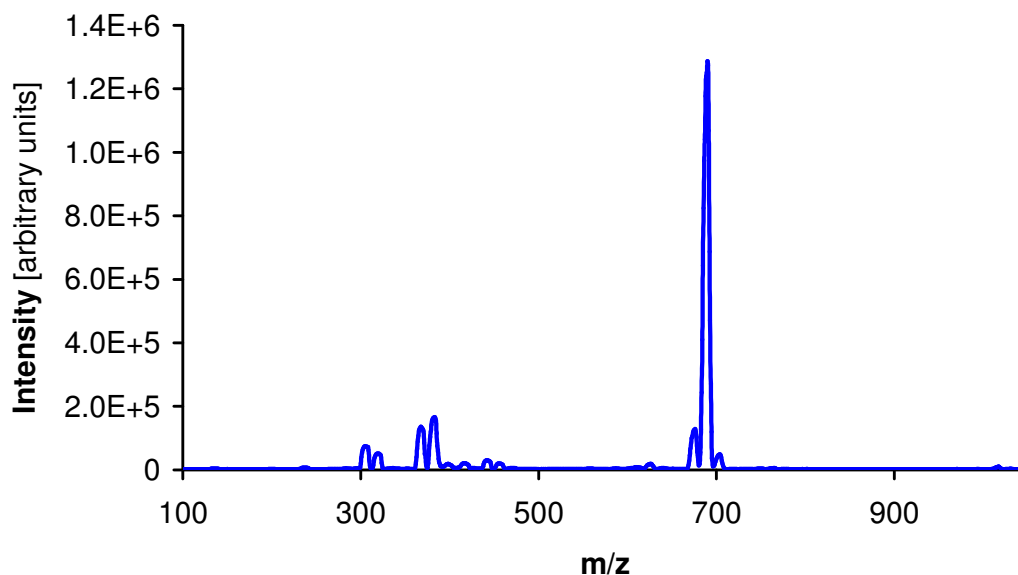
CID measurement of the heterochiral complex (*R,R*-**2a**)(*S,S*-**2b**)Cu$^+$ with loss of *S,S*-**2b** or *R,R*-**2a** (689 → 369 and 689 → 383) at 128 μtorr. The half-width of the kinetic energy distribution without collision gas is 2.2146 eV, the variation is 0.86318.
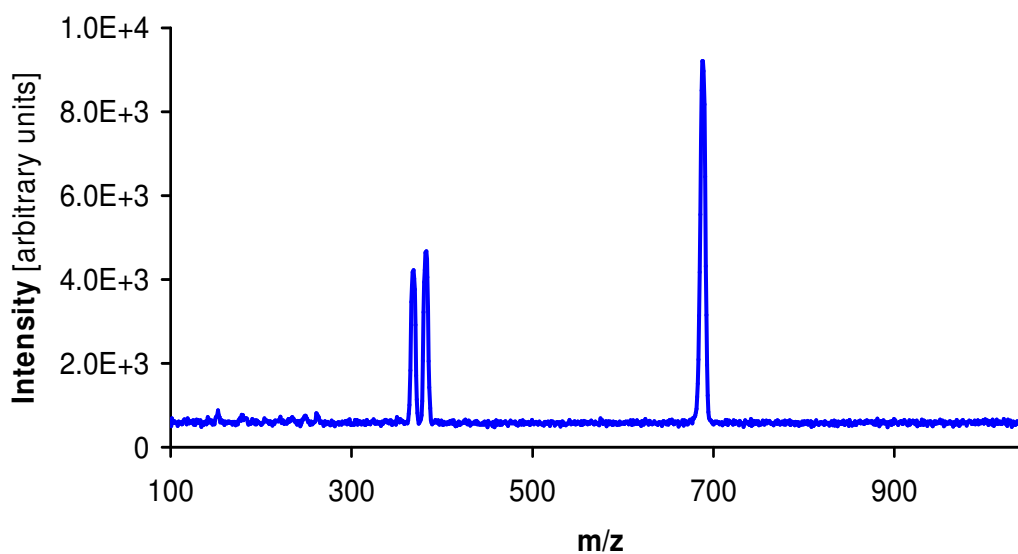
Extrapolation to zero pressure (green line) for the heterochiral complex (*R*,*R*-**2a**)(*S*,*S*-**2b**)Cu⁺ with loss of *S*,*S*-**2b** (689 → 369): black squares: 51.00 µtorr, blue squares: 72.00 µtorr, red squares: 91.70 µtorr; offset scan range: −100 to 10 V
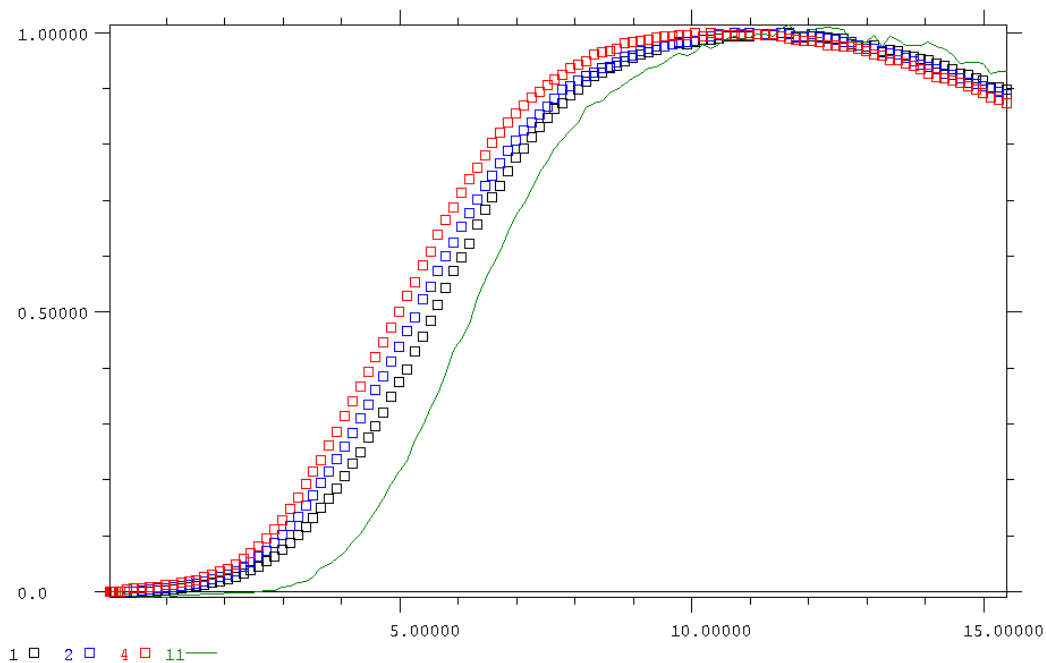
Fitted zero-pressure-extrapolation curve of the heterochiral complex (*R*,*R*-**2a**)-(*S*,*S*-**2b**)Cu⁺ with loss of *S*,*S*-**2b**:
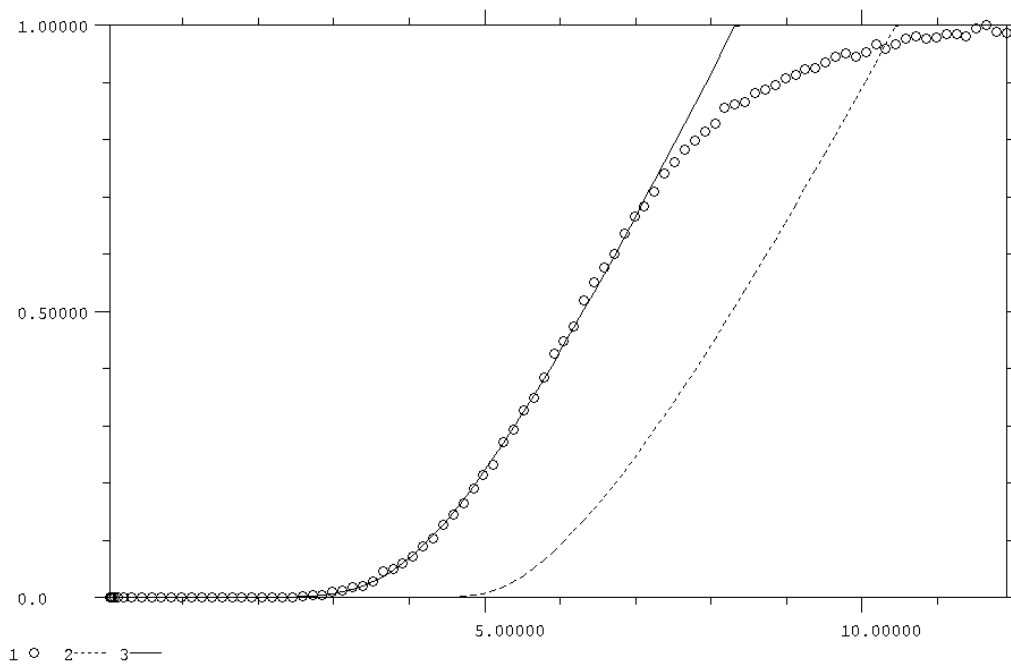
Extrapolation to zero pressure (green line) for the heterochiral complex
$(R,R$-**2a**$)(S,S$-**2b**$)$Cu$^+$ with loss of R,R-**2a**: $(689 \rightarrow 383)$: black squares: 51.00 µtorr,
blue squares: 71.00 µtorr, red squares: 93.00 µtorr; offset scan range: -100 to 10 V
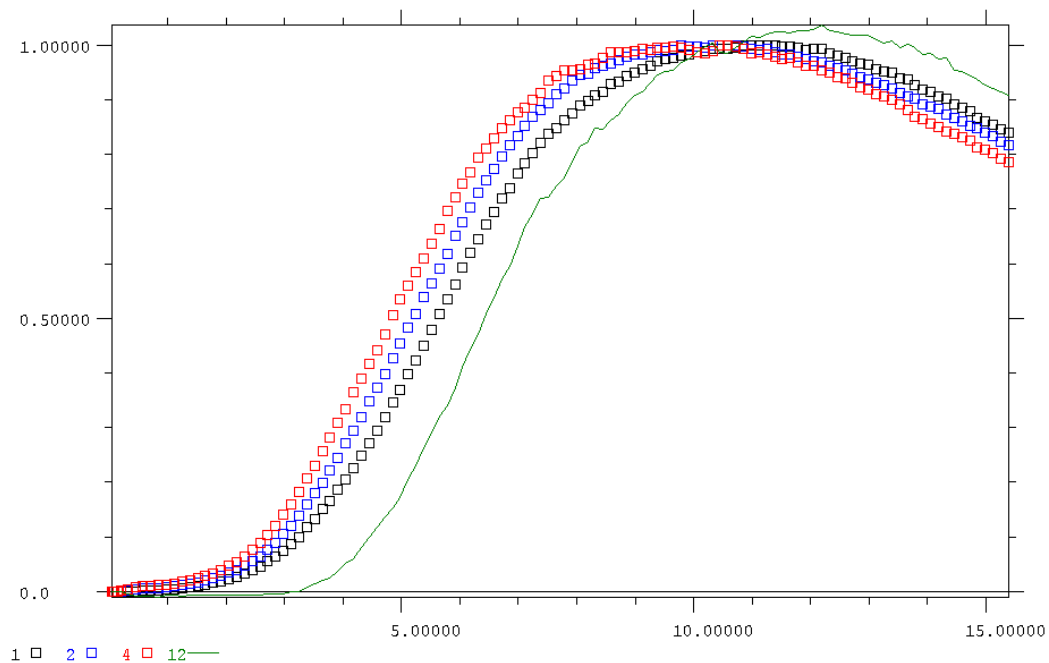
Fitted zero-pressure-extrapolation curve of the heterochiral complex $(R,R$-**2a**$)$-
$(S,S$-**2b**$)$Cu$^+$ with loss of R,R-**2a**:
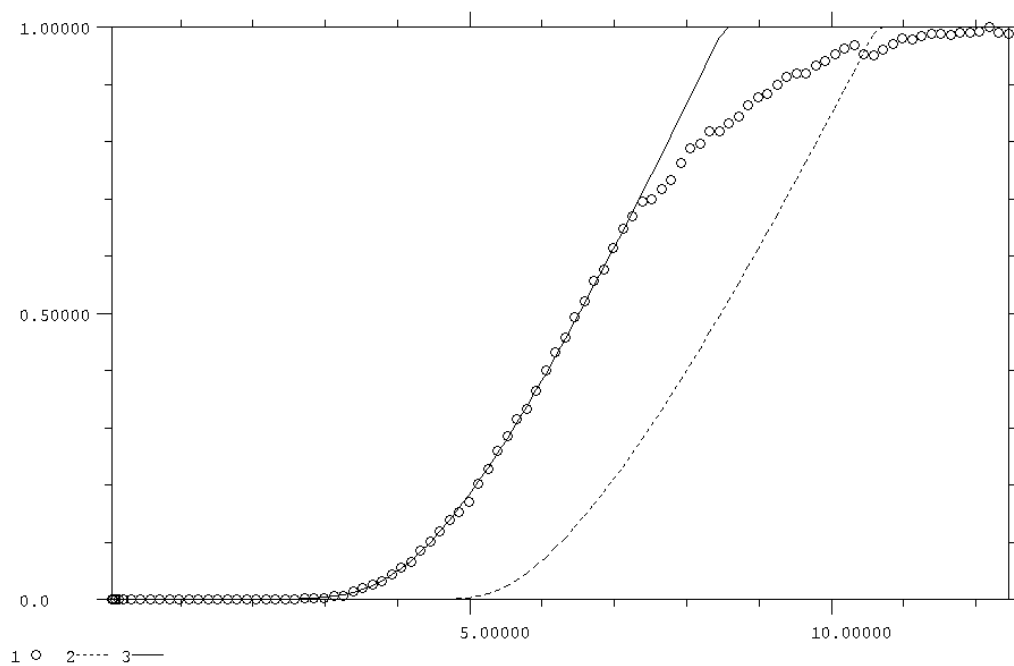
Two-Channel-Fit with the daughter peaks of the heterochiral complex (*R*,*R*-**2a**)(*S*,*S*-**2b**)Cu⁺ showing the relative intensity scaling for the two channels. The black data points and the black fitted curve belong to the (*S*,*S*-**2b**)Cu⁺ fragment, whereas the blue ensemble belongs to the (*R*,*R*-**2a**)Cu⁺ fragment.
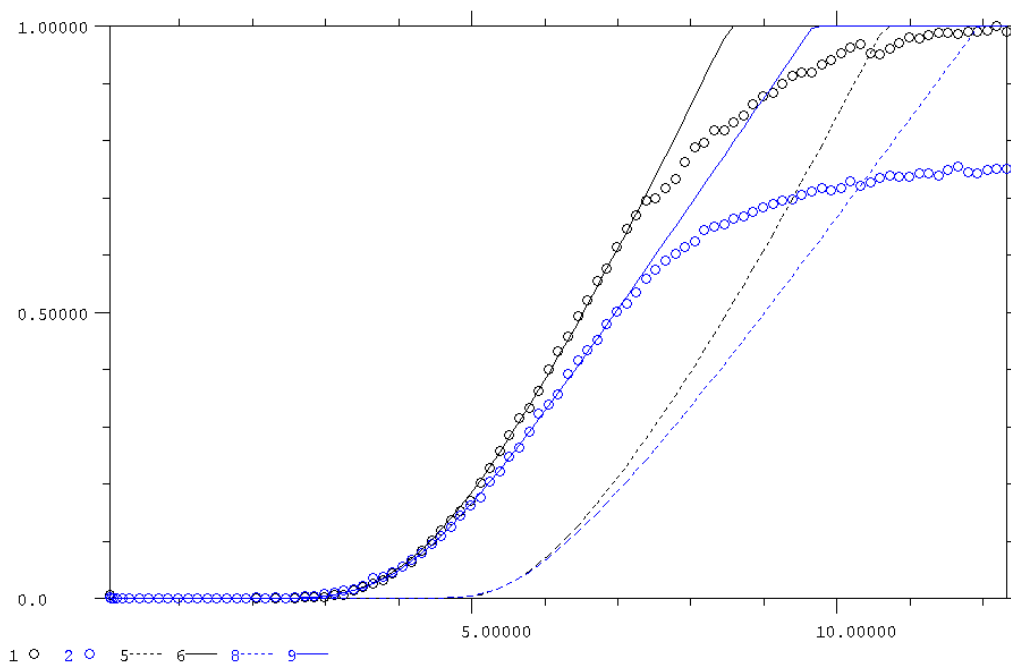

For relative scaling of the two product channels at m/z = 368 and m/z = 383 the ratio of the integrated peak areas (scaling factor: 0.797) was determined at an instrument offset of −50 V.
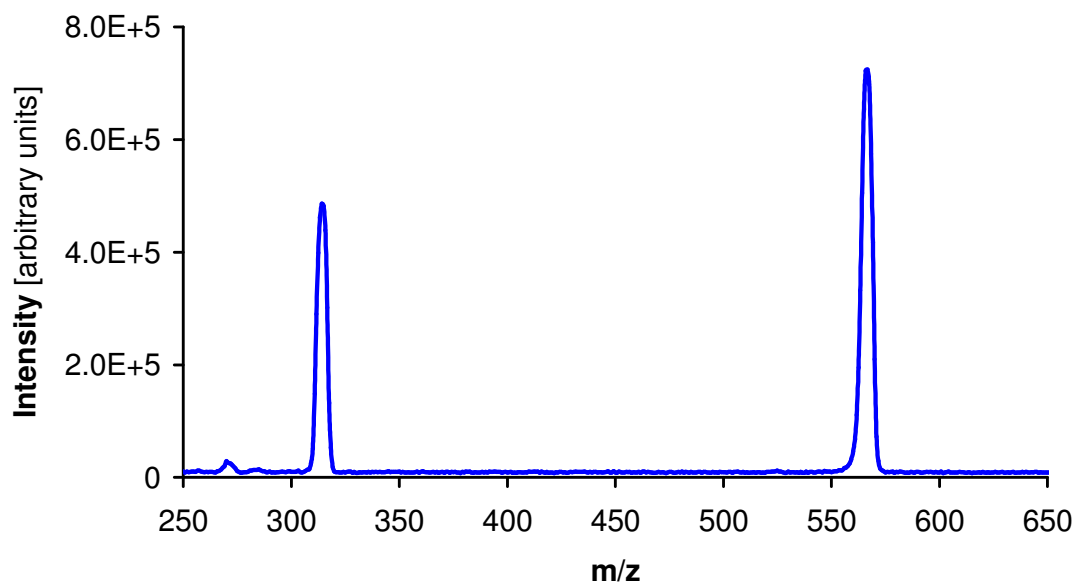
CID of the heterochiral complex (*R*,*R*-**2a**)(*S*,*S*-**2b**)Cu⁺
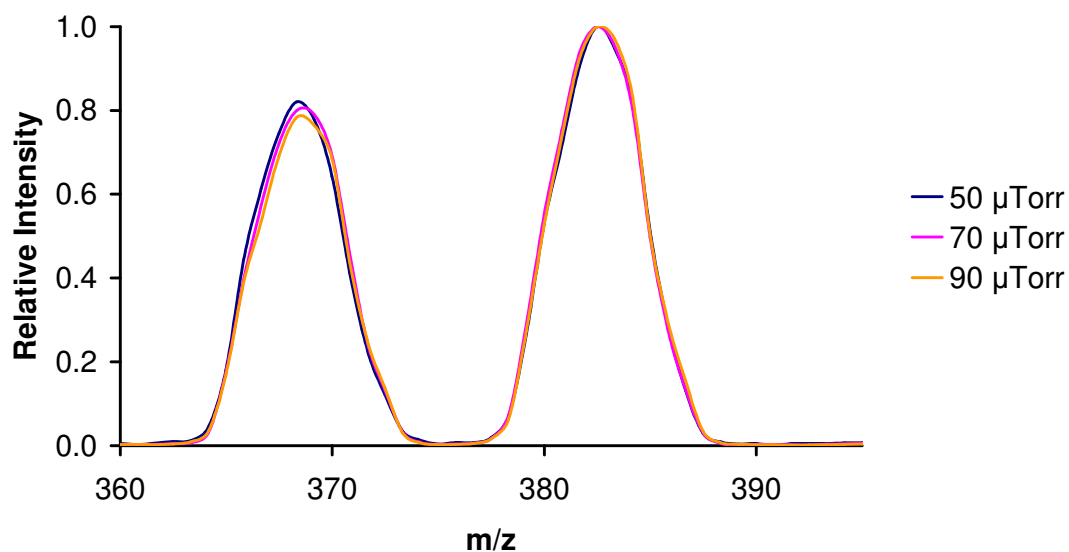
10.3.2 CID Threshold Results for the Phenyl-Azabox-Ligands

Mass scan of the (R,R-**4a**)$_2$Cu$^+$ solution: the homochiral complex (677) as well as the 1:1 complex (370), free ligand (307) and some fragmentation products appear.
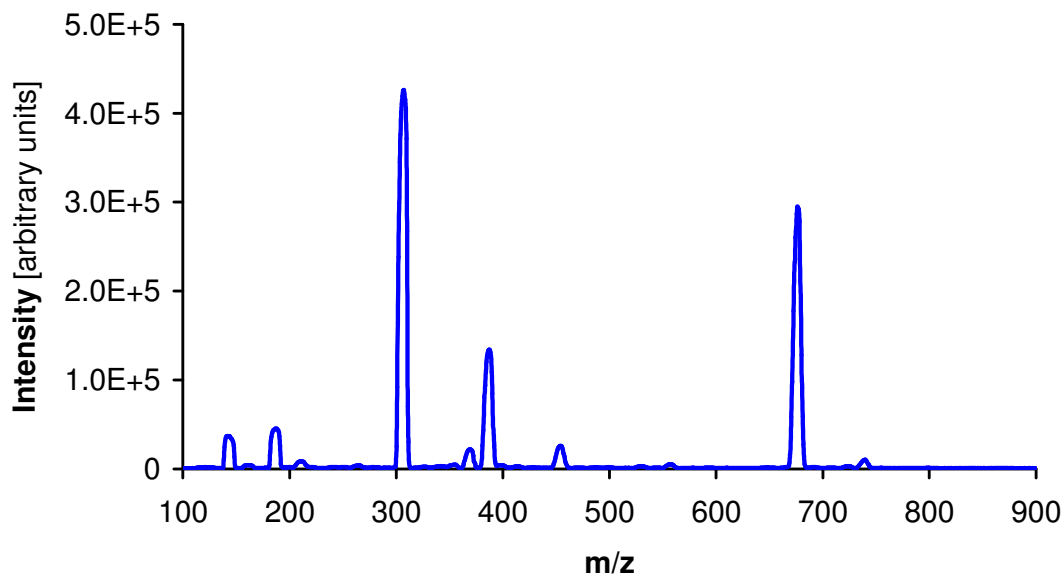
CID measurement of the homochiral complex (R,R-**4a**)$_2$Cu$^+$ with loss of R,R-**4a** (677 → 370) at 50 μtorr and an instrument offset of −110 V. The half-width of the kinetic energy distribution without collision gas is 1.8506 eV, the variation is 0.60549.
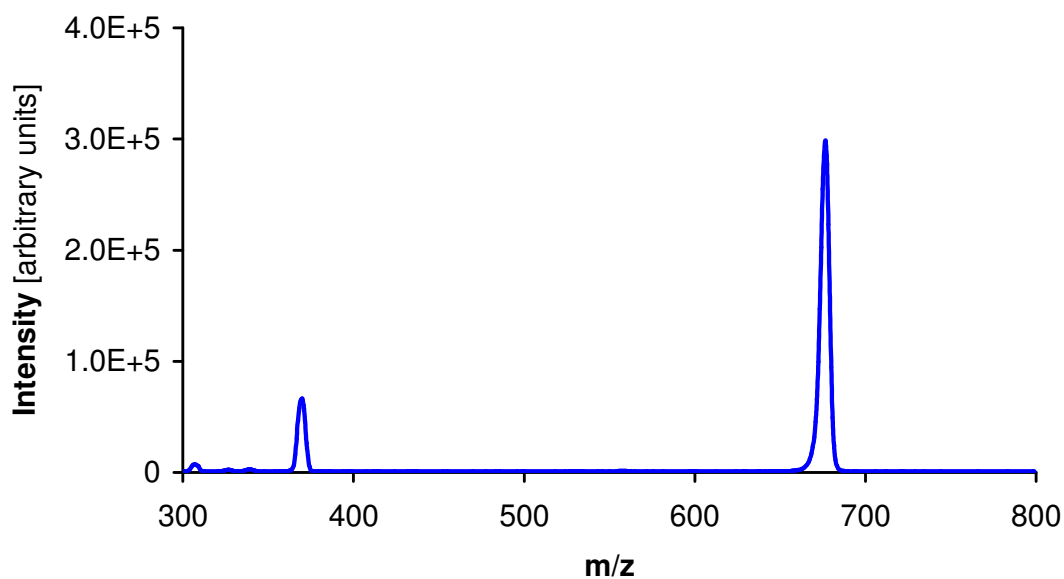
Extrapolation to zero pressure (green line) for the homochiral complex $(R,R\text{-}\mathbf{4a})_2\text{Cu}^+$ with loss of $R,R\text{-}\mathbf{4a}$ (677 $\rightarrow$ 370): red squares: 47.27 μtorr, green squares: 61.00 μtorr, blue squares: 78.31 μtorr; black squares: 109.00 μtorr; offset scan range: −110 to 0 V.
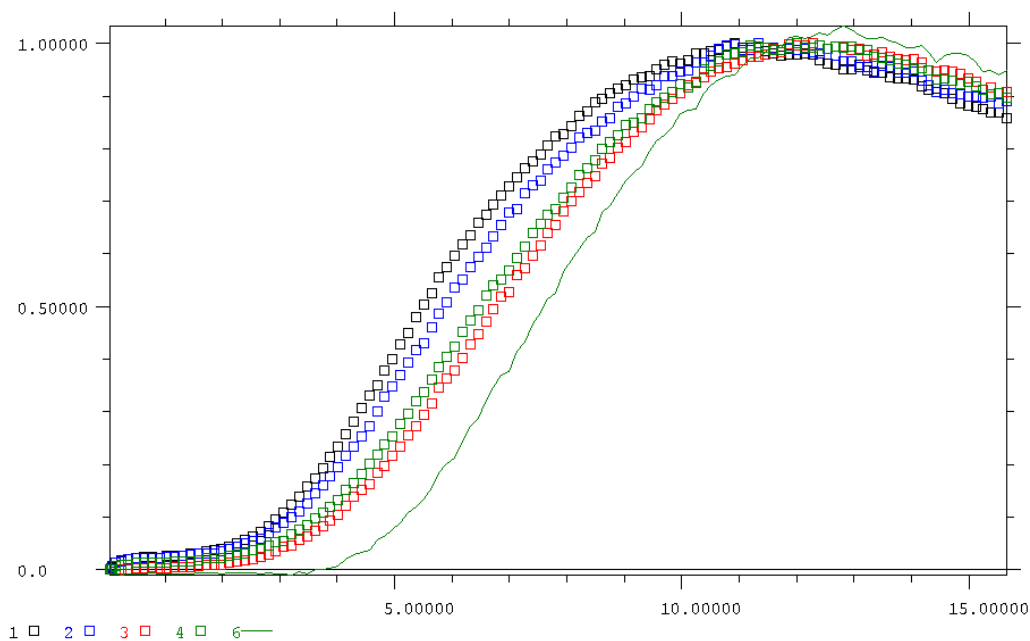
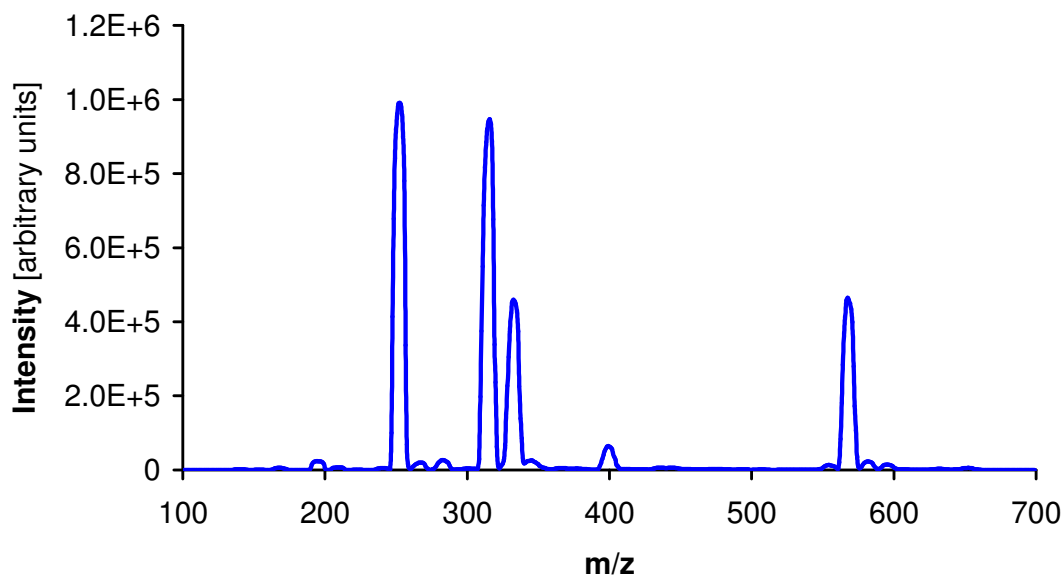Fitted zero-pressure-extrapolation curve of the homochiral complex $(R,R\text{-}\mathbf{4a})_2\text{Cu}^+$ with loss of $R,R\text{-}\mathbf{4a}$:
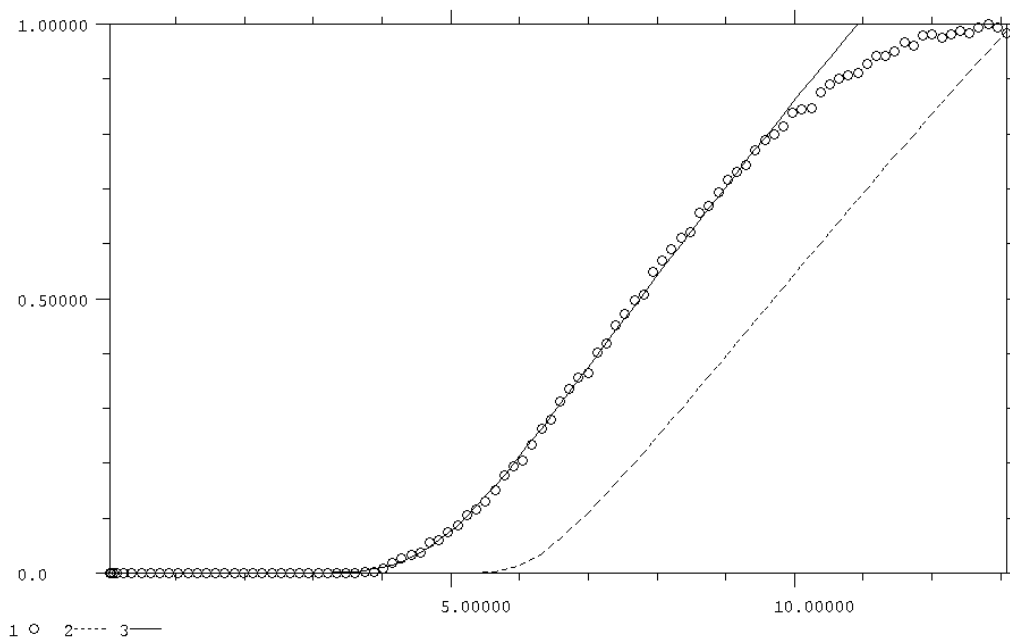
Mass scan of the (*R,R*-**4a**)(*S,S*-**4b**)Cu⁺ solution: the heterochiral complex (691), the homochiral complex (*S,S*-**4b**)$_2$Cu⁺ (705), the free ligands (307, 321) and some copper containing fragmentation products appear in this solution.
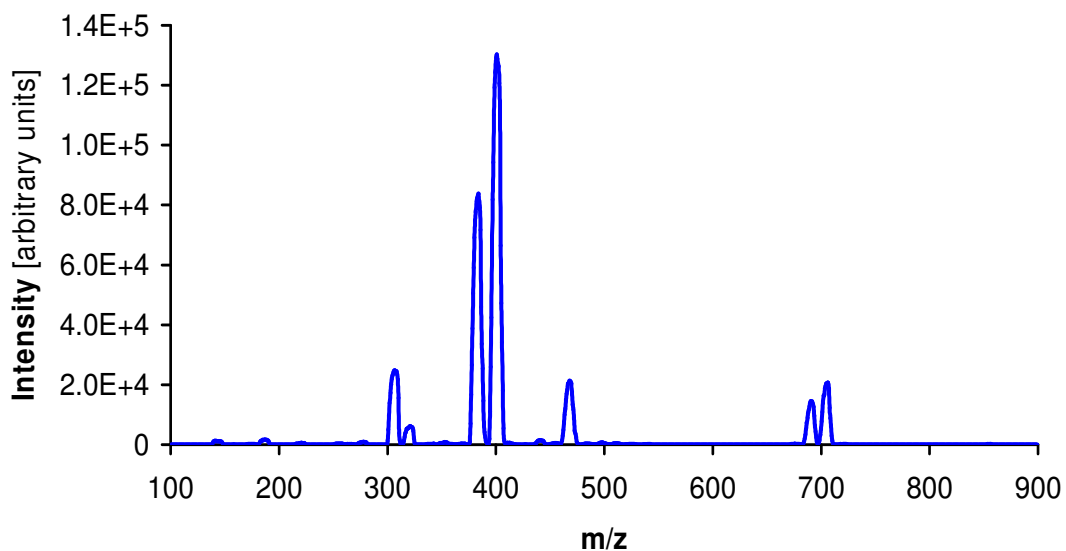
CID measurement of the heterochiral complex (*R,R*-**4a**)(*S,S*-**4b**)Cu⁺ with loss of *R,R*-**4a** or *S,S*-**4b** (691 → 384 and 691 → 370) at 50 μtorr and an instrument offset of −110 V. The half-width of the kinetic energy distribution without collision gas is 1.9304 eV, the variation is 0.71140.
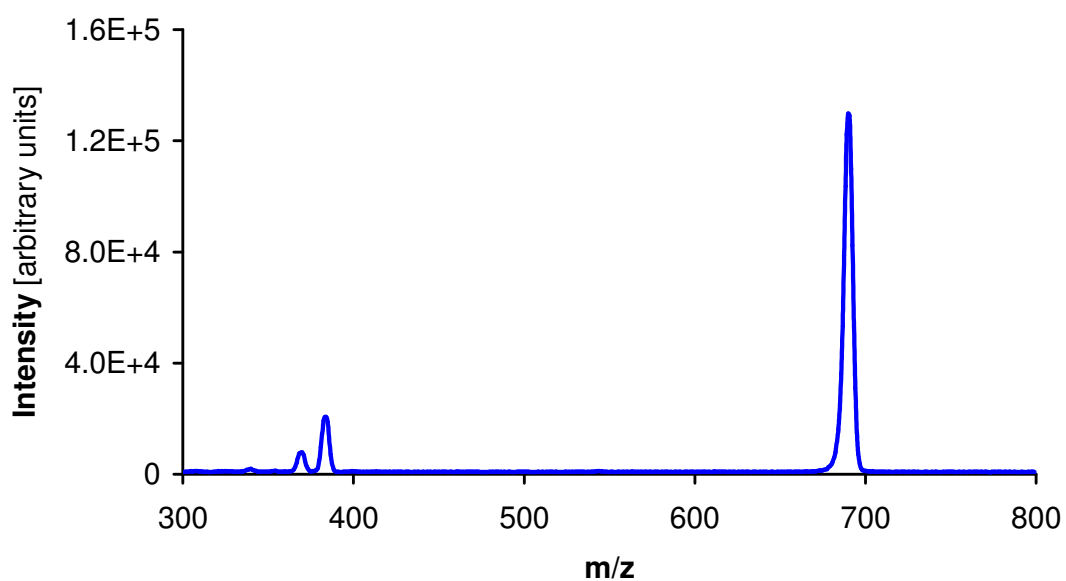
Extrapolation to zero pressure (green line) for the heterochiral complex
(*R*,*R*-**4a**)(*S*,*S*-**4b**)Cu$^+$ with loss of *R*,*R*-**4a** (691 → 384): black squares: 46.50 μtorr,
blue squares: 70.30 μtorr, red squares: 96.80 μtorr; green squares: 121.8 μtorr; offset
scan range: −110 to 0 V.
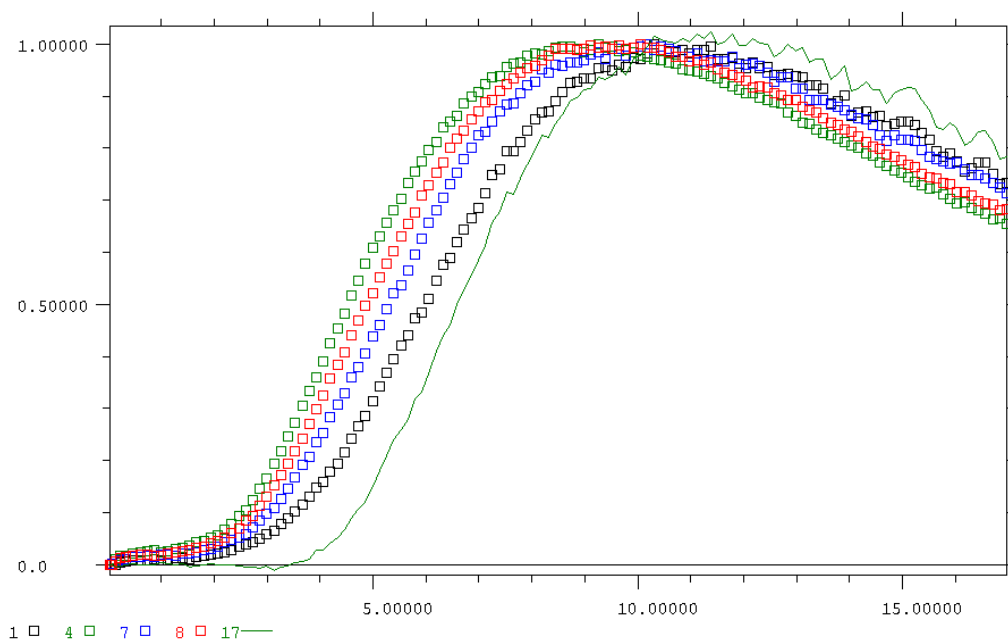
Fitted zero-pressure-extrapolation curve of the heterochiral complex (*R*,*R*-**4a**)-
(*S*,*S*-**4b**)Cu$^+$ with loss of *R*,*R*-**4a**:
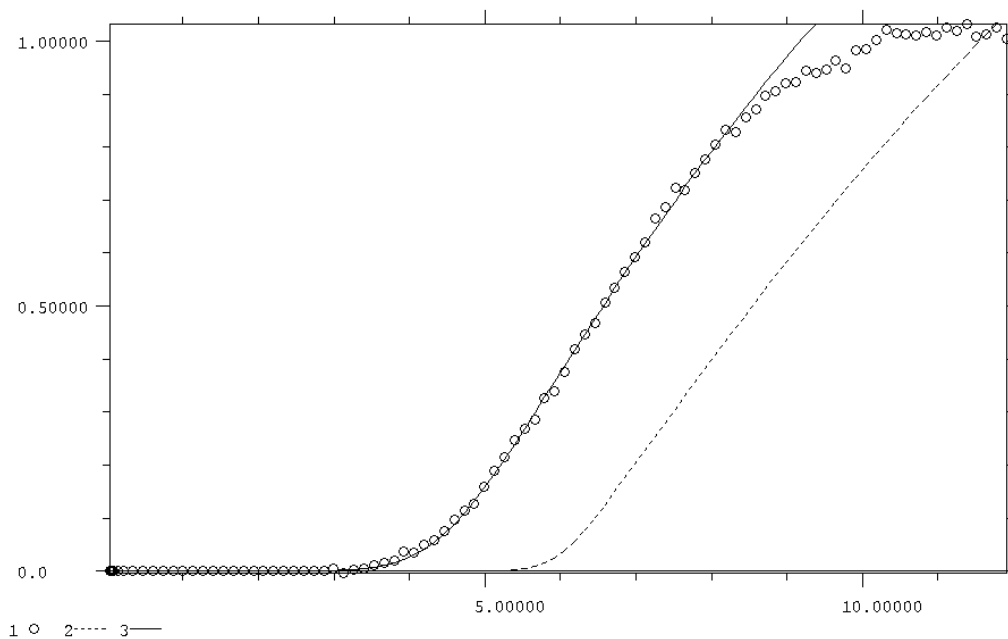
Extrapolation to zero pressure (green line) for the heterochiral complex (R,R-**4a**)(S,S-**4b**)Cu$^+$ with loss of S,S-**4b** (691 → 370): pink squares: 25.00 μtorr, black squares: 48.50 μtorr, green squares: 73.90 μtorr; blue squares: 97.1 μtorr, red squares: 122.50 μtorr; offset scan range:−110 to 0 V.
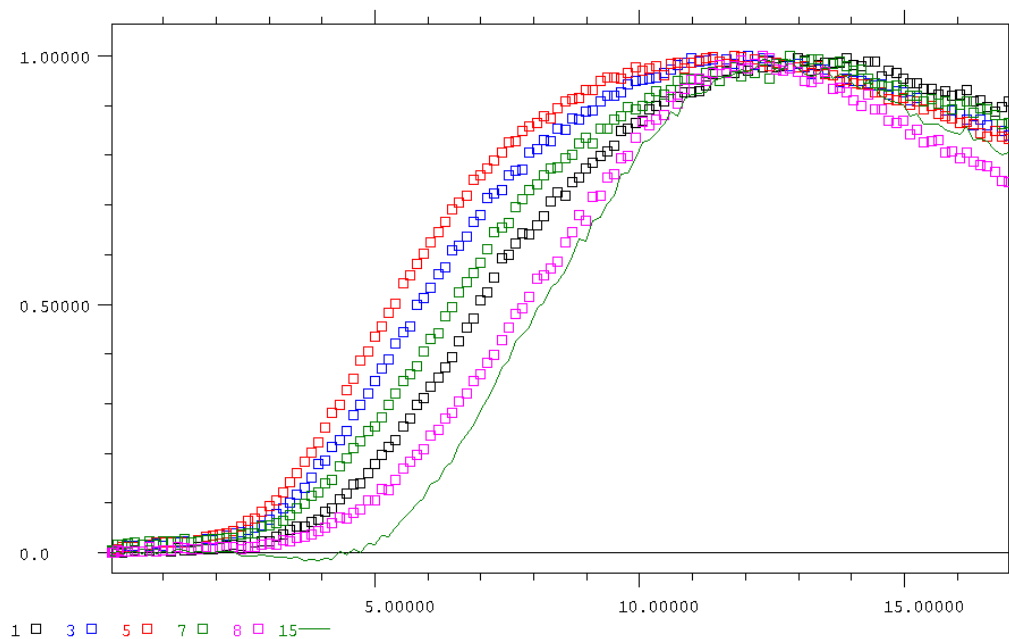
Fitted zero-pressure-extrapolation curve of the heterochiral complex (R,R-**4a**)-(S,S-**4b**)Cu$^+$ with loss of S,S-**4b**:
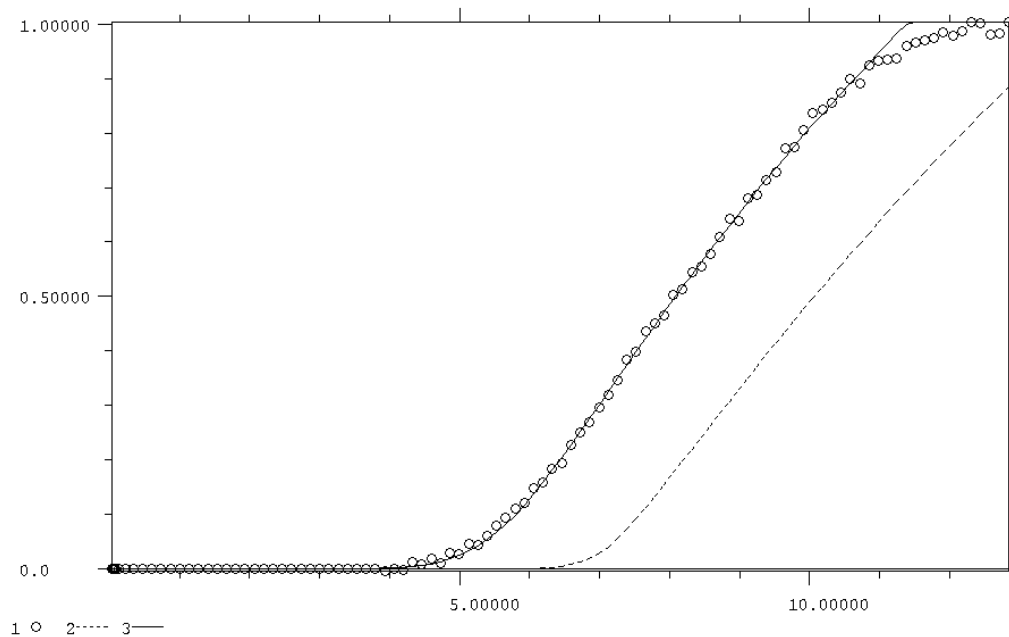
Two-Channel-Fit with the daughter peaks of the heterochiral complex (*R*,*R*-**4a**)(*S*,*S*-**4b**)Cu$^+$ showing the relative intensity scaling for the two channels. The black data points and the black fitted curve belong to the (*S*,*S*-**4b**)Cu$^+$ fragment, whereas the blue ensemble belongs to the (*R*,*R*-**4a**)Cu$^+$ fragment.
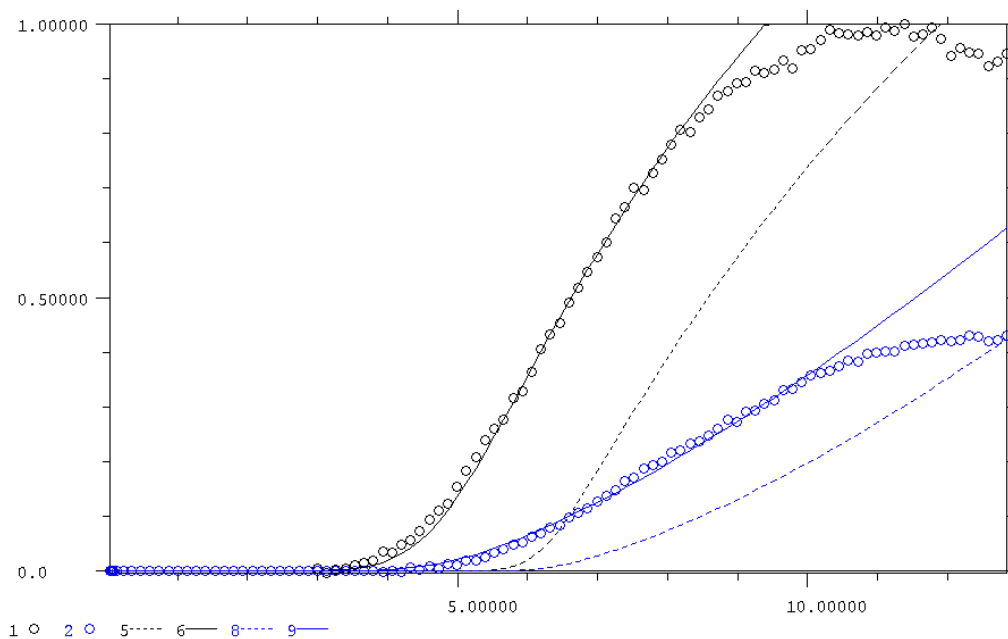
For relative scaling of the two product channels at *m/z* = 370 and *m/z* = 384 the ratio of the integrated peak areas (scaling factor: 0.431) was determined at an instrument offset of −65 V.

CID of the heterochiral complex (*R*,*R*-**4a**)(*S*,*S*-**4b**)Cu$^+$
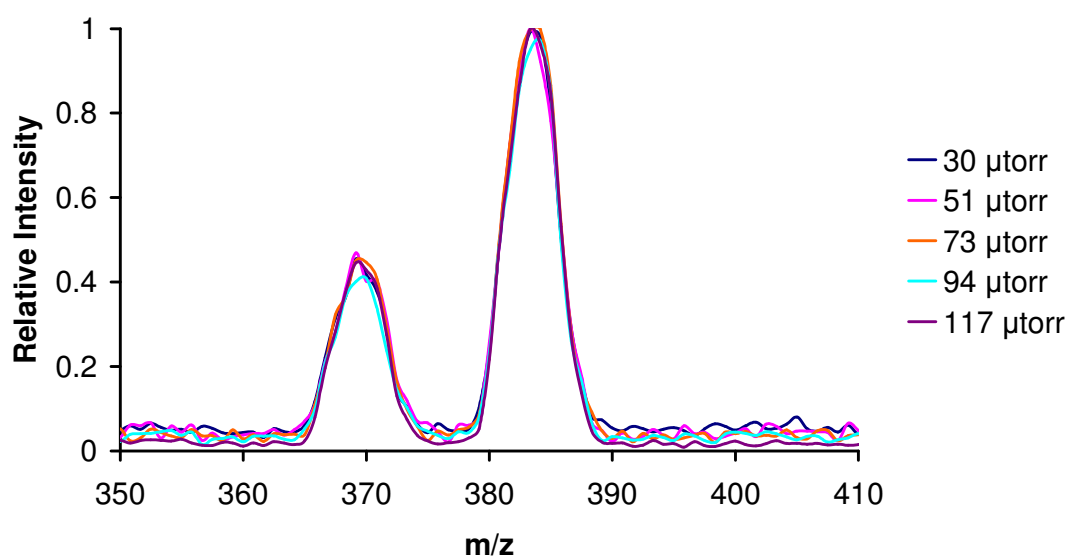
Mass scan of the $(R,R\text{-}\mathbf{4a})(S,S\text{-}\mathbf{4b})Cu^+$ solution: the homochiral complex $(S,S\text{-}\mathbf{4b})_2Cu^+$ (705), the heterochiral complex (691), the free ligands (307, 321) and some copper containing fragmentation products appear in this solution.
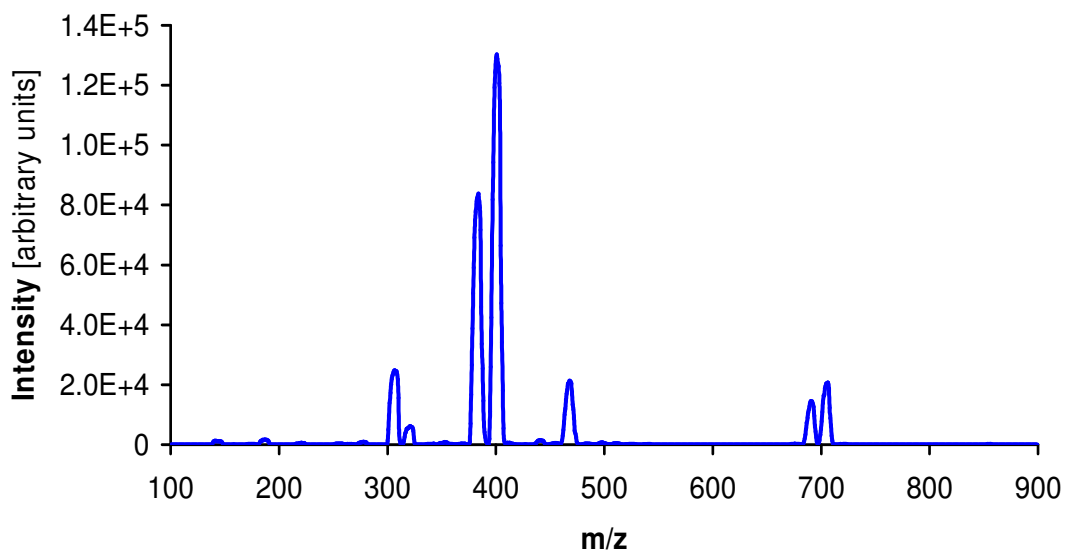
CID measurement of the homochiral complex $(S,S\text{-}\mathbf{4b})_2Cu^+$ with loss of $S,S\text{-}\mathbf{4b}$ (705 $\rightarrow$ 384) at 50 μtorr and an instrument offset of –110 V. The half-width of the kinetic energy distribution without collision gas is 1.9578 eV, the variation is 0.70578.
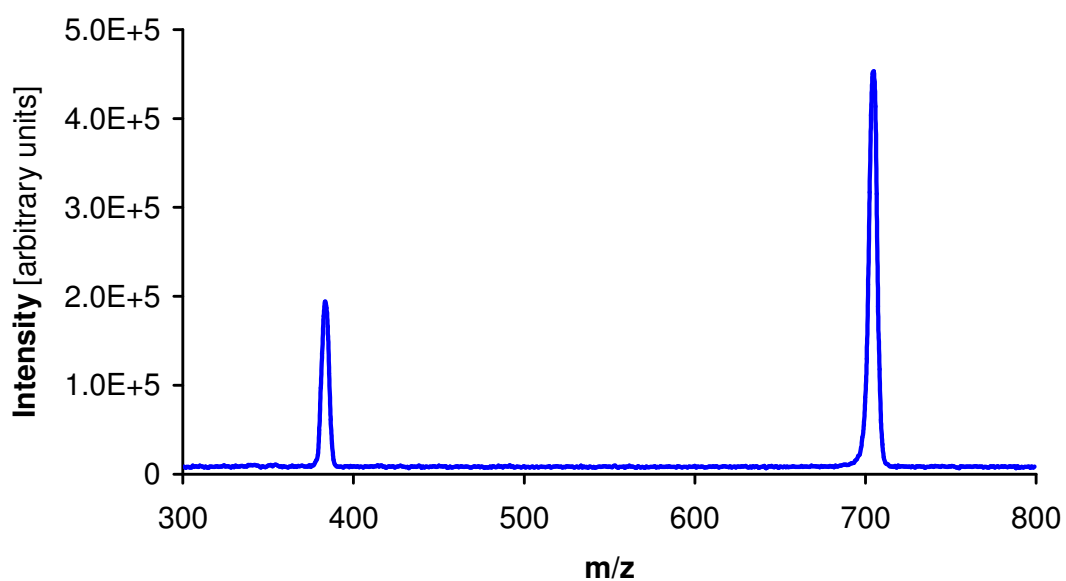
Extrapolation to zero pressure (green line) for the homochiral complex (*S,S*-**4b**)$_2$Cu$^+$ with loss of *S,S*-**4b** (705 → 384): black squares: 48.00 µtorr, red squares: 67.50 µtorr, blue squares: 93.00 µtorr; green squares: 124.28 µtorr; offset scan range: −110 to 0 V.
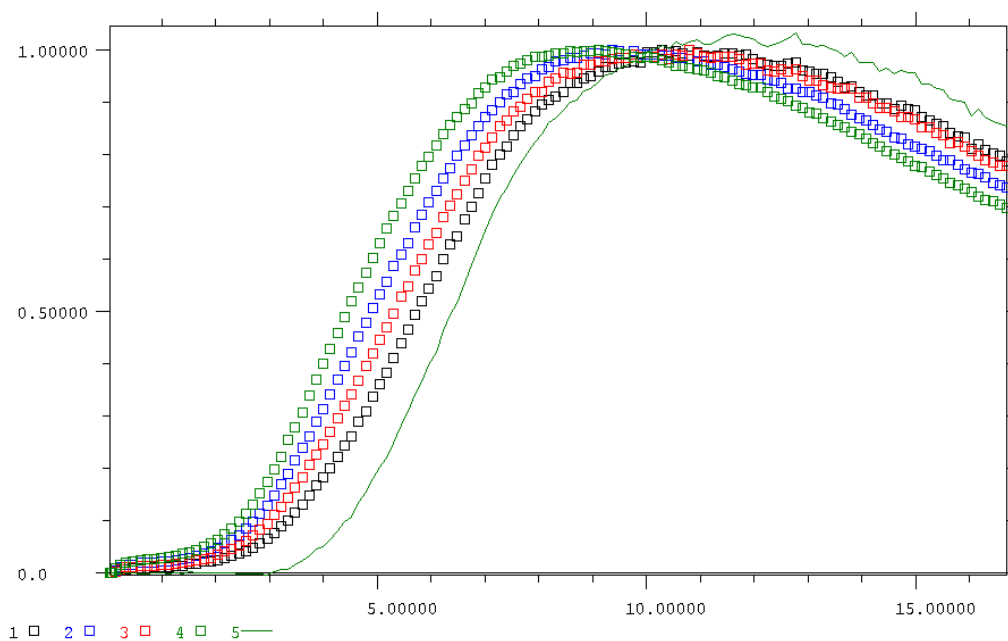
Fitted zero-pressure-extrapolation curve of the homochiral complex (*S,S*-**4b**)$_2$Cu$^+$ with loss of *S,S*-**4b**:
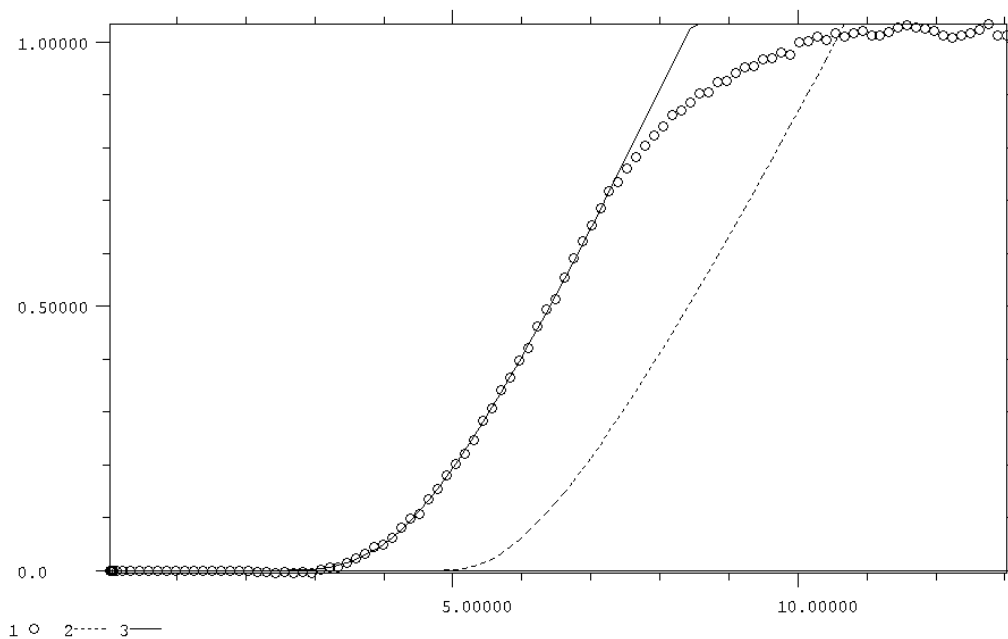
Mass scan of the $(S,S\text{-}4a)(S,S\text{-}4b)Cu^+$ solution: the *pseudo*-homochiral complex $(S,S\text{-}4a)(S,S\text{-}4b)Cu^+$ (691), the homochiral complex $(S,S\text{-}4b)_2Cu^+$ (705) as well as some copper containing fragmentation products appear in this solution.
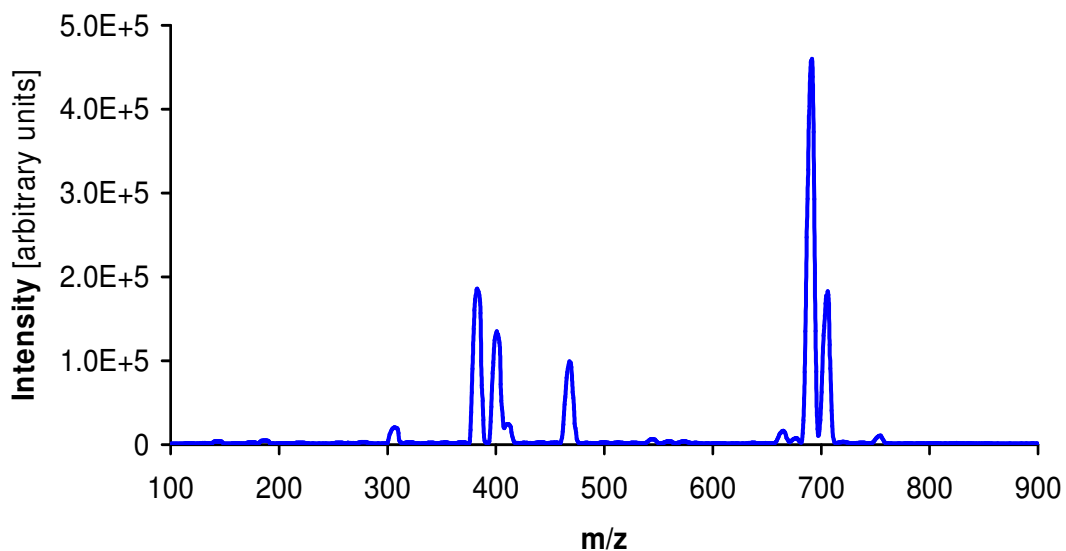
CID measurement of the *pseudo*-homochiral complex $(S,S\text{-}4a)(S,S\text{-}4b)Cu^+$ with loss of $S,S\text{-}4a$ or $S,S\text{-}4b$ ($705 \rightarrow 384$ and $705 \rightarrow 370$) at 50 μtorr and an instrument offset of -110 V. The half-width of the kinetic energy distribution without collision gas is 1.9693 eV, the variation is 0.53215.
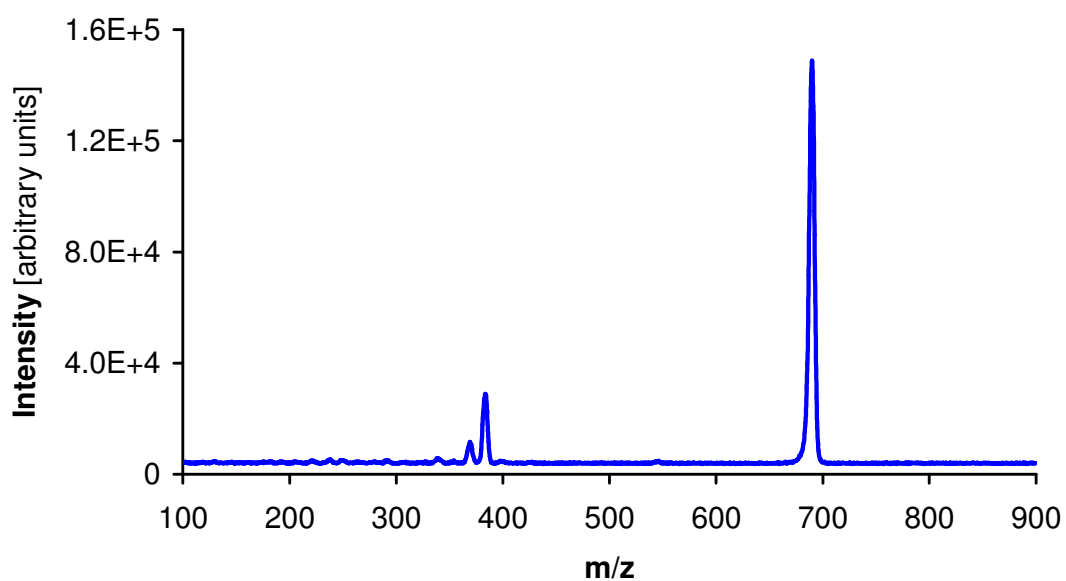
Extrapolation to zero pressure (green line) for the *pseudo*-homochiral complex (*S*,*S*-**4a**)(*S*,*S*-**4b**)Cu$^+$ with loss of *S*,*S*-**4a** (691 g/mol → 384 g/mol): black squares: 30.73 µtorr, blue squares: 50.05 µtorr, red squares: 73.07 µtorr; offset scan range: −110 to 0 V.
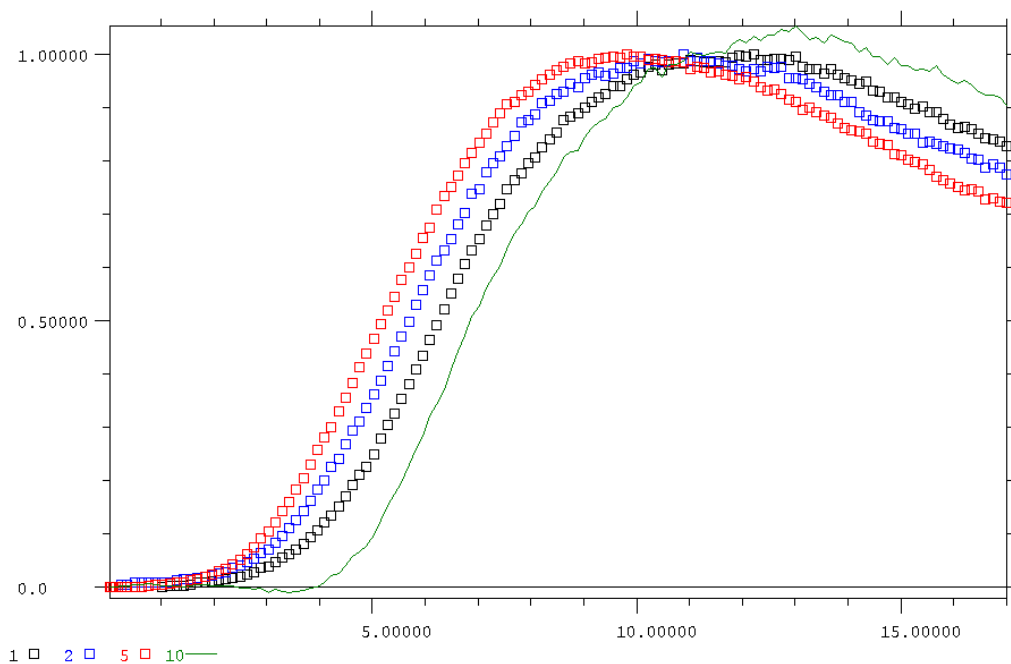
Fitted zero-pressure-extrapolation curve of the *pseudo*-homochiral complex (*S*,*S*-**4a**)(*S*,*S*-**4b**)Cu$^+$ with loss of *S*,*S*-**4a**:
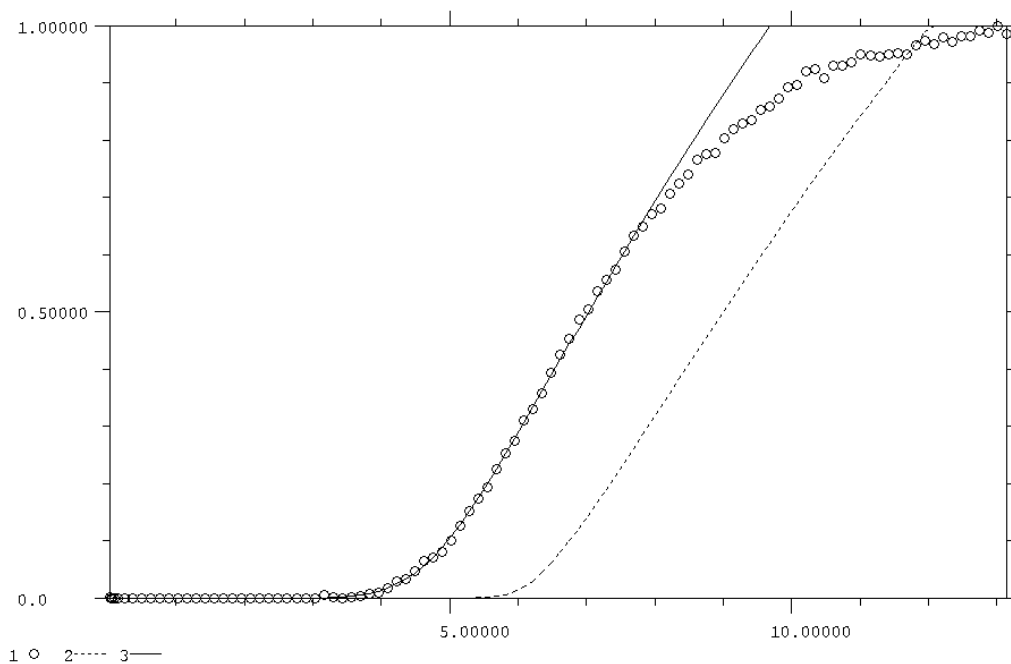
Extrapolation to zero pressure (green line) for the *pseudo*-homochiral complex (*S*,*S*-**4a**)(*S*,*S*-**4b**)Cu$^+$ with loss of *S*,*S*-**4b** (691 → 370): black squares: 31.75 µtorr, blue squares: 50.04 µtorr, red squares: 72.55 µtorr; offset scan range: −110 to 0 V.
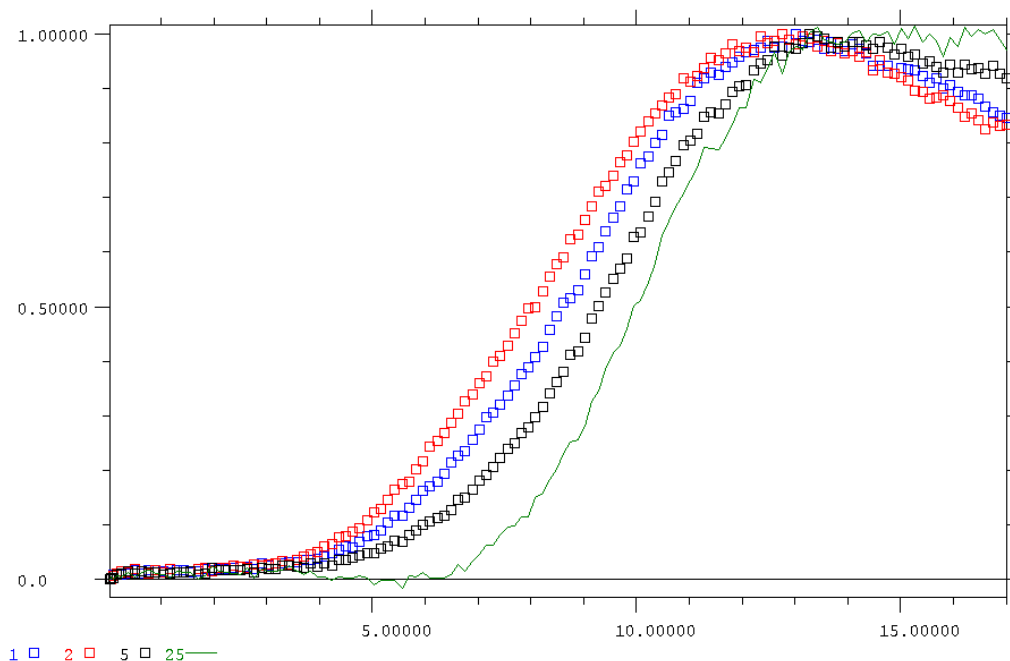
Fitted zero-pressure-extrapolation curve of the *pseudo*-homochiral complex (*S*,*S*-**4a**)(*S*,*S*-**4b**)Cu$^+$ with loss of *S*,*S*-**4b**:
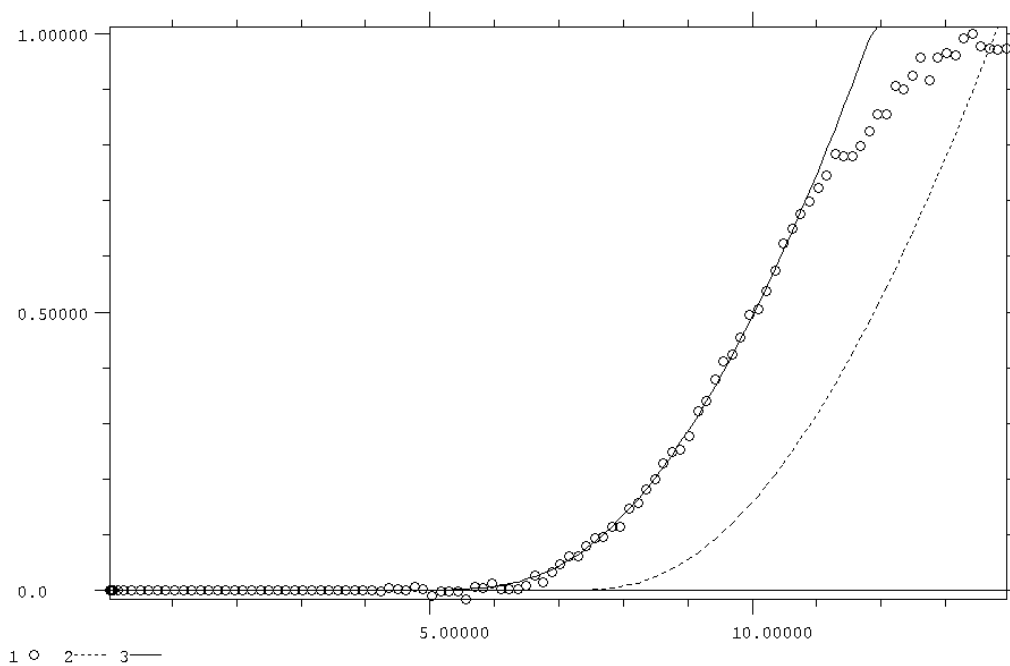
Two-Channel-Fit with the daughter peaks of the *pseudo*-homochiral complex (*S*,*S*-**4a**)(*S*,*S*-**4b**)Cu$^+$ showing the relative intensity scaling for the two channels. The black data points and the black fitted curve belong to the (*S*,*S*-**4b**)Cu$^+$ fragment, whereas the blue ensemble belongs to the (*S*,*S*-**4a**)Cu$^+$ fragment.
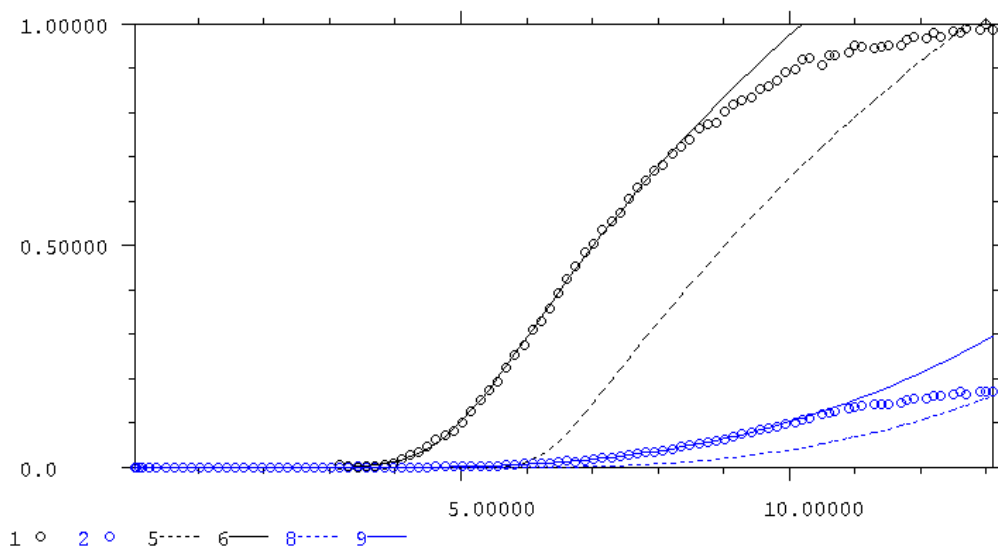
For relative scaling of the two product channels at *m/z* = 370 and *m/z* = 384 the ratio of the integrated peak areas was determined at an instrument offset of −80 V. Scaling factor(30 μTorr): 0.127, f(50 μTorr): 0.111, f(70 μTorr): 0.086. The zero-pressure-extrapolation was carried out with the scaled pressure curves.

CID of the *pseudo*-homochiral complex (*S*,*S*-**4a**)(*S*,*S*-**4b**)Cu$^+$
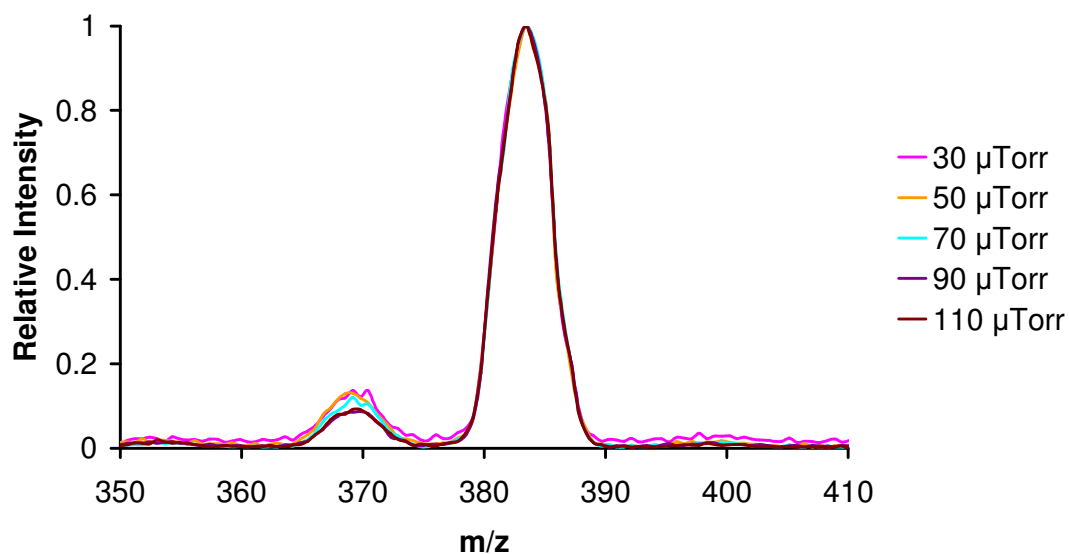
10.3.3 CID Threshold Results for the Isopropyl-Box-Ligands

Mass scan of the $(S,S\text{-}\mathbf{1a})(R,R\text{-}\mathbf{1b})Cu^+$ solution: the homochiral complex $(S,S\text{-}\mathbf{1a})_2Cu^+$ (539), the heterochiral complex $(S,S\text{-}\mathbf{1a})(R,R\text{-}\mathbf{1b})Cu^+$ (553), the second homochiral complex $(R,R\text{-}\mathbf{1b})_2Cu^+$ (567), as well as the 1:1 complexes (301, 315) and the free ligands (238, 252) appear in this solution.
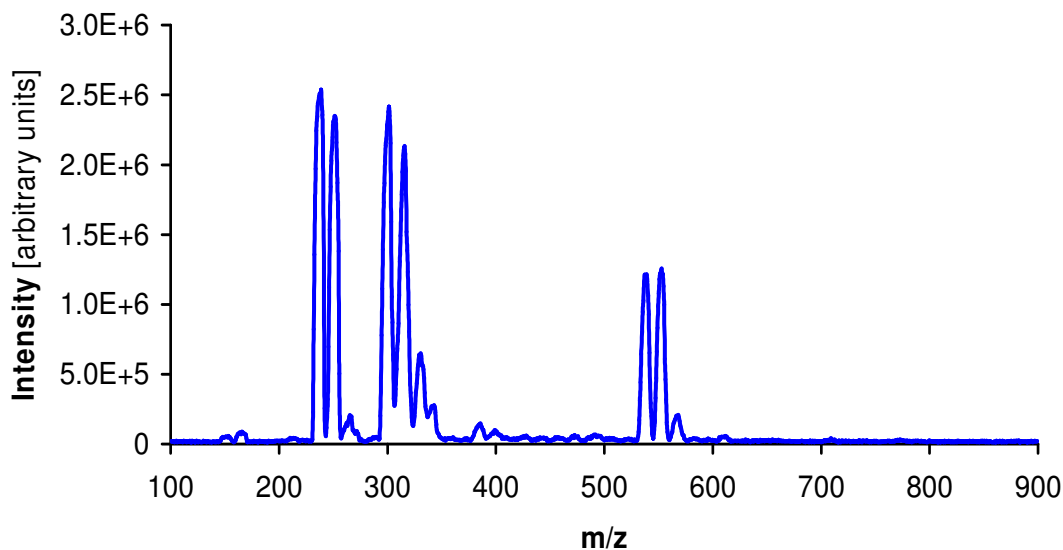
CID measurement of the homochiral complex $(S,S\text{-}\mathbf{1a})_2Cu^+$ with loss of $S,S\text{-}\mathbf{1a}$ (539 $\rightarrow$ 301) at 110 μtorr and an instrument offset of −90 V. The half-width of the kinetic energy distribution without collision gas is 2.3245 eV, the variation is 0.88865.
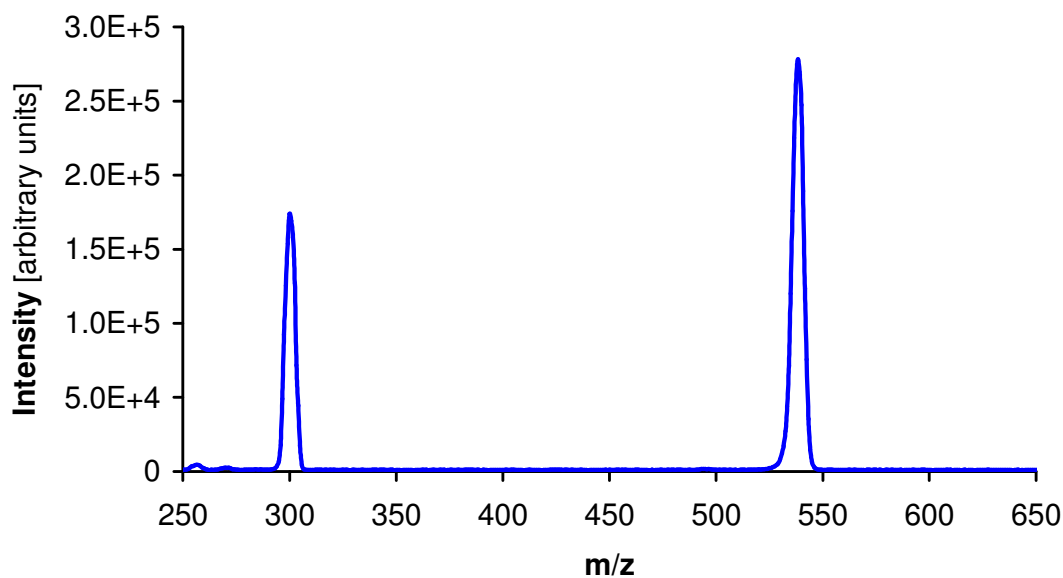
Extrapolation to zero pressure (green line) for the homochiral complex (*S*,*S*-**1a**)$_2$Cu$^+$ with loss of *S*,*S*-**1a** (539 → 301): black squares: 40.00 μtorr, blue squares: 68.00 μtorr, red squares: 89.00 μtorr; offset scan range: −90 to 10 V.
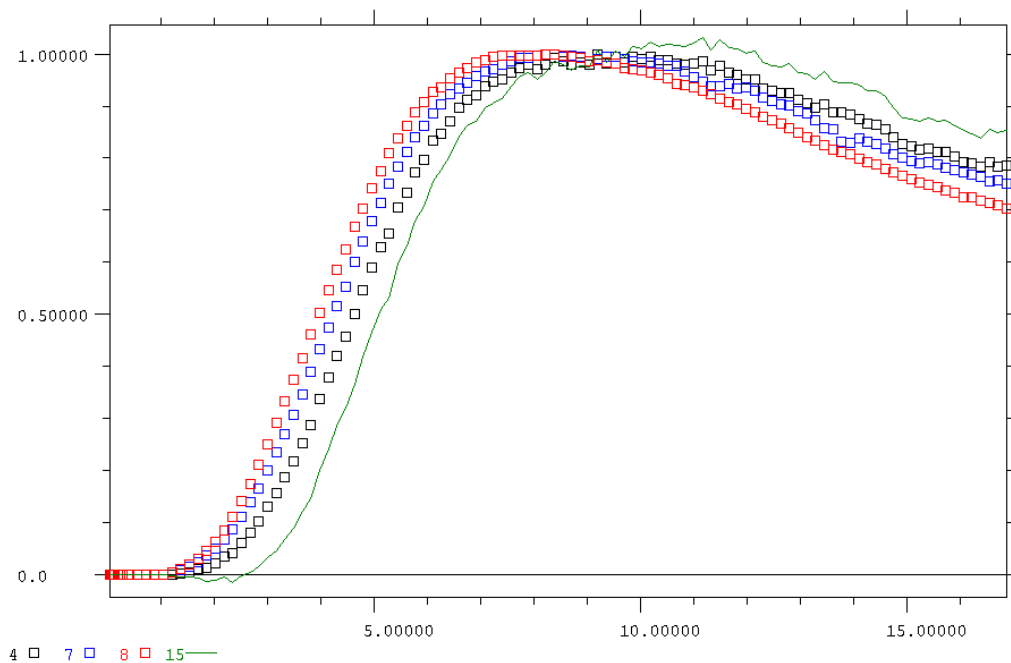
Fitted zero-pressure-extrapolation curve of the homochiral complex (*S*,*S*-**1a**)$_2$Cu$^+$ with loss of *S*,*S*-**1a**:
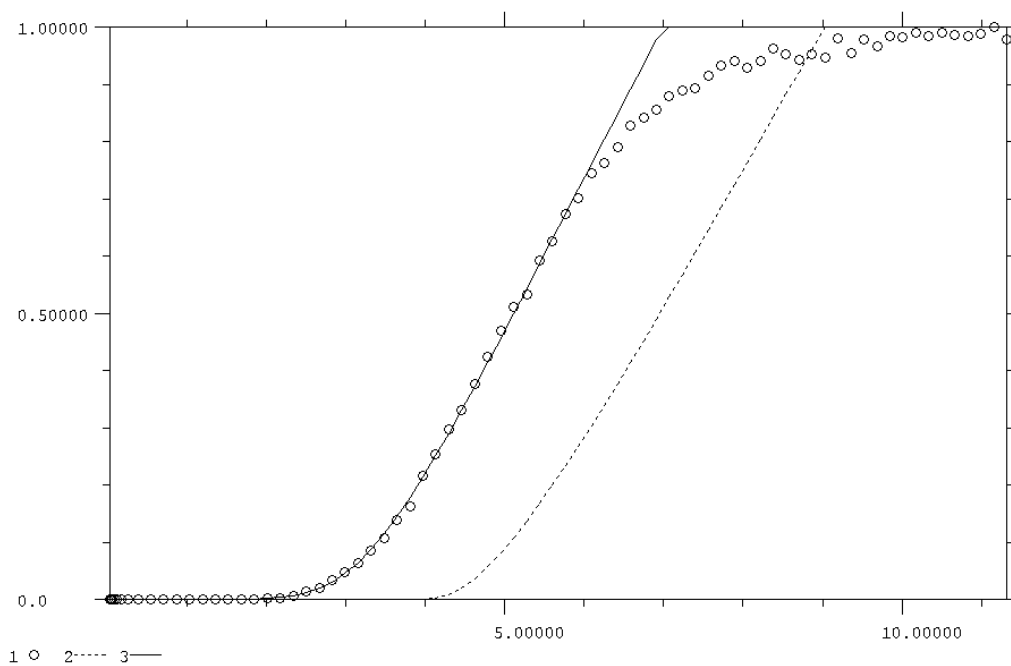
Mass scan of the (*S*,*S*-**1a**)(*R*,*R*-**1b**)Cu$^+$ solution: the homochiral complex (*S*,*S*-**1a**)$_2$Cu$^+$ (539), the heterochiral complex (*S*,*S*-**1a**)(*R*,*R*-**1b**)Cu$^+$ (553), the second homochiral complex (*R*,*R*-**1b**)$_2$Cu$^+$ (567), as well as the 1:1 complexes (301, 315) and the free ligands (238, 252) appear in this solution.
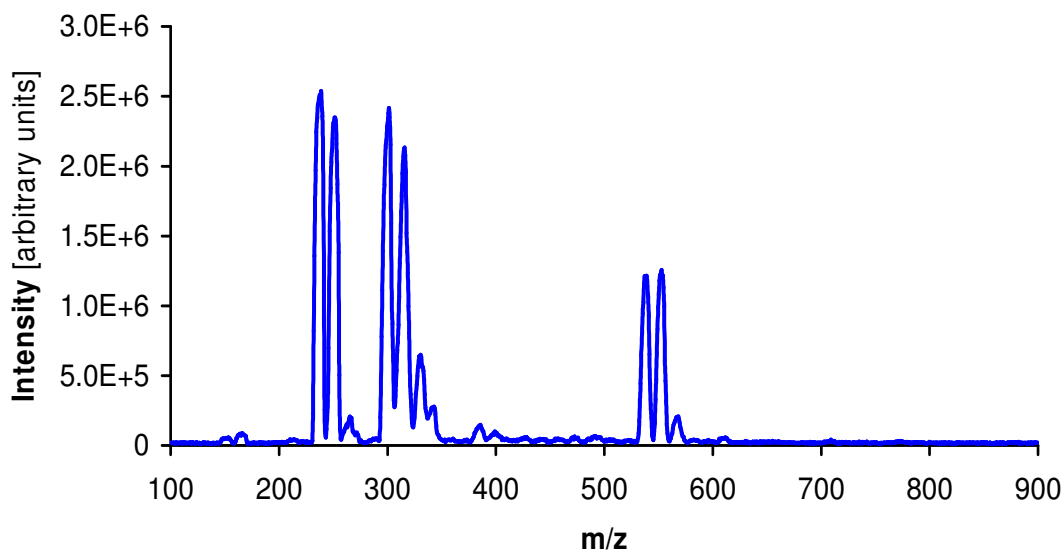
CID measurement of the heterochiral complex (*S*,*S*-**1a**)(*R*,*R*-**1b**)Cu$^+$ with loss of *S*,*S*-**1a** or *R*,*R*-**1b** (553 → 315 and 553 → 301) at 110 µtorr and an instrument offset of −90 V. The half-width of the kinetic energy distribution without collision gas is 2.3298 eV, the variation is 0.88655.
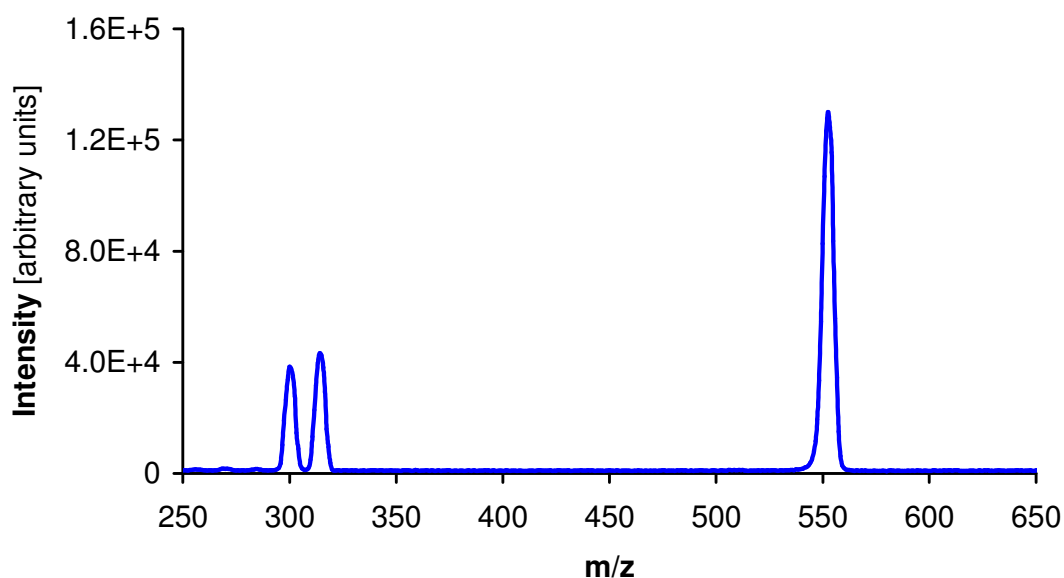
Extrapolation to zero pressure (green line) for the heterochiral complex (*S*,*S*-**1a**)(*R*,*R*-**1b**)Cu$^+$ with loss of *S*,*S*-**1a** (553 → 315): black squares: 35.00 μtorr, blue squares: 71.00 μtorr, red squares: 99.00 μtorr; offset scan range: −90 to 10 V.
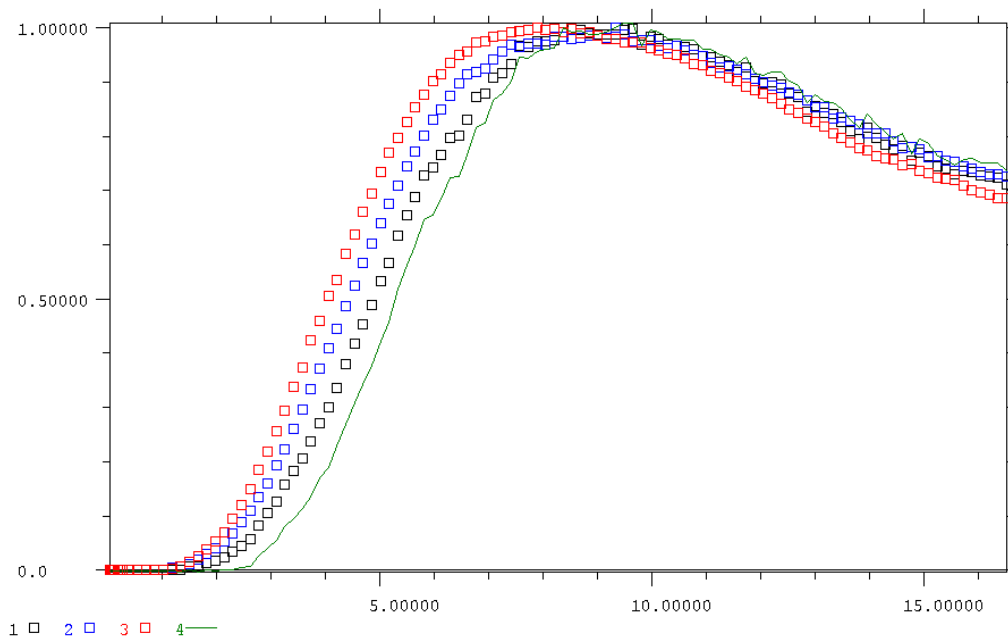
Fitted zero-pressure-extrapolation curve of the heterochiral complex (*S*,*S*-**1a**)-(*R*,*R*-**1b**)Cu$^+$ with loss of *S*,*S*-**1a**:
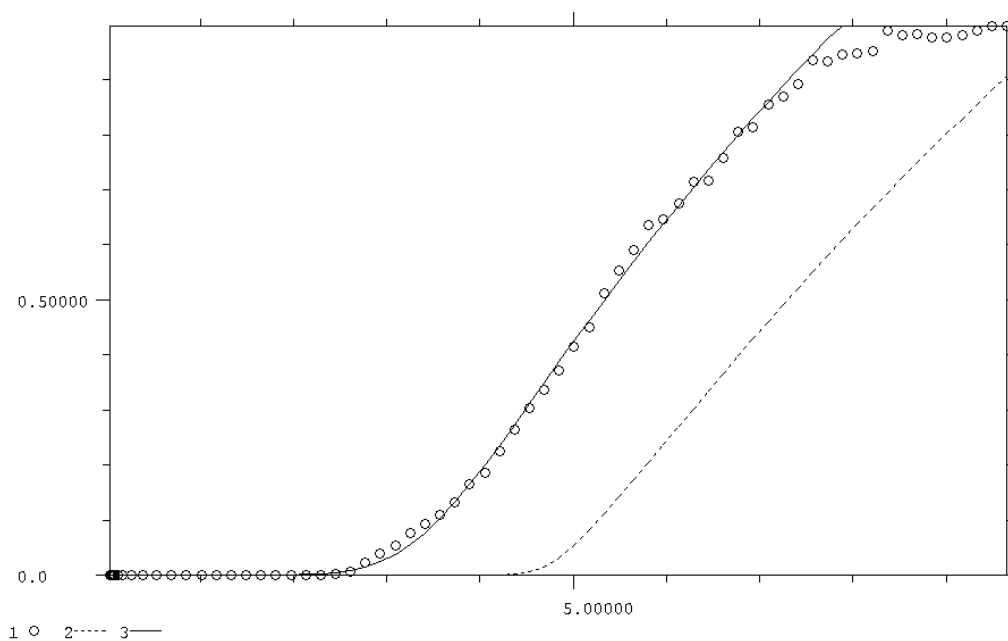
Extrapolation to zero pressure (green line) for the heterochiral complex (S,S-**1a**)(R,R-**1b**)Cu$^+$ with loss of R,R-**1b** ($553 \rightarrow 301$): black squares: 35.00 μtorr, blue squares: 72.00 μtorr, red squares: 97.00 μtorr; offset scan range: -90 to10 V.
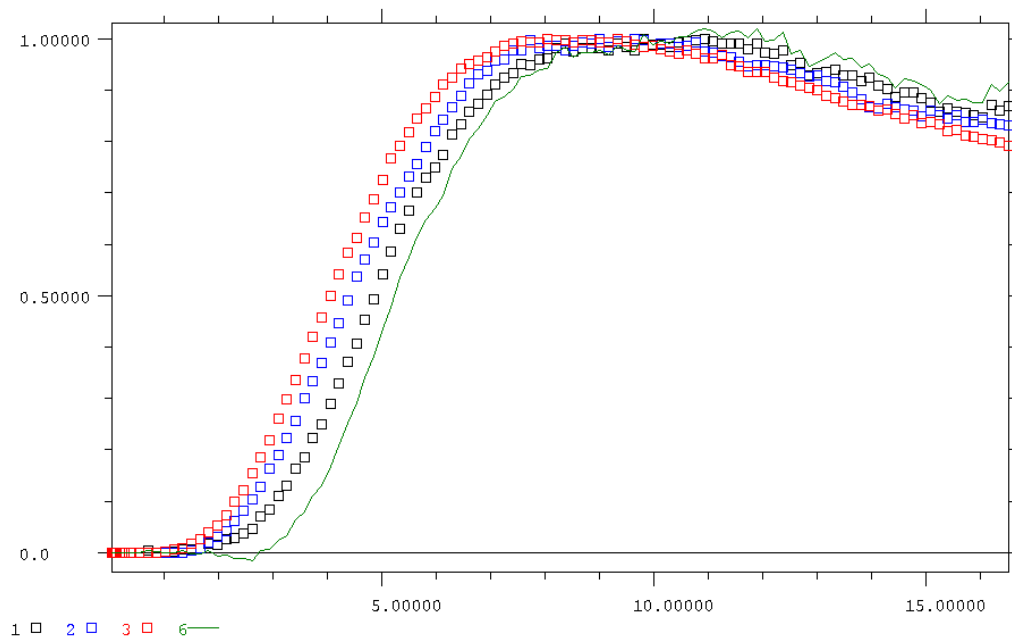
Fitted zero-pressure-extrapolation curve of the heterochiral complex (S,S-**1a**)-(R,R-**1b**)Cu$^+$ with loss of R,R-**1b**:
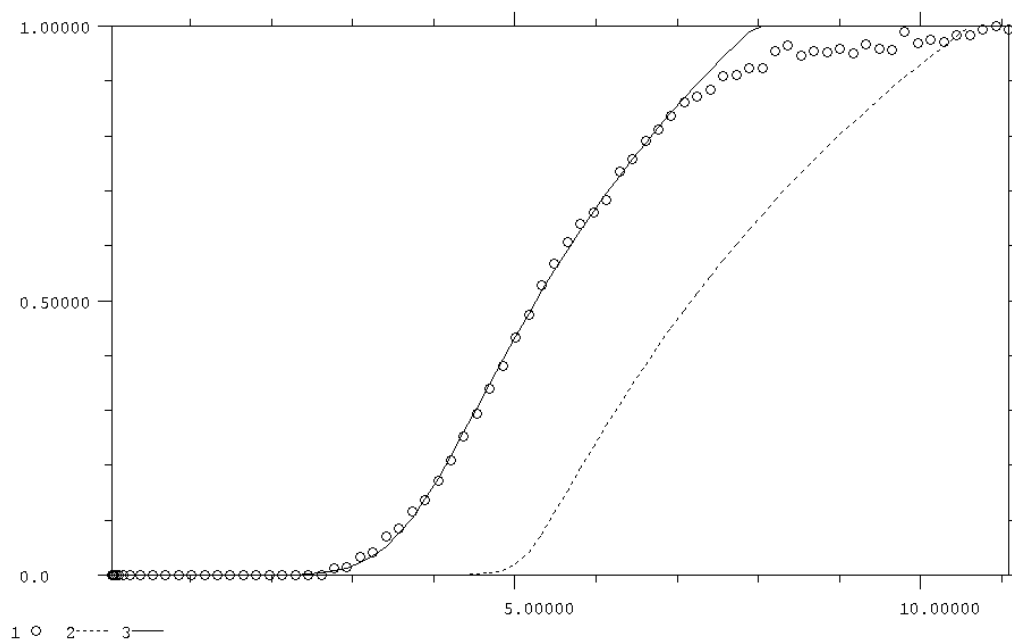
Two-Channel-Fit with the daughter peaks of the heterochiral complex (*S*,*S*-**1a**)(*R*,*R*-**1b**)Cu⁺ showing the relative intensity scaling for the two channels. The black data points and the black fitted curve belong to the (*R*,*R*-**1b**)Cu⁺ fragment, whereas the blue ensemble belongs to the (*S*,*S*-**1a**)Cu⁺ fragment.
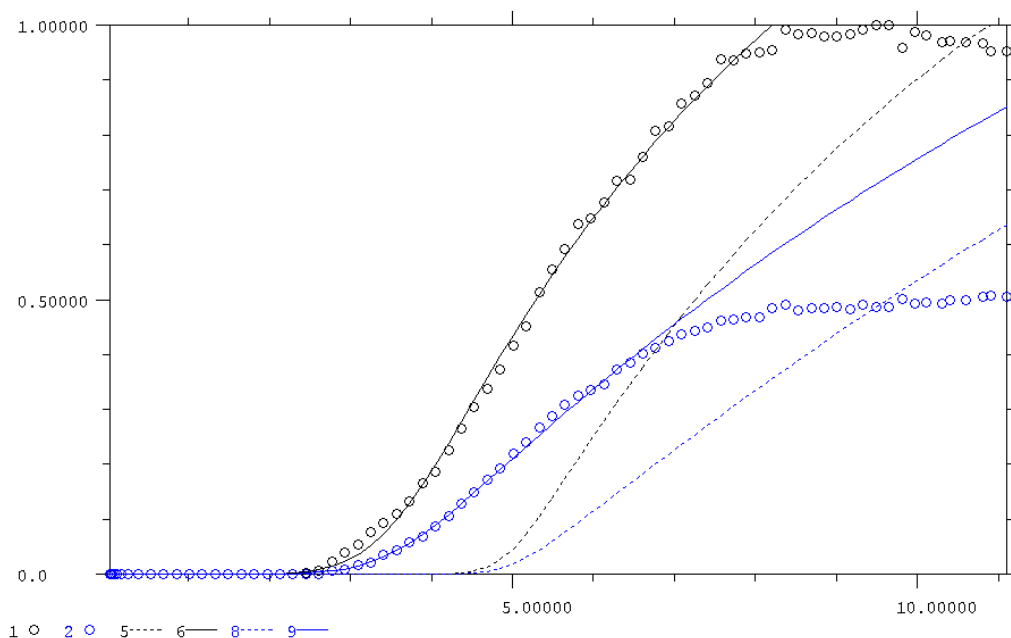
For relative scaling of the two product channels at *m/z* = 301 and *m/z* = 315 the ratio of the integrated peak areas (scaling factor: 0.633) was determined at an instrument offset of −37 V.

CID of the heterochiral complex (*S*,*S*-**1a**)(*R*,*R*-**1b**)Cu⁺
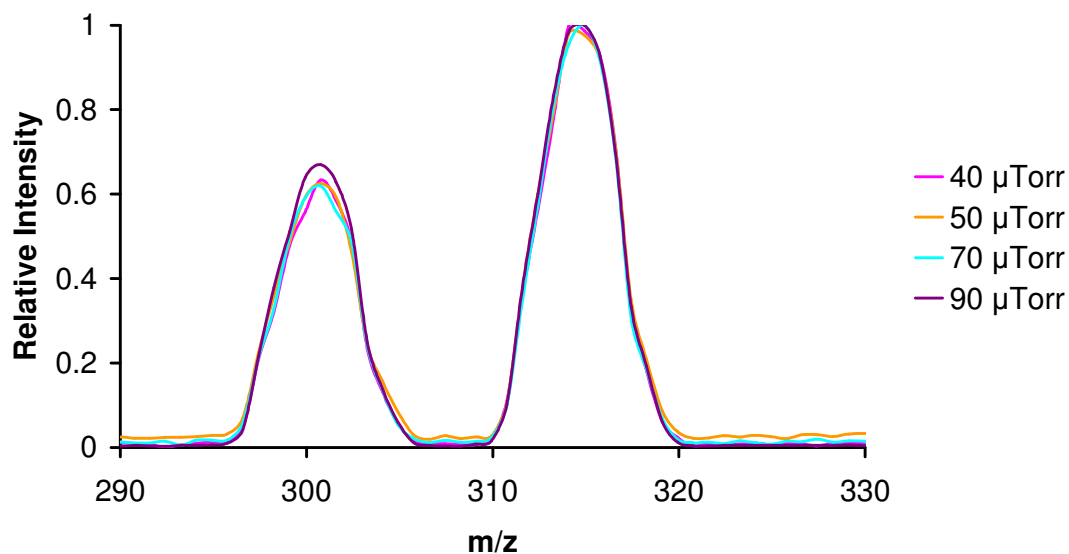
Mass scan of the $(R,R\text{-}\mathbf{1b})_2Cu^+$ solution: the homochiral complex $(R,R\text{-}\mathbf{1b})_2Cu^+$ (568), the 1:1 complex (315) as well as free ligand (252) appear in this solution.
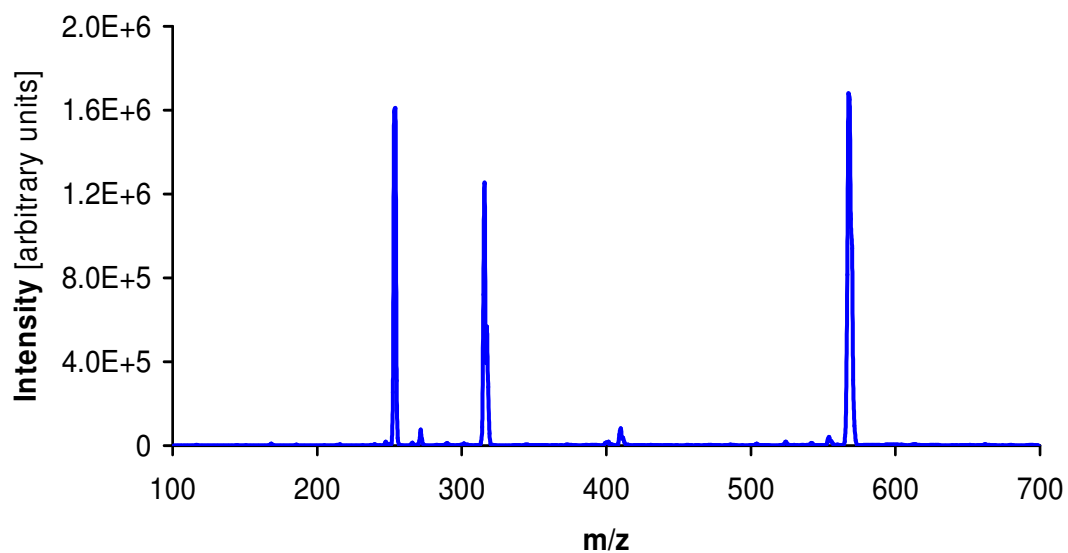
CID measurement of the homochiral complex $(R,R\text{-}\mathbf{1b})_2Cu^+$ with loss of $R,R\text{-}\mathbf{1b}$ (568 → 315) at 110 μtorr and an instrument offset of −90 V. The half-width of the kinetic energy distribution without collision gas is 2.2896 eV, the variation is 0.81209.

Extrapolation to zero pressure (green line) for the homochiral complex $(R,R\text{-}\mathbf{1b})_2Cu^+$ with loss of $R,R\text{-}\mathbf{1b}$ (568 → 315): black squares: 50.00 μtorr, blue squares: 70.00 μtorr, red squares: 90.00 μtorr; offset scan range: −90 to 10 V.
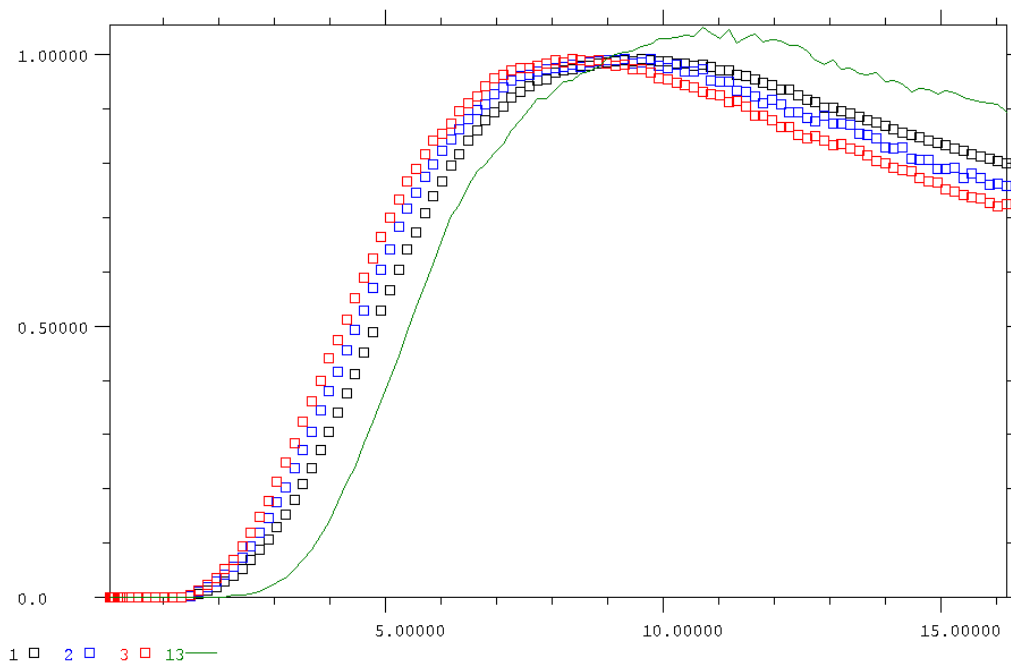
Fitted zero-pressure-extrapolation curve of the homochiral complex $(R,R\text{-}\mathbf{1b})_2Cu^+$ with loss of $R,R\text{-}\mathbf{1b}$:
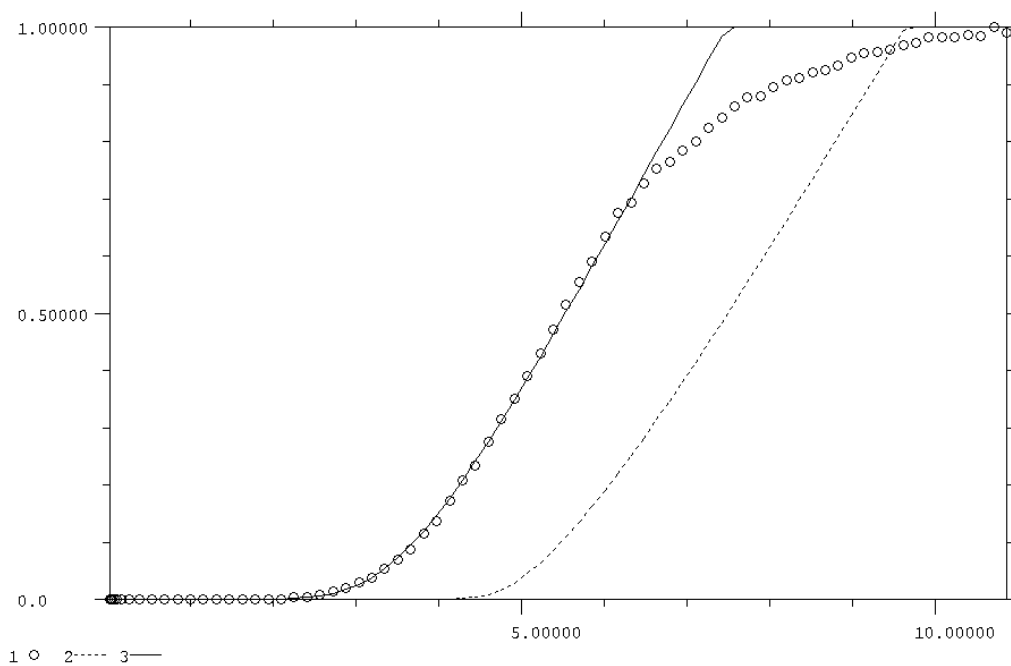
10.3.4 CID Threshold Results for the Isopropyl-Azabox-Ligands

Mass scan of the $(S,S$-$\textbf{3b})_2Cu^+$ solution: the homochiral complex (569), the 1:1 complex (316), free ligand (253) and some fragmentation products appear in this solution.

CID measurement of the homochiral complex $(S,S$-$\textbf{3b})_2Cu^+$ with loss of S,S-$\textbf{3b}$ (569 $\rightarrow$ 316) at 60 µtorr and an instrument offset of -90 V. The half-width of the kinetic energy distribution without collision gas is 2.1463 eV, the variation is 0.65352.
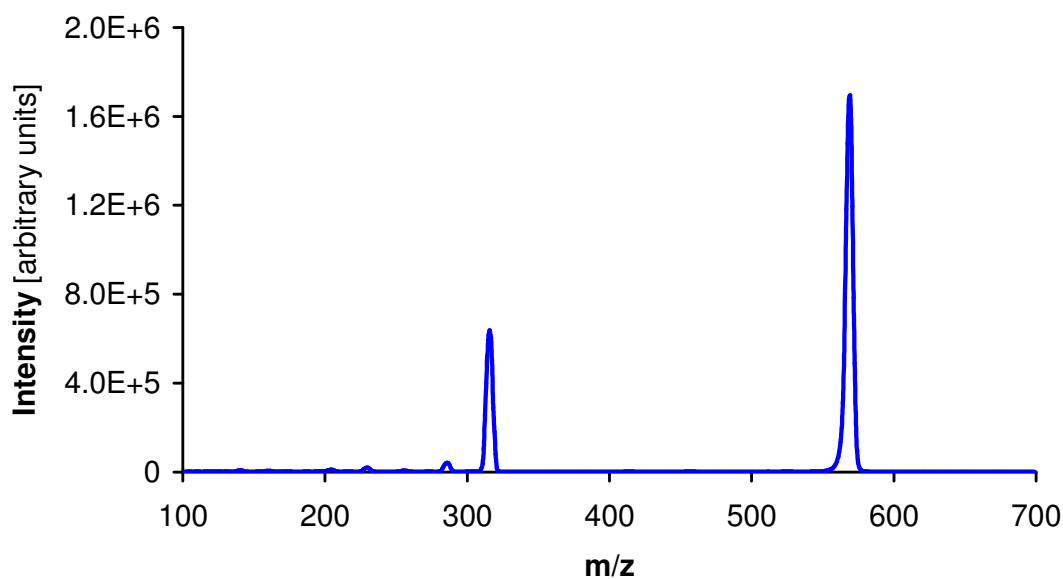
Extrapolation to zero pressure (green line) for the homochiral complex $(S,S\text{-}\mathbf{3b})_2Cu^+$ with loss of $S,S\text{-}\mathbf{3b}$ (569 → 316): black squares: 30.00 μtorr, blue squares: 50.00 μtorr, red squares: 70.00 μtorr; offset scan range: −90 to 10 V.
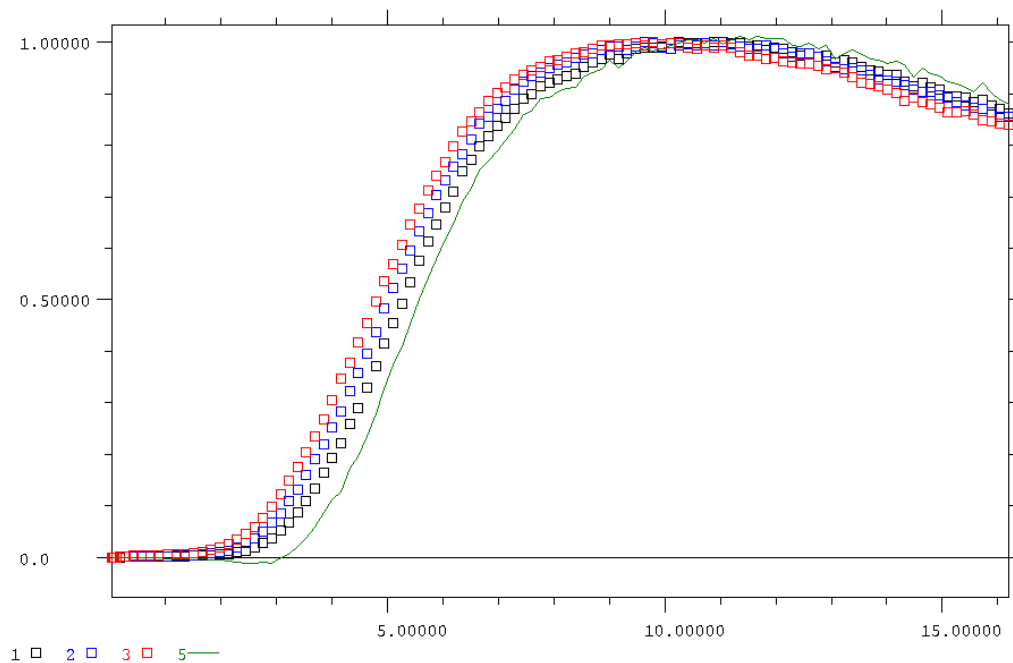
Fitted zero-pressure-extrapolation curve of the homochiral complex $(S,S\text{-}\mathbf{3b})_2Cu^+$ with loss of $S,S\text{-}\mathbf{3b}$:
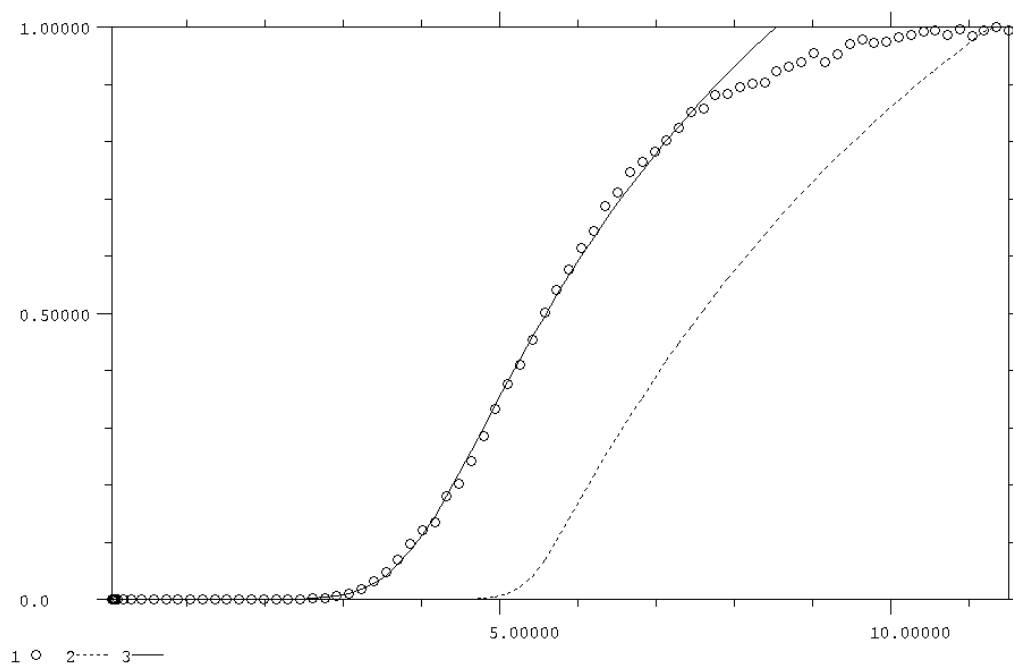
Mass scan of the $(S,S\text{-}\textbf{3b})(R,R\text{-}\textbf{3c})_2Cu^+$ solution: the heterochiral complex (583), the 1:1 complexes (316, 330) as well as the free ligands (253, 267) appear in this solution.
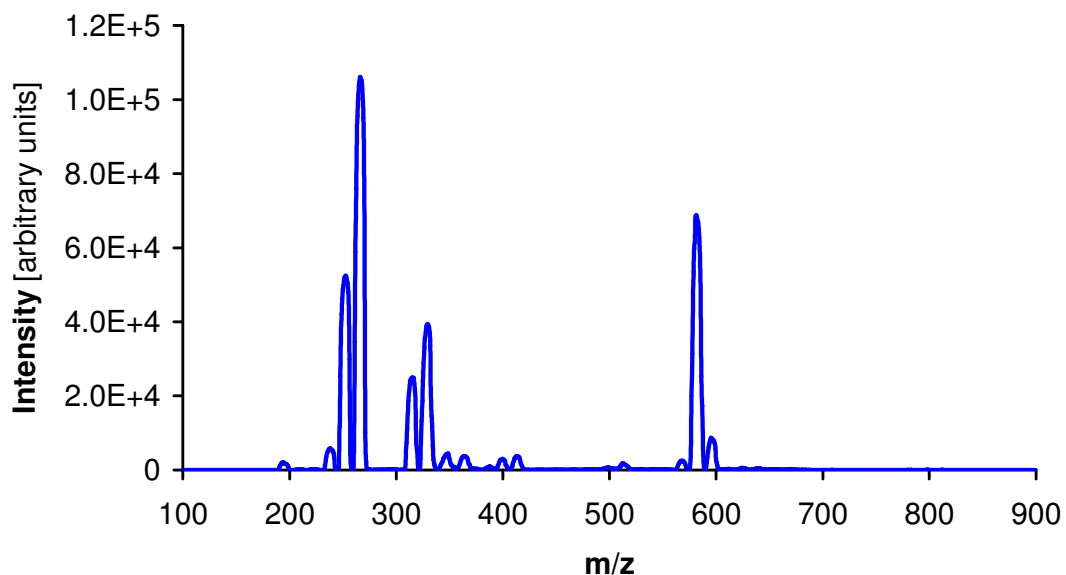
CID measurement of the heterochiral complex $(S,S\text{-}\textbf{3b})(R,R\text{-}\textbf{3c})_2Cu^+$ with loss of $S,S\text{-}\textbf{3b}$ or $R,R\text{-}\textbf{3c}$ (583 → 330 and 583 → 316) at 60 µtorr and an instrument offset of −90 V. The half-width of the kinetic energy distribution without collision gas is 2.1129 eV, the variation is 0.60236.
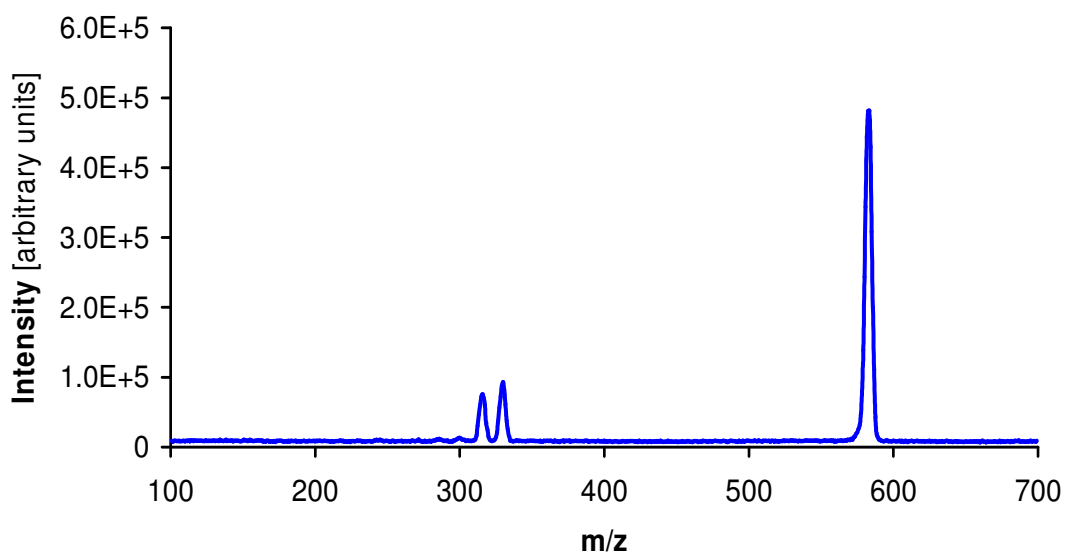
Extrapolation to zero pressure (green line) for the heterochiral complex $(S,S\text{-}\mathbf{3b})(R,R\text{-}\mathbf{3c})_2\text{Cu}^+$ with loss of $S,S\text{-}\mathbf{3b}$ (583 → 330): blue squares: 30.00 μtorr, black squares: 50.00 μtorr, red squares: 70.00 μtorr; offset scan range: −90 to 10 V.
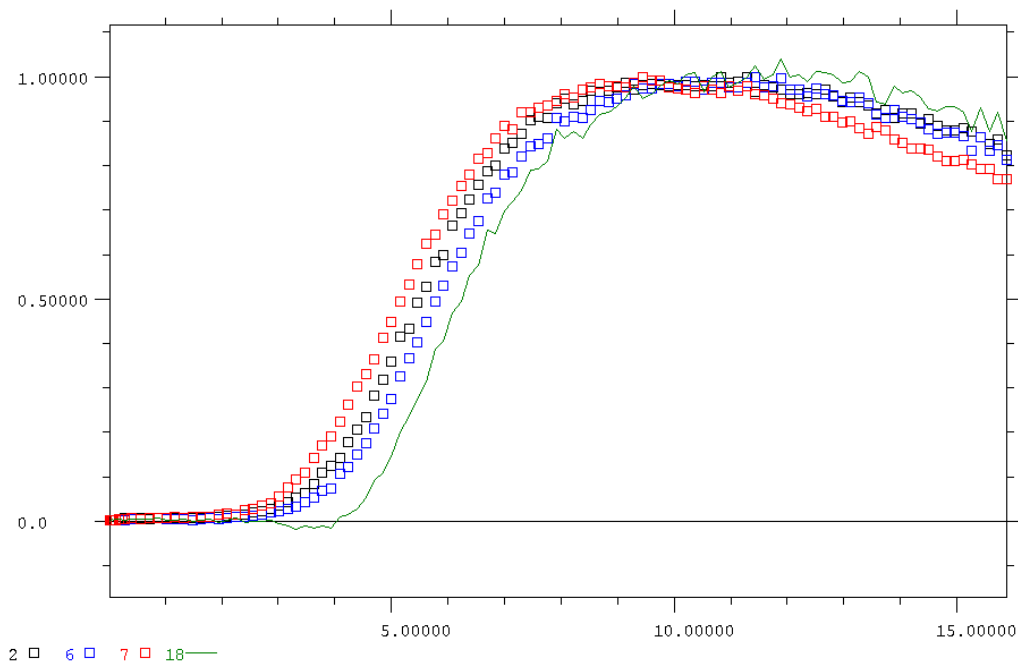
Fitted zero-pressure-extrapolation curve of the heterochiral complex $(S,S\text{-}\mathbf{3b})\text{-}(R,R\text{-}\mathbf{3c})_2\text{Cu}^+$ with loss of $S,S\text{-}\mathbf{3b}$:
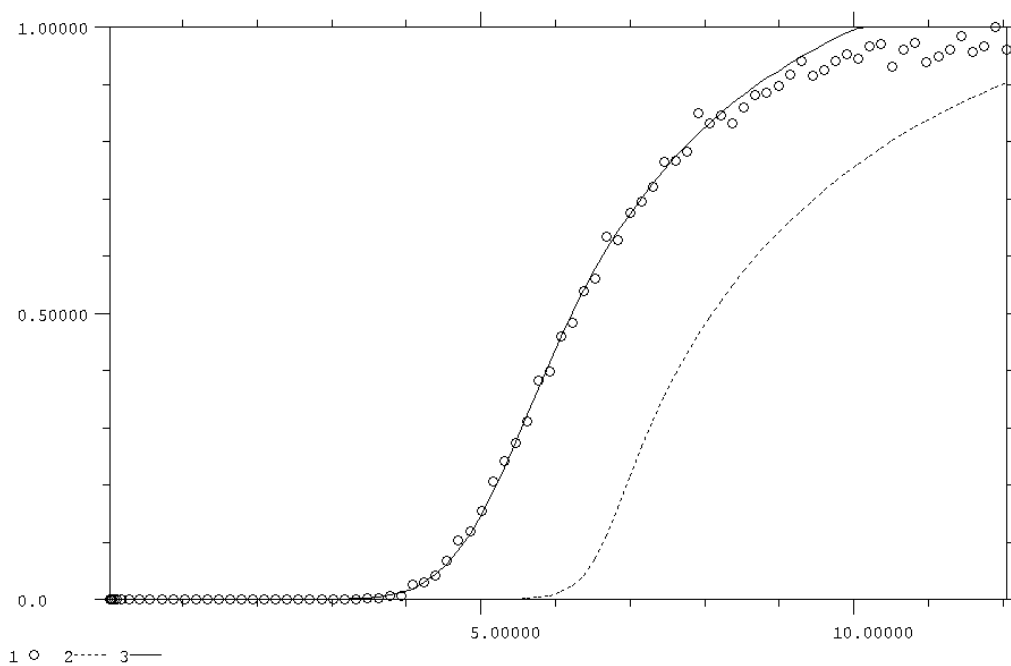
Extrapolation to zero pressure (green line) for the heterochiral complex (S,S-**3b**)(R,R-**3c**)$_2$Cu$^+$ with loss of R,R-**3c** (568 → 316): black squares: 50.00 μtorr, blue squares: 70.00 μtorr, red squares: 90.00 μtorr; offset scan range: −90 to 10 V.
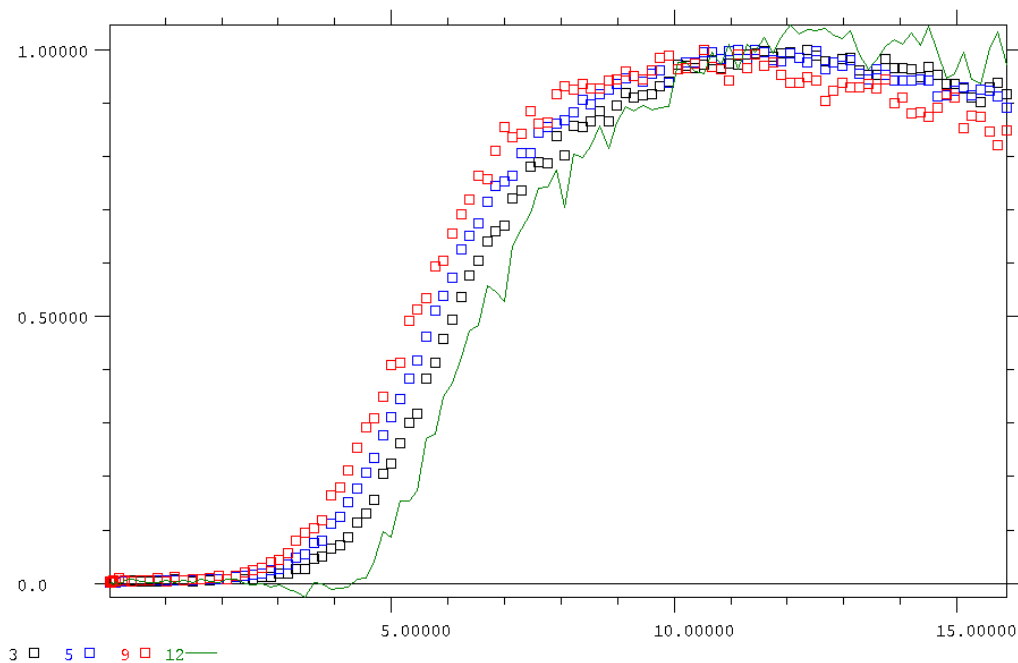
Fitted zero-pressure-extrapolation curve of the heterochiral complex (S,S-**3b**)-(R,R-**3c**)$_2$Cu$^+$ with loss of R,R-**3c**:
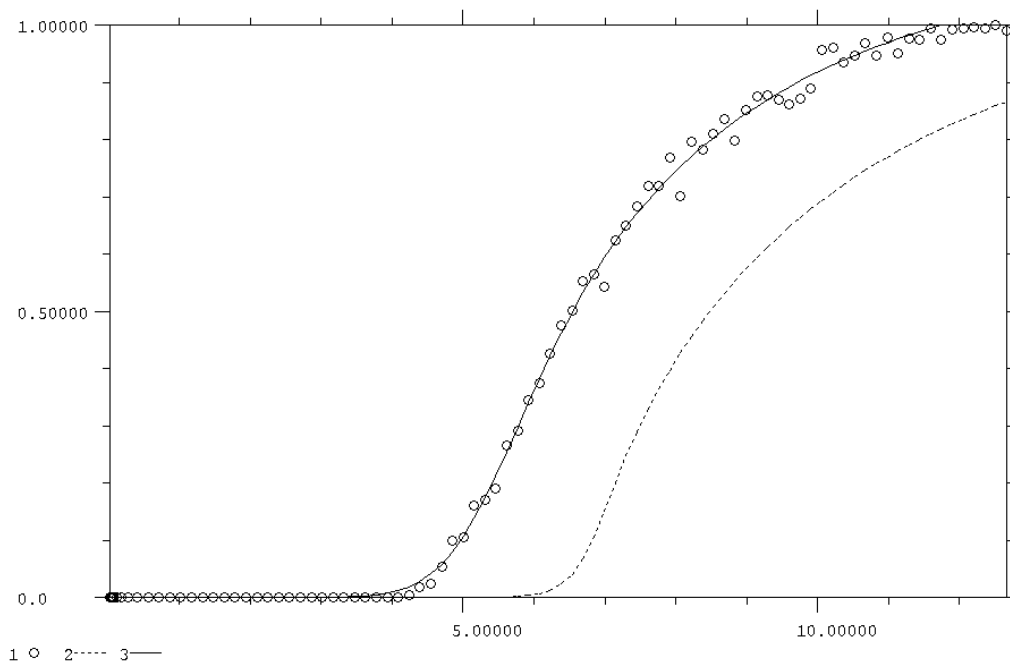
Two-Channel-Fit with the daughter peaks of the heterochiral complex (*S*,*S*-**3b**)(*R*,*R*-**3c**)$_2$Cu$^+$ showing the relative intensity scaling for the two channels. The black data points and the black fitted curve belong to the (*R*,*R*-**3c**)Cu$^+$ fragment, whereas the blue ensemble belongs to the (*S*,*S*-**3b**)Cu$^+$ fragment.
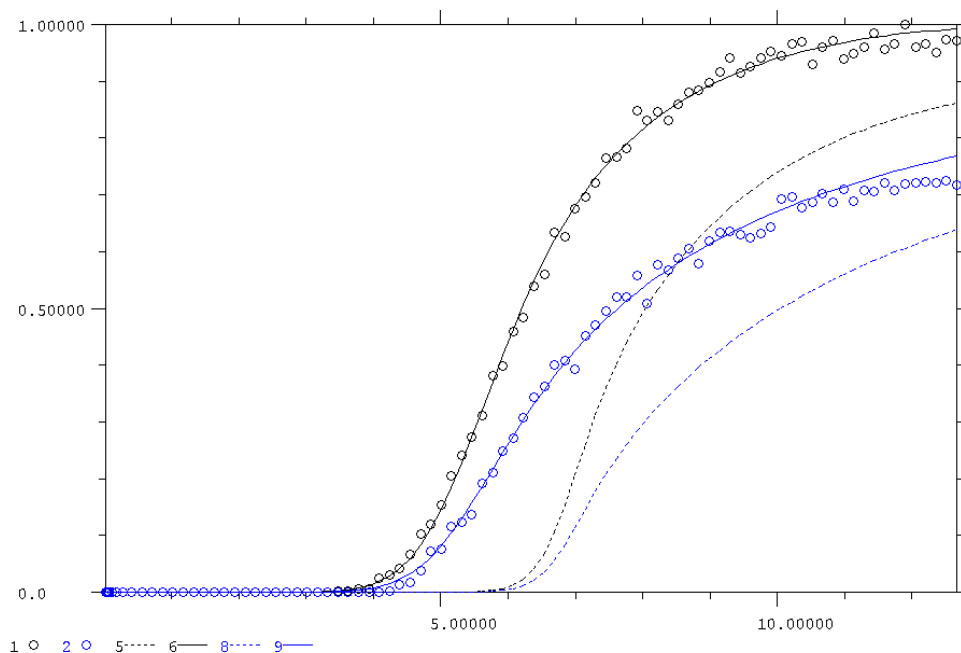
For relative scaling of the two product channels at *m/z* = 316 and *m/z* = 330 the ratio of the integrated peak areas (scaling factor: 0.725) was determined at an instrument offset of −33 V.

CID of the heterochiral complex (*S*,*S*-**3b**)(*R*,*R*-**3c**)Cu$^+$
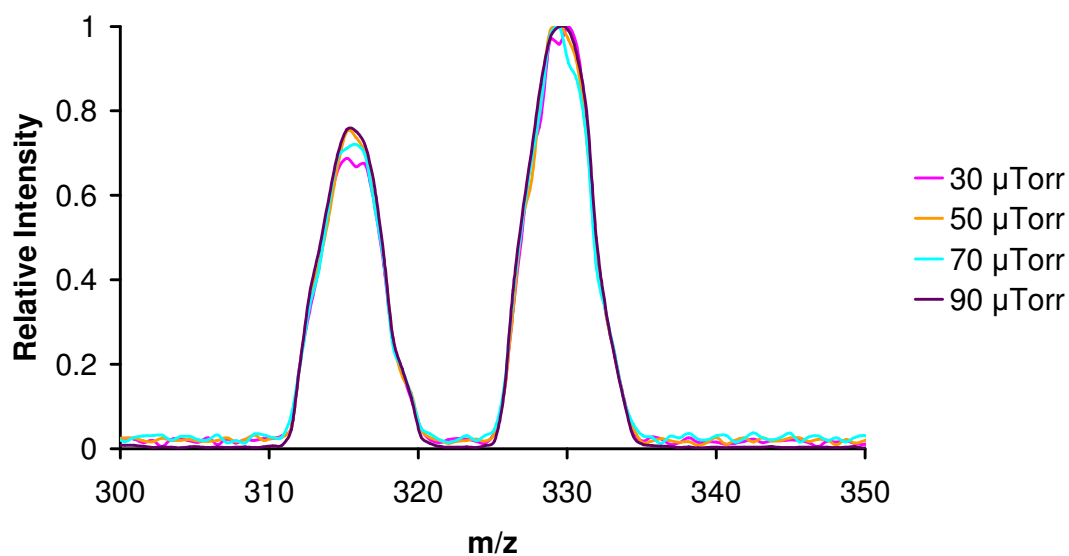
10.4 Data Sets processed with L-CID

Mass scan of the $(R,R\text{-}\mathbf{4c})_2Cu^+$ solution: the homochiral complex (733) as well as 1:1 complex (398) and free ligand (335) are visible.
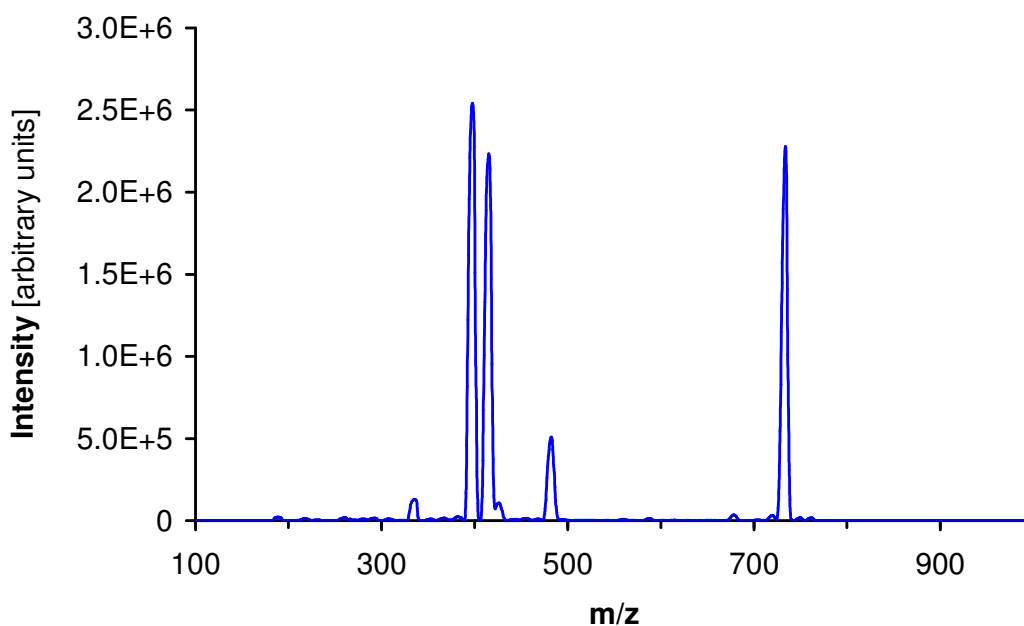
CID measurement of the homochiral complex $(R,R\text{-}\mathbf{4c})_2Cu^+$ (733 → 398) at 92 µtorr. The half-width of the kinetic energy distribution without collision gas is 1.90 eV, the variation is 0.39.
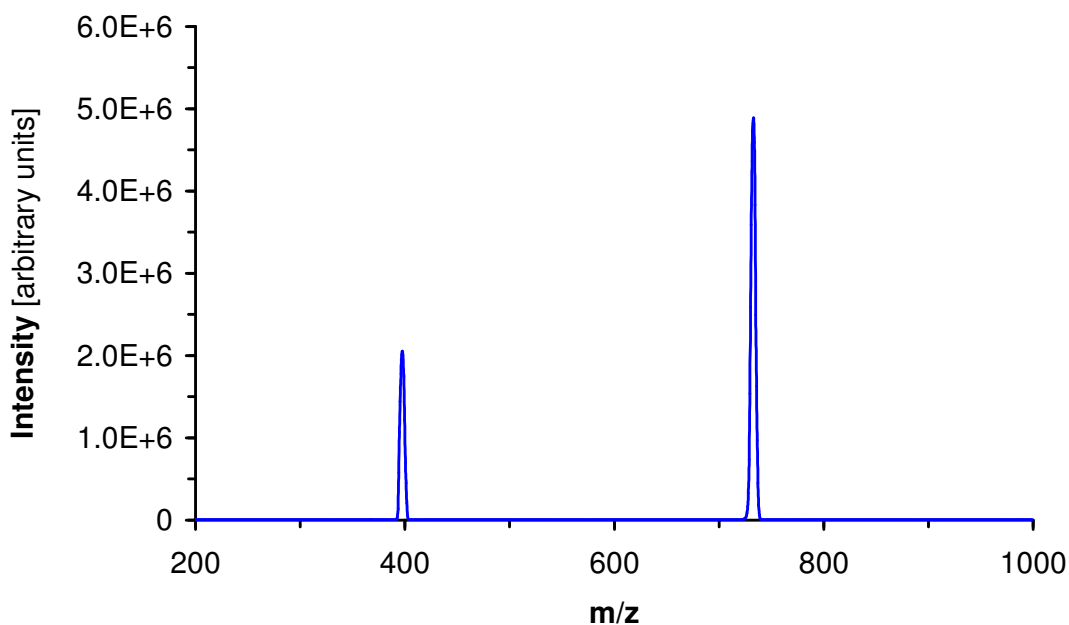
Extrapolation to zero pressure (green line) for the homochiral complex $(R,R\text{-}\mathbf{4c})_2Cu^+$ with loss of $R,R\text{-}\mathbf{4c}$ (733 → 398): orange squares: 30 µtorr, red squares: 51 µtorr, violet squares: 72 µtorr , blue squares: 95 µtorr, green squares: 120 µtorr; offset scan range: −120 to 20 V.
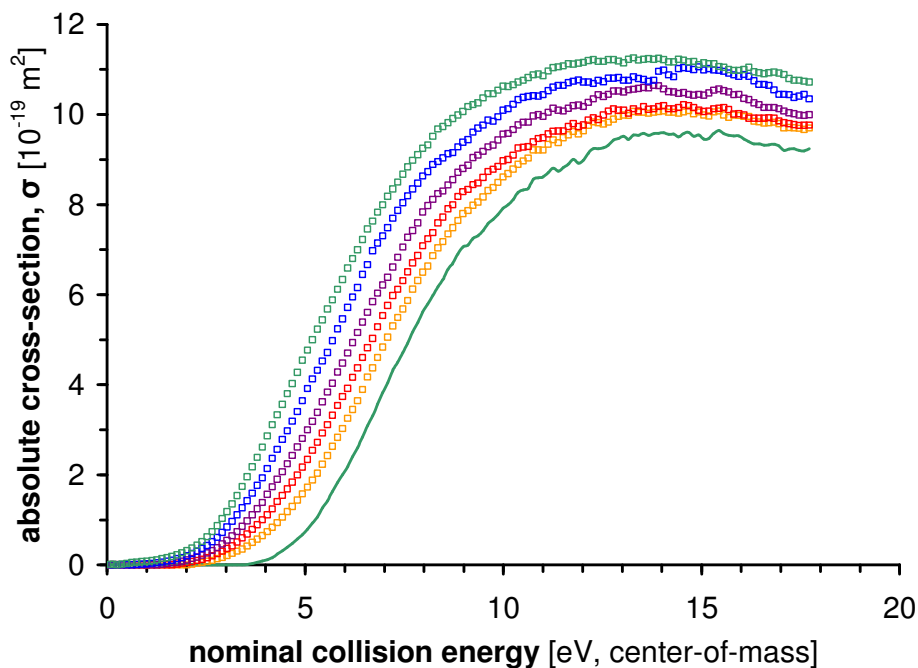
Fitted zero-pressure-extrapolation curve of the homochiral complex $(R,R\text{-}\mathbf{4c})_2Cu^+$ with loss of $R,R\text{-}\mathbf{4c}$:
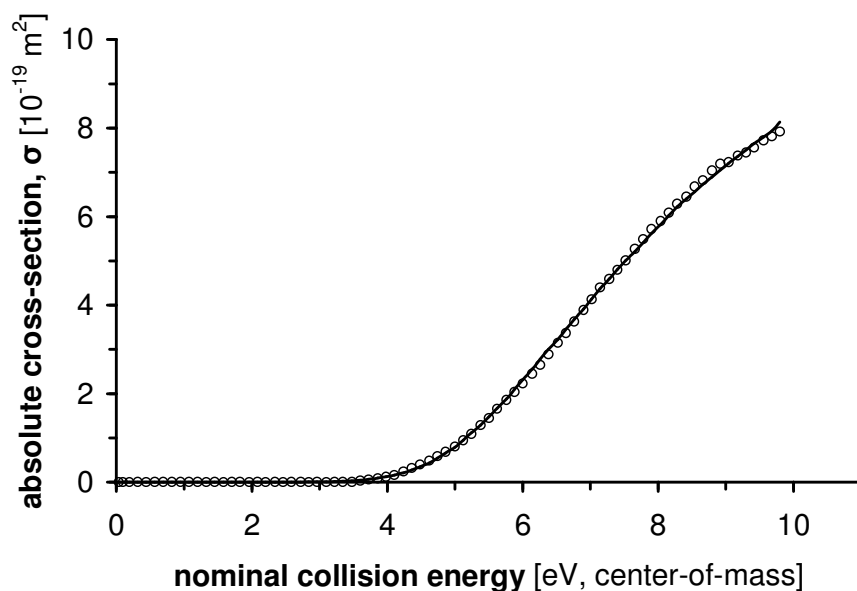
Mass scan of the $(S,S\text{-}\mathbf{4b})(R,R\text{-}\mathbf{4c})\text{Cu}^+$ solution: the heterochiral complex (719) as well as the 1:1 complexes (384, 398) and free ligand (321, 335) are visible.
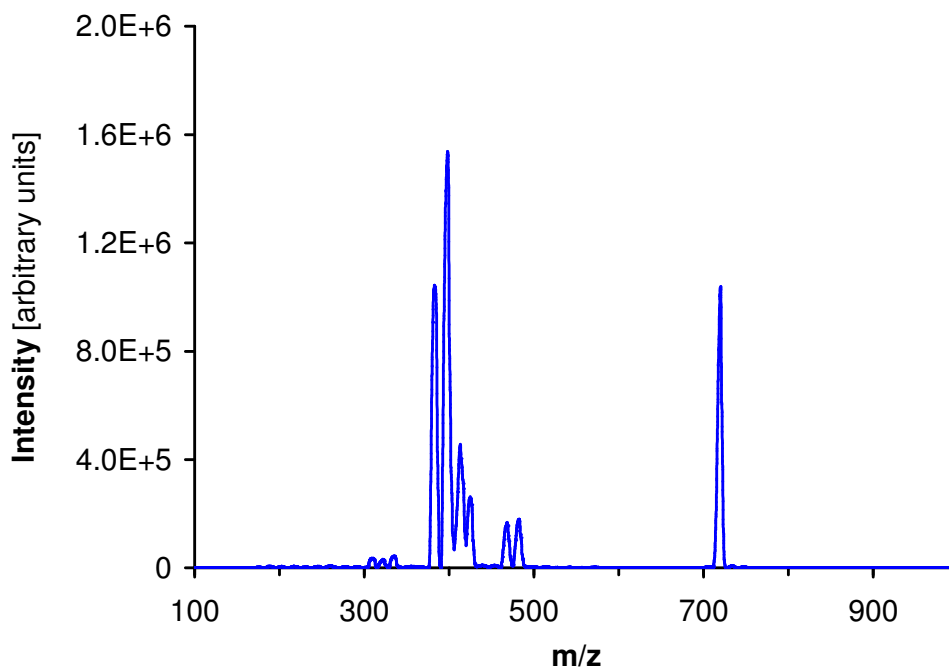
CID measurement of the heterochiral complex $(S,S\text{-}\mathbf{4b})(R,R\text{-}\mathbf{4c})\text{Cu}^+$ (719 → 384 and 398) at 93 µtorr. The half-width of the kinetic energy distribution without collision gas is 1.92 eV, the variation is 0.42.
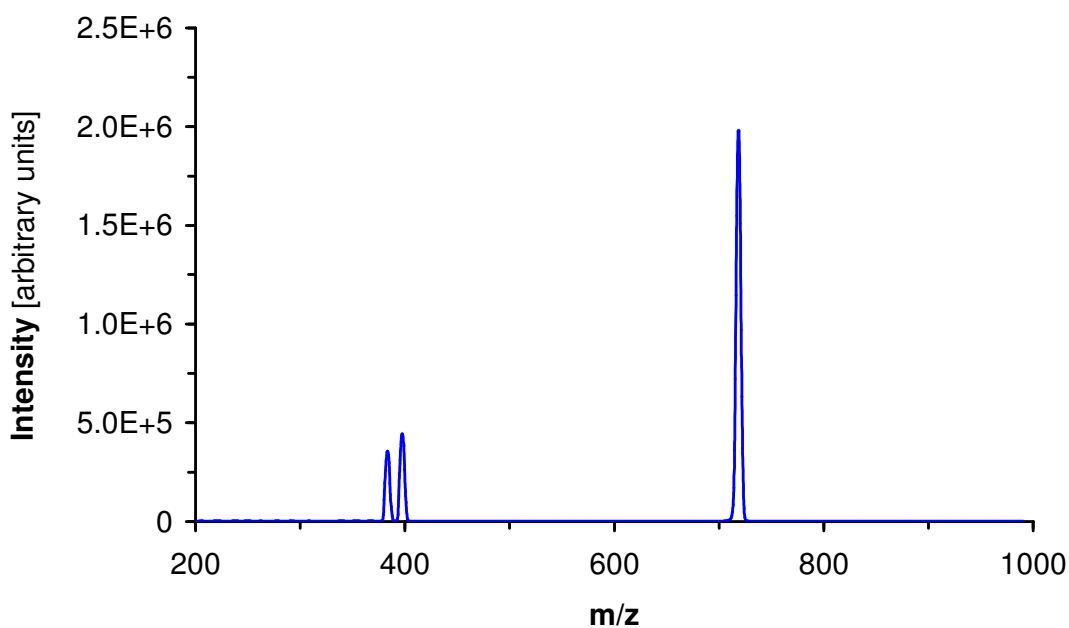
Extrapolation to zero pressure (green line) for the heterochiral complex (*S,S*-**4b**)(*R,R*-**4c**)Cu⁺ with loss of *R,R*-**4b** (719 → 398): orange squares: 32 µtorr, red squares: 52 µtorr, violet squares: 71 µtorr, blue squares: 93 µtorr, green squares: 113 µtorr; offset scan range : −120 to 20 V.
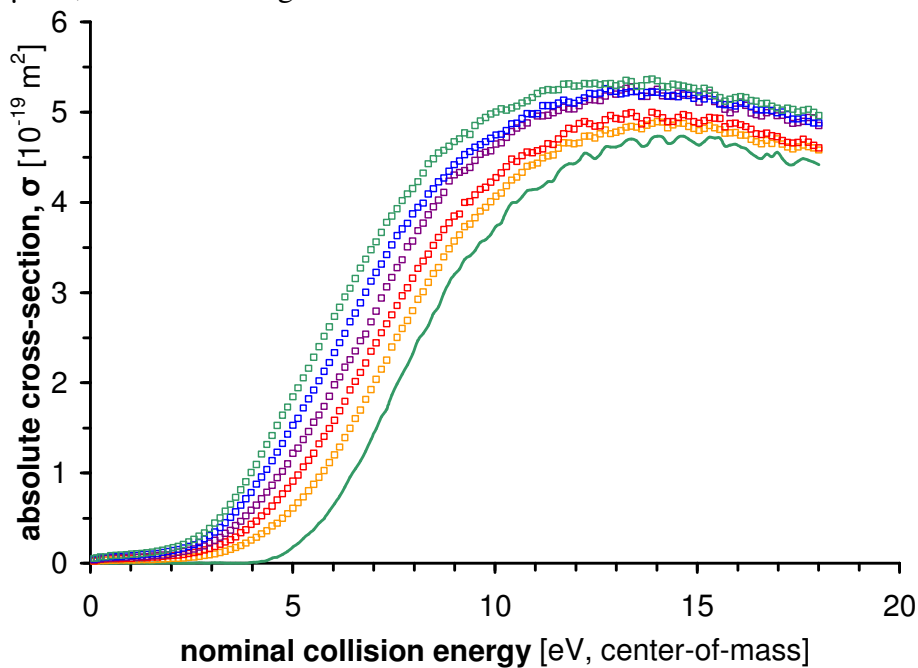
Extrapolation to zero pressure (green line) for the heterochiral complex (*S,S*-**4b**)(*R,R*-**4c**)Cu⁺ with loss of *R,R*-**4c** (719 → 384): orange squares: 32 µtorr, red squares: 52 µtorr, violet squares: 71 µtorr, blue squares: 93 µtorr, green squares: 113 µtorr; offset scan range: −120 to 20V.
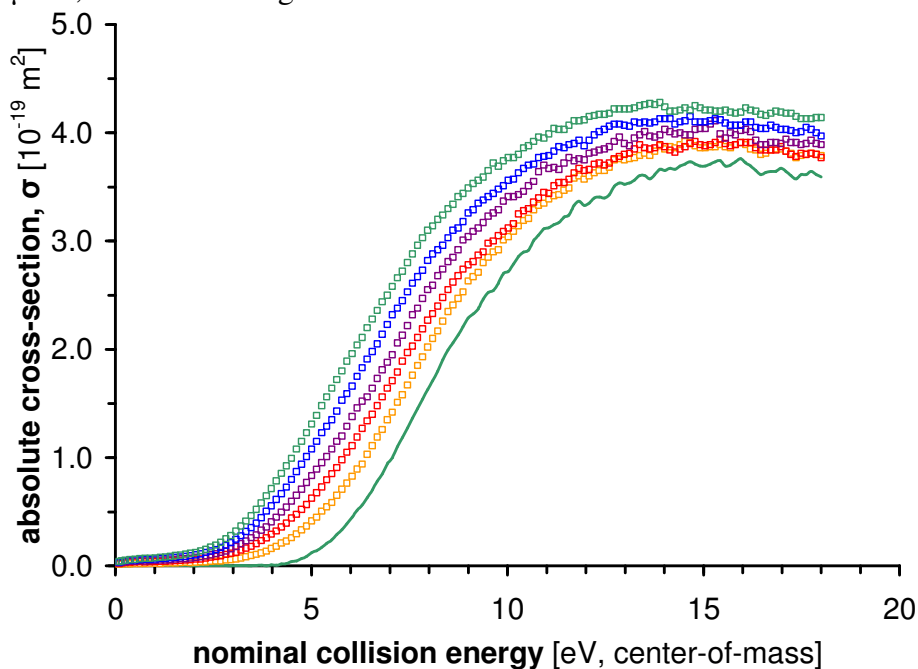
Fitted zero-pressure-extrapolation curves of the heterochiral complex (*S,S*-**4b**)-(*R,R*-**4c**)Cu$^+$ with loss of *S,S*-**4b** (black data points and black fitted curve) and loss of *R,R*-**4c** (depicted in blue):
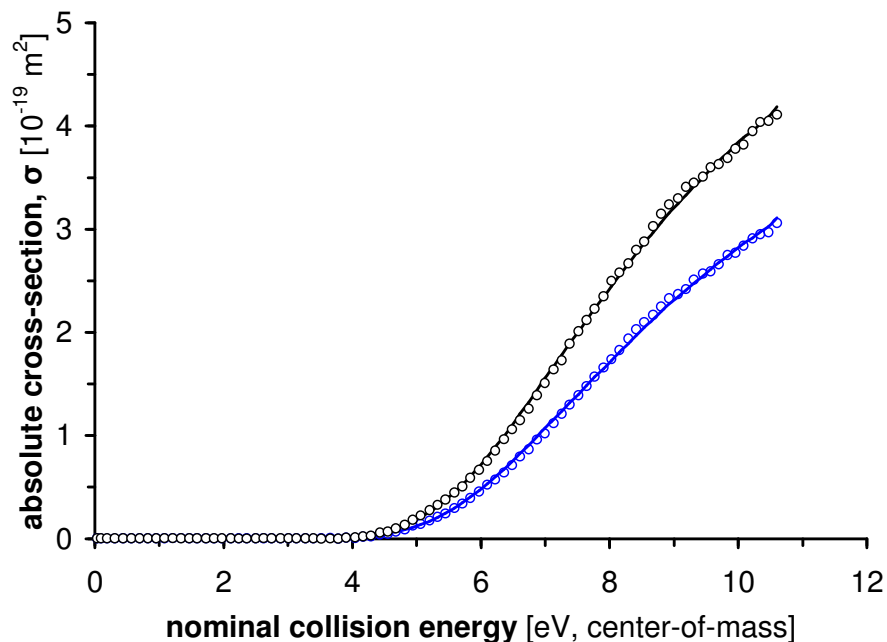
Fitted zero-pressure-extrapolation curve of the homochiral complex (*R,R*-**4b**)$_2$Cu$^+$ with loss of *R,R*-**4b**. The fitting was performed with L-CID.
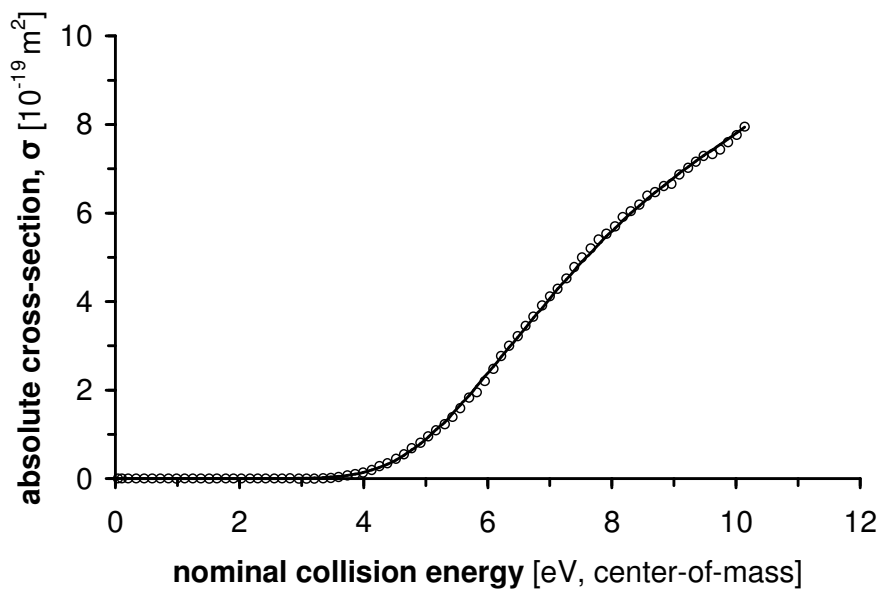
For comparison: CRUNCH-D1 fitted zero-pressure-extrapolation curve of the homochiral complex $(R,R\text{-}\mathbf{4b})_2Cu^+$ with loss of $R,R\text{-}\mathbf{4b}$:
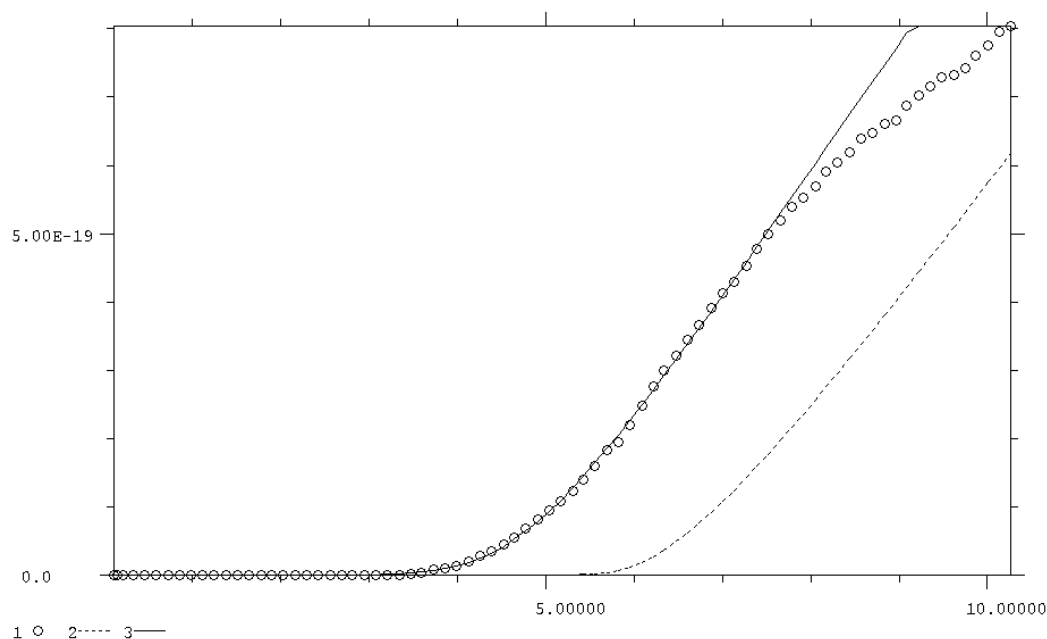
10.5 Probing Nonlinear Effects with Catalytic Cyclo-propanation Reactions

0.03 mmol (nonenantiopure) chiral ligand(s) **1a** or **2a** are joined in the glovebox with 2.6 mg CuOTf (0.01 mmol) in 2 mL dry CH_2Cl_2. After 5 minutes stirring and the occurrence of a pink colour 70 μL styrene (0.6 mmol) are added. The Schlenk tube is then transferred to the Schlenk line (Argon, room temperature) and the solution is stirred for 40 minutes, leading to a even more intense colouring. As next step 53 μL EDA (0.5 mmol), diluted in the glovebox with 0.8 mL dry CH_2Cl_2, are added with a syringe pump over 8 hours. After 16 hours additional reaction time the reaction mixture is concentrated and separated from the catalyst by filtration over silica (PE:EA = 15:1). The obtained solution is again concentrated and the asymmetric inductions are determined by chiral GC-MS over a SUPELCO BETADEX^{TM} 120 FUSED SILICA Capillary column (30 m × 0.25 mm × 0.25 μm). Best separation of the enantiomeric cyclopropanes is obtained with a constant Helium flow of 0.9 mL/min at 115 °C isotherm (split flow 26 mL/min, split ratio 17, interface

temperature 170 °C, filament current 150 µA). The elution order (($1S,2R$)-cis, ($1R,2S$)-cis, (R,R)-trans, (S,S)-trans) has been assigned by comparing the product peaks for enantiopure chiral ligand **1a** with literature values.[2]

A typical GC-MS spectrum with zoom in the region of interest is displayed below.
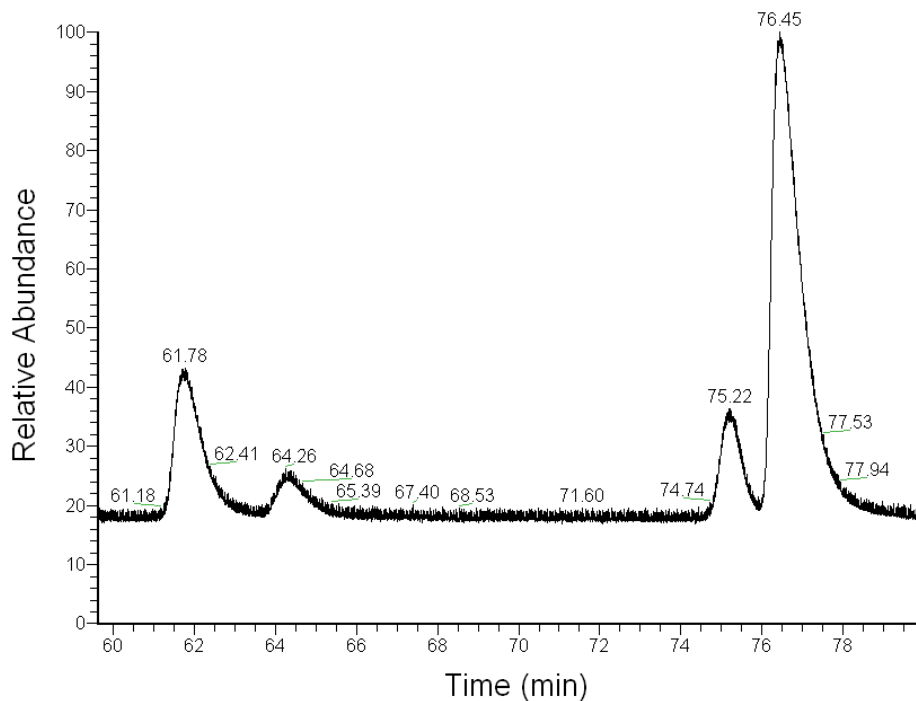
10.6 References

[1]   a) Rodgers, M. T.; Armentrout, P. B.; *J. Chem. Phys.* **1998**, *109*, 1787; b) Amicangelo, J. C.; Armentrout, P. B.; *International Journal of Mass Spectrometry* **2001**, *212*, 301; c) Amicangelo, J. C.; Armentrout, P. B.; *J. Phys. Chem. A* **2004**, *108*, 10698

[2]   a) Lowenthal, R. E., Abiko, A.; Masamune, S.; *Tetrahedron. Lett.* **1991**, *31*, 6005–6008; b) Fritschi, H.; Leutenegger, U.; Pfaltz, A.; *Helvetica Chimica Acta* **1988**, *71*, 1553–1565

List of Figures

List of Schemes

List of Tables

List of Abbreviations and Acronyms

box	bisoxazoline
azabox	aza-bisoxazoline
COD	1,4-cyclooctadiene
ESI-MS	electrospray ionization mass-spectrometry
CID	collision induced dissociation
L-CID	ligand collision induced dissociation
NLE	nonlinear effect
p-TSA	*para*-toluene sulfonic acid
C_2	twofold symmetry axis
THF	tetrahydrofuran
EDA	ethyl-diazoacetate
HMPA	hexamethylphosphoric triamide
Rg	rare gas atom
RRKM	Rice-Ramsperger-Kassel-Markus (theory)
IVR	intramolecular vibrational energy redistribution
RF	radiofrequency
Q1, Q2	first/second quadrupole
AC	alternating current
DC	direct current
KERD	kinetic energy release distribution
NMR	nuclear magnetic resonance

CuOTf	copper(I) triflate
DFT	density functional theory
CCSD(T)	coupled cluster theory with triple excitation
Bp	dihydridobis-(1-pyrazolyl) borate
bipy	2,2'-bipyridine
GC	gas-chromatography
VT-NMR	variable temperature (NMR)
HOMO	highest occupied molecular orbital
LUMO	lowest unoccupied molecular orbital
S_N1	nucleophilic substitution type one
S_N2	nucleophilic substitution type two
Å	Ångstrœm; 1 Å = 10^{-10} m
Me	methyl
Et	ethyl
^{i}Pr	iso-propyl
ee	enantiomeric excess
E_{cm}	energy in center of mass frame
E_{lab}	energy in laboratory frame
TS	transition state

"Not everything that can be counted counts,
and not everything that counts can be counted."

Albert Einstein
(1879−1955)

Curriculum Vitae

Eva Maria Zocher
Born January 3rd, 1980 in Altoetting, Bavaria
Citizen of Germany

Education

1986–1990	Primary School in Burghausen, Germany
1990–1999	Gymnasium in Burghausen

University Education

10/1999–12/2003	Studies in Chemistry at the University of Regensburg, Germany
01/2004–10/2004	Diploma thesis in the group of Prof. Dr. O. Reiser, University of Regensburg, Prof. Dr. MG Finn, Scripps Research Institute, San Diego, USA, on the subject: "Immobilisation of Metal-Ligand Systems to Cowpea Mosaic Virus (CPMV) and PAMAM Dendrimers"
12/2004–09/2008	PhD thesis in the group of Prof. Dr. P. Chen, ETH Zurich, on the subject: "Gas-Phase and Solution-State Chemistry of Copper(I) Bis-oxazoline Complexes"

Teaching Experience

2005–2008	Teaching assistant for organic chemistry exercises
2006–2007	Supervision of two undergraduate research projects

Awards

07/1999	Award of the German Chemical Industries for the best marks of the year in chemistry in the school-leaving exam
1999–2004	Scholarship of Bavaria for highly gifted students
2001–2004	Membership at the nationwide scholarship of the "Studienstiftung des deutschen Volkes"